Hydrogen Adsorption by Alkali Metal Graphite Intercalation Compounds

Thesis by

Justin Purewal

In Partial Fulfillment of the Requirements

for the Degree of

Doctor of Philosophy

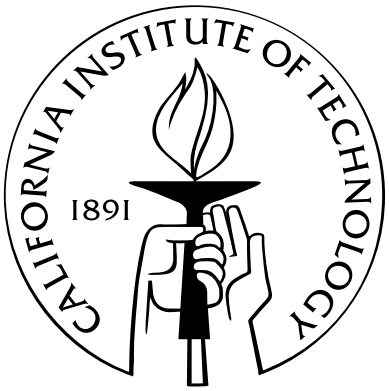

California Institute of Technology

Pasadena, California

2010

(Defended February 9, 2010)

Acknowledgements

There are many people that I would like to acknowledge for their help during my Ph.D. studies. First, I thank my thesis advisor, Prof. Brent Fultz, for his exceptionally thoughtful guidance and advice. It has been a privilege, and also a pleasure, to be able to discuss research with such a distinguished scientist each week. I am also deeply indebted to my co-advisor, Dr. Channing Ahn. In addition to providing exciting research projects to work on, he has also provided a great deal of practical research knowledge.

There are many people at Caltech who helped to teach me new research techniques. I particularly thank Carol Garland for her time and patience in teaching me how to use the TEM. Other people to whom I owe gratitude include: Sonjong Hwang, for collecting the NMR measurements; Liz Miura, for collecting the Raman measurements; Houria Kabbour, who taught me how to use the Sieverts instrument and was always happy to answer my many questions; Mike Vondrus, for machining a number of neutron scattering sample cans; Itzhak Halevy, for providing insight into high-pressure spectroscopy measurements; Brandon Keith, for extensive help with the molecular dynamics simulations, particularly in setting up the potentials, and for the help in answering my many UNIX-related questions. Max, Nick and Hillary, thanks for your help and company during the long trips to national labs. I also wish to express gratitude to the other current Fultz group members: David, Hongjin, Lisa, Jorge, Kun-Woo, Chen, and Mike. Lunch-times and conversations were always fun.

There are many outside collaborators who also need to be thanked, particularly Craig Brown and Madhu Tyagi at the NIST Center for Neutron Research. They played a huge role in helping me collect and interpret the neutron scattering data reported in this thesis. I owe a great deal of gratitude to Ron Cappelletti (NIST), who was happy to discuss the honeycomb jump diffusion model with me, and also made available some of his old computer codes for performing the fits. Also, I would like to thank Jason Simmons for helping with the isotherm measurements at NCNR. Lastly, I thank my family for their constant support over the years.

Financial support for this thesis was provided by the U. S. Department of Energy.

Abstract

Adsorption occurs whenever a solid surface is exposed to a gas or liquid, and is characterized by an increase in fluid density near the interface. Adsorbents have attracted attention in the ongoing effort to engineer materials that store hydrogen at high densities within moderate temperature and pressure regimes. Carbon adsorbents are a logical choice as a storage material due to their low costs and large surface areas. Unfortunately, carbon adsorbents suffer from a low binding enthalpy for H_2 (about $5\,\mathrm{kJ\,mol^{-1}}$), well below the 15 to $18\,\mathrm{kJ\,mol^{-1}}$ that is considered optimal for hydrogen storage systems. Binding interactions can be increased by the following methods: (1) adjusting the graphite interplanar separation with a pillared structure, and (2) introducing dopant species that interact with H_2 molecules by strong electrostatic forces. Graphite intercalation compounds are a class of materials that contain both pillared structures and chemical dopants, making them an excellent model system for studying the fundamentals of hydrogen adsorption in nanostructured carbons.

Pressure-composition-temperature diagrams of the $MC_{24}(H_2)_x$ graphite intercalation compounds were measured for M = (K, Rb, Cs). Adsorption enthalpies were measured as a function of H_2 concentration. Notably, CsC_{24} had an average adsorption enthalpy of $14.9\,\mathrm{kJ\,mol^{-1}}$, nearly three times larger than that of pristine graphite. The adsorption enthalpies were found to be positively correlated with the interlayer spacing. Adsorption capacities were negatively correlated with the size of the alkali metal. The rate of adsorption

is reduced at large H_2 compositions, due to the effects of site-blocking and correlation on the H_2 diffusion.

The strong binding interaction and pronounced molecular-sieving behavior of KC_{24} is likely to obstruct the translational diffusion of adsorbed H_2 molecules. In this work, the diffusivity of H_2 adsorbed in KC_{24} was studied by quasielastic neutron scattering measurements and molecular dynamics simulations. As predicted, the rate of diffusion in KC_{24} is over an order of magnitude slower than in other carbon sorbents (e.g. carbon nanotubes, nanohorns and carbon blacks). It is similar in magnitude to the rate of H_2 diffusion in zeolites with molecular-sized cavities. This suggests that H_2 diffusion in adsorbents is influenced very strongly by the pore geometry, and less strongly by the chemical nature of the pore surface. Furthermore, the H_2 diffusion mechanism in KC_{24} is complex, with the presence of at least two distinct jump frequencies.

Bound states of adsorbed H_2 in KC_{24} were investigated by inelastic neutron scattering measurements and first-principles DFT calculations. Spectral peaks in the neutron energy loss range of 5 meV to 45 meV were observed for the first time. These peaks were interpreted as single- and multi-excitation transitions of the H_2 phonon and rotational modes. The rotational barrier for H_2 molecules is many times larger in KC_{24} than in other carbon adsorbents, apparently due to the confinement of the molecules between closely-spaced graphitic layers. Evidence was found for the existence of at least three H_2 sorption sites in KC_{24}, each with a distinctive rotational barrier.

Contents

List of Figures

List of Tables

Chapter 1

Hydrogen Storage Materials

1.1 Introduction

Hydrogen has drawn attention as a next-generation energy carrier for mobile and stationary power sources [1]. It has a number of advantages over other chemical energy carriers. First, the energy conversion process is a clean one, with water as the waste product. Second, hydrogen can be produced reversibly by the dissociation of water. Lastly, hydrogen has a large chemical energy density per mass of around $39\,\mathrm{kWhkg^{-1}}$, about three times larger than that of chemical fuels such as liquid carbons [2]. For applications with fuel cell vehicles, hydrogen needs to be stored at high densities . Ideally, it should be contained within a small volume without adding too much additional weight to the vehicle. A driving range of at least 300 miles is considered crucial for the commercial success of a light-duty vehicle. This translates into an on-board storage requirement of 5 kg to 13 kg of hydrogen based on projected future fuel cell efficiencies [3]. Unlike other chemical fuels, however, the intermolecular forces in hydrogen are very weak. At ambient conditions of 20 ℃ and 1 bar, a mass of 1 kg of hydrogen occupies a volume of $11.9\,\mathrm{m^3}$. The goal of hydrogen storage research is to decrease this volume while staying within specific temperature and pressure limits.

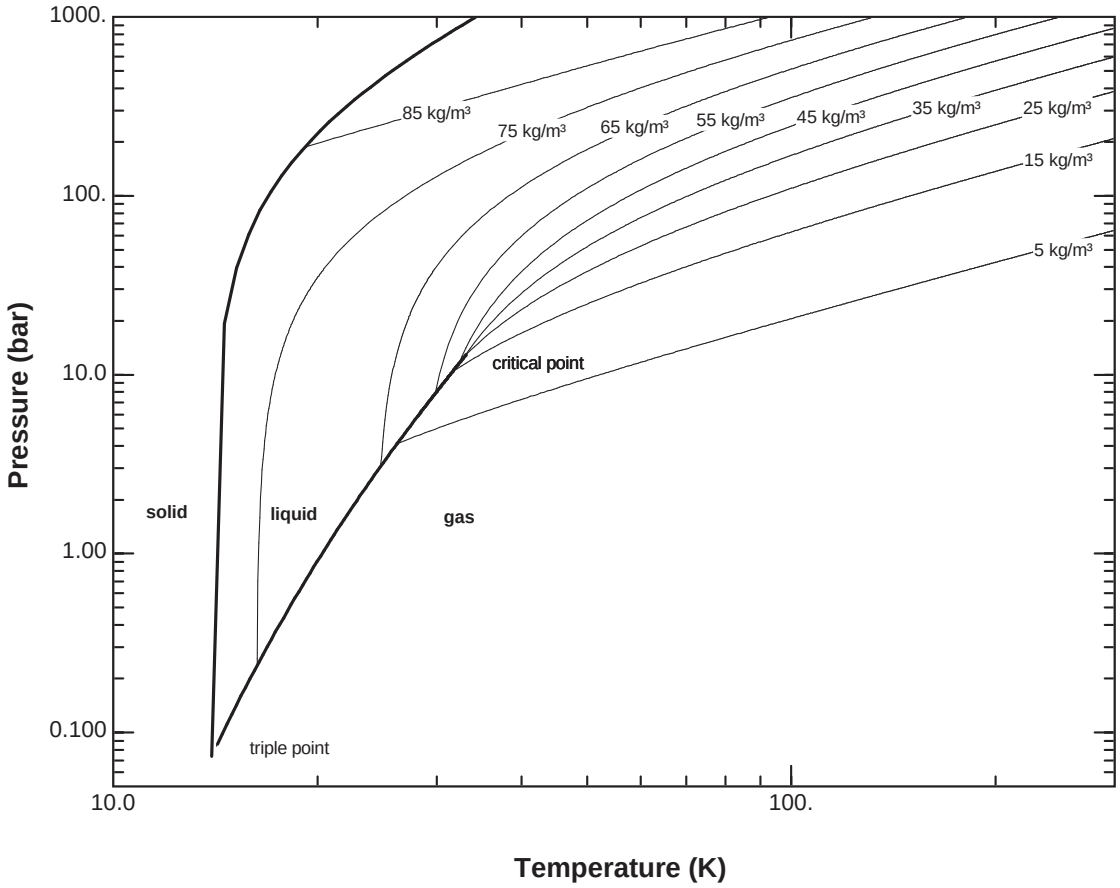

Figure 1.1: Phase diagram for H_2. The melting line and the liquid-vapor line are drawn as bold lines. The triple point and the critical point are both labeled. Constant density contours are drawn as thin lines.

1.2 Physical storage of hydrogen

The fundamental difficulty of storing hydrogen as a liquid or compressed gas is evident in the hydrogen p-T phase diagram shown in Fig. 1.1. At the triple point ($T = 13.803\,\mathrm{K}$, $p = 0.0704\,\mathrm{bar}$) the solid density is $\rho_\mathrm{s} = 86.48\,\mathrm{kg\,m^{-3}}$, the liquid density is $\rho_\mathrm{l} = 77.03\,\mathrm{kg\,m^{-3}}$, and the vapor pressure is a modest 0.07 bar. In the small region between the triple point and the critical point, hydrogen exists as a liquid with a normal boiling point of 20.39 K. If liquid hydrogen is stored in a closed vessel, continuous boil-off can lead to pressures of $10^4\,\mathrm{bar}$. The critical point ($T_\mathrm{c} = 32.98\,\mathrm{K}$, $p_\mathrm{c} = 13.25\,\mathrm{bar}$) of H_2 occurs at a temperature

Table 1.1: Current DOE revised technical targets for on-board hydrogen storage systems for light-duty vehicles

Storage Parameter	Units	2010	2015	Ultimate
System gravimetric capacity[a]	$kg(H_2)/kg(System)$[b]	0.045	0.055	0.075
	kWh/kg	(1.5)	(1.8)	(2.5)
System volumetric capacity	kg/m^3	28	40	70
	kWh/m^3	(900)	(1300)	(2300)
Min/max delivery temperature	K	233/358	233/358	233/358
Cycle life	Cycles	1000	1500	1500
Min delivery pressure	atm	4FC/35ICE[c]	3FC/35ICE	3FC/35ICE
Max delivery pressure	atm	100	100	100
System fill time	kg/min	1.2	1.5	2.0
Fuel purity	Percent H_2		99.99 (dry basis)	

[a] The listed gravimetric and volumetric capacities are *system* targets that include the mass and volume of the system itself, including the tank, material, valves, regulators and other parts. Material capacities may need to be up to twice as large as system capacities. See Ref. [4].
[b] The standard practice here is to define the gravimetric (volumetric) density relative to the maximum final mass (volume) of the combined hydrogen-host system.
[c] FC=fuel cell, ICE=internal combustion engine

which is quite low compared to other gases. Above this temperature hydrogen cannot be liquefied by increasing the pressure. Therefore if the storage system is to operate at higher temperatures, the hydrogen will exist in the gas phase. From the constant density contours in Fig. 1.1, it is clear that at room temperature a pressure of over 1000 bar is required to achieve densities on the order of the liquid or solid phases. This is possible using carbon-fiber-reinforced high-pressure cylinders, but is undesirable for on-board vehicle storage.

1.3 Technical targets for hydrogen storage materials

The U.S. Department of Energy's 2010 and 2015 technical targets for on-board vehicular hydrogen storage are a useful benchmark for comparing different storage methods [4]. Several of the current DOE technical targets are listed in Table 1.1. Operational characteristics such as the temperature, the min/max delivery pressure, the re-filling time, the cycle life, and the fuel purity are also crucial to the performance of the storage system.

Table 1.2: Comparison of hydrogen storage methods

Method	ρ_m (wt%)[a]	ρ_v (kg m^{-3})[b]	T (K)[c]	p (bar)[d]	Description
Compressed gas	13	< 40	273	800	Compressed hydrogen gas; lightweight, high-pressure cylinder
Liquid	Varies	70.8	21.5	1	Liquid hydrogen, continuous loss of a few % per day at RT
Physisorption	≈ 2	20	77	100	Physical adsorption by porous materials, fully reversible
Interstitial metal hydrides	≈ 2	150	273	1	Atomic hydrogen occupies interstitial sites, fully reversible, metals are heavy
Complex hydrides	< 18	150	> 100	1	Complex compounds $[BH_4]^-$ or $[AlH_4]^-$, desorption at elevated temperature, adsorption at high pressure
Chemical hydrides	< 40	> 150	273	1	Thermal decomposition of chemical hydrides, not directly reversible

[a] Gravimetric storage density [b] Volumetry storage density [c] Operational temperatures for storage method
[d] Operational pressures for the storage method [e] Table adapted from Ref. [2]

It is these criteria that make physical adsorption (i.e., physisorption) an attractive storage method. Adsorbed hydrogen does not chemically react during adsorption and, therefore, does not accumulate impurities which can poison the fuel-cell downstream. Because it does not involve bulk solid diffusion or chemical dissociation, the physisorption process is also extremely fast and fully reversible, allowing it to meet both the cycle-life and refilling-time targets. In Table. 1.2, physisorption is compared to the five other basic storage methods. The fundamental problem with physisorption-based storage is that, due to the weak binding interaction between the H_2 and the adsorbent surface, the hydrogen density at ambient conditions is too small.

1.4 Storage based on physisorption

Physical adsorption is a process where gas admolecules bind weakly onto the adsorbent surface by van der Waals (vdW) forces. Chemical bonds are not formed. The equilibrium

adsorption amount $n(T,p)$ is determined by the effective surface area of the adsorbent and the strength of the surface interaction. The adsorbed layer and the bulk gas are in equilibrium so the Gibbs free energies must be equal: $G_{\text{gas}} = G_{\text{ads}}$. Substituting $G = H - TS$ yields

$$H_{\text{ads}} - H_{\text{gas}} = T\left(S_{\text{ads}} - S_{\text{gas}}\right). \tag{1.1}$$

Adsorption involves a reduction in the degrees of freedom of the gas molecules so a tentative assumption $S_{\text{gas}} \gg S_{\text{ads}}$ can be made. For many adsorbents a change in entropy of $-8R$ can be estimated [5]. A simple estimate of the required enthalpy for room temperature storage is

$$\Delta H = H_{\text{ads}} - H_{\text{gas}} \approx -8RT_{\text{room}} = -20\,\text{kJ}\,\text{mol}^{-1}. \tag{1.2}$$

The importance of adsorption thermodynamics can be better illustrated using the Langmuir model.[1] For an equilibrium pressure p, the amount of adsorbed gas is given by

$$n(p) = n_{\max}\left(\frac{Kp}{1+Kp}\right), \tag{1.3}$$

where $n_{\max}$ is the maximum adsorption capacity of the material, and K is the equilibrium constant (which depends on both the temperature and the change in Gibbs free energy). As indicated in Table 1.1, hydrogen should be delivered between a minimum pressure of $p_{\min} = 3\,\text{bar}$ and a maximum pressure of $p_{\max} = 100\,\text{bar}$. The storage system cycles between these operational pressure limits, and the total delivered hydrogen is the difference between $n(p_{\max})$ and $n(p_{\min})$. We want to determine the enthalpy which optimizes the hydrogen delivery between these pressure limits [5]. For an operating temperature of 298 K,

[1] Although the Langmuir model is meant to describe non-interacting adsorbed monolayers on a homogeneous surface, it also works well for describing hydrogen adsorption in microporous materials [6].

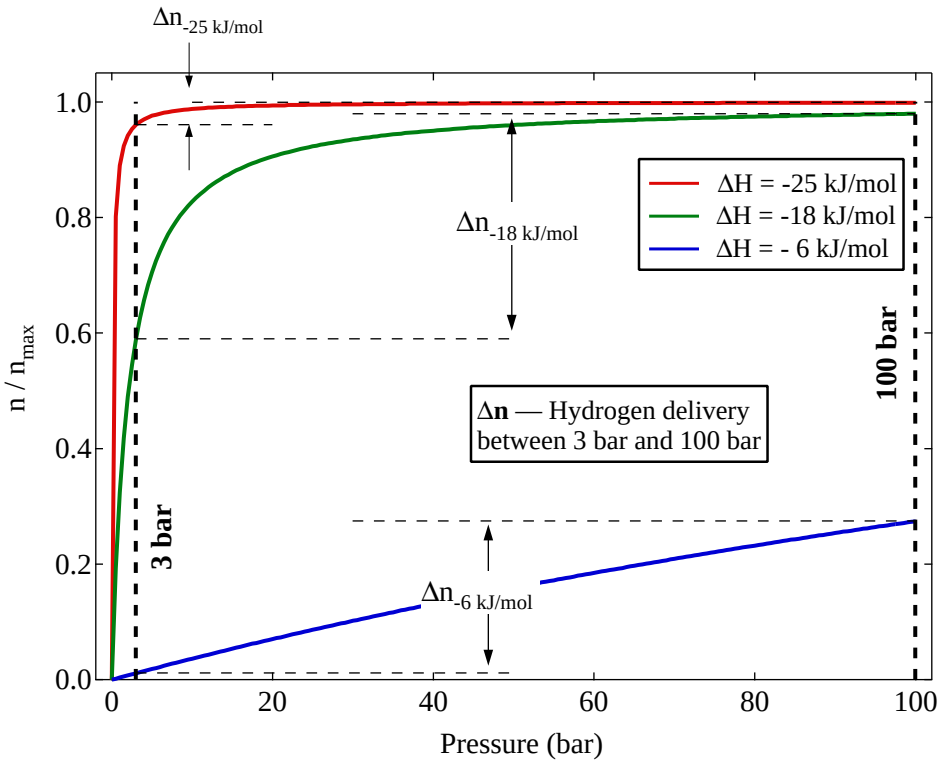

Figure 1.2: Langmuir isotherms for three different adsorption enthalpies (ΔH). Hydrogen delivery (Δn) for each isotherm is indicated by the vertical distance between the adsorption amounts at 3 bar and 100 bar.

realistic estimates of the optimum adsorption enthalpy typically give values around $\Delta H = -18\,\mathrm{kJ\,mol^{-1}}$ [7]. In Fig. 1.2, Langmuir adsorption isotherms are illustrated for various enthalpies of adsorption. It can be seen that the hydrogen delivery depends very strongly on the enthalpy. Because the isotherm for $\Delta H = -25\,\mathrm{kJ\,mol^{-1}}$ is very steep, for example, most hydrogen remains adsorbed when the pressure cycles down to 3 bar. On the other hand, the $-6\,\mathrm{kJ\,mol^{-1}}$ isotherm is very low, containing only a small amount of adsorbed hydrogen at 100 bar. An optimal adsorption enthalpy would occur between these two extremes, providing a larger amount of deliverable hydrogen capacity.

This example demonstrates the importance of *adsorption enthalpy* in determining the properties of a physisorption-based storage system. Because heterogeneous adsorption sites and hydrogen-hydrogen lateral interactions are omitted from the model, the adsorption

enthalpy remains constant as a function of n. But if the constant ΔH is replaced by one that decreases as a function of n, then hydrogen delivery is typically reduced [5]. This makes sense because a single enthalpy can be better optimized than a varying one simply by choosing the optimum enthalpy for every adsorption site. The ideal adsorbent for an isothermal storage system will likely have a constant ΔH of around $-18\,\mathrm{kJ\,mol^{-1}}$, although the specific values will depend on the operational pressure and temperature ranges.

1.5 The mechanism of physisorption

1.5.1 Overview

In Section 1.4 it was illustrated that the enthalpy of adsorption plays a central role in the operational characteristics of a physisorption-based system. To determine the thermodynamic limits of such a storage system a detailed understanding of this interaction energy is critical. Unfortunately, *ab initio* modeling of physisorption is much less developed than it is for chemisorption. The reason is that dispersion forces play a large role in the physisorption mechanism. Although density functional theory works quite well for chemically bound systems, it does not accurately treat long-range interactions of weakly-bound systems [8]. First principles methods capable of treating dispersion forces include the MP2 method (second-order Møller-Plesset perturbation theory) and CCSD(T) method (coupled cluster with single, double, and triple excitations). However these methods are too computationally expensive to apply to realistic adsorbent systems. In fact, empirical potentials are still a starting point for many computational studies of physisorption. In this section, the three main types of hydrogen physisorption interactions will be described.

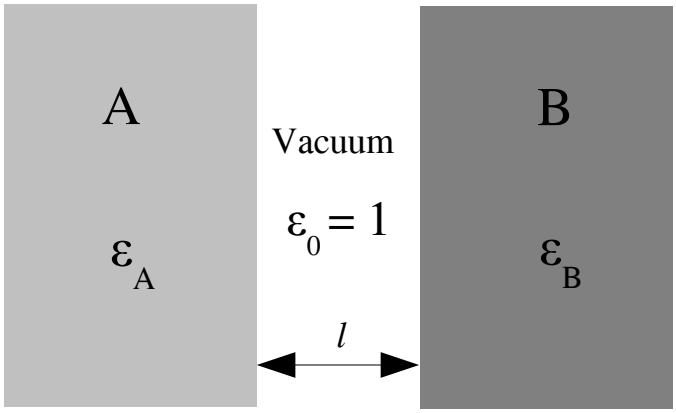

Figure 1.3: Schematic drawing of two semi-infinite slabs of material A and material B with a separation length of l. The region between the two slabs is vacuum. The dielectric constants of the three regions are denoted ϵ_A, ϵ_B and ϵ_0. Adapted from Ref. [9].

1.5.2 Dispersion interactions[2]

A famous example of dispersion forces is provided by the interactions between electrically neutral gas particles which cause deviations from ideal gas behavior at high densities. In brief, dispersion interactions are weak, long-range, nonspecific interactions which are due to charge fluctuations in the two interacting materials. These fluctuations can be due to phenomena such as ionic movements, dipole rotations, and dipole vibrations at the lower frequency end. However, it is the higher frequency electron fluctuations caused by the quantum mechanical uncertainty in position and momentum which contribute most to the interaction. A simple macroscopic system of dispersion interactions between material A and material B across a region of vacuum is illustrated in Fig. 1.3. An electron fluctuating in material A emits an oscillating electric field across the vacuum into material B. This in turn enhances charge fluctuations in material B which lower the overall electromagnetic energy. The mutual fluctuations in material A and material B are not simply random, but have a correlation that affects the total energy and results in a net force. The susceptibility

[2]The analysis presented in this section closely follows Ref. [9].

of each region to the time-varying electric fields, given by the dielectric response ϵ_{A}, ϵ_{B}, itself depends on the frequency of the oscillations. The free energy per unit area required to bring slabs A and B from infinity to a separation l is given by the Hamaker equation,

$$G(l) = \frac{k_{\mathrm{B}}T}{8\pi l^2} \sum_{n=0}^{\infty} d_{\mathrm{A}}(\xi_n)\, d_{\mathrm{B}}(\xi_n)\, R_n(l), \tag{1.4}$$

where the relative difference between the material dielectric responses $\epsilon_{\mathrm{A}}(\xi)$ and $\epsilon_{\mathrm{B}}(\xi)$ and the vacuum dielectric response $\epsilon_0 = 1$ is given by

$$d_{\mathrm{A}}(\xi) = \frac{\epsilon_{\mathrm{A}}(\xi) - 1}{\epsilon_{\mathrm{A}}(\xi) + 1}, \qquad d_{\mathrm{B}}(\xi) = \frac{\epsilon_{\mathrm{B}}(\xi) - 1}{\epsilon_{\mathrm{B}}(\xi) + 1}. \tag{1.5}$$

The relativistic screening term, $R_{\mathrm{n}}(l)$, damps the electron correlations at large distances due to the finite time that the fluctuating electric fields take to reach the other material. Since $R_{\mathrm{n}}(l)$ is only important at large separation distances, it can be ignored for physisorption. The sum in Eq. 1.4 is taken over a discrete sampling of the frequency (ξ_n).[3] The lowest frequencies are on the order of the thermal energy and may originate from vibrations or rotations of polar molecules. However, the sum is dominated by the larger UV and X-ray frequency range.

This macroscopic analysis can be reduced to the familiar point-particle interaction formulas if we assume material A and material B are regions of a dilute gas. In this case $\epsilon = 1 + N\alpha$, where N gives the number density of the dilute gas. The total polarizability

[3]The variable ξ is the imaginary component of the complex frequency, $\omega = \omega_{\mathrm{R}} + i\xi$. Another way to write this is $\exp(i\omega t) = \exp(-\xi t)\exp(i\omega_{\mathrm{R}} t)$. The real frequency, ω_{R}, corresponds to sinusoidal behavior, while the imaginary frequency represents a decaying exponential. The dielectric responses are expressed in terms of a characteristic relaxation time (τ) over which a spontaneous charge fluctuation dies out. For example, the UV and X-ray regions have relaxation times on the order of $\tau \leq 10^{-17}$ sec while molecular vibrations have $\tau \leq 10^{-16}$ sec. When written in terms of the relaxation time, the dielectric response is a smoothly varying curve. This is preferable to the large spikes near resonance that occur when the dielectric response is expressed in terms of ω_{R}.

α of each gas molecule consists of the permanent dipole moment (μ_{dip}) and the inducible polarizability (α_{ind}). If the molecules have a permanent dipole moment, then dipole-dipole (Keesom) and dipole-induced-dipole (Debye) interactions are present. These are the "zero-frequency" electrostatic interactions, given by

$$\text{(Keesom)} \qquad g(r) = -\frac{\mu_{\text{dipole}}^4}{3k_{\text{B}}Tr^6}, \tag{1.6a}$$

$$\text{(Debye)} \qquad g(r) = -\frac{2\mu_{\text{dipole}}^2}{r^6}\alpha_{\text{ind}}(0). \tag{1.6b}$$

The London force is caused by electron correlations at all frequencies. When the retardation screening factor is omitted, this interaction reads as

$$\text{(London)} \qquad g(r) = -\frac{6k_{\text{B}}T}{r^6}\sum_{n=0}^{\infty}\alpha_{\text{ind}}^2(i\xi_n). \tag{1.7}$$

London originally derived the r^{-6} expression in 1930 for two hydrogen atoms at large separation. From accurate first-principles calculations it is known that when hydrogen interacts with large molecules, the energy minimum for the London force occurs at about one molecular radius and has a binding energy on the order of several $\text{kJ}\,\text{mol}^{-1}$ [10]. When the charge distributions overlap at small separations, Pauli repulsion becomes the dominant force; it is typically modeled with a repulsive r^{-12} component in a Lennard-Jones potential.

1.5.3 Electrostatic interactions

The hydrogen molecule does not have a permanent dipole moment. Due to the prolate, non-spherical shape of the H_2 molecule, the first non-zero multipole moment is the quadrupole moment. The ion-quadrupole interaction goes as r^{-3} as a function of distance. Further, the hydrogen molecule is polarizable in the presence of external fields, and the ion-induced-

dipole interaction goes as r^{-4} as a function of distance. For a hydrogen molecule interacting with a unit charge at a distance of 3 Å, the ion-quadrupole interaction energy is about $3.5\,\mathrm{kJ\,mol^{-1}}$ [10]. The associated ion-induced-dipole interaction energy is about $6.8\,\mathrm{kJ\,mol^{-1}}$ [10]. In the presence of a strong external field, it would appear that electrostatic interactions are considerably larger than dispersion interactions. In reality, though, few adsorbent systems actually contain unscreened ionic charges. Even in a first approximation, dispersion forces cannot be ignored for physisorption systems.

1.5.4 Orbital interactions

Molecular hydrogen contains a ground state bonding orbital σ_g with an energy level of about $-11.7\,\mathrm{eV}$. There is a relatively large energy gap between the bonding orbital σ_g and the unoccupied anti-bonding orbital σ_u^* with a magnitude of about 2 eV [10]. Interactions between filled molecular orbitals are primarily repulsive. However interactions between filled and unfilled orbitals can result in charge transfer, donor-acceptor bonding, and overall stabilization. Orbital interactions have shorter bond lengths and larger binding energies than dispersion interactions. Charge transfer causes an elongation of the H_2 bond length, which is directly measurable by a softening of the intramolecular vibrational modes. Transition metals (TM) are known to form H_2 coordination complexes (i.e., "Kubas" complexes) in which H_2-σ to TM-d electron-transfer is coupled with TM-d to H_2-σ^* electron back-donation [11]. In reality, though, hydrogen does not easily donate or accept charge due to the large separation between its σ_g and σ_u^* orbitals. In fact, the adsorption mechanism in many metal-organic frameworks with exposed transition metal sites can actually be explained in terms of electrostatic interactions, without the need for orbital interactions [12].

1.6 Carbon adsorbents

1.6.1 Overview

Carbon adsorbents are attractive for physisorption storage systems due to their simplicity, light weight, and low manufacturing cost. Considerable work has been performed in this field, and at least two review articles are available which describe the status of hydrogen storage in carbon materials [13, 14]. Non-carbon adsorbents which are of particular importance to the hydrogen storage field are described briefly in Sec. 1.6.5.

Nonporous amorphous carbons can be thought of as agglomerates of spheroidal particles. In this case the specific surface area (SSA) consists of the external particle areas, typically in the range of $2\,\mathrm{m^2\,g^{-1}}$ to $200\,\mathrm{m^2\,g^{-1}}$, depending on the particle size. A porous material contains narrow internal cavities or channels which connect to the particle surface. Pore sizes are classified by IUPAC as micropores (pore width $< 2\,\mathrm{nm}$), mesopores (pore width 2–50 nm) and macropores (pore width $> 50\,\mathrm{nm}$) [6]. Microporous carbons are of particular importance for hydrogen storage since they contain large surface areas and provide strong binding sites.

1.6.2 Graphite

Graphite is an ordered carbon allotrope consisting of alternating layers of sp^2 bonded trigonal planer sheets. Neighboring planes interact by overlapping π-bonds between the unhybridized carbon 2p orbitals. The stacking sequence of the basal planes along the c-axis follows a staggered -ABAB- pattern, so that half of the carbon atoms in a given plane sit between the hexagon centers of the layers above and below it.[4] The carbon-carbon bond

[4] Rhombohedral graphite follows an -ABCABC- stacking sequence.

length in the basal planes is $a = 1.421\,\text{Å}$, and the interlayer spacing is $3.354\,\text{Å}$.[5]

Graphitic carbons are nonporous, with surface areas typically under $20\,\text{m}^2\,\text{g}^{-1}$, and negligibly small hydrogen uptake at low temperature [6]. The measured adsorption enthalpy of hydrogen on Graphon[6] is $3.8\,\text{kJ}\,\text{mol}^{-1}$ [15], well below the targeted value. One strategy for increasing the binding energy for carbon adsorbents is to open up space between the layer planes in order to accommodate guest molecules. In fact, this hypothetical graphene slit-pore structure has been the subject of numerous computational studies [16–18]. Due to the overlapping potential fields from opposing slit-pore walls, the heat of adsorption is enhanced. The optimal interlayer spacing would be large enough to accommodate two hydrogen monolayers (i.e., one monolayer per slit pore wall). Any additional interlayer expansion would not be useful because hydrogen only adsorbs in monolayers at supercritical temperatures.

Although the graphene slit pore structure is well-suited for optimizing the carbon-hydrogen binding interaction, the general consensus is that the gravimetric density is intrinsically low due to the geometry. This can be illustrated by considering H_2 monolayers on an ideal graphene sheet. An estimate of the graphene specific surface area is obtained from the fact that a single hexagon contains a net total of two carbon atoms with an area of $1.5\sqrt{3}a^2$. This gives an SSA of $2633\,\text{m}^2\,\text{g}^{-1}$ on double-sided graphene. Two possible configurations for a hydrogen monolayer on a graphene surface are illustrated in Figure 1.4. Commensurate structures are energetically favorable since the hydrogens sit in the hexagon centers, but they have a lower density than a close-packed structure. If both sides of the graphene surface are occupied, then the gravimetric density is 5.6 wt% for the commensurate

[5] This structure corresponds to an ideal graphite crystal, whereas natural graphite contains both hexagonal and rhombohedral modifications, as well as large deviations from the ideal stacking sequence. Natural graphite also contains large amounts of chemical impurities.

[6] Graphon is a graphitized carbon black material with a surface area of $90\,\text{m}^2\,\text{g}^{-1}$ which is typically used as a substitute for graphite in adsorption measurements

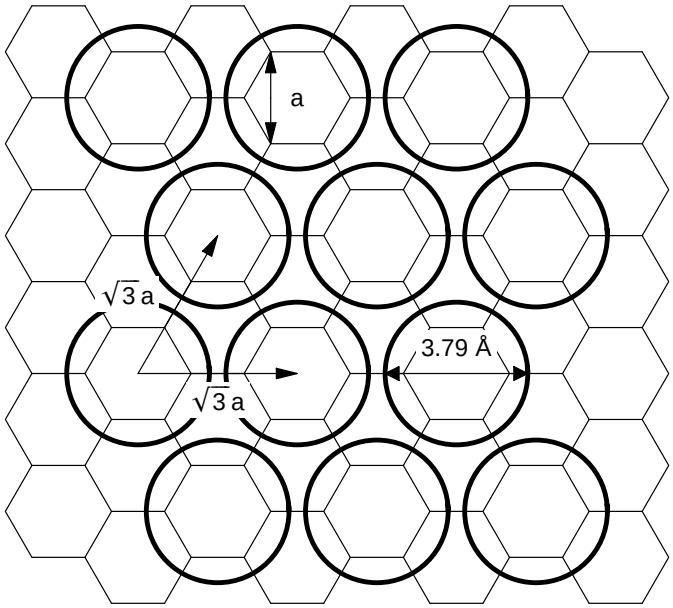

(a) $\left(\sqrt{3} \times \sqrt{3}\right) R30°$

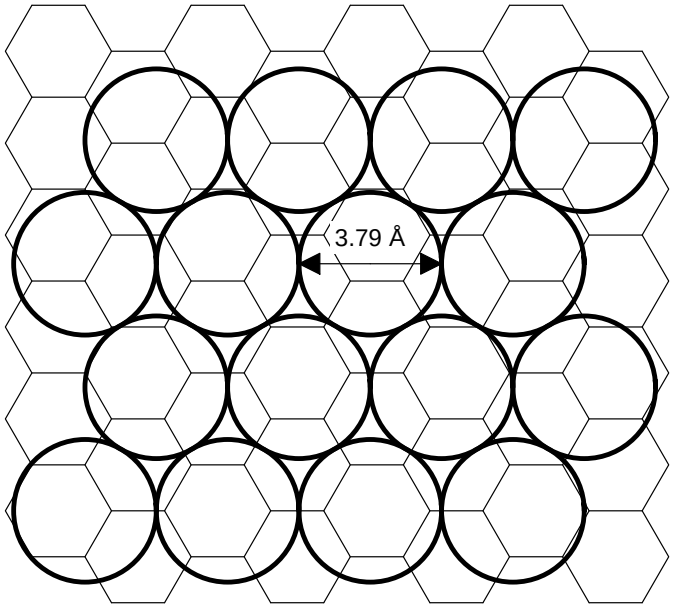

(b) Close-packed

Figure 1.4: Two possible structures for a hydrogen monolayer on a graphene sheet.

$\left(\sqrt{3} \times \sqrt{3}\right) R30°$ structure.[7] The gravimetric density of a close-packed H_2 monolayer can be obtained by using the standard method of estimating the BET cross-sectional area [6]. For a hexagonal close-packed structure, the cross-sectional area of a hydrogen molecule is given by

$$\sigma = f\left(\frac{M}{\rho N_a}\right)^{2/3}, \tag{1.8}$$

where the HCP packing factor f is 1.091, ρ is the density of liquid hydrogen, M is the molar mass, and N_a is Avogadro's number. Taking the solid H_2 density as $\rho = 86.48\,\mathrm{kg\,m^{-3}}$, the cross-sectional area is $\sigma = 0.124\,\mathrm{nm}^2$. If the carbon specific surface area is $a(\mathrm{SSA})$, then the hydrogen monolayer adsorption in wt% is

$$\mathrm{wt\%} = \left(\frac{a(\mathrm{SSA})}{\sigma}\right)\left(\frac{M}{N_a}\right) \times 100. \tag{1.9}$$

This gives $1.34\,\mathrm{wt\%}$ per $500\,\mathrm{m^2\,g^{-1}}$ carbon surface area. Double-sided graphene has a surface area of $a(\mathrm{SSA}) = 2633\,\mathrm{m^2\,g^{-1}}$, which translates to a maximum hydrogen adsorption of $7.04\,\mathrm{wt\%}$. This represents the theoretical limit for H_2 density in a pillared graphene structure.

1.6.3 Fullerenes

Another strategy to enhance hydrogen binding in carbon adsorbents is to use a curved carbon surface. Fullerenes, such as single-walled carbon nanotubes (SWCN) and C_{60} buckeyballs, are well-known examples. They are formed from graphene-like sheets composed of five or six-member rings. The presence of pentagonal rings results in the curvature of the carbon planes, allowing the formation of C_{60} spheres. Similarly, the hollow cylindrical

[7] We can adopt the nearest-neighbor distance of solid hydrogen (3.79 Å) as a conservative estimate of the hard sphere diameter.

structure of single- and multi-wall carbon nanotubes is obtained by rolling up graphene sheets along different directions. Unfortunately, a large amount of variation and irreproducibility has plagued both experimental and theoretical work on hydrogen adsorption in fullerenes. Recent studies have indicated that carbon nanotubes have the same adsorption properties as activated carbons and other amorphous carbons [19, 20]. Nevertheless, as the only ordered allotropes of carbon that adsorb hydrogen, fullerenes provide a unique platform for rigorously studying the hydrogen-carbon interaction from both an experimental and theoretical level. For example, the diameter of the SWCNs is a tunable parameter which can be used to optimize the adsorption behavior.

1.6.4 Activated Carbons

Activated carbons are predominantly amorphous materials with large surface areas and pore volumes, often containing BET areas in excess of $2000\,\mathrm{m^2\,g^{-1}}$. They are best described as "a twisted network of defective carbon layer planes cross-linked by aliphatic bridging groups [21]." The pore structure of an activated carbon is complex and ill-defined, making it challenging to study. An example of this complex, cross-linked structure is illustrated in Fig. 1.5c. Activated carbons are produced in industrial quantities from a carbon-rich precursor by a physical or chemical activation process. Physically activated carbons commonly use bituminous coal or coconut shells as a starting material. The two-stage activation process consists of carbonization, where oxygen and hydrogen are burned off, and gasification where the char is heated in a steam or carbon dioxide atmosphere to create a highly porous structure from carbon burn-off. Carbon aerogels are a separate class of amorphous carbons which can mimic the properties of activated carbons. They are prepared by a sol-gel polymerization process and can be activated using the standard methods.

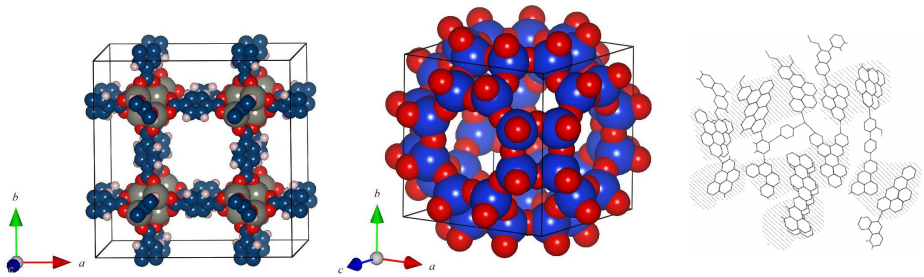

(a) MOF-5 **(b)** Zeolite A **(c)** Activated carbon

Figure 1.5: Structure of (a) MOF-5, (b) zeolite A, and (c) activated carbon.

1.6.5 Zeolites

Zeolites are crystalline materials composed of SiO_4 or AlO_4 building blocks. They contain an intra-crystalline system of channels and cages which can trap guest H_2 molecules. The adsorption capacity of zeolites at 77 K is typically below 2 wt%. A theoretical capacity of 2.86 wt% has been suggested as being an intrinsic geometric constraint of zeolites [22]. Due to this low gravimetric density, zeolites are not typically considered feasible hydrogen storage materials. Isosteric heats on the order of 6–7 $kJ\,mol^{-1}$ are typical for hydrogen-zeolite systems [23]. Zeolite structures such as LTA (see Fig. 1.5b) can have intra-crystalline cavities on the order of the H_2 diameter itself. They function as molecular sieves, blocking adsorption of larger gas molecules by steric barriers. They also exhibit quantum sieving effects on hydrogen isotopes. When confined inside a molecular-sized cavity, the heavier D_2 molecule is adsorbed preferentially over the lighter H_2 molecule due to its smaller zero-point motion [24].

1.6.6 Metal-organic frameworks

Metal-organic frameworks (MOFs) are synthetic crystalline materials which are somewhat analogous to zeolites. Organic linker molecules form the building blocks of MOFs, coordina-

tively binding to inorganic clusters to form a porous framework structure. A good example of a MOF structure is provided by MOF-5, which consists of $Zn_4O(CO_2)_6$ units connected by benzene linkers in a simple cubic fashion (Fig. 1.5a). It was not until fairly recently that MOFs were studied as a potential hydrogen storage material [25]. By modifying the organic linkers, the pore size and effective surface area can be tailored quite effectively. Hydrogen adsorption capacities of up to 7.5 wt% at 77 K have been measured for MOF-177 [26, 27]. A number of MOFs contain coordinatively unsaturated metal centers which are known to enhance hydrogen binding interactions [28]. In most cases this interaction is dominated by electrostatic contributions [12, 29, 30], but the possibility of stronger "Kubas" orbital interactions between the hydrogen and the open metal sites has generated considerable interest.

1.6.7 Hydrogen adsorption by porous carbons

Hydrogen adsorption at supercritical temperatures is characterized by weak interactions between the adsorbed hydrogens. Interactions between the hydrogen and the adsorbent surface are dominant, favoring the formation of adsorbate monolayers. Multilayer formation has a characteristic energy on the order of the hydrogen heat of condensation ($0.9\,\mathrm{kJ\,mol^{-1}}$) and does not occur above the critical temperature. Capillary condensation of H_2 inside large pores or cavities is not possible, resulting in a reduction of the usable pore volume. Therefore, micropores are the most important feature of an adsorbent while mesopores contribute little to the total hydrogen capacity.

Many studies have noted a roughly linear relationship between the BET surface area and the maximum H_2 adsorption capacity at 77 K [20,31]. The simple rule-of-thumb for this behavior is 1 wt% per $500\,\mathrm{m^2\,g^{-1}}$. This can be compared to the 1.34 wt% per $500\,\mathrm{m^2\,g^{-1}}$

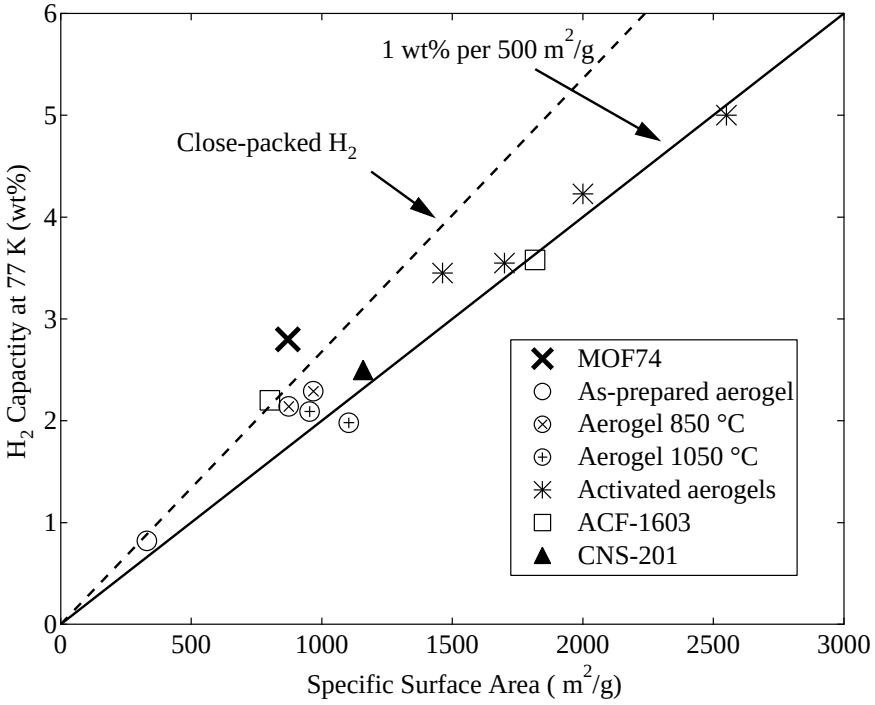

Figure 1.6: Maximum hydrogen adsorption capacities at 77 K of various adsorbents plotted against their BET specific surface areas. Materials include a series of carbon aerogels, two activated carbon fibers (ACF-1603), one activated coconut carbon (CNS-201) and one metal-organic-framework (MOF-74). Straight lines indicate scaling between the specific surface area and storage capacity for close-packed hydrogen and for the rule-of-thumb (1 wt% per 500 $m^2\,g^{-1}$).

obtained for close-packed hydrogen on a double-sided graphene sheet. A sampling of data that was measured in our laboratory is summarized in Fig. 1.6. These samples included carbon aerogels (both activated and as-prepared), activated coconut-shell carbons, activated carbon fibers, and a metal-organic-framework (MOF-74). The scaling between hydrogen capacity and surface area is also plotted for both the empirical rule-of-thumb and the theoretical close-packed limit.

Surface areas do not always have a simple physical meaning for the complex disordered structure of activated carbons. What we should expect, however, is for a correlation to exist between the H_2 uptake and the total *micropore* volume. Studies of both carbon and zeolite adsorbents have found that this type of correlation exists and is actually stronger than the correlation with total BET surface area [19, 32]. In fact, the pore volume obtained from

CO_2 adsorption at 273 K is suggested as better reflecting the total micropore volume due to the faster admolecule diffusion. Hydrogen adsorption is therefore thought to be better correlated to the CO_2 pore volume than to the standard N_2 pore volume [32].

1.6.8 Chemically modified carbon adsorbents

There is a general consensus that carbon adsorbents will not meet density or operational targets for a hydrogen storage system at ambient temperatures [2, 33]. Maximum hydrogen capacity rarely exceeds 1 wt% at room temperature, even at pressures as high as 100 bar [34, 35]. This is an intrinsic property which is due to the low heat of adsorption. It applies equally to carbon nanostructures like SWCNs and to amorphous structures like activated carbons. The most promising strategy for increasing the adsorption enthalpy is through chemical modification of carbon adsorbents.

There are numerous computational studies of hydrogen uptake by hypothetical metal-doped carbon nanostructures. Decoration of C_{60} buckeyballs with scandium [36] or titanium [37] is known to create strong binding sites for multiple H_2 molecules. Metal-decorated SWCNs also exhibit enhanced hydrogen binding energies relative to the pristine material [38]. Computational studies of alkali metal doped graphene and pillared graphite structures have noted the importance of electrostatic effects in enhancing hydrogen binding [39, 40]. Experimental data exists for several metal-doped carbon adsorbents. Potassium-doped activated carbons show enhanced hydrogen adsorption at low pressures relative to the raw material, indicating a larger adsorption enthalpy [41]. Ball-milled mixtures of graphite and potassium adsorb modest amounts of hydrogen between 313 K and 523 K, but the adsorption is not reversible [42].

1.7 Conclusion

The understanding of the effect of chemical modifications on hydrogen adsorption is incomplete. Numerous computational studies exist for hypothetical structures which are not easily synthesized. A large amount of experimental data exists for ill-defined structures such as activated carbons, which are difficult to model theoretically. Research on the fundamental thermodynamics of hydrogen adsorption remains important. In particular, a combination of experimental and computational data on the interaction of hydrogen with a well-defined, chemically-modified carbon adsorbent would provide much needed information. It was for this reason that I chose to study H_2 adsorption in graphite intercalation compounds. This class of materials is introduced in the next chapter.

Chapter 2

Potassium Intercalated Graphite

2.1 Introduction

Graphite intercalation compounds (GICs) are a unique class of lamellar materials formed by the insertion of atomic or molecular guests between the layer planes of the host graphite. Electrical, thermal and magnetic properties can be varied by intercalation, making these materials interesting technologically. Graphite intercalation compounds exist for all alkali metals, but only the K, Rb, and Cs compounds are known to adsorb hydrogen. The maximum adsorption capacity of these materials is only around 1 wt%, but their high degree of structural ordering makes them a model system for studying hydrogen adsorption in a carbon nanostructure. They share many similarities with a chemically-modified carbon slit-pore structure, and are readily synthesized. Due to the attractiveness of potassium as a lightweight dopant for carbon adsorbents, potassium intercalated graphite is the focus of this thesis.

2.2 History

Alkali metal GICs were first prepared by Fredenhagen and co-workers in the 1920's with the compositions C_8M and $C_{16}M$ [43]. Further studies were carried out on the potassium com-

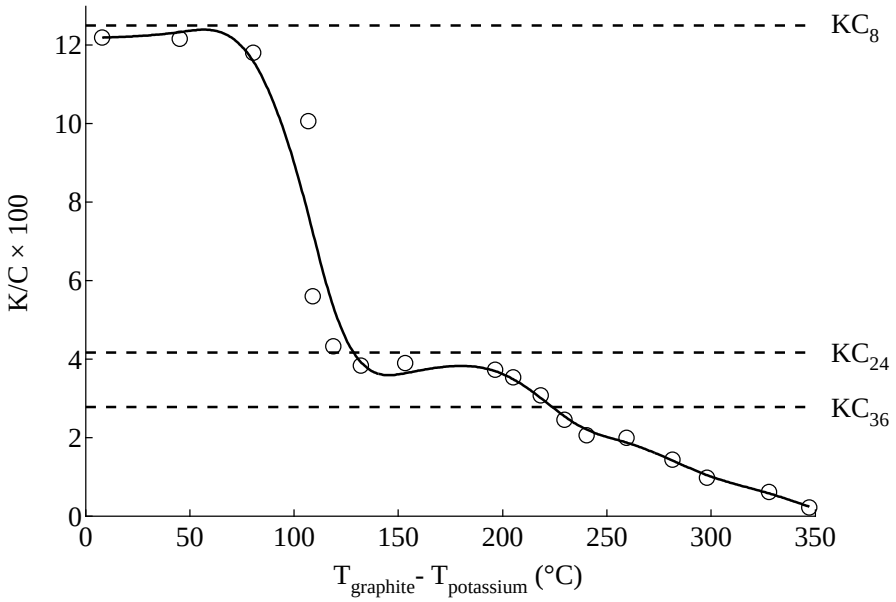

Figure 2.1: Composition of the potassium-graphite system based on the temperature difference between the graphite host and potassium vapor. Adapted from Ref. [44].

pound in the 1950's by Hérold, who developed a two-zone, vapor-phase synthesis technique where the potassium melt was kept at a constant temperature (250 ℃) while the graphite temperature was varied (250 ℃ to 600 ℃) [44]. Stoichiometric compounds of KC_8 and KC_{24} are visible as plateaus in the potassium-graphite isobar illustrated in Fig. 2.1. Structural studies of *staging* in potassium GICs were performed by Rüdorff and Schulze [45]. Discrete compositions of MC_8, MC_{24}, and MC_{36} were linked to the formation of stage 1, stage 2, and stage 3 intercalation compounds, respectively. The staging index, n, of the GIC indicates that the intercalant layer is found between every nth pair of host graphite planes. The stacking sequences in the alkali-metal GICs were further characterized by Perry and Nixon in the 1960's [46]. In the early 1960's, Saehr and Hérold discovered that KC_8 chemisorbs hydrogen at elevated temperatures up to maximum values of about $KC_8H_{0.67}$ [47]. Chemisorption was also noted for RbC_8 and KC_{24}, but not for CsC_8. Physisorption of H_2 by the stage 2 compounds of K, Rb, and Cs at low temperatures was discovered by Tamaru and co-

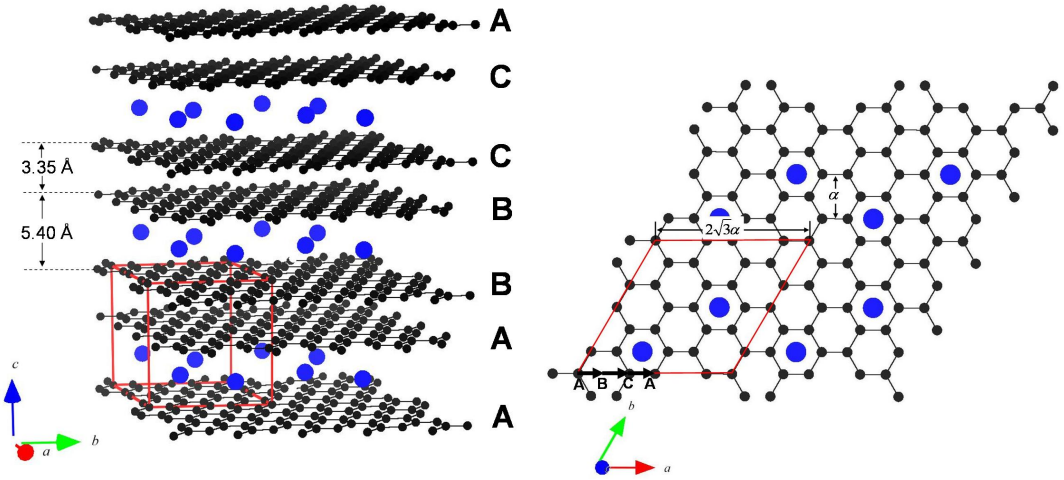

(a) Side view **(b)** Top view

Figure 2.2: Structure of KC_{24}. (a) The A|AB|BC|CA stacking sequence. (b) Possible in-plane potassium structure. Arrows from A→B→C describe the relative positions of the layer planes in the stacking sequence.

workers in the early 1970s [48]. These measurements were reproduced by a number of subsequent studies [49, 50]. The first inelastic neutron scattering studies of H_2 adsorbed in the stage-2 alkali metals compounds were performed by White and co-workers in the early 1980's [51]. Low-energy "rotational tunneling" peaks observed in the spectra indicated that the adsorbed hydrogen was in a strong anisotropic field. They were explained in terms of a one-dimensional hindered diatomic rotor model [52, 53]. By the late 1980's, a substantial body of research existed on hydrogen-alkali-metal graphite intercalation systems (see Ref. [54] and [55] for reviews on this subject). Interest in the area dwindled during the 1990's, as reflected in the small number of publications during the period. However with the emergence of hydrogen storage materials as a major topic of research, there has been a resurgence of interest in the hydrogen adsorption properties of the alkali-metal GICs.

2.3 Structure of potassium-intercalated graphite

2.3.1 Stacking sequence

Potassium GICs are formed by inserting potassium atoms into the galleries between the host graphitic layers. There are two competing forces in this system. First, the K atoms want to sit at the hexagon centers due to the strong graphite corrugation potential. This would cause the opposing basal planes to overlap exactly in an A|A sequence, where the vertical bar refers to the potassium layer. Second, the host graphite planes want to form a staggered sequence, ABAB, where half the carbon atoms in a given plane sit over the hexagon centers of the adjacent planes. It is the competition between these two driving forces that leads to the formation of discrete GIC stages. At low metal concentrations like KC_{24} and KC_{36}, it is apparently energetically favorable for metal layers to only occupy every 2^{nd} and 3^{rd} graphite gallery, respectively. For this reason, KC_{24} and KC_{36} are called the stage-2 and stage-3 compounds. The non-intercalated layers can maintain a staggered AB sequence, while the intercalated layers have an A|A sequence. If the potassium concentration is increased further, the system will eventually adopt a KC_8 stoichiometry, where the potassium atoms occupy every interlayer gallery in a close-packed 2×2 registered structure. The actual concentration of potassium within the GIC is determined by its relative chemical potential in the intercalated phase and in the vapor phase. By controlling the graphite temperature and the potassium vapor pressure (via the temperature of the melt), different potassium GIC stages can be synthesized (see Fig. 2.1).

The stage-1 compound has an orthorhombic symmetry with a known stacking sequence of AαAβAγAδA [45]. Unfortunately, the long-range stacking sequences for the stage-2 (and higher) GICs are not as well characterized. Nixon and Perry recommend the following [46]:

stage 4 ABAB|BCBC|CACA|

stage 3 ABA|ACA|A

stage 2 AB|BC|CA|A

An *in situ* X-ray diffraction study of the potassium GIC was actually able to identify stages 1 to 7, observing no evidence of microscopic mixing of the different stages [56]. The nominal stacking sequence of KC_{24} is illustrated in Fig. 2.2b, where the arrow from A to B indicates how the plane "A" is shifted with respect to the plane "B." When potassium is inserted into the host graphite, the interlayer spacing expands from 3.35 Å to 5.40 Å in the potassium-containing galleries, as indicated in Fig. 2.2a. The unintercalated galleries remain at 3.35 Å.

2.3.2 In-plane potassium structure

At room temperature, the potassium atoms are disordered within the graphite galleries and are often described in terms of a two-dimensional liquid [58]. A series of low-temperature phase transformations are known to occur in KC_{24} in which both the in-plane structure and stacking sequence assume long-range order [59, 60]. Unfortunately, the in-plane potassium structure has not been conclusively determined. While the stage-1 compound KC_8 has a commensurate (2×2) $R\,0°$ in-plane structure, stage-n compounds (KC_{12n} for $n > 1$) have a lower potassium density in each layer. The potassium atoms are likely to be commensurate with the host graphite at low temperatures, but simple periodic registered structures are not consistent with X-ray data [57, 61]. Graphite has a honeycomb lattice structure, so the minimum-energy sites at the hexagon centers form a triangular lattice. It would make sense to populate this triangular lattice in a periodic fashion to give the correct KC_{24} stoichiometry. The $\left(\sqrt{12} \times \sqrt{12}\right)$ $R\,30°$ structure depicted in Fig. 2.3a gives the correct

24:1 stoichiometry, but it is not consistent with X-ray diffraction patterns [61]. Another idea is to take an incommensurate close-packed potassium monolayer with a liquid-like separation of roughly 6 Å, rotate the layer around the c-axis by an arbitrary angle, and then relax the potassium atoms into the nearest hexagon centers [57]. This relaxed close-packed structure contains nearest-neighbor distances of $2a$, $\sqrt{7}a$, and $3a$ and has reasonable agreement with single-crystal X-ray data [61]. An example is illustrated in Fig. 2.3c.

Unlike KC_{24}, the low-temperature in-planes structures of RbC_{24} and CsC_{24} are well

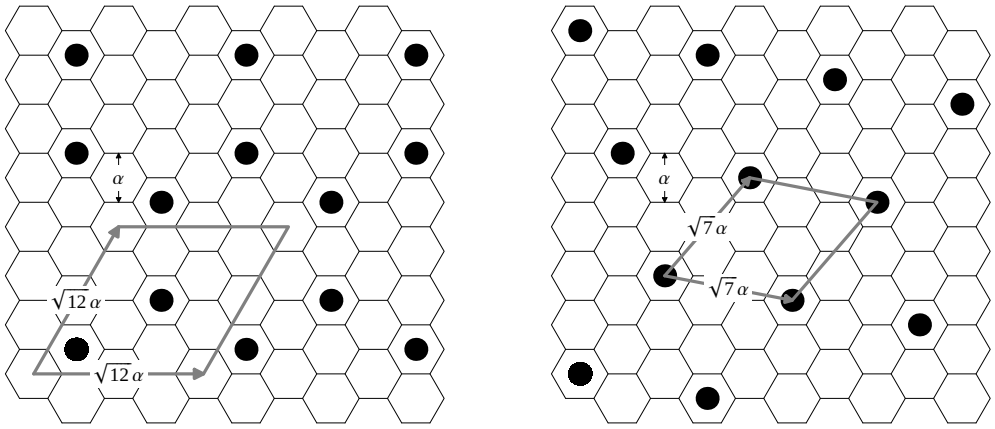

(a) $\left(\sqrt{12} \times \sqrt{12}\right) R\,30°$ structure

(b) $\left(\sqrt{7} \times \sqrt{7}\right) R\,19.11°$ structure

(c) Relaxed Close-Packed

Figure 2.3: In-plane potassium structures in registry with the graphite host. The $\left(\sqrt{12} \times \sqrt{12}\right)$ structure corresponds to a KC_{24} stoichiometry. The $\left(\sqrt{7} \times \sqrt{7}\right)$ structure has a KC_{28} stoichiometry. The relaxed close-packed structure (adapted from Ref. [57]) consists of a close-packed potassium layer which has been rotated in-plane and relaxed into the nearest hexagon centers.

described by a domain model [62, 63]. As illustrated in Fig. 2.4, they contain locally commensurate $\left(\sqrt{7} \times \sqrt{7}\right) R\,19.11°$ patches surrounded by domain walls. The idealized $\sqrt{7} \times \sqrt{7}$ structure (see Fig. 2.3b) has been the basis of most *ab initio* studies of the H_2/KC_{24} system [64,65]. Unfortunately the $\sqrt{7} \times \sqrt{7}$ structure has a KC_{28} stoichiometry. In the domain model the boundary regions have a greater alkali metal density, causing the total stoichiometry to even out at about 24 to 1. However, the domain model with discommensurations has not been consistent with single-crystal diffraction data measured on KC_{24} [61]. It seems that the relaxed close-packed structure, an analogue of the random lattice-gas model, is the most compelling structural model for the in-plane potassium arrangement.

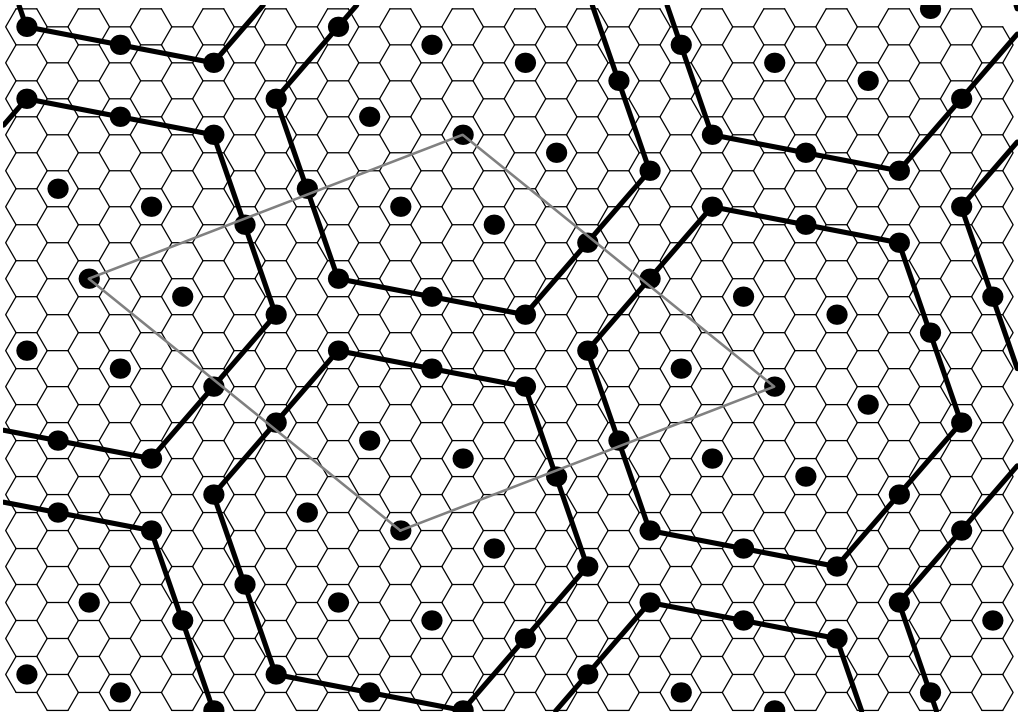

Figure 2.4: Domain model for CsC_{24} in which $\sqrt{7} \times \sqrt{7}$ islands are separated by domain walls, or discommensurations. Adapted from Ref. [62].

2.4 Properties of potassium-intercalated graphite

Graphite is a semi-metal with a complex band structure. It has only about 10^{-4} charge carriers per carbon atom. Alkali metal GICs, like KC_{24}, are classified as *donor* compounds because the metal atoms donate charge to the graphite conduction band. This results in a large increase in both the in-plane conductivity (σ_a) and c-axis conductivity (σ_c). Due to the layered structure of GICs, there is also considerable anisotropy in the charge transport properties. For KC_{24}, the c-axis conductivity is about 24 times larger than for pristine graphite, and the anisotropy factor σ_a/σ_c is about 860 [66]. Partial charge transfer from potassium to the empty graphite bands appears to be experimentally established [67].

Hydrogen physisorption in KC_{24}, RbC_{24}, and CsC_{24} has been previously investigated [48]. The Li and Na compounds do not physisorb hydrogen because the widths of the metal-containing galleries are too small. Notably, KC_{24} has molecular sieving properties in which it adsorbs smaller molecules (e.g., hydrogen), but does not adsorb larger molecules (e.g. methane). Quantum sieving effects are also present in KC_{24}, in which D_2 is adsorbed preferentially over H_2 [50]. The hydrogen adsorption characteristics depend on the quality of the starting graphite. The best adsorption is obtained for high purity, natural flake crystalline graphite. As the amount of amorphous impurities in the starting graphite increases, the H_2 adsorption amount decreases [68].

Hydrogen is adsorbed into the metal-containing layers of KC_{24}, forming a quasi-two-dimensional binary solution with potassium. There is no evidence for anything other than a monolayer structure in which the potassium and H_2 are mixed. The potassium-containing layer expands from 5.4 Å to 5.6 Å following hydrogen adsorption. This is an interlayer expansion of almost 5 %, which is surprisingly large, but is still too small to support a bilayer or

trilayer H_2-K-H_2 structure. There is also no evidence for H_2 dissociation during physisorption, as verified by a chromatographic analysis of an H_2/D_2 mixture [48]. It is unclear whether the potassium superstructure is rigid, or whether it undergoes rearrangement after the introduction of hydrogen.

Interactions between hydrogen and KC_{24} are likely to have both dispersion and electrostatic components. Charge transfer from potassium to graphite results in a strongly polarized potential field which can have significant charge-quadrupole and charge-induced-dipole interactions with the adsorbed H_2 molecules. However, charge density surrounding the potassium atoms, and present in the bounding graphite layers, can also lead to an enhanced dispersion interaction with the H_2 molecule. Computational studies report an enhancement of the energy for the H_2 interaction with an alkali-doped graphene surface, due largely to the increased electron density on the surface surrounding the alkali impurity [39, 69]. The reported H_2 isosteric heat on KC_{24} is $8.4\,\mathrm{kJ\,mol^{-1}}$, about twice as large as for adsorption on bare graphite [48]. It is also known that the in-plane resistivity in $KC_{24}(H_2)_x$ is larger than in KC_{24} [55]. This is explained by the observed c-axis expansion, which effectively reduces the in-plane carrier density. Charge back-donation from the conducting π bands to the hydrogen σ^* anti-bonding orbital seems unlikely and has not been conclusively demonstrated [54, 55].

2.5 Synthesis of KC_{24} samples

Samples of KC_{24} used in this work were synthesized using a modified single-temperature-zone technique. The starting materials were thermally purified natural flake graphite (Superior Graphite Co., 99.95–99.99% purity, 50 mesh) and potassium metal (Alfa Aesar, 99.9%). Since the starting graphite had already been subject to a high-temperature purifi-

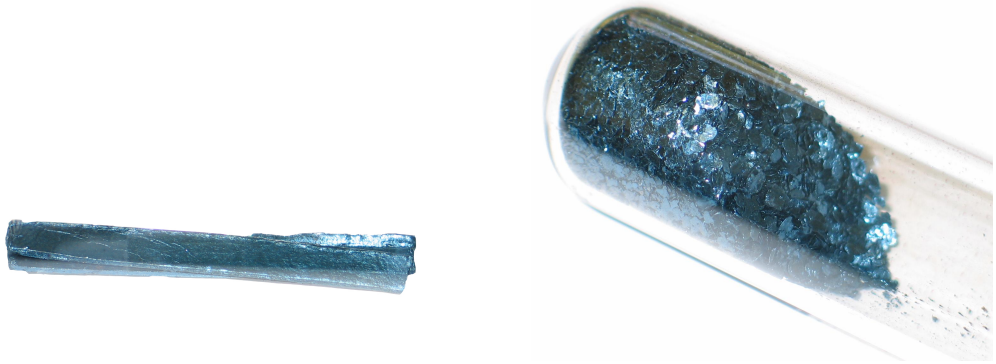

(a) Grafoil **(b)** Flake graphite

Figure 2.5: Samples of KC_{24} synthesized from Grafoil and natural flake graphite.

cation process, it was not necessary to puruse further purification.[1] Stoichiometric amounts of graphite and potassium were weighed out inside an argon glovebox, transferred to a glass ampoule, and connected to a threaded glass vacuum valve with an O-ring sealed Teflon plug. The ampoule was then evacuated to 60 Torr and sealed with an oxygen torch. Samples were heated at 300 °C for 24 h to 48 h and shaken occasionally to ensure homogeneity. This last step was required to make sure that a homogenous stage-2 compound was produced instead of a mixture of stage-1 and higher-stage compounds. Samples produced with this method are pictured in Fig. 2.5.

Measuring out exact amounts of potassium was probably the trickiest part of the synthesis and required a certain amount of trial by error. Coating the surface of individual potassium pieces with a layer of flaked graphite prevented them from sticking to the ampoule walls during loading. By measuring the initial and final masses of both the ampoule and the source graphite, it was possible to determine the exact amounts of both the potassium and the graphite. Further, I found that using a 22:1 molar ratio of graphite to potassium produced the best samples. A thin film of potassium was typically plated onto the glass which meant that not all of the loaded potassium was necessarily intercalated into the sam-

[1] As a precaution, the graphite was outgassed under dynamic vacuum at 200 °C to remove any residual water that may have been adsorbed on the surface.

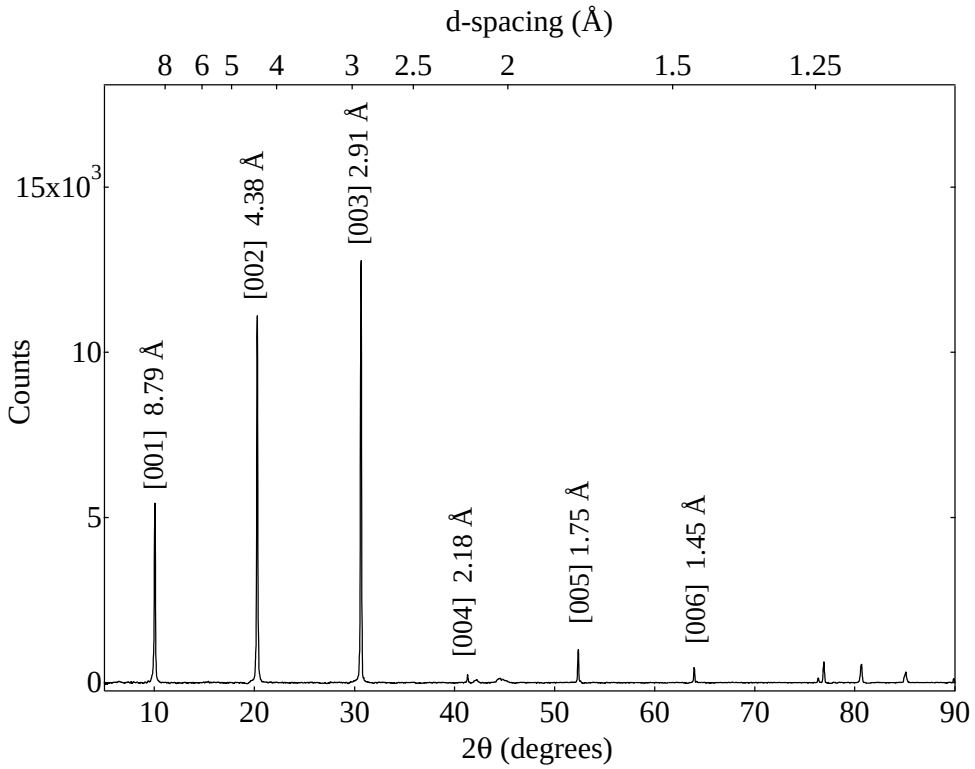

Figure 2.6: Powder XRD pattern of KC_{24} at room temperature.

ple. Samples of RbC_{24} and CsC_{24} were synthesized using the same method, substituting for different alkali metals. An additional KC_{24} sample was synthesized from a nuclear grade Grafoil® (99.5% graphite, 0.152 cm thickness) starting material used without further purification. The Grafoil-based sample had a stoichiometry of $KC_{21.7}$ and a helium density of $2.03(6)\,\mathrm{g\,ml^{-1}}$.

2.6 Characterization of KC_{24} samples

2.6.1 Powder X-ray diffraction

Powder X-ray diffraction (XRD) measurements verified the phase purity of KC_{24} samples synthesized from natural flake graphite. Rubidium and cesium GIC samples were also characterized. The XRD patterns were collected on a PANalytical X'pert PRO X'celerator

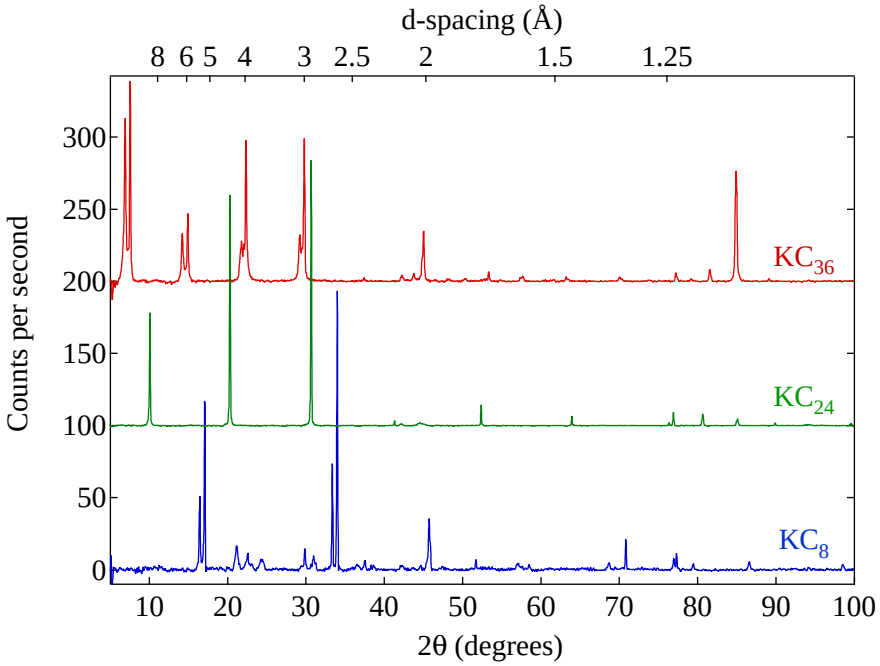

Figure 2.7: Comparison of the powder XRD patterns of stage-1, stage-2, and stage-3 potassium graphite intercalation compounds.

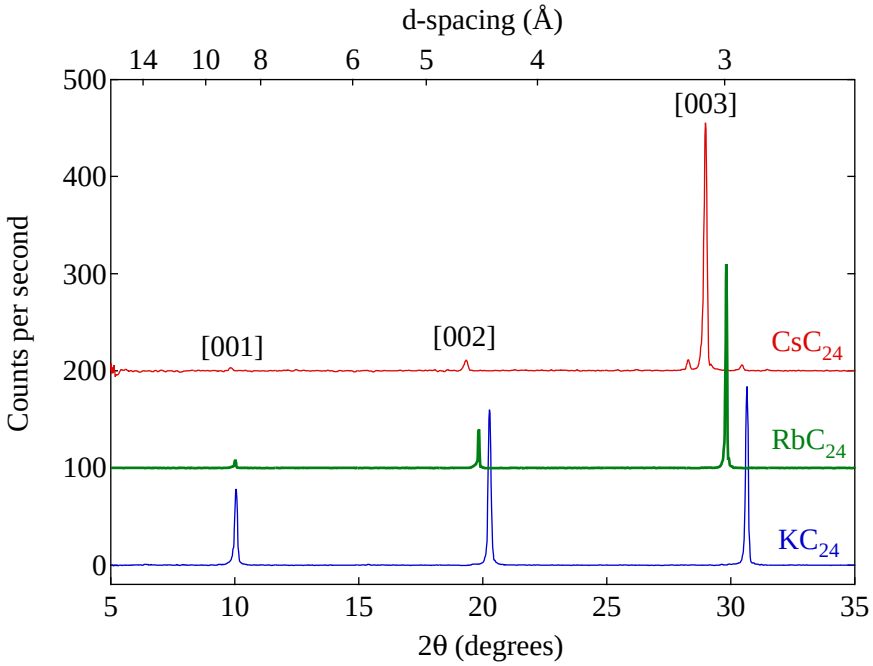

Figure 2.8: Comparison of the powder XRD patterns of KC_{24}, RbC_{24}, and CsC_{24} graphite intercalation compounds.

Table 2.1: Lattice parameters of synthesized graphite intercalation compounds

Sample	Lattice parameter(Å)[a]	Interlayer spacing (Å)[b]
KC_{24}	8.76 ± 0.02	5.41 ± 0.02
KC_{36}	12.1 ± 0.30	5.40 ± 0.30
RbC_{24}	8.95 ± 0.08	5.60 ± 0.08
CsC_{24}	9.25 ± 0.05	5.90 ± 0.05

[a] This c-axis lattice parameter gives the combined interlayer width of an AB|B sequence for a stage-2 compound (or an ABA|A sequence for a stage-3 compound). Values were averaged from the 001, 002, and 003 reflections.

[b] The interlayer spacing refers to the width of a metal-containing layer. It is equal to the c-axis lattice parameter minus the widths of the non-intercalated layers (e.g., 3.35 Å for a single non-intercalated layer.)

diffractometer using Cu Kα radiation ($\lambda = 1.5418$ Å). Samples were sealed within an argon atmosphere inside 1.5 mm ID glass capillary tubes using a low vapor pressure vacuum epoxy (TorrSeal™, Varian Inc.), and mounted onto a specialized capillary goniometer. I chose not to spin the capillary holder during data collection in order to not disturb the alignment. All measurements were collected at room temperature. An XRD pattern for KC_{24} is shown in Fig. 2.6. The dominant features in the KC_{24} diffraction pattern are the [00l] basal-plane reflections, which indicate a repeat distance of 8.76 ± 0.02 Å. This gives an interlayer spacing of $d = 8.76 - 3.35 = 5.41$ Å, compared to the literature value of 5.40 Å [45]. The higher order reflections follow the expected d_{001}/l spacing. Reflections with non-zero h and k are not visible in the powder diffraction pattern.

For comparison, additional powder XRD patterns were collected for the stage-1 and stage-3 potassium GICs. This data is pictured in Fig. 2.7. As desired, there are no Bragg peaks from either the stage-1 or stage-3 impurities in the prepared KC_{24} sample. The presence of a fine structure in the diffraction peaks of KC_8 and KC_{36} is very likely to be an artifact from the large diameter of the XRD capillary tubes. If two graphite flakes meet the same diffraction condition but are separated by a distance of 1.5 mm, the resulting diffraction peaks could easily be shifted by about 1°, producing the observed fine structure. Further,

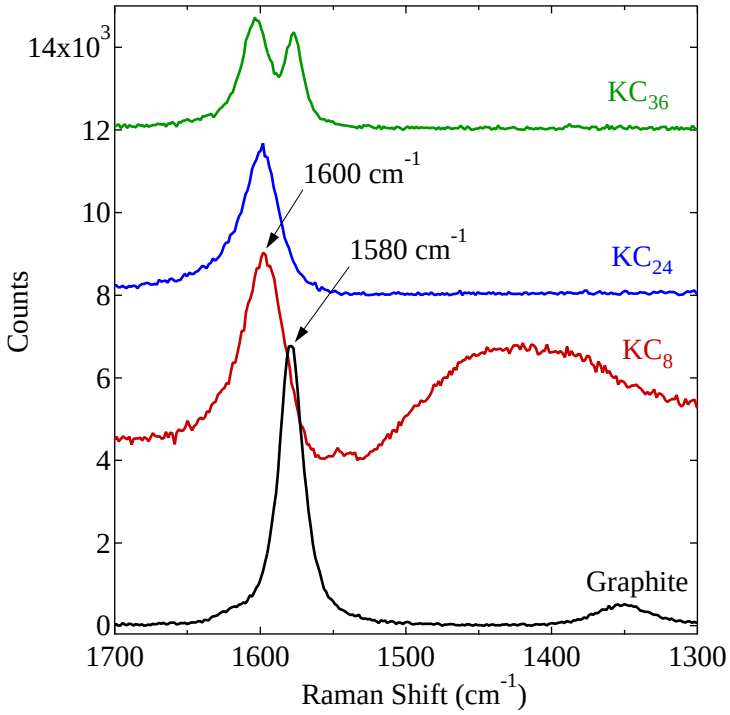

Figure 2.9: Raman scattering spectra of the potassium graphite intercalation compounds at room temperature. Measured scattering was from individual flakes.

the capillary tubes were usually not aligned perfectly on the goniometer head (alignment was done "by eye"), creating a second, perhaps larger, source of error. Admittedly, using wide-diameter capillary tubes was not the most accurate way to determine lattice parameters. Graphite flakes do not fit into smaller diameter capillary tubes without first being ground up (which I wanted to avoid for these materials). Nevertheless, powder XRD provided us the qualitative information we needed: KC_{24} samples were synthesized correctly and were not contaminated by impurities from stage-1 or stage-3. Additional powder XRD patterns were collected for RbC_{24} and CsC_{24} samples, as illustrated in Fig. 2.8. A summary of lattice parameter data for all of the synthesized alkali metal GICs is provided in Table 2.1.

2.6.2 Raman spectroscopy

Raman spectroscopy was used as an alternative method of verifying the phase purity of prepared KC_{24} samples. Measurements were collected on Renishaw M1000 Micro-Raman spectrometer, operating at $1\,cm^{-1}$ spectral resolution with a 514.5 nm argon laser. Samples were sealed in 1.5 mm glass capillary tubes and data was collected at room temperature. Data for KC_8, KC_{24}, and KC_{36} are displayed in Fig. 2.9. The peak at around $1600\,cm^{-1}$ is typically assigned to the E_{2g2} mode of graphite where the graphite layer is bounded by an intercalant layer on one side and a graphite layer on the other side [70]. The peak near $1580\,cm^{-1}$ is typically assigned to an E_{2g2} mode where the layer is bounded on both sides by a graphite plane. As expected, the $1580\,cm^{-1}$ mode is present for pristine graphite and for KC_{36} (which contains an intercalant layer in every third gallery). The $1600\,cm^{-1}$ mode is present as expected in both the KC_{24} and KC_{36} spectra, though it is unclear why it is also present in KC_8 (which contains an intercalant in every layer).

2.6.3 Neutron diffraction

Neutron diffraction work on a D_2/KC_{24} system was performed at the NPDF beamline at the Lujan Center, located at the Los Alamos National Laboratory.[2] Approximately 1 g of powder was loaded into a leak-tight vanadium sample can with an attached capillary line for dosing with D_2 gas. The diffraction pattern of KC_{24} without D_2 was measured at both 298 K and 35 K. Interestingly, there is no notable difference in these two diffraction patterns except for small shifts due to thermal expansion.[3] Deuterium gas was introduced to the sample at 300 K, and the temperature was lowered at intervals down to a base temperature

[2] Measurements performed by C. C. Ahn, B. Fultz, and R. Yazami in 2001 [71].

[3] The observable powder diffraction peaks are apparently not sensitive to the order-disorder transformation that occurs in the potassium intercalate layers at low temperatures.

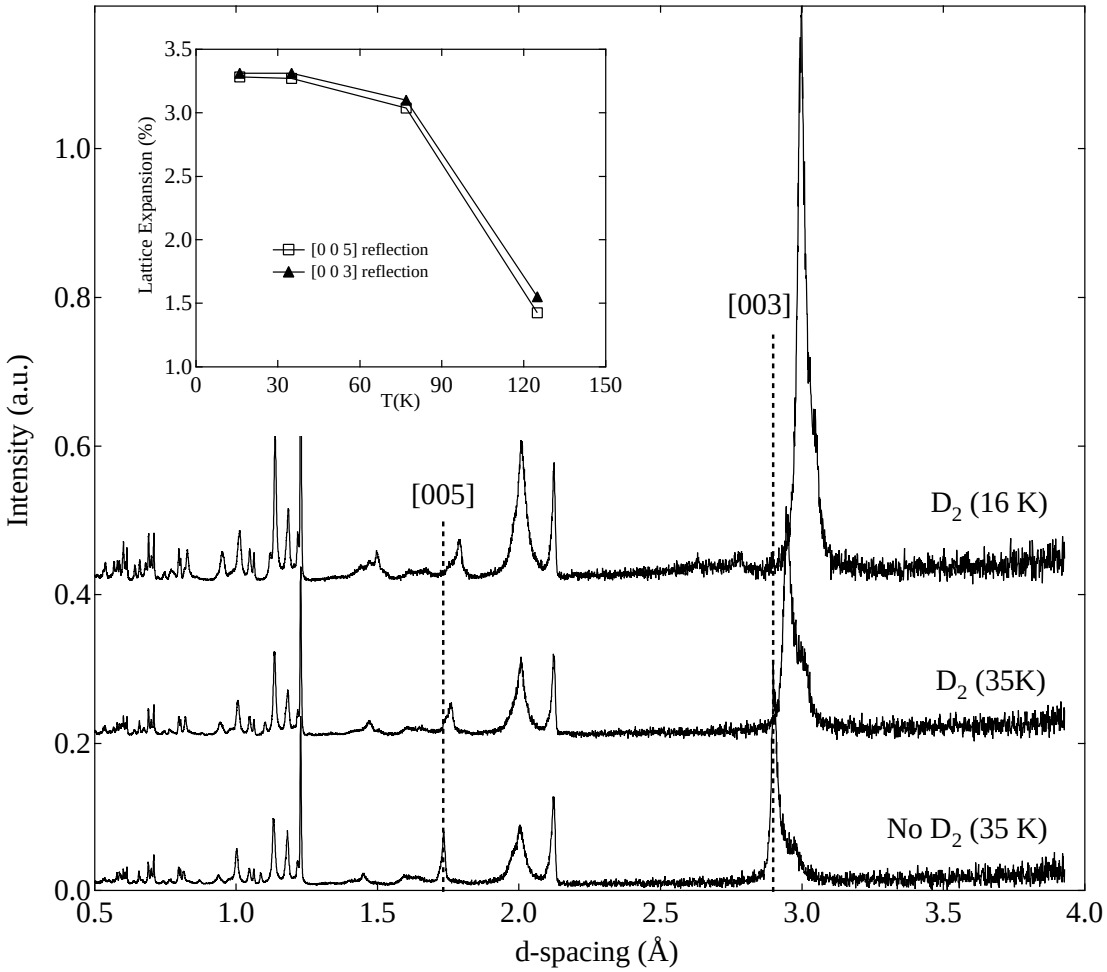

Figure 2.10: Neutron diffraction pattern for KC_{24} powder. Displayed data is for a KC_{24} sample at 35 K, and a $KC_{24} + D_2$ sample at 35 K and 16 K. Inset shows the percent increase of the *c*-axis lattice parameter from the [003] and [005] peak-shifts of the deuterated sample as a function of temperature. Diffraction patterns from 77 K and 120 K are not pictured.

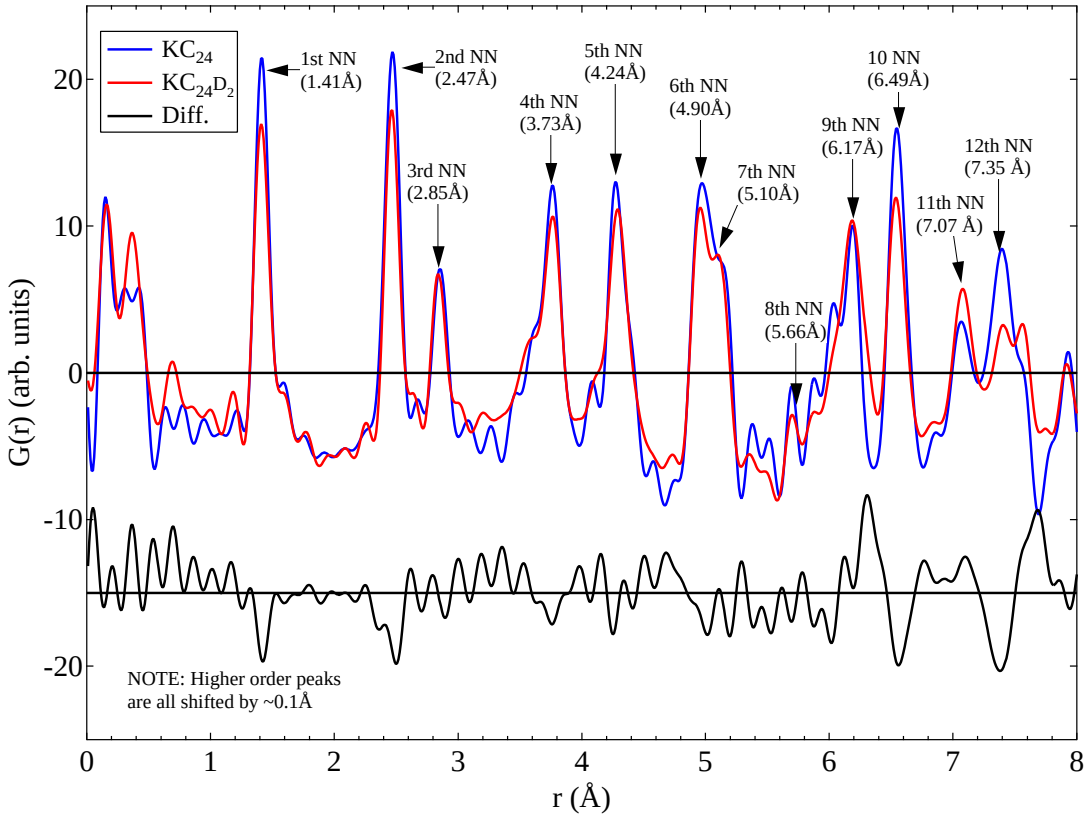

Figure 2.11: Pair distribution function calculated from the KC_{24} and $KC_{24} + D_2$ powder neutron diffraction patterns at 35 K. The difference spectrum is also displayed at a negative offset along the y-axis. All major peaks are assigned to carbon nearest-neighbor distances within a graphite plane.

of 16 K. The c-axis repeat distance, as determined from the [003] and [005] peaks, increases from 8.69 Å for the un-deuterated sample to 8.97 Å for the deuterated sample at 16 K (Fig. 2.10). This corresponds to a 5 % expansion in the interlayer spacing from 5.34 Å to 5.62 Å, roughly consistent with previous results [48].

Pair distribution functions (PDF) for both KC_{24} and KC_{24}+D_2 were back-transformed from the diffraction profiles of each sample collected at 35 K. The results are displayed in Fig. 2.11. Peaks in the PDF can almost entirely be assigned to nearest-neighbor distances of carbons in a graphite layer. Referring to Fig. 2.3c, the expected K−K distances are roughly 4.9 Å, 6.47 Å, and 7.34 Å. Deuterium might be expected to have similar nearest-neighbor distances at low loadings. Interestingly, there are some areas of intensity in the difference plot around 6.3 Å and 7.8 Å which may correspond to the latter two of the expected distances. Unfortunately, it is difficult to draw any information about either the potassium or deuterium structures from the PDF plot.

Chapter 3

Experimental Methods

3.1 Gas Adsorption Measurements

3.1.1 Introduction

To characterize a potential hydrogen storage material, we must measure the amount of hydrogen it adsorbs at various temperatures and pressures. The adsorption amount is typically measured as a function of pressure while the temperature is held constant. These isothermal pressure-composition curves are called "isotherms". Two important quantities can be derived from the isotherm: (a) the maximum adsorption capacity, and (b) the isosteric heat of adsorption. The heat of adsorption is particularly significant as an indicator of the interaction strength between the hydrogen molecules and the adsorbent host.

3.1.2 Theoretical framework

3.1.2.1 Surface excess adsorption

Quantifying the amount of an adsorbed gas is a deceptively subtle task. The important quantities pertaining to a solid/gas interface are illustrated in Fig. 3.1. Near the adsorbent surface, in the region labeled "adsorbed layer", the local adsorptive density is considerably

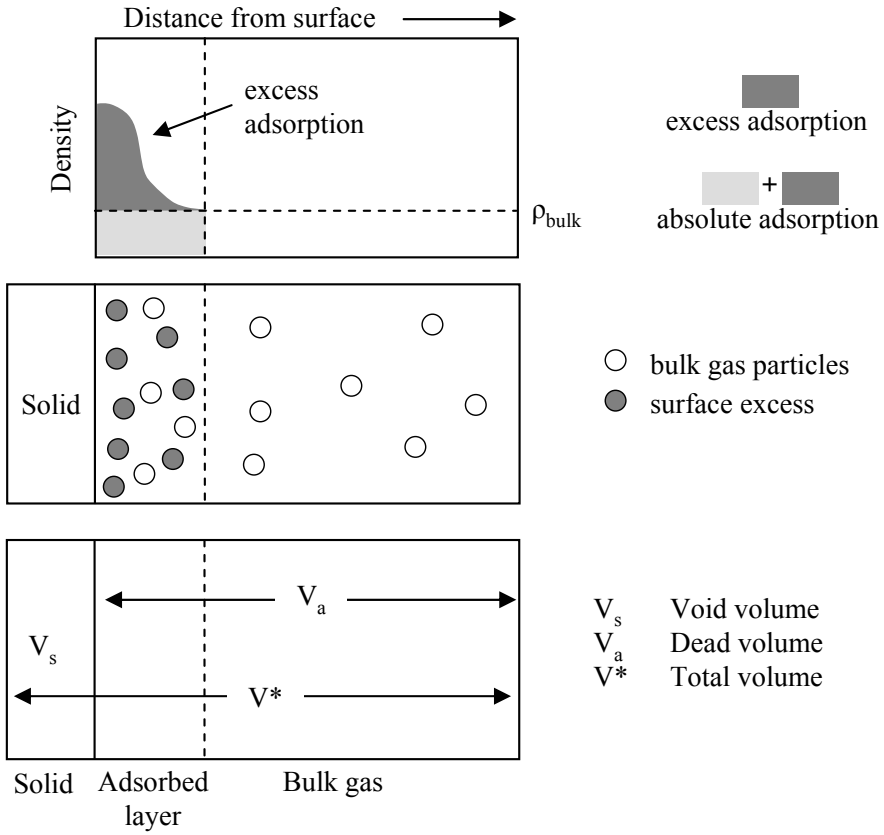

Figure 3.1: Illustration of surface excess adsorption and absolute adsorption. (Top) Density profile of the adsorptive gas as a function of distance from the adsorbent surface. Dark gray areas denote the adsorbed molecules, whereas light gray areas represent bulk gas amounts which are not counted towards adsorption in the surface excess scheme. (Middle) Illustration of the concept of bulk and adsorbed molecules. (Bottom) Important volumes of the adsorption system.

Table 3.1: Important definitions for adsorption

Symbol	Description
n^*	The total amount of adsorptive in the system (both adsorbed and bulk)
V^*	The total volume of the system (including the volume occupied by the adsorbent). It is known by calibrating the instrument.
V_s	The "void volume." This is the volume of the solid which is impenetrable for the adsorptive gas. It is typically measured by helium pycnometry.
m_s	Mass of the adsorbent.
V_a	The "dead volume." It is the difference between the total system volume and the void volume, $V_\mathrm{a} = V^* - V_\mathrm{s}$.

[a] *Adsorptive* refers to the chemical identity of the adsorbed and bulk molecules interacting with the adsorbent surface. *Adsorbate* refers specifically to the adsorbed molecules. Only a single-component adsorptive is considered here.

higher than in the bulk gas phase.[1] It is assumed that at a suitably large distance from the adsorbent surface, the adsorptive density decays back to a constant bulk density (ρ_{bulk}). This region is labeled as the "bulk gas." Important quantities for the adsorption model are defined in Table 3.1.

The standard practice is to express adsorption as a Gibbs *surface excess* quantity. This is the amount of adsorptive which is present in the adsorbed layer in excess of the bulk gas density, indicated in Fig. 3.1 by the dark gray region. Conveniently, the surface excess amount is the quantity which is measured in a standard volumetric measurement. The expression for the Gibbs surface excess amount is therefore

$$n^{\sigma} = n^{*} - \rho_{\text{bulk}} V_{\text{a}}. \tag{3.1}$$

The surface excess amount n^{σ} is an extensive quantity. Typically, however, data are presented as a specific surface excess amount

$$n = n^{\sigma}/m_s, \tag{3.2}$$

where m_s is the sorbent mass. It is also common to present the excess adsorption as a weight percent,

$$n(\text{wt}\%) = \left(\frac{m^{\sigma}}{m_s}\right) \times 100, \tag{3.3}$$

where m^{σ} is the surface excess mass. Both formats are used interchangeably in this thesis depending on the context.[2]

[1] This density profile is not known experimentally.

[2] It may seem attractive to consider the *absolute adsorption* amount, which is the total number of adsorptive molecules that are located within the adsorbate volume V_{ad}. However, V_{ad} cannot be measured directly since the density profile is not experimentally known. From an engineering viewpoint, therefore, the absolute adsorption amount is not particularly useful. It can be approximated as $n^{\text{a}} = n^{\sigma} + \rho_{\text{bulk}} V_{\text{ad}}$,

Most hydrogen adsorption measurements are performed well above the critical temperature of hydrogen (33 K). Supercritical H_2 cannot be liquefied by increasing the pressure, and therefore there is no saturation pressure. Consequently, hydrogen adsorption isotherms can extend up to high pressures and are often denoted "high-pressure isotherms." Supercritical isotherms often exhibit a local maximum when plotted versus pressure [73]. Above a certain pressure the bulk density begins to increase faster than the adsorbate density, and the excess adsorption actually decreases. Supercritical isotherms are characterized by monolayer adsorption and by a general decrease of the maximum adsorption amount with temperature [73].

3.1.2.2 Thermodynamics

A complete thermodynamic theory can be developed for a surface excess phase in equilibrium with a bulk gas phase, and a brief summary is provided here. The equations, notation, and terminology used in this section are taken directly from Ref. [6]. The surface excess layer can be considered as a distinct phase, with a thermodynamic state that is completely characterized by an area A, a spreading pressure Π, and a surface excess concentration $\Gamma = n^\sigma/A$. The differential energy of adsorption is the change in internal energy of the entire adsorption system upon the addition of an infinitesimal surface excess amount $\mathrm{d}n^\sigma$. In principle this can be measured directly by calorimetry. A more useful quantity is the differential enthalpy of adsorption ($\Delta\dot{h}_{T,\Gamma}$), which can be measured indirectly by the isosteric method. From the equilibrium condition between the surface excess phase and the bulk gas

where V_{ad} is approximated as the specific pore volume determined from surface texture analysis. Adsorption amount can also be reported as the total amount of hydrogen contained in the sample vessel [72]. This amount includes both the hydrogen that fills the dead volume of the vessel and the hydrogen that is bound on the adsorbent. Since this number is influenced by both the system volume and the adsorbent packing, it is not useful in describing intrinsic material properties. It may have some use in characterizing system volumetric densities in engineered storage systems, for example.

phase (i.e., $\mu^\sigma = \mu^\mathrm{g}$), the following expression can be derived,

$$\begin{aligned} \ln\left(\frac{p}{p^\circ}\right) &= \frac{\dot{u}^\sigma_{T,\Gamma} - u^\mathrm{g}_T - RT}{RT} - \frac{\dot{s}^\sigma_{T,\Gamma} - s^{\mathrm{g},\circ}_T}{R} \\ &= \frac{\Delta\dot{h}_{T,\Gamma}}{RT} - \frac{\Delta\dot{s}_{T,\Gamma}}{R}, \end{aligned} \tag{3.4}$$

where the differential enthalpy and entropy of adsorption are implicitly defined. The term $s^{\mathrm{g},\circ}_T$ is the standard molar entropy of the ideal gas at the standard pressure $p^\circ = 1$ bar. The quantity u^g_T is the internal energy of an ideal gas particle, and $\dot{u}^\sigma_{T,\Gamma}$ is the differential surface excess internal energy (i.e., the derivative of the total surface excess internal energy with respect to n^σ).

3.1.2.3 Isosteric heat of adsorption

We would like to calculate the differential enthalpy of adsorption from the experimentally measured quantities n^σ, p, and T. This is done using the *isosteric method* where a series of isotherms are measured at different temperatures. Equation 3.4 is differentiated with respect to temperature while holding Γ constant. If we assume that $\Delta\dot{h}_{T,\Gamma}$ and $\Delta\dot{s}_{T,\Gamma}$ are not dependent on temperature, then

$$\left(\frac{\partial}{\partial T}\ln[p]\right)_\Gamma = -\frac{\Delta\dot{h}_{T,\Gamma}}{RT^2}, \tag{3.5}$$

and we obtain,

$$\Delta\dot{h}_{T,\Gamma} = R\left(\frac{\partial \ln[p]}{\partial\,(1/T)}\right)_\Gamma, \tag{3.6}$$

where p is the pressure corresponding to the surface excess concentration Γ. When Eq. 3.6 is used to determine the differential enthalpy, at least two isotherms need to be measured

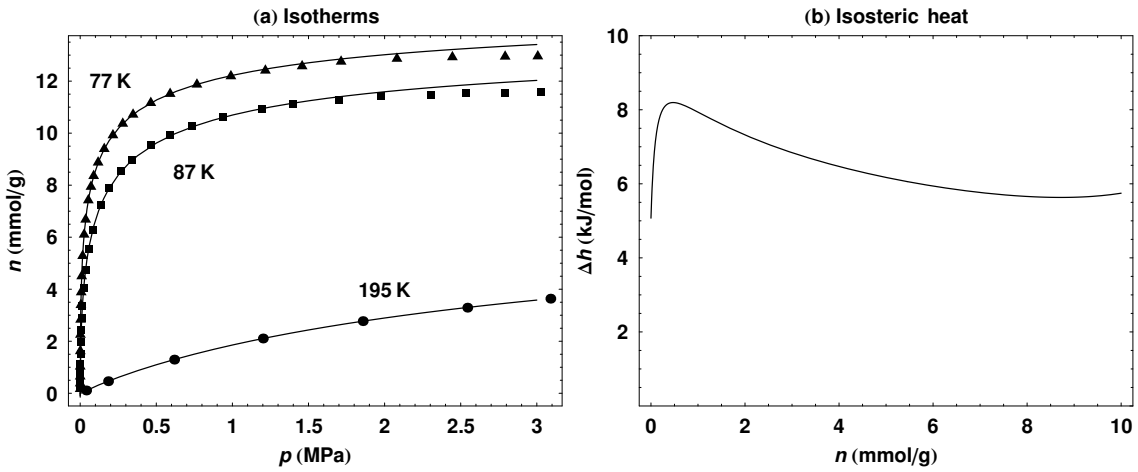

Figure 3.2: Isosteric heat derived from empirical functions fitted independently to each isotherm. (Left) Hydrogen adsorption isotherms of activated carbon CNS-201, each fitted to a Hill equation. (Right) Isosteric heat calculated from the fits (using Eq. 3.7).

at different temperatures which are not too far apart (a separation of 10 K is good).[3] The quantity obtained by this method is sometimes called the *isosteric heat*, to indicate that it has been determined by the isosteric method.

Experimental isotherms are not measured at perfectly spaced n intervals. Therefore it is necessary to either fit the isotherm to some function, or to interpolate the appropriate n from the isotherm data points. Because the isosteric method is very sensitive to errors in the equilibrium pressure, interpolation can sometimes introduce significant artifacts into the calculated isosteric heat. Our standard approach is to fit the 77 K and 87 K isotherms individually to an empirical function, $n = f(p)$. The isosteric heat can now be estimated

[3] It is better to measure more than two isotherms and then plot the isosteres ($\ln p$ versus $1/T$ for a constant value of n) to check for linearity.

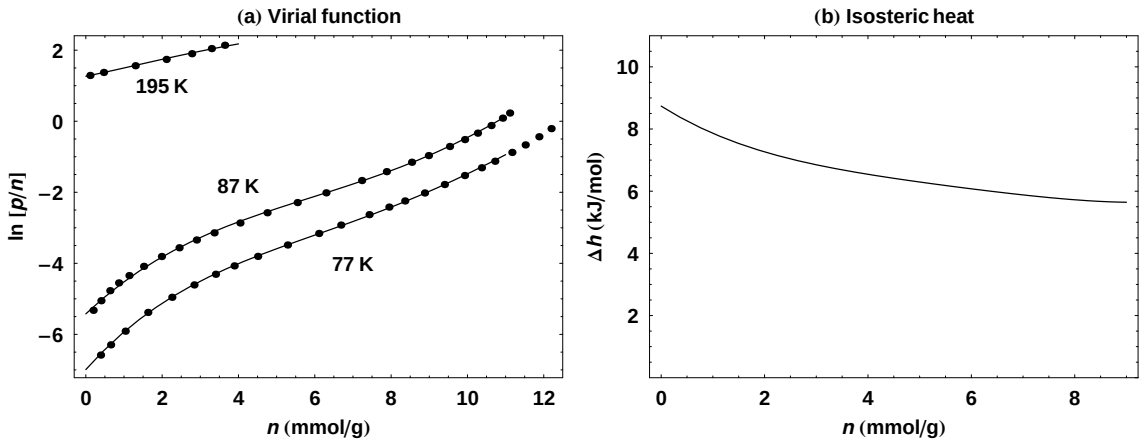

Figure 3.3: (a) Hydrogen adsorption isotherms of CNS-201 fitted to a single model-independent virial equation given by Eq. 3.8. The data is plotted as $\ln[p/n]$ versus n. (b) Isosteric heat calculated from Eq. 3.9.

from the inverse of the fitting functions,

$$\begin{aligned}\Delta\dot{h}_{T,\Gamma} &= R\left(\frac{\partial \ln[p]}{\partial\,(1/T)}\right)_{\Gamma} \\ &\approx \left(\frac{\ln\left[f_{77}^{-1}(n)\right] - \ln\left[f_{87}^{-1}(n)\right]}{(77\,\mathrm{K})^{-1} - (87\,\mathrm{K})^{-1}}\right) \times \left(8.314\,\mathrm{J\,mol^{-1}\,K^{-1}}\right) \\ &= \left(\ln\left[\frac{f_{77}^{-1}(n)}{f_{87}^{-1}(n)}\right]\right) \times \left(5.57\,\mathrm{kJ\,mol^{-1}}\right).\end{aligned} \tag{3.7}$$

The units of the fitting function cancel out in the last expression as long as they are used consistently. One problem with this method is that it is often difficult to fit the experimental isotherms in the low pressure region. This is especially true for the steep isotherms which are typical of microporous adsorbents. An example of the problems with fits to empirical equations at low pressures is illustrated in Fig. 3.2. The 77 K and 87 K hydrogen adsorption isotherms collected on an activated carbon (CNS-201) were individually fitted to the Hill equation.[4] The isosteric heat was calculated from the fits (using Eq 3.7). It is clear that there is an artificial drop in the isosteric heat as n approaches zero.

[4]The Hill equation utilized here is actually equivalent to the Langmuir equation. It is given by $f(p) = n_{\max}/\left[1 + (a/p)^r\right]$, where r sets rate at which the function grows, and a sets the p-value at which the function is at half-maximum.

I found that a better method for calculating isosteric heats is to fit all the hydrogen adsorption isotherms to a single model-independent virial-type thermal equation [74]. This equation is given by

$$\ln p = \frac{1}{T}\sum_{i=0}^{l} a_i n^i + \sum_{i=0}^{m} b_i n^i + \ln n. \tag{3.8}$$

Equation 3.8 is fit simultaneously to the 77 K, 87 K, and 195 K data. Fitting parameters $\{a_i,b_i\}$ are temperature independent, and the sum limits l and m are increased until a sufficient goodness-of-fit is reached. The isosteric heat can be easily calculated from Eq. 3.8 by taking the derivative with respect to T,

$$\Delta\dot{h}_{T,\Gamma} = R\left(\frac{\partial \ln[p]}{\partial\,(1/T)}\right)_{\Gamma} = -R\sum_{i=0}^{l} a_i n^i. \tag{3.9}$$

In the zero-coverage limit the enthalpy equals $\Delta\dot{h}_{T,\Gamma} = -R\,(a_0)$. An example of the model-independent virial equation for the same CNS-201 sample is displayed in Fig. 3.3. The adsorption data is presented in terms of $\ln(p/n)$ versus n and is fit simultaneously to the virial-type thermal equation. Values of $l = m = 5$ were sufficient for the fit. The isosteric heat now has the correct shape in the low pressure region, without the artificial drop obtained from the individual fits to the empirical equation (Eq. 3.7). All of the isosteric heats presented in this thesis were calculated using the model-independent virial equation method, unless otherwise specified.

3.1.2.4 Henry's law

In the low pressure region, surface excess adsorption is proportional to the equilibrium pressure (Henry's law). This is basically a consequence of the dilute adsorbed phase behaving

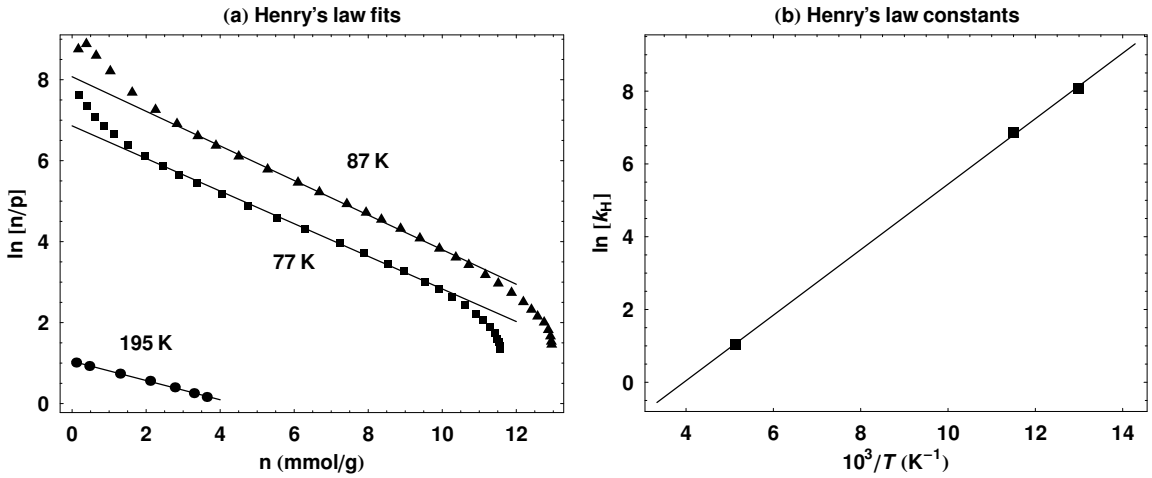

Figure 3.4: Differential enthalpy of adsorption in the zero-coverage limit calculated from Henry's law. (a) Adsorption isotherm points from CNS-201 presented in the $\ln[n/p]$ versus n format. The Henry's law constant for each temperature is equal to the y-intercept of the fitted line. (b) Henry's law constants at 77 K, 87 K and 195 K are plotted against $1/T$.

like a two dimensional ideal gas. The relation is given by

$$n = k_{\mathrm{H}} p, \tag{3.10}$$

where k_{H} is known as the Henry's law constant. To calculate Henry's law constants, adsorption in the low-pressure region can be accurately modeled by a virial-type equation to take into account small deviations from linearity

$$\ln(n/p) = K_0 + K_1 n + K_2 n^2 + \cdots . \tag{3.11}$$

Since $k_{\mathrm{H}} = \lim_{n \to 0} (n/p)$, the Henry's law constant can be obtained from the zero-order virial coefficient $K_0 = \ln(k_{\mathrm{H}})$. By carefully measuring adsorption amounts in the low-pressure region using a high resolution gauge, we can therefore obtain accurate Henry's law constants at 77 K, 87 K, 195 K, and 298 K. An example for the CNS-201 sample is provided in Fig. 3.4. The y-intercepts of the fitted lines are used to calculate the Henry's law constant at each

temperature.[5] The differential enthalpy of adsorption in the limit of zero coverage ($\Delta\dot{h}_0$) can be calculated from the van't Hoff equation

$$\Delta\dot{h}_0 = R\left(\frac{\partial \ln [k_{\mathrm{H}}]}{\partial 1/T}\right)_n . \tag{3.12}$$

Therefore, the zero coverage enthalpy is simply equal to the slope of the line in Fig. 3.4b multiplied by the ideal gas constant $R = 8.314\,\mathrm{J\,mol^{-1}\,K^{-1}}$. What makes the zero coverage enthalpy so interesting is that it represents the pure sorbent-hydrogen interaction with little contribution from the hydrogen-hydrogen interactions. It can therefore be used to probe systematic trends, for example, in a series of chemically-modified carbon sorbents. However, because of the inaccuracy of low-pressure measurements the Henry's law analysis needs to be done carefully.

3.1.3 Sieverts apparatus

3.1.3.1 Description

Hydrogen adsorption measurements were collected with a custom-built, manually-operated Sieverts instrument [75]. Because the instrument is custom-built and information about it is not readily available, a detailed description will be provided in this section. The operating limits for the instrument are 100 bar and 600 ℃. A schematic drawing of the Sieverts apparatus is shown in Fig. 3.5. The instrument is equipped with both a high-resolution manometer (MKS-120, Baratron capacitance gauge, 25 000 Torr max) and a wide-range manometer (MKS-833, Baratron capacitance gauge, 3000 psi max). Temperature is monitored with platinum resistance thermometers (PRT) bonded to the exterior of the steel

[5] The deviations from linearity at small n may be due to errors in the response of the pressure transducer at very low pressures, which is then amplified by taking the algorithm. They are also sometimes characteristic of adsorption by microporous materials [6].

tubing. The vacuum system consists of a high-vacuum molecular drag pump (Alcatal MDP 5011) connected to an oil-free diaphragm backing pump (KNF, Model N880.3 AN22 E). Vacuum pressure is monitored with a cold cathode vacuum gauge. Base pressure is typically around 7×10^{-7} Torr. The instrument contains manual (DL-type) and air-actuated (HB-type) stainless steel Swagelok valves. All tubing and fittings are made from electropolished 316L stainless steel. Leak-tight Swagelok VCR® fittings are used for connections between tubing and valves. The only exception is the reactor fitting, which uses a Conflat flange copper gasket (1.33 in. flange). To prevent fine powders from being sucked into the

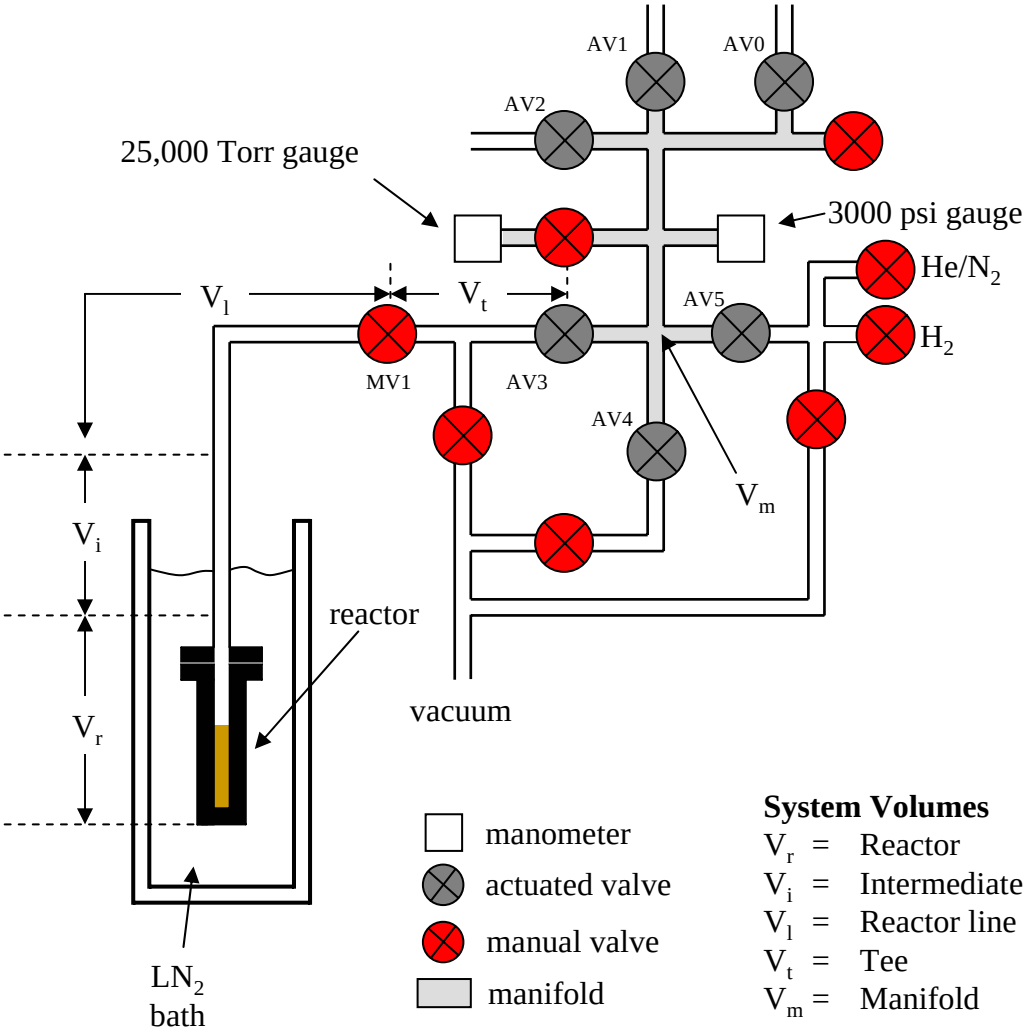

Figure 3.5: Schematic illustration of the Sieverts instrument.

manifold, a 2 µm filter gasket is typically placed into a small seat in the reactor and secured by an internal retaining ring. All components all welded, except for valves and sensors. The accuracy of the high-resolution MKS120 manometer is approximately 0.08 % of the readout, and is used with the factory calibration. The pressure gauges exhibit hysteresis, particularly following high-pressure measurements. Therefore the zero point pressure is typically reset prior to each experiment. Research-grade H_2 (99.98 %) was used for all measurements, in conjunction with an in-stream filter assembly (Millipore Corp., Inert II Reactive Micro Matrix). For air-sensitive samples, the entire reactor assembly can be brought into a glovebox and then sealed off with valve MV1 after sample loading.

3.1.3.2 Volumetric method

Measurements are collected using an extremely simple volumetric method. As pictured in Fig. 3.5, the reactor volume is kept at a constant temperature by either a liquid N_2 bath (77 K), a liquid Ar bath (87 K) or a dry ice bath (195 K). An intermediate temperature region (V_i) is assumed to have a constant temperature gradient between the bath temperature and room temperature, and is assigned an average value of $T_\mathrm{int} = (T_\mathrm{bath} + T_\mathrm{room})/2$. The remainder of the instrument volume remains at ambient room temperature, which is measured by a PRT bonded to the exterior of the manifold region. Hydrogen is first introduced into the manifold volume V_m by opening and then closing valve AV5. The gas is then expanded into the tee volume, V_t, by opening valve AV3. The pressure can be fine-tuned by opening valve AV4 and adjusting a manual needle valve which connects to the vacuum system. The initial pressure and manifold temperature are now recorded (p_1, T_room). Hydrogen is finally expanded into the reactor volume $V_\mathrm{l} + V_\mathrm{i} + V_\mathrm{r}$ by opening manual valve MV1. After allowing the adsorption system to reach equilibration (typically 15 min),

the final pressure and manifold temperature are recorded (p_2, T_{room}). Assuming it does not fluctuate too much in the course of the experiment, it is typically acceptable to use an average value of the room temperature.

Gas densities, $\rho\left(p,T\right)$, are determined from the measured pressure and temperature using the NIST Reference Fluid Thermodynamics and Transport Properties (REFPROP) database [76]. The initial and final amounts of non-adsorbed, bulk hydrogen are given by

$$n_i = \rho\left(p_1, T_{\mathrm{room}}\right)\left[V_{\mathrm{m}} + V_{\mathrm{t}}\right] \tag{3.13a}$$

$$n_f = \rho\left(p_2, T_{\mathrm{room}}\right)\left[V_{\mathrm{m}} + V_{\mathrm{t}} + V_{\mathrm{l}}\right] + \rho\left(p_2, T_{\mathrm{int}}\right)\left[V_{\mathrm{i}}\right] + \rho\left(p_2, T_{\mathrm{bath}}\right)\left[V_{\mathrm{r}} - V_{\mathrm{sample}}\right], \tag{3.13b}$$

where V_{sample} refers to the void volume displaced by the sample.[6] The surface excess adsorption is simply given by the decrease in the mass of bulk hydrogen, $n^{\sigma} = n_i - n_f$. This procedure measures the excess adsorption that occurs with a single dose of hydrogen. To collect a complete isotherm, this step is performed repeatedly at incrementally higher pressures. In the incremental method the hydrogen is not desorbed between isotherm points. This results in considerable time savings, but can also lead to incrementally increasing errors if the measurements are not done carefully. At the end of an adsorption series, we can begin a desorption series by essentially running the same procedure in reverse. With MV1 closed, the manifold + tee volume is opened to vacuum until a specific pressure is reached. Then MV1 is opened, the system is allowed to equilibrate, and the final pressure is recorded.

[6] To determine V_{sample} it is necessary to perform a set of helium expansion measurements prior to the experiment.

3.1.3.3 Errors in volumetric adsorption measurements

The volumetric method is a standard method for measuring gas adsorption and is very simple to implement. However, if adsorption measurements are collected in a cumulative fashion without desorbing between each point, errors in the data can accumulate linearly. Therefore it is important to identify all the major sources of error in a volumetric adsorption measurement.

For example, uncertainty in the void volume of the sample can to lead to large errors in the measured hydrogen adsorption, particularly for low-density materials [77]. The standard method we use to determine the void volume of the sample is to expand helium into the reactor (loaded with sample) at room temperature. It is assumed that the helium is not adsorbed and that the micropores impenetrable to helium are also impenetrable to hydrogen. I tested the accuracy of the helium volume technique on our Sieverts instrument by measuring a non-porous aluminum spacer of known dimensions. Helium was expanded into the reactor from nine different initial pressures between 1000 Torr and 9000 Torr, and measurements were simultaneously recorded using both the 25 000 Torr gauge and the 3000 psi gauge. There was considerably more variation in the measurements made by the lower resolution 3000 psi gauge. Based on its physical dimensions, the volume of the aluminum spacer was 0.99 ml. This compares to 1.01(2) ml obtained with the high-resolution gauge and 0.9(2) ml obtained with the lower resolution gauge. For many carbon adsorbents we find that it is sufficient to use a generic *skeletal density* of $2.1\,\mathrm{g\,ml^{-1}}$ (roughly the mass divided by the void volume) to calculate the void volume based on the sample mass. In cases where H_2 uptake amounts are large, we can use this approximation.

If single-point measurements are collected for long time periods (i.e., several hours), then daily fluctuations in the ambient temperature can affect the data in several ways. First,

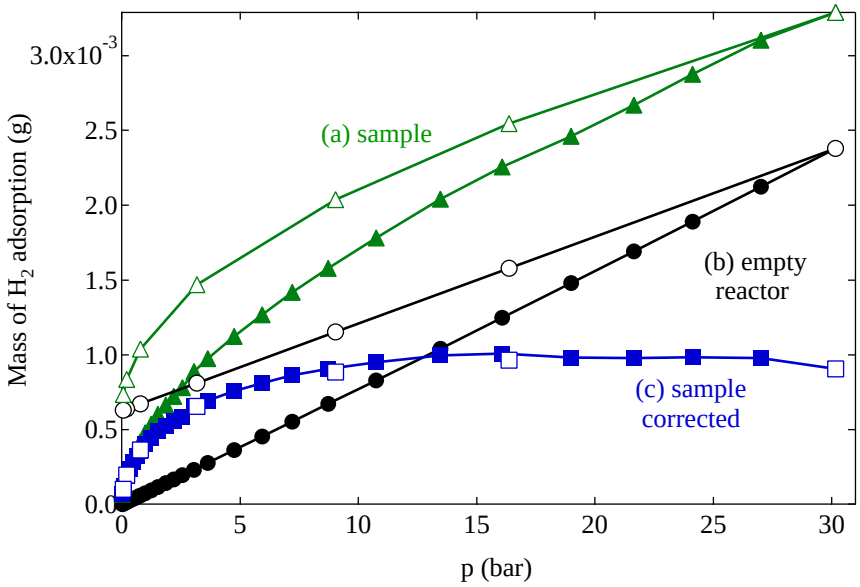

Figure 3.6: Illustration of the effect of empty reactor adsorption. (a) Hydrogen adsorption by reactor containing a sample (Cr_2O_3 aerogel). (b) Adsorption by the empty reactor. (c) Corrected sample adsorption after subtracting the empty reactor background. Sample temperature was 77 K and pressure was measured on the high-resolution gauge. Solid symbols are adsorption points and open symbols are desorption points. Total H_2 adsorption amount is presented rather than the specific adsorption amount.

the hydrogen density in the manifold can change slightly, which can be significant at high pressures. Second, the signals from the capacitance pressure gauges themselves change with temperature. Leaks within the system can also cause problem for measurements that involve either long collection times or small adsorption amounts. To test these temperature effects, I filled the instrument volume with H_2 and logged all system temperatures and pressures for up to 80 hours. At 50 bar pressure there were not any detectable leaks in the system, and the pressure was well-correlated with the ambient temperature. There did appear to be a leak at 80 bar, in which the pressure dropped substantially without any correlation with the ambient temperature. Therefore leaks can indeed be a major source of error on this instrument at high pressures. Fortunately none of the adsorption measurements presented in this thesis exceed 50 bar pressure.

A useful way to determine the accuracy of the Sieverts instrument is to collect a hydrogen

adsorption isotherm with an empty reactor. If the reactor is at 298 K, there should be no real adsorption. Any measured adsorption is due to experimental errors. If the reactor is at 77 K or 87 K, there may be a small amount of adsorption on the reactor walls or in the filter gasket mesh, but any substantial measured adsorption is indicative of cumulative error. We have performed numerous empty reactor measurements at the standard sample temperatures. An illustrative example of the effect of empty reactor adsorption is presented in Fig. 3.6. In this case the total H_2 adsorption by the sample (a Cr_2O_3 aerogel) was very small, on the order of the empty reactor adsorption itself. To determine the true adsorption by the sample, the background adsorption by the empty reactor needs to be subtracted. Hysteresis is present for the empty reactor adsorption and desorption runs, so they need to be fit to separate linear equations. The corrected sample adsorption and desorption is obtained once the reactor background has been subtracted.

3.2 Neutron scattering

3.2.1 Introduction

Neutron scattering is a powerful method for investigating the structure and dynamics of condensed matter. It is particularly useful as a tool for studying H_2 as a guest species inside of a host adsorbent. There are several reasons for this. First, compared to electrons and X-rays, neutrons interact weakly with matter. This means that they can probe the hydrogen dynamics within bulk materials instead of simply being scattered at the surface. Second, hydrogen contains a comparatively large neutron scattering cross-section. Neutrons are scattered by nuclear forces, and the scattering cross-sections do not vary systematically with the atomic number Z. This is different than X-ray scattering cross-sections, which vary

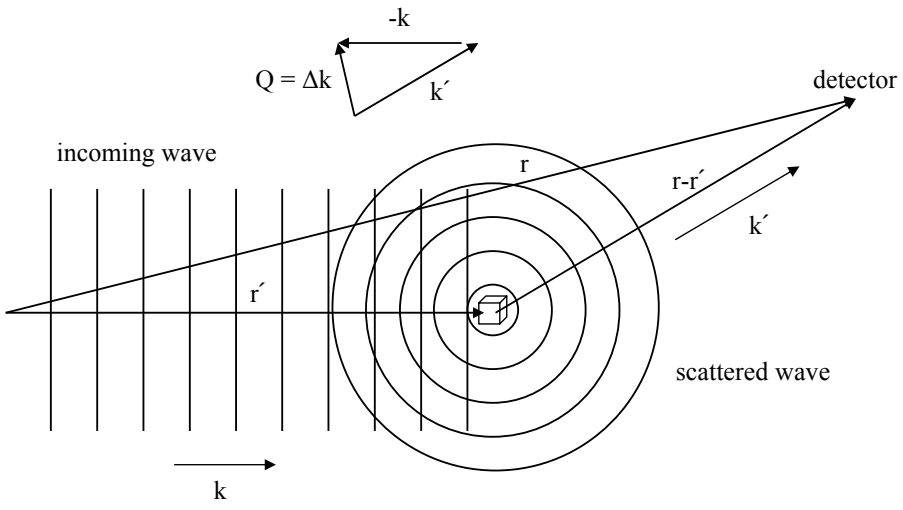

Figure 3.7: Wavevectors and position vectors for a neutron scattering event. The vector **Q** is defined as $\mathbf{k}' - \mathbf{k}$ at the top-center of the illustration. Adapted from Ref. [78].

with Z^2. Therefore, even in a carbon adsorbent system consisting of only 1% hydrogen by mass, more than half of the neutron scattering is due to hydrogen. Finally, thermal neutrons conveniently have wavelengths similar to the interatomic distances in solids and kinetic energies on the order of excitations in condensed matter (e.g., phonons). In this section, a brief overview of neutron scattering theory will be presented as well as an introduction to the instrumental methods used to collect the data.

3.2.2 Theory

A neutron scattering event with a single nucleus is illustrated in Fig. 3.7. Neutrons have both particle-like and wave-like properties. The incident neutron can be described by a plane wave $\psi_{inc} = e^{i(\mathbf{k}\cdot\mathbf{r}'-\omega t)}$. The wavefunction of the scattered neutron emanates from the center of the scattering and is described by a spherical wave $\psi_{sc} = \frac{b}{|\mathbf{r}-\mathbf{r}'|}e^{ik'|\mathbf{r}-\mathbf{r}'|}$, where b is the scattering length of the nucleus. The neutron wavevector $\mathbf{k}$ points in the direction of the velocity and has the magnitude $k = 2\pi/\lambda$, where λ is the de Broglie wavelength. The neutron momentum is $\mathbf{p} = \hbar\mathbf{k}$ and the energy is $E = \frac{1}{2m}\hbar^2k^2$. For the scattered neutron,

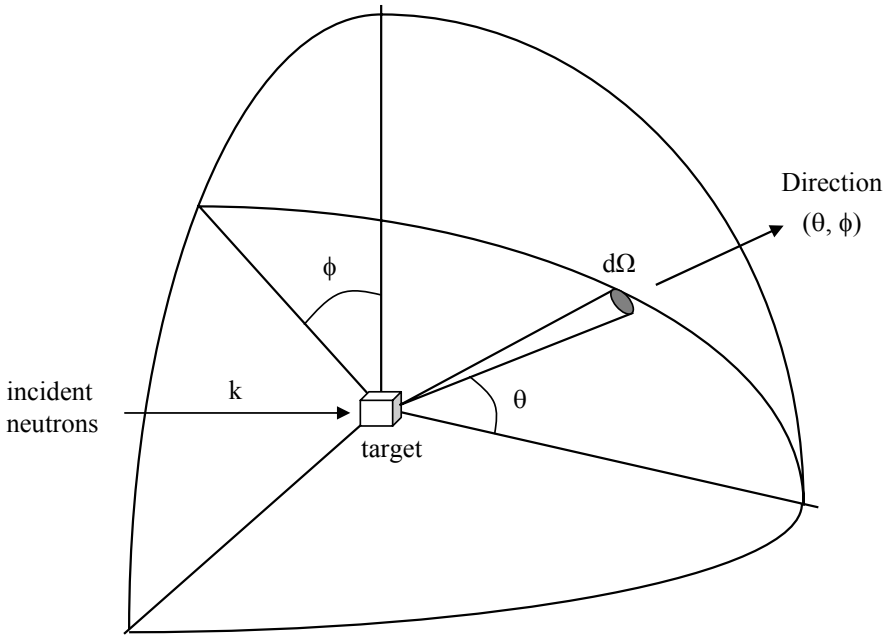

Figure 3.8: Simplified layout of the typical geometry of a neutron scattering experiment. Adapted from Ref. [79].

the momentum transfer has the magnitude

$$\hbar\mathbf{Q} = \hbar\left(\mathbf{k}' - \mathbf{k}\right), \tag{3.14}$$

and the neutron energy transfer is

$$\hbar\omega = E' - E = \frac{\hbar}{2m}\left(k'^2 - k^2\right). \tag{3.15}$$

The momentum transfer depends both on the scattering angle and the energy transfer. The wavevector transfer $\mathbf{Q}$ is often used to represent the momentum transfer (especially in figure annotations) and is reported in units of Å^{-1}. When the sample is at low temperatures, the scattered neutrons typically lose energy, but $\hbar\omega$ is typically still reported as a positive quantity to denote energy loss (the convention used in this thesis).

The quantity that is directly measured in a neutron scattering experiment is the double

differential cross-section. As illustrated in Fig. 3.8, the neutrons are incident on some target. They have a known initial energy E and a known flux Φ. What the neutron spectrometer typically measures is the number of neutrons of final energy E' scattered in a particular direction (θ, ϕ). This quantity can be formalized by considering the double differential cross-section, $\mathrm{d}^2\sigma/\mathrm{d}\Omega\mathrm{d}E$, which gives the number of neutrons scattered per second into the solid angle $\mathrm{d}\Omega$ with a final energy in the range $\mathrm{d}E$, divided by the incident flux Φ. The cross-section has dimensions of [area] and is typically expressed in units of barn, where $1\,\mathrm{b} = 10^{-28}\,\mathrm{m}^2$. The total scattering by the nucleus is obtained by integrating over solid angle and energy,

$$\sigma = \int \mathrm{d}E \int \mathrm{d}\Omega \frac{\mathrm{d}^2\sigma}{\mathrm{d}\Omega\mathrm{d}E} = 4\pi b^2, \tag{3.16}$$

where b is the scattering length of the nucleus.

We do not study scattering from a single nucleus but from a large system of scatterers. Even if the system consists of a single element, the scattering length b_i of each individual nuclei can differ depending on nuclear spin or the presence of isotopes. This leads to the presence of coherent and incoherent scattering from a sample. The coherent and incoherent cross-sections are given by

$$\sigma_{\mathrm{coh}} = 4\pi\langle b\rangle^2 \tag{3.17}$$

$$\sigma_{\mathrm{inc}} = 4\pi\left(\langle b^2\rangle - \langle b\rangle^2\right). \tag{3.18}$$

Incoherent scattering arises from random deviations of scattering lengths from their mean value. The hydrogen isotope ^{1}H has oppositely signed scattering lengths for its two nuclear spin states ($\pm\frac{1}{2}$) with a weighted mean close to zero. It is therefore an overwhelmingly incoherent scatterer. In incoherent scattering, the phase relationship between the incident

wave and the scattered wave is not preserved. We cannot directly sum the scattered waves to obtain the total outgoing wave. Instead, we sum the individual intensities of the scattered waves to obtain the total incoherent intensity,

$$I_{\text{inc}} = \sum_{\mathbf{r}_i} I_{\mathbf{r}_i} = \sum_{\mathbf{r}_i} |\psi_{\mathbf{r}_i}|^2. \tag{3.19}$$

The waves do not interfere constructively or destructively and do not provide direct information on the material structure. However, incoherent scattering does provide information on the self-correlation function of the scatterers. The van Hove self-correlation function, $G_{\text{s}}(\mathbf{r}, t)$, can be interpreted as giving the probability that a particle will be found at position $\mathbf{r}(t)$ at time t if it was initially located at the origin at time zero. The incoherent scattering function, $S_{\text{inc}}(\mathbf{Q}, \omega)$, is the Fourier transform in time and space of the van Hove self-correlation function:

$$S_{\text{inc}}(\mathbf{Q}, \omega) = \frac{1}{2\pi} \iint \exp\left[i\left(\mathbf{Q} \cdot \mathbf{r} - \omega t\right)\right] G_{\text{s}}(\mathbf{r}, t)\, \mathrm{d}\mathbf{r}\mathrm{d}t. \tag{3.20}$$

The quantity which is actually measured by the instrument, however, is the double differential scattering cross-section,

$$\left(\frac{\mathrm{d}^2\sigma}{\mathrm{d}\Omega \mathrm{d}E'}\right)_{\text{inc}} = \frac{\sigma_{\text{inc}}}{4\pi\hbar}\frac{k'}{k} S_{inc}(\mathbf{Q}, \omega) \tag{3.21}$$

from which $S_{\text{inc}}(\mathbf{Q}, \omega)$ is typically extracted (to within some arbitrary prefactor). In this context, $\mathbf{Q}$ and ω are the spatial and temporal frequencies obtained by Fourier transform from the real-space variables $\mathbf{r}$ and t. Measurements at small $\mathbf{Q}$ are therefore sensitive to processes with large characteristic lengths. Similarly, measurements at small energy loss $\hbar\omega$

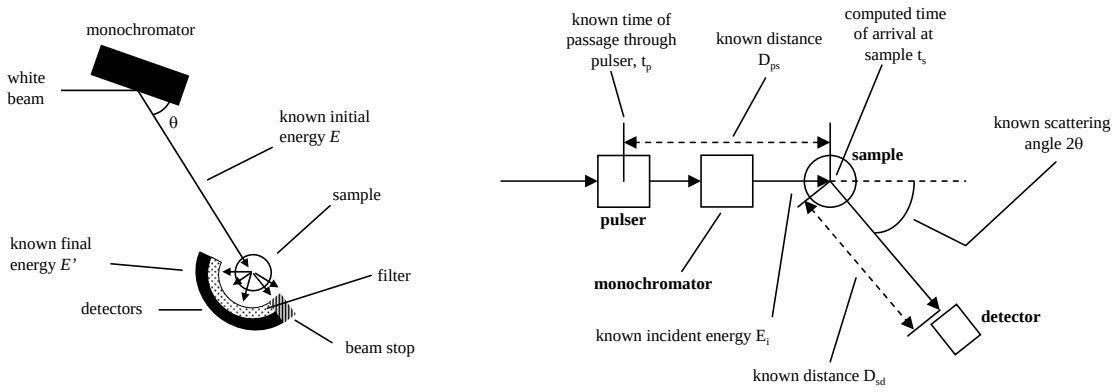

(a) Inverse Geometry **(b) Direct Geometry**

Figure 3.9: Schematic illustration of (a) an inverse geometry neutron spectrometer and (b) a direct geometry spectrometer.

correspond to slow processes with large characteristic times, τ.

3.2.3 Indirect geometry spectrometers

An instrument with a fixed final neutron energy is called an inverse geometry spectrometer. The Filter Analyzer Spectrometer (FANS) instrument at the NIST Center for Neutron Research (NCNR) is an example of an inverse geometry instrument [80]. This instrument was used for most of my inelastic measurements on KC_{24}, and a schematic is illustrated in Fig. 3.9a. An incoming white beam contains a distribution of wavelengths. The crystal monochromator selects a particular wavelength at the angle θ by Bragg diffraction. The initial neutron energy is then given by $E = h^2/\left(2m\lambda^2\right)$. The sample is moved step-wise across a range of θ which allows the initial energy to be varied. The final energy is fixed by a low-pass graphite/beryllium filter which has a cutoff of around $E' = 1\,\text{meV}$. Data is collected at each angle, θ, for a specific number of monitor counts, and the neutrons which reach the detector during this interval are known have an energy loss of about E, with the resolution set primarily by the low-pass filter. At each step counts are summed over the entire pie-shaped detector array. Due to the low final energy, however, the final wavevector

is negligible compared to the initial wavevector and therefore $\mathbf{Q}$ is largely independent of the scattering angle (i.e., $\mathbf{Q} \approx \mathbf{k}$). This means that $E \sim Q^2$ and that peaks at large energy also have a large Q. What is measured is not actually the scattering function, $S_{\text{inc}}(\mathbf{Q}, \omega)$, but a quantity which is approximately proportional to the vibrational density of states of the sample.

3.2.4 Direct geometry spectrometers

Direct geometry spectrometers use a chopper to produce a neutron beam with fixed initial energy. As illustrated in Fig. 3.9b, the final neutron energy is calculated from the time-of-flight from the sample to the detector. From the angle of the detector, and the initial and final energies, the magnitude of the momentum transfer can be calculated:

$$\frac{\hbar^2 Q^2}{2m} = E + E' - 2\left(EE'\right)^{1/2} \cos\theta. \tag{3.22}$$

Based on position, each detector has a different trajectory through (Q, ω) space. It is important to normalize the detector efficiencies by measuring the scattering from a purely incoherent scatterer such as vanadium. The Disc-Chopper Spectrometer (DCS) at NCNR is an example of a direct-geometry spectrometer [81]. It was used for most of the quasielastic measurements on KC_{24}. Because it is located at a reactor neutron source, it has a disc chopper component to artificially create a pulsed source.

Chapter 4

Hydrogen adsorption by graphite intercalation compounds

4.1 Introduction

Understanding the thermodynamics of H_2 adsorption in chemically modified carbons remains an important area of fundamental research. One reason is that physisorption of H_2 by carbons is significantly influenced by dispersion forces, which are notoriously difficult to calculate by first-principles methods. Further, most high-surface-area carbons have disordered structures which are difficult to model by simulations. As discussed in Sec. 1.7, graphite intercalation compounds provide an model system for systematically studying the effects of chemical modification and slit pore spacing on hydrogen adsorption thermodynamics. In this chapter, accurate measurements of the isosteric heat of H_2 adsorption in KC_{24}, RbC_{24}, and CsC_{24} are presented. The effect of alkali-metal doping and graphite interlayer spacing on the adsorption enthalpy are discussed. The effect of adsorption kinetics is also investigated.

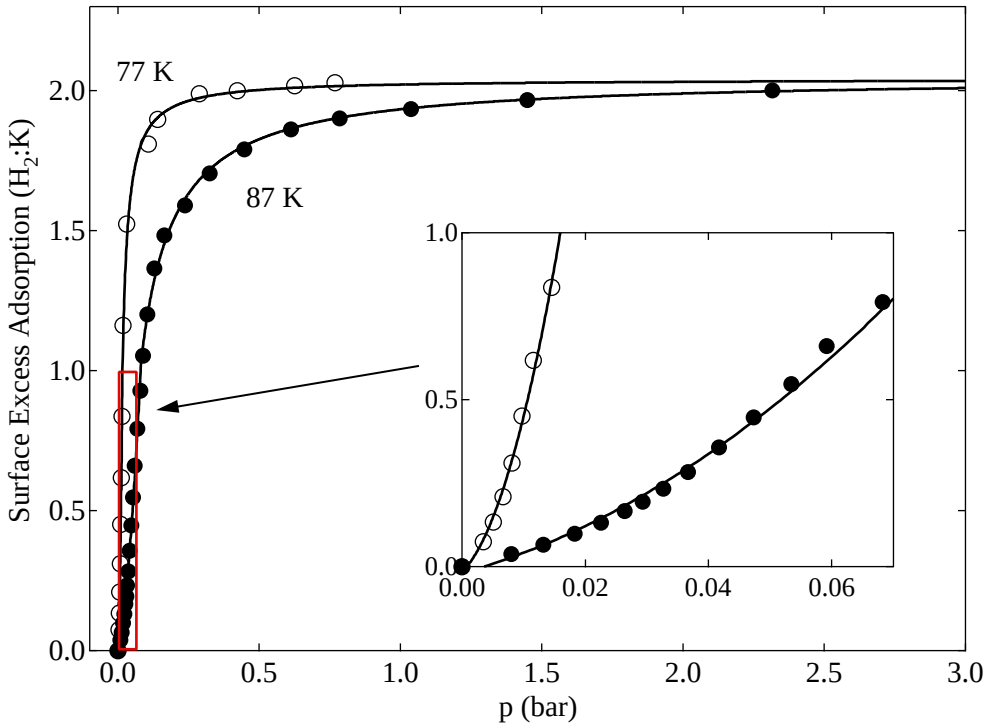

Figure 4.1: Hydrogen adsorption isotherms of KC_{24} at 77 K and 87 K. Inset shows a magnified view of the low-pressure portion of the isotherm contained within the red box. Lines are only a guide for the eye.

4.2 Hydrogen adsorption isotherms of KC_{24}

Hydrogen adsorption isotherms were measured for a 0.787 g sample of KC_{24} synthesized from flake graphite. Loading was done in an argon glovebox so that the sample was not exposed to air at any stage of the experiment. Adsorption isotherms were collected at 77 K and 87 K, and are displayed in Fig. 4.1. The isotherms are steep, and a magnified view of the low-pressure region is provided in the inset. For this sample, the maximum hydrogen composition after adsorption was $KC_{24}(H_2)_{2.03}$, which is equivalent to 1.24 wt%. Both the 77 K and 87 K isotherms reached the same maximum capacity, which is not typically observed for supercritical adsorption in porous carbons [73].

As explained further in Sec. 4.4, adsorption is kinetically limited at a hydrogen com-

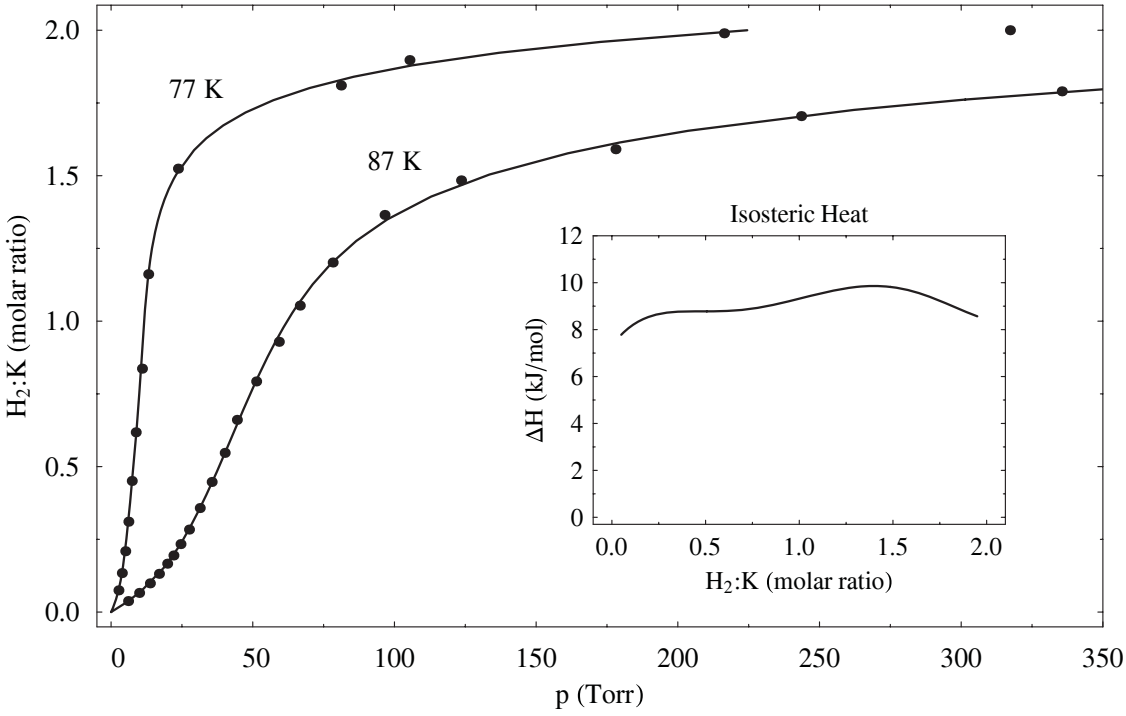

Figure 4.2: Adsorption isotherms of KC_{24} at 77 K and 87 K fitted to a virial-type thermal equation. Inset: Isosteric heat as a function of adsorption amount.

position greater than $KC_{24}(H_2)_{1.6}$, which means that isotherm points in this region do not necessarily correspond to true equilibrium states. At 77 K and 87 K the hydrogen adsorption was fully reversible, and there was not any evidence of dissociation or reaction. Further, there was no reduction in adsorption capacity during three consecutive adsorption/desorption cycles at 77 K. Hydrogen adsorption at 195 K, however, was not completely reversible. When measured after 195 K isotherms, the 77 K isotherms displayed a greatly reduced maximum adsorption capacity. It is very likely that the hydrogen chemically reacted with the potassium intercalant at 195 K [55]. A full characterization of the reaction products was not pursued. It is known that KC_{24} chemisorbs a small amount of hydrogen at elevated temperatures to form a $KC_{24}H_{0.25}$ stoichiometry [47].

The isosteric heat for KC_{24} was calculated from fits of the virial-type thermal equation (Eq. 3.8) to the isotherm data, following the procedure explained in Sec. 3.1.2.3. The

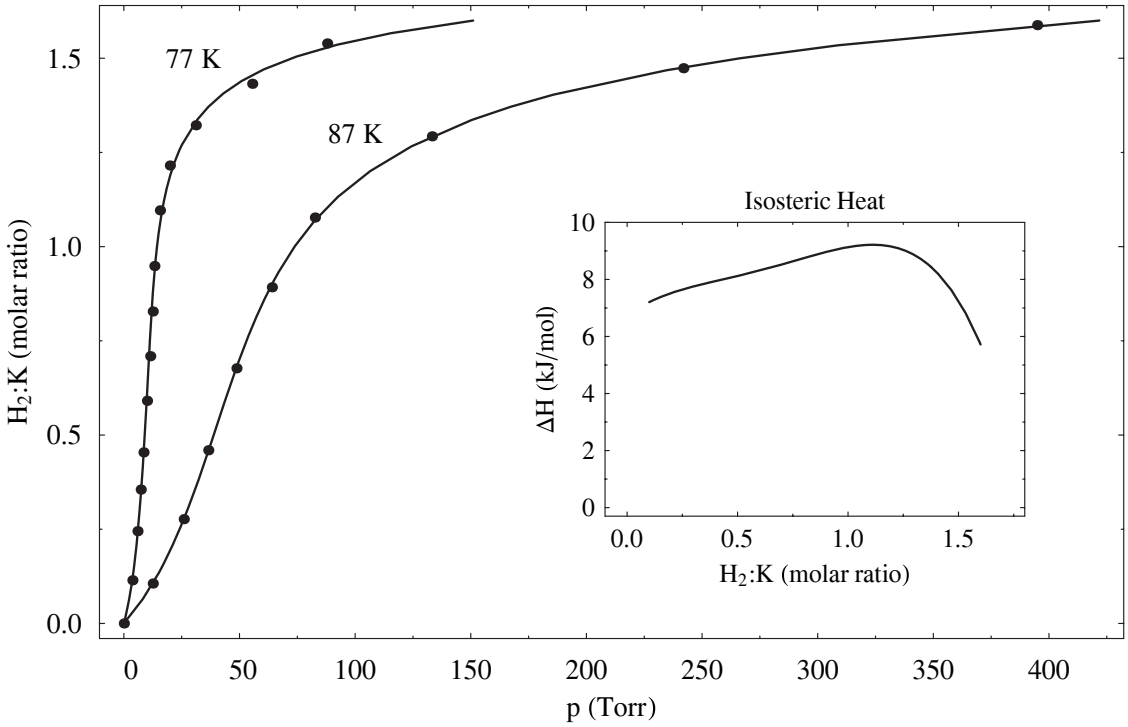

Figure 4.3: Adsorption isotherms of Grafoil-based KC_{24} at 77 K and 87 K fitted to a virial-type thermal equation. Inset: Isosteric heat as a function of adsorption amount.

isotherms, fits, and calculated isosteric heat are displayed in Fig. 4.2. The zero coverage limit of the isosteric heat is $7.3\,\mathrm{kJ\,mol^{-1}}$. The average value of the isosteric heat for $KC_{24}(H_2)_x$ in the range of $0.25 < x < 1.5$ is equal to $9.2\,\mathrm{kJ\,mol^{-1}}$.[1] The detailed shape of the isosteric heat is probably influenced by systematic instrument errors, among other things. The unique "S" shaped curve of the KC_{24} isotherms has been remarked upon previously [48] and is thought to originate from the expansion of the c-axis spacing with H_2 adsorption. Energy losses from mechanical work associated with lattice expansion can be used to explain the anomalous positive slope of the isosteric heat.

Hydrogen adsorption isotherms were also measured for a Grafoil-based KC_{24} sample. The hydrogen adsorption behavior for this sample was markedly different than for the

[1] To be consistent with standard practices in the literature, positive enthalpies are reported throughout the remainder of the thesis, even though the adsorption is exothermic.

Table 4.1: Hydrogen adsorption by alkali metal graphite intercalation compounds

	Max. adsorption[a]		
Sample	wt%	H_2:M	Isosteric heat ($kJ\,mol^{-1}$)[b]
KC_{24}	1.24	2.03	9.2
RbC_{24}	1.03	1.92	12.6
CsC_{24}	0.85	1.79	14.9

[a] Maximum adsorption capacity was measured at 77 K for KC_{24} and at 120 K for RbC_{24} and CsC_{24}.
[b] Isosteric heats were average over H_2:M between 0.25 and 1.5.

flake graphite sample. Measurements were only taken up to a pressure of about 1100 Torr, where the maximum hydrogen composition was $KC_{24}(H_2)_{1.82}$. Adsorption kinetics were much slower at all compositions compared to the flake graphite sample. The adsorption isotherms and calculated isosteric heat are displayed in Fig. 4.3. The isosteric heat follows a physically intuitive pattern. There is an initial increase due to the energy losses in the lattice expansion, followed by a decrease due to the filling of the optimal adsorption sites. The zero coverage enthalpy is only $6.8\,kJ\,mol^{-1}$, while the average isosteric heat between $0.25 < x < 1.5$ is given by $8.5\,kJ\,mol^{-1}$. Interestingly, the average isosteric heat of the Grafoil sample is about $1\,kJ\,mol^{-1}$ smaller than that of the flake graphite sample. The Grafoil used for the synthesis probably had a lower purity than the natural flake graphite. It is possible that surface impurities may have hindered the hydrogen adsorption. Flake graphite GIC samples were used for all future experimental work.

4.3 Hydrogen adsorption isotherms of RbC_{24} and CsC_{24}

Hydrogen adsorption isotherms were collected for RbC_{24} and CsC_{24} samples. These measurements were performed on a Sieverts instrument at NCNR [82]. Temperature control was provided by a closed-cycle helium refrigeration unit, which enabled data to be collected

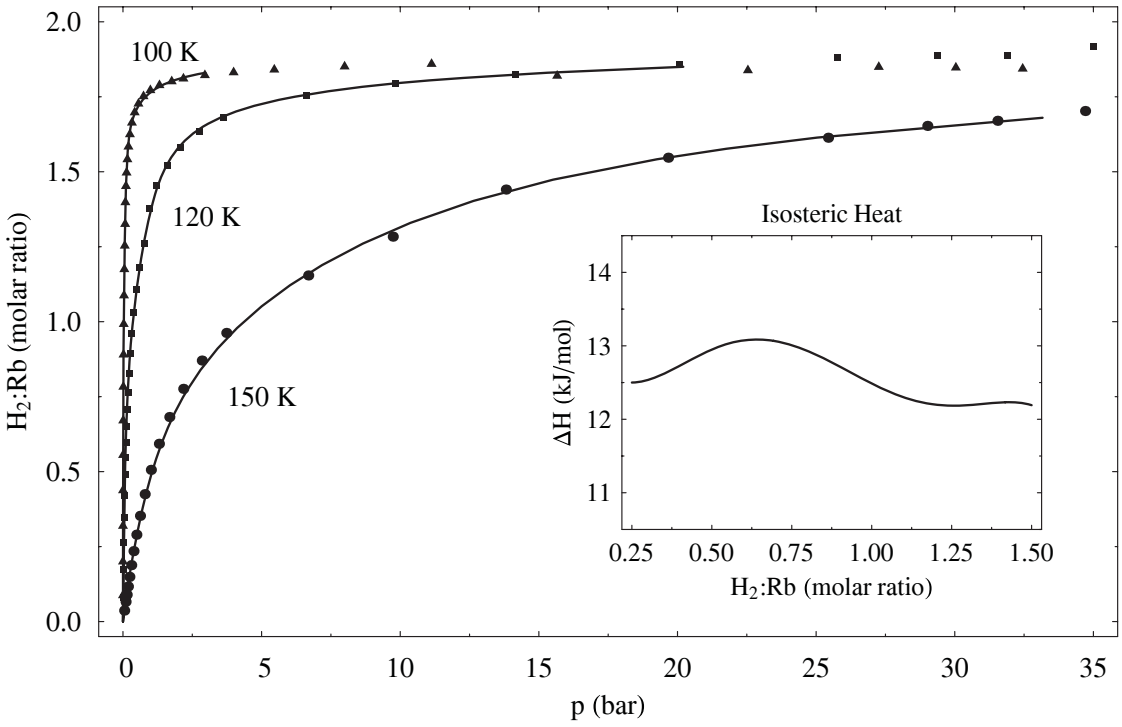

Figure 4.4: Adsorption isotherms of RbC_{24} at 100 K, 120 K, and 150 K fitted to a virial-type thermal equation. Inset: Isosteric heat as a function of adsorption amount.

at temperatures different than the standard 77 K and 87 K. The collection time for each isotherm point was 15 min, regardless of whether equilibrium was reached within that duration. Isotherms for RbC_{24} and CsC_{24} are presented in Fig. 4.4 and Fig. 4.5, respectively.[2] The RbC_{24}, and CsC_{24} isotherms have the classic Langmuir isotherm shape. This reflects the fact that there is apparently no lattice expansion in RbC_{24} or CsC_{24} in response to hydrogen adsorption. For both samples, the largest adsorption amounts were actually obtained at a sample temperature of 120 K. Adsorption at lower temperatures appeared to be reduced due to sluggish kinetics. Isosteric heats for RbC_{24} and CsC_{24}, averaged over $0.25 < x < 1.5$, are an astonishing $12.6\,\mathrm{kJ\,mol^{-1}}$ and $14.9\,\mathrm{kJ\,mol^{-1}}$, respectively. This is close to the optimal adsorption enthalpy of $\Delta H = 18\,\mathrm{kJ\,mol^{-1}}$ for engineering applications

[2] A 77 K isotherm for RbC_{24} and a 100 K isotherm for CsC_{24} were also collected, but are not included in the figures.

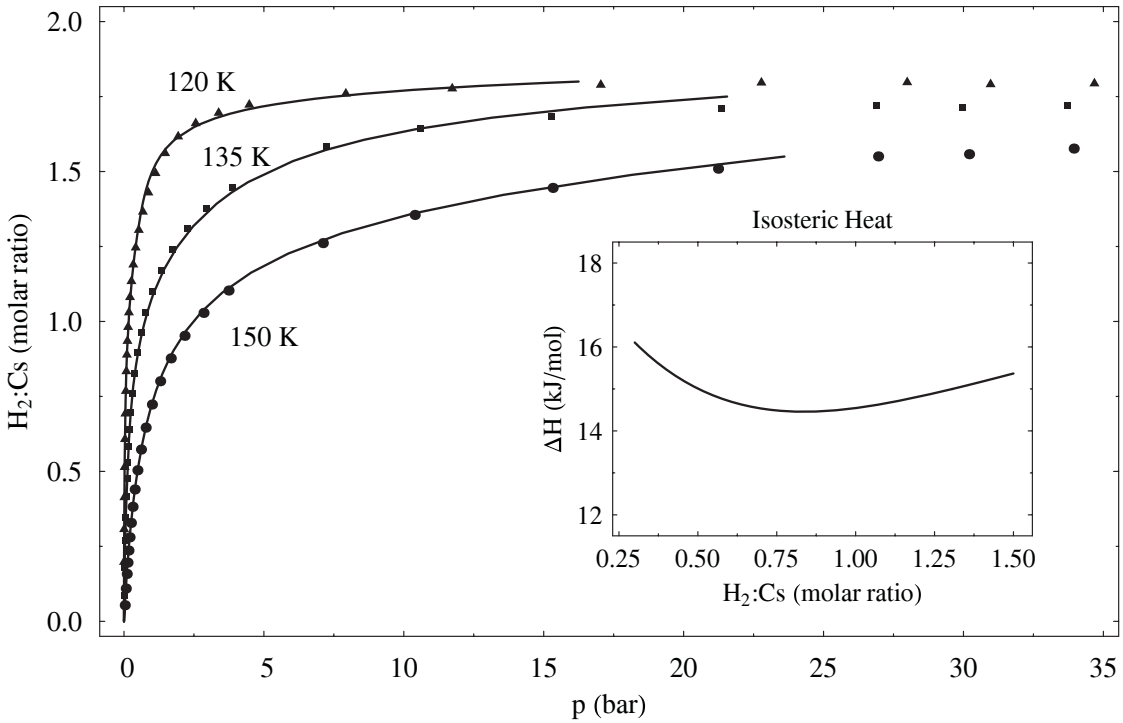

Figure 4.5: Adsorption isotherms of CsC_{24} at 120 K, 135 K, and 150 K fitted to a virial-type thermal equation. Inset: Isosteric heat as a function of adsorption amount.

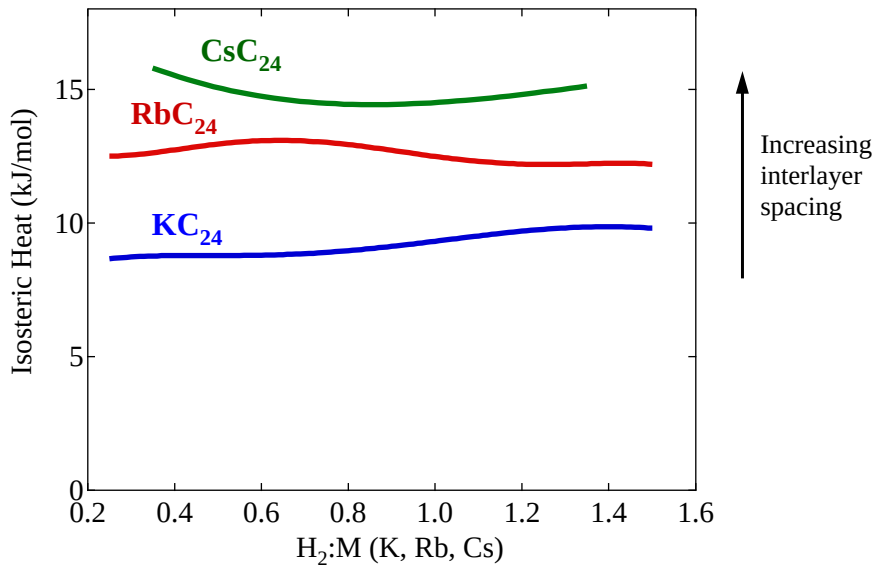

Figure 4.6: Comparison of hydrogen adsorption enthalpies for KC_{24}, RbC_{24} and CsC_{24}, plotted as a function of composition.

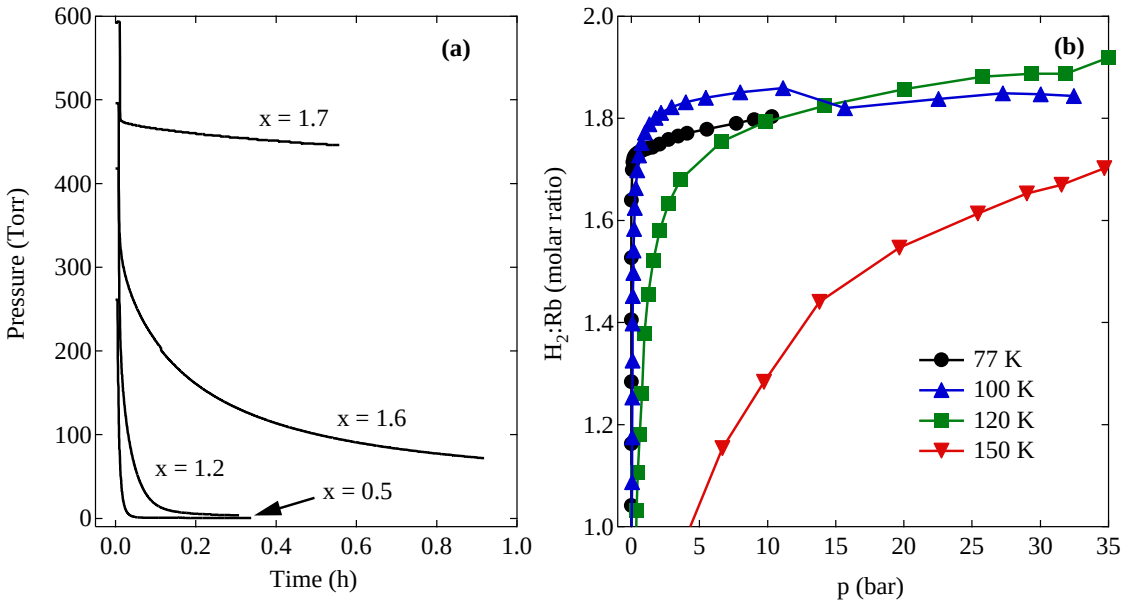

Figure 4.7: Hydrogen adsorption kinetics of RbC_{24}. (a) Manifold pressure is plotted versus time for several compositions at 77 K. Traces are identified by their final composition $RbC_{24}(H_2)_x$. Pressure decreases versus time due to adsorption. (b) Plateau regions of the H_2 adsorption isotherms of RbC_{24} at 77 K, 100 K, 120 K, and 150 K.

(see Sec. 1.4). Of course, it would have been very interesting to measure the adsorption at room temperature to determine the delivery between 3 bar and 100 bar. Unfortunately, the RbC_{24} and CsC_{24} samples also appear to react with hydrogen at 195 K and higher temperatures. Experimentally, we observe a reduction in the maximum 77 K hydrogen adsorption capacity following adsorption at 195 K. A summary of maximum H_2 adsorption capacities and average isosteric heats for KC_{24}, RbC_{24}, and CsC_{24} is listed in Table 4.1.

4.4 Hydrogen adsorption kinetics

Kinetic limitation of adsorption appears to be significant in KC_{24} (as well as in RbC_{24} and CsC_{24}) at hydrogen compositions greater than $x = 1.5$. There are few vacant adsorption sites for the H_2 molecules to diffuse through, leading to site-blocking and correlation effects. Combined with the small jump attempt frequency which exists at these low temperatures,

the result is a reduction in the transport-diffusivity of the adsorbed hydrogen phase. Adsorption kinetics were measured for RbC_{24} at 77 K at various hydrogen compositions, as illustrated in Fig. 4.7a. The manifold pressure is plotted versus time for several different final compositions. At low H_2 compositions (e.g., $x = 0.5$) the adsorption is rapid, and the equilibrium pressure is reached within a minute or two. At higher H_2 compositions (e.g., $x = 1.6$) the adsorption is extremely sluggish, and equilibrium is still not reached after an hour. Diffusion-limited adsorption is more significant at low temperatures due to the lower jump attempt frequency. This is evident in Fig. 4.7b, where the 77 K isotherm actually drops below the 100 K isotherm near $x = 1.7$ because the slower adsorption kinetics reduces the adsorption amount that is measured within a specific time (15 min in this case).

4.5 Discussion

Comprehensive measurements of the adsorption enthalpies and adsorption kinetics of the MC_{24} compounds (for M = K, Rb, Cs) were collected over the entire H_2 composition range. The H_2 binding enthalpies for all three compounds are summarized in Fig. 4.6. Compared to activated carbons, there appears to be less energetic heterogeneity in the adsorption potentials of the MC_{24} compounds. The isosteric heats are relatively flat, in contrast to the monotonically decreasing isosteric heats for activated carbons (see Fig. 3.3). Because the MC_{24} compounds have more long-range order than activated carbons, it is intuitive that they would have fewer distinct adsorption sites. In addition, the interlayer spacing is wide enough to accept only a single layer of H_2 molecules, further restricting the distribution of distinct adsorption sites. A positive correlation between the adsorption enthalpy and the interlayer spacing is clearly illustrated in Fig. 4.6. The wider 5.9 Å slit pores of CsC_{24} have a stronger adsorption potential than the narrower 5.4 Å slit pores of KC_{24}. However, this

trend may also be affected by differences in the electrostatic interaction, due to varying degrees of charge transfer between the graphite and alkali metals. As listed in Table 4.1, there is also a negative correlation between alkali metal size and adsorption capacity. This is expected, due to the decrease in free volume within the interlayer galleries that occurs with larger alkali metal atoms.

Geometry appears to play a significant role in the sluggish adsorption kinetics observed at large H_2 compositions. Intra-crystalline diffusion in KC_{24} is two-dimensional, which means that site-blocking and correlation effects can be even greater due to the reduction in the number of nearest-neighbor sites. Adsorption kinetics, however, is a macroscopic transport phenomenon which can depend on both inter- and intra-crystalline diffusion as well as surface impurities. It is possible that using flake graphite starting material with smaller particle sizes may improve kinetics, but this was not investigated. It was found that Grafoil-based KC_{24} samples had significantly slower adsorption rates than the flake graphite samples. This may have been due to surface impurities blocking H_2 entry at the crystallite surface. A study of microscopic hydrogen self-diffusion within KC_{24} is presented in Sec. 5.4, and is largely consistent with the slow macroscopic adsorption kinetics measured here.

4.6 Conclusion

Pressure-composition-temperature diagrams were measured for hydrogen adsorption in the intercalated graphite samples KC_{24}, RbC_{24}, and CsC24. Adsorption capacities and isosteric heats were determined and are summarized in Table 4.1. A model-independent, virial-type thermal equation was used to calculate isosteric heats from the experimental isotherms. Consistent with the literature, the KC_{24} isotherm has an "S" shape due to lattice expansion associated with H_2 adsorption [48, 49]. The isosteric heat is positively correlated with the

size of the alkali metal intercalant. Hydrogen adsorption is kinetically-limited at large H_2 compositions.

Chapter 5

Hydrogen diffusion in potassium-intercalated graphite

5.1 Introduction

Hydrogen is adsorbed in large amounts by KC_{24} at low temperatures. The potassiums, hydrogens and vacancies essentially form a two-dimensional ternary lattice gas between the host graphitic layers. Due to the ionized metal atoms and the overlapping graphite corrugation potentials, adsorbed H_2 molecules experience a strong anisotropic potential. This provides an opportunity to study both the effect of steric barriers and strong binding interactions on the diffusion of the adsorbed H_2 molecules. As an indicator of macroscopic transport behavior, we know that hydrogen adsorption in KC_{24} is kinetically-limited at large fillings (see Sec. 4.4). In this chapter, the microscopic self-diffusion of hydrogen in KC_{24} is investigated using quasielastic neutron scattering (QENS) and molecular dynamics simulations. Neutron scattering is an experimental technique particularly well-suited to quantitatively studying the molecular motions of hydrogen (and other hydrogen-rich fluids) adsorbed in host frameworks. It also provides a unique opportunity to directly compare the simulated and experimental values of fluid diffusivities at the microscopic level.

Portions of this chapter were published in the article: J. J. Purewal, J. B. Keith, C. C. Ahn, C. M. Brown, M. Tyagi and B. Fultz, *Phys. Rev. B* **2009**, *79*, p. 054305.

5.2 Quasielastic neutron scattering

5.2.1 Description

Quasielastic scattering is a broadening of final neutron energies caused by the diffusion of atoms within a material. Consider an atom which jumps to a new lattice site before it completes the scattering of a neutron wavepacket. It will continue to scatter the neutron wavepacket from its new position. In "quasielastic" scattering the neutron does not cause transitions between the quantum states of the target material. The two scattered waves will typically interfere destructively (unless of course the initial and final positions are separated by an arbitrary fraction of the neutron wavelength). The uncertainty principle tells us that $\Delta E = \hbar/\Delta t$, where Δt is the average time that an atom resides on a particular site. The final neutron energies are symmetrically broadened around $\Delta E = 0$ due to the uncertainty in Δt. Based on this idea, quasielastic scattering can be used to measure the time scale of the diffusive jumps. Spectrometers can currently measure quasielastic broadening over an energy range of 1 μeV to 1 meV, which corresponds to characteristic jump times of 10^{-9} s to 10^{-12} s. When diffusion occurs on a fixed sublattice the quasielastic scattering can exhibit a Q-dependence which provides information on the geometry of the diffusive jumps.

5.2.2 Continuous diffusion

The simplest model for long-range diffusion is isotropic, three-dimensional, continuous diffusion. The starting profile at $t = 0$ is a delta function, and at finite time it is a Gaussian in $\mathbf{r}$. The variation of the Gaussian distribution of molecular displacements gives a mean-squared displacement of $\langle r^2 \rangle = 6Dt$, where D is the self-diffusion coefficient. As described

in Sec. 3.2.2, the incoherent scattering function is the Fourier transform in time and space of the van Hove autocorrelation function. Vineyard [83] calculated the incoherent scattering function for this system,

$$S_{\mathrm{inc}}(\mathbf{Q},\omega) = \frac{1}{\pi}\frac{DQ^2}{\left(DQ^2\right)^2 + \omega^2}, \tag{5.1}$$

which is a Lorentzian with a width (HWHM) of $\Gamma = DQ^2$. This law is typically valid at small Q, where distances are large compared with the individual steps of the diffusion process. Large deviations from the $\Gamma = DQ^2$ behavior is observed at large Q, however, where underlying jump mechanism becomes important.

When the continuous diffusion is two-dimensional (such as between the graphite planes in KC_{24}) the limiting form of the scattering function assumes the following form,

$$S^{\mathrm{2D}}_{\mathrm{inc}}(\mathbf{Q},\omega) = \frac{1}{\pi}\frac{D_{\mathrm{2D}}\left(Q\sin\theta\right)^2}{\left[D_{\mathrm{2D}}\left(Q\sin\theta\right)^2\right]^2 + \omega^2}, \tag{5.2}$$

where D_{2D} is the self-diffusion in two dimensions, and θ is the angle that the normal to the diffusion plane makes with $\mathbf{Q}$ [84]. This model predicts that elastic scattering is obtained when $\mathbf{Q}$ is perpendicular to the diffusion plane (i.e., $\theta = 0$). Lorentzians of increasing width are obtained as θ increases. The powder-averaged scattering function then has a cusp-like shape with a logarithmic singularity at $\omega = 0$. This is illustrated in Fig. 5.1. For continuous diffusion in a general lamellar system of arbitrary width, the scattering function is actually an infinite sum of Lorentzians with Q-dependent amplitudes [85].

5.2.3 Jump diffusion

A jump diffusion model takes into account the microscopic diffusive steps and therefore provides more accurate predictions at large Q. The standard model for jump diffusion is

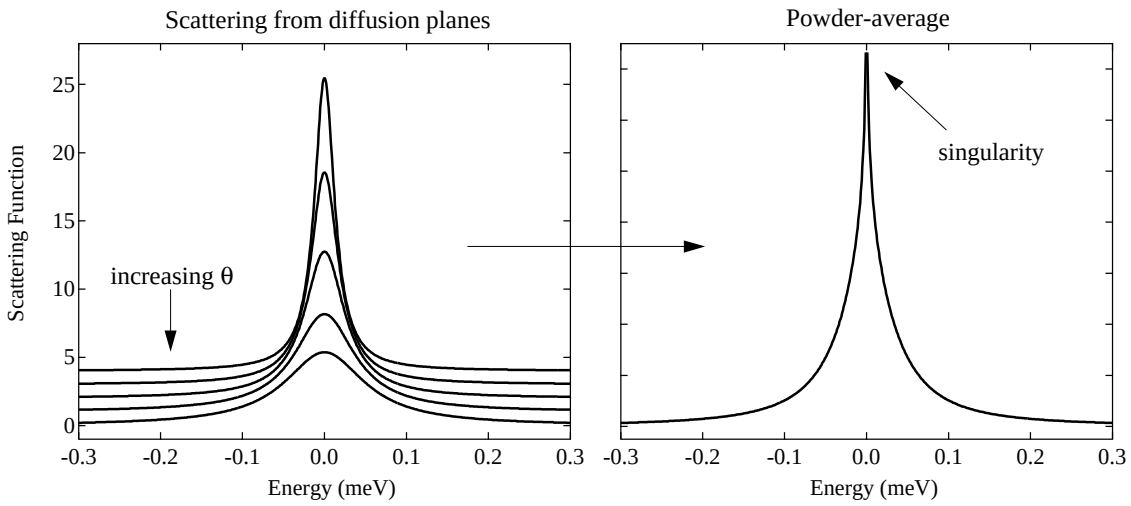

Figure 5.1: Left: Scattering functions for continuous two-dimensional diffusion. The angle θ between the diffusion plane normal and $\mathbf{Q}$ increases going down the set of curves. Right: Scattering function obtained by taking a powder average over all orientations.

the *Chudley-Elliott* model [86]. This model assumes that the sublattice on which diffusion occurs is a Bravais lattice and that successive jumps are uncorrelated. The latter assumption means that the model is only valid in the dilute limit where correlation effects are absent. The particle stays at a site for a mean residence time τ and jumps to one of its z nearest-neighbor sites. There are then a set of z possible jump vectors, which are denoted $\{\mathbf{l}_i\}$. The scattering function can be calculated as

$$S_{\mathrm{inc}}(\mathbf{Q},\omega) = \frac{1}{\pi}\frac{|\Gamma(\mathbf{Q})|}{|\Gamma(\mathbf{Q})|^2 + (\hbar\omega)^2}, \tag{5.3}$$

where the peak width is given by

$$\Gamma(\mathbf{Q}) = \frac{\hbar}{z\tau}\sum_{j=1}^{z}\left(1 - e^{-i\mathbf{Q}\cdot\mathbf{l}_j}\right). \tag{5.4}$$

In the low-Q limit, it reduces to the continuous diffusion form $\Gamma = \hbar D Q^2$, with $D = l^2/6\tau$. The peak-shape is Lorentzian with a width that varies sinusoidally depending on the

sublattice geometry. This model can be extended to a non-Bravais lattice, as described in Ref. [87]. In this case the scattering function contains a sum of m weighted Lorentzians, where m is the number of inequivalent sites in the unit cell.

5.2.4 Concentration effects

For a finite concentration, equal to c, there are correlations between successive jumps on the sublattice. After a single jump, a particle has an increased probability of jumping back to its initial (now unoccupied) site compared to a jump to other nearest-neighbor sites (which are occupied with probability c). In the mean-field approximation, we can simply adjust the mean residence time to allow for site-blocking:

$$\tau(c) = \frac{\tau(0)}{1-c}. \tag{5.5}$$

The scattering function is still a Lorentzian but now with a width that has been corrected by a site-blocking factor. If we also consider memory effects due to correlation between successive jumps, then the effective self-diffusion coefficient has a concentration-dependent expression

$$D = \frac{f(c)l^2}{\tau(c)}, \tag{5.6}$$

where $f(c)$ is the tracer correlation factor for long-range diffusion. There have been a number of studies to determine whether $S_{\mathrm{inc}}(Q,\omega)$ at high concentrations can still be described by a Lorentzian with a width corresponding to the effective diffusivity (Eq. 5.6). The results seem to depend both on the computational method and on the assumptions made [88]. Nevertheless, the jump diffusion model should not be applied at high concentrations.

5.3 Experimental methods

Neutron scattering measurements were performed on the Disc Chopper Spectrometer (DCS) at the NIST Center for Neutron Research [81]. For the current measurements, a KC_{24} sample with a mass of approximately 2.2506 g was transferred in a high-purity helium glovebox to an annular-geometry aluminum sample cell, sealed with an indium o-ring. The sample thickness was chosen for 10% total scattering. The sample can was mounted onto a sample stick which was adapted for a top-loading, closed-cycle helium refrigerator system. The sample can was connected with a stainless steel capillary line to a gas handling rig containing a calibrated volume and a high resolution pressure transducer. Hydrogen loading was performed at 60 K by filling the calibrated volume with the precise amount of H_2 gas needed for a $KC_{24}(H_2)_{0.5}$ composition, opening the valve to the sample, and monitoring the pressure as it dropped to approximately 0 Torr.

Scattering from bare KC_{24} was measured at 40 K and 60 K on DCS. The neutron scattering spectra at the different temperatures were identical within the instrument resolution. Scattering from $KC_{24}(H_2)_{0.5}$ was collected at 80 K, 90 K, 100 K, and 110 K. By monitoring the pressure, we confirmed that there was not any significant desorption of H_2 at these temperatures. Since the incoherent scattering cross-section of hydrogen is very large, approximately 35 % of the total scattering is from hydrogen. The background signal from KC_{24} is subtracted to isolate the scattering from hydrogen alone. Diffraction peaks from the host KC_{24} material are a significant feature in the $S(Q, \omega)$. Because the metal-containing graphite galleries expand approximately 5% upon H_2 adsorption, the KC_{24} diffraction peaks shift to slightly lower Q values, causing the KC_{24} background to over-subtract on the high Q side. Therefore it is necessary to mask the detector banks containing the diffraction peaks in

both the KC_{24} and $KC_{24}(H_2)_{0.5}$ samples. To improve statistics and make up for missing data in the masked detector groups, the reduced $S(Q,\omega)$ was binned into momentum-transfer increments of $0.15\,\text{Å}^{-1}$ and into energy increments of $0.01\,\text{meV}$.

The DCS measurements in this chapter were collected using an incident neutron wavelength of $\lambda = 6.0\,\text{Å}$, operating the choppers in low resolution mode, with a speed ratio of 2/3, a sample-detector minimum time of 500, and a master speed of 20 000 rpm. These settings give an energy resolution of approximately $65\,\mu\text{eV}$ at the elastic line. The kinematically-allowed region includes a maximum neutron energy loss of $1.35\,\text{meV}$, and a wavevector transfer between $0.1\,\text{Å}^{-1}$ to $2.0\,\text{Å}^{-1}$.

5.4 Quasielastic scattering results

An example of the QENS spectra of $KC_{24}(H_2)_{0.5}$ measured on DCS is shown in Fig. 5.2. The instrument resolution is plotted as a dashed red line. A low concentration ($x = 0.5$) was used for these measurements in order to minimize the effects of correlation and site-blocking. The QENS spectra consist entirely of scattering from H_2 since the signal from bare KC_{24} was subtracted as a background. There is a considerable amount of quasielastic line broadening due to the diffusion of adsorbed H_2 molecules. At $80\,\text{K}$, the spectrum contains both a broad quasielastic component and a sharp elastic component. Elastic scattering can originate from either the geometry of the hydrogen diffusion, or from a population of H_2 molecules whose motions are too slow to be resolved by the instrument. The intensity from the elastic component decreases with temperature, and is fairly small at $110\,\text{K}$. Since the amount of hydrogen was confirmed to be constant in all of the spectra, the decrease in total intensity is simply due to a decrease in elastic scattering at higher temperatures (i.e., the Debye-Waller factor). To obtain information from the QENS spectra about the diffusion

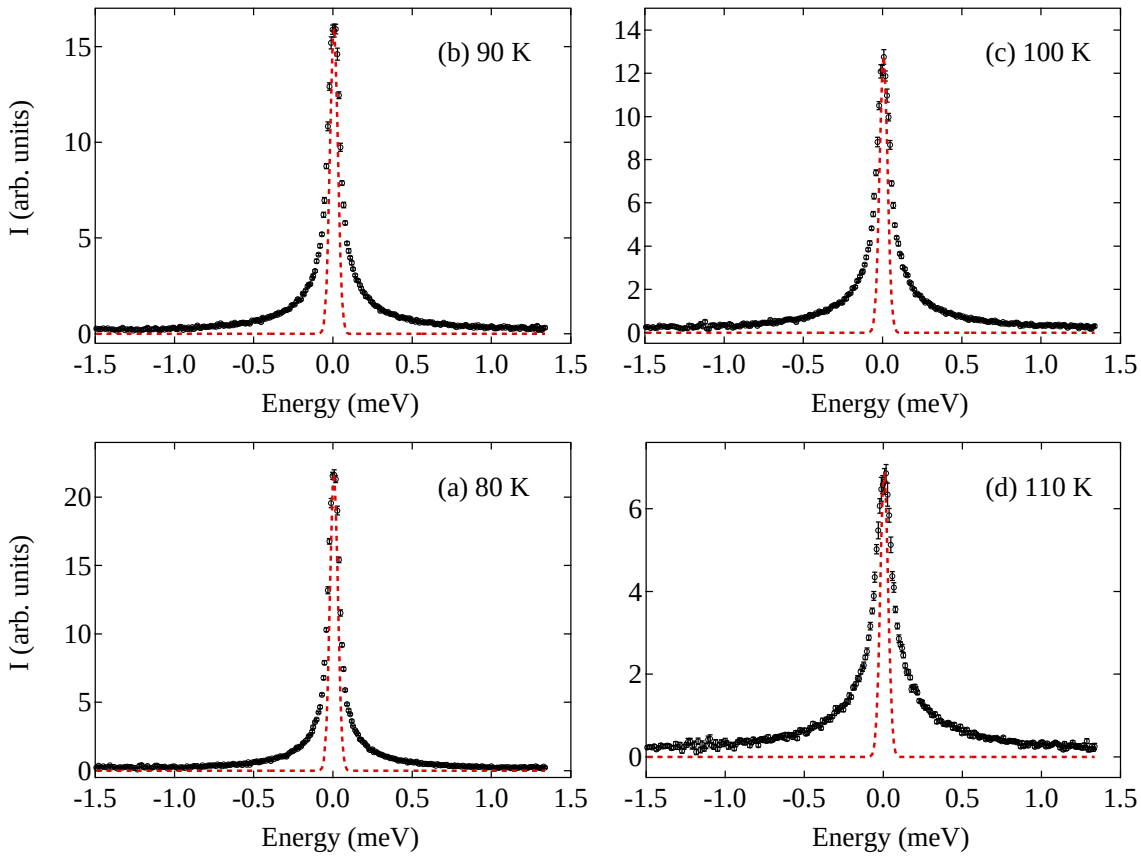

Figure 5.2: QENS scattering of $KC_{24}(H_2)_{0.5}$ at $Q = 1.61\,\text{Å}^{-1}$ measured on DCS with wavelength $\lambda = 6\,\text{Å}$, after subtracting scattering from bare KC_{24}. Dashed red lines indicate instrument resolution.

mechanism, it is necessary to develop a detailed jump diffusion model and then fit it to the experimental data. This is done in the next section.

5.5 Honeycomb lattice diffusion model

In a first approximation the diffusion of H_2 molecules in KC_{24} is two-dimensional. It is unlikely that the hydrogen will pass through two graphite planes into the neighboring intercalate layers (if it does happen it will be on a vastly slower time scale than in-plane diffusion). We assume that the $\left(\sqrt{7} \times \sqrt{7}\right) R\,19.11°$ structure adequately describes the in-plane structure of KC_{24} at low temperature. As depicted in Fig. 5.3, the sublattice of H_2

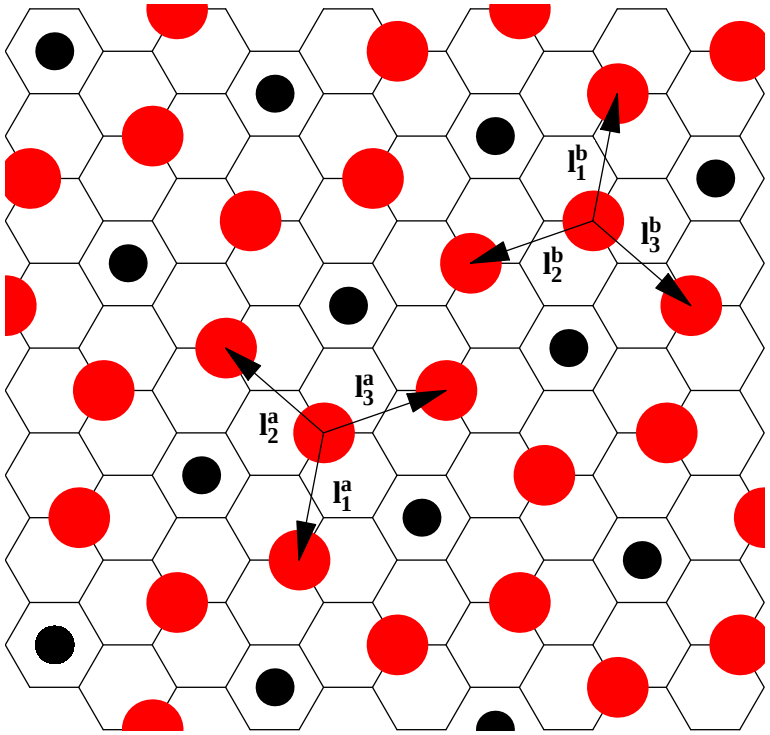

Figure 5.3: Hydrogen sorption sites in a $\left(\sqrt{7}\times\sqrt{7}\right) R19.11^\circ$ structure. The sorption sites form a 2D honeycomb net. Potassiums are represented by black dots while hydrogen sorption sites are represented by red dots. Sets of jump vectors for the two non-equivalent basis points are labeled $\{\mathbf{l}_i^a\}$ and $\{\mathbf{l}_i^b\}$. The length of each jump vector is 3.7 Å.

sorption sites forms a honeycomb net, which is *not* a Bravais lattice. The primitive unit cell contains a basis of two nonequivalent sites, and thus there are two distinct sets of jump vectors $\{\mathbf{l}_1^a, \mathbf{l}_2^a, \mathbf{l}_3^a\}$ and $\{\mathbf{l}_1^b, \mathbf{l}_2^b, \mathbf{l}_3^b\}$.[1] In calculating the scattering function, we assume that τ is the mean residence time of H_2 molecules on the honeycomb sublattice sites, and also assume that there is no correlation between consecutive jumps. The honeycomb lattice has a basis of two lattice points, and the scattering function is calculated using the procedure described in Ref. [87]. The result of these calculations is a sum of two Lorentzians [89],

$$S_{\text{inc}}(\mathbf{Q},\omega) = \frac{1}{\pi}\sum_{j=1}^{2}\frac{w_j(\mathbf{Q})\Gamma_j(\mathbf{Q})}{\omega^2+\Gamma_j^2(\mathbf{Q})}, \tag{5.7}$$

[1]The fact that the $\{\mathbf{l}_i^a\}$ jump vectors are simply the negative of the $\{\mathbf{l}_i^b\}$ jump vectors is implicitly included in the remainder of the calculation. Therefore only one set of jump vectors will be referenced in the derivation in this section.

where the weights $w_j(\mathbf{Q})$ and linewidths $\Gamma_j(\mathbf{Q})$ of the two Lorentzians are given by

$$w_1(\mathbf{Q}) = \tfrac{1}{2}\left(1 + \mathrm{Re}(\mathbf{K})/|\mathbf{K}|\right) \qquad w_2(\mathbf{Q}) = \tfrac{1}{2}\left(1 - \mathrm{Re}(\mathbf{K})/|\mathbf{K}|\right) \tag{5.8}$$

$$\Gamma_1(\mathbf{Q}) = L - |\mathbf{K}| \qquad \Gamma_2(\mathbf{Q}) = L + |\mathbf{K}| \tag{5.9}$$

and values of L and $\mathbf{K}$ are given by

$$L = \frac{1}{\tau} \qquad \mathbf{K} = \frac{1}{3\tau}\sum_{i=1}^{3} \exp\left(-i\mathbf{Q}\cdot\mathbf{l}_i\right). \tag{5.10}$$

The value of $\mathbf{K}$ can be calculated from a single set of jump vectors,

$$\mathbf{l}_1 = \langle l, 0, 0\rangle \qquad \mathbf{l}_2 = \langle -l/2, -\sqrt{3}l/2, 0\rangle \qquad \mathbf{l}_3 = \langle -l/2, \sqrt{3}l/2, 0\rangle \tag{5.11}$$

and for a randomly oriented wavevector transfer $\mathbf{Q}$,

$$\mathbf{Q} = \langle Q\cos\phi\sin\theta, Q\sin\phi\sin\theta, Q\cos\theta\rangle. \tag{5.12}$$

We need to calculate the dot product for the three jump vectors,

$$\mathbf{Q}\cdot\mathbf{l}_1 = Ql\cos\phi\sin\theta \tag{5.13}$$

$$\mathbf{Q}\cdot\mathbf{l}_2 = -\tfrac{1}{2}Ql\cos\phi\sin\theta - \tfrac{\sqrt{3}}{2}Ql\sin\phi\sin\theta \tag{5.14}$$

$$\mathbf{Q}\cdot\mathbf{l}_3 = -\tfrac{1}{2}Ql\cos\phi\sin\theta + \tfrac{\sqrt{3}}{2}Ql\sin\phi\sin\theta. \tag{5.15}$$

To simplify notation, we substitute in the following expressions,

$$a = Ql\cos\phi\sin\theta \qquad b = \tfrac{\sqrt{3}}{2}Ql\sin\phi\sin\theta. \tag{5.16}$$

The dot products are now substituted into the exponentials in Eq. 5.10,

$$\exp\left(-i\mathbf{Q}\cdot\mathbf{l}_1\right) = \cos a - i\sin a \tag{5.17}$$

$$\exp\left(-i\mathbf{Q}\cdot\mathbf{l}_2\right) = \left[\cos\tfrac{a}{2} - i\sin\tfrac{a}{2}\right]\left[\cos b - i\sin b\right] \tag{5.18}$$

$$\exp\left(-i\mathbf{Q}\cdot\mathbf{l}_3\right) = \left[\cos\tfrac{a}{2} - i\sin\tfrac{a}{2}\right]\left[\cos b + i\sin b\right], \tag{5.19}$$

and the value of $\mathbf{K}$ is calculated,

$$\mathbf{K} = \frac{1}{3\tau}\sum_{i=1}^{3}\exp\left(-i\mathbf{Q}\cdot\mathbf{l}_i\right) = \frac{1}{3\tau}\left[\cos a + 2\cos\tfrac{a}{2}\cos b\right] - \frac{i}{3\tau}\left[\sin a + 2\sin\tfrac{a}{2}\cos b\right]. \tag{5.20}$$

We can now readily determine the magnitude and real part of $\mathbf{K}$,

$$|\mathbf{K}| = \frac{1}{3\tau}\left[1 + 4\cos^2 b + 4\cos b\cos\tfrac{3a}{2}\right]^{1/2} \tag{5.21}$$

$$\frac{\mathrm{Re}(\mathbf{K})}{|\mathbf{K}|} = \frac{\cos a + 2\cos\frac{a}{2}\cos b}{\left[1 + 4\cos^2 b + 4\cos b\cos\frac{3a}{2}\right]^{1/2}}. \tag{5.22}$$

This is the QENS function for a single-crystal honeycomb lattice. The KC_{24} samples measured in this experiment are polycrystalline however, so it is necessary to take an orientational average over θ and ϕ:

$$\langle S_{\mathrm{inc}}(Q,\omega)\rangle = \frac{1}{4\pi}\int_0^{2\pi}\int_0^{\pi}\left[S_{\mathrm{inc}}(\mathbf{Q},\omega)\right]\sin\theta\,\mathrm{d}\theta\mathrm{d}\phi. \tag{5.23}$$

To take into account a fraction of H_2 molecules which are not diffusing, we add a delta function[2] weighted by a Q-independent elastic-like factor (f). The experimentally measured scattering function is broadened by the instrumental resolution, $R(\omega)$. Therefore, the model

[2]It is not clear what the origin of the elastic-like intensity is, but from a practical point of view it is necessary to include the delta function to obtain good fits to the experimental data.

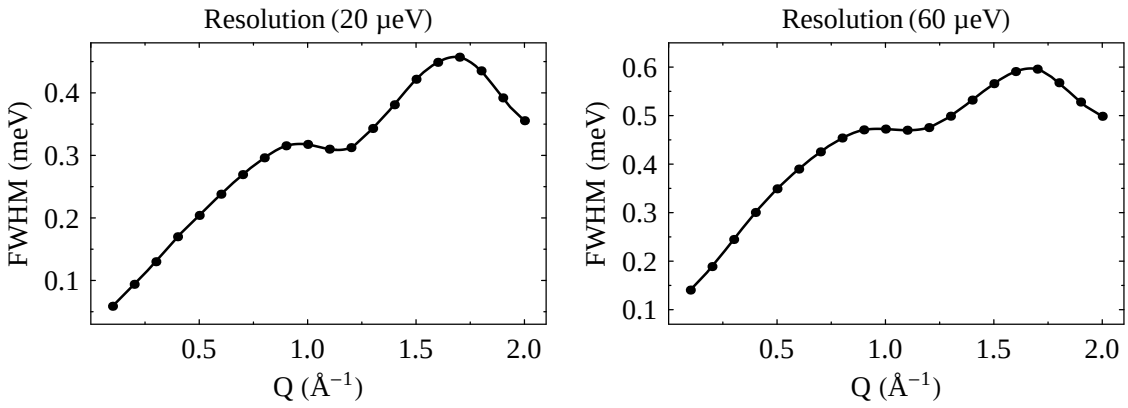

Figure 5.4: Linewidth (FWHM) of the honeycomb net model function $F(Q, \omega, \tau = 5\,\mathrm{ps}, l = 3.7\,\text{Å}, f = 0, A = 1)$ plotted versus momentum-transfer, Q. Resolution is a Lorentzian function with HWHM of 20 μeV (left) and 60 μeV (right).

function in its final form is obtained after taking the convolution of the powder-averaged honeycomb net model plus delta function with the instrument resolution,

$$F(Q, \omega, \tau, l, f, A) = A\left[(f)\delta(\omega) + (1-f)\langle S_{\mathrm{inc}}(Q, \omega)\rangle\right] * R(\omega) \tag{5.24}$$

$$= A\left[(f)R(\omega) + (1-f)\int_{-\infty}^{\infty} R(\omega - \omega')\langle S_{\mathrm{inc}}(Q, \omega)\rangle \mathrm{d}\omega'\right], \tag{5.25}$$

where (Q, ω) are variables and (τ, l, f, A) are the parameters to be fitted. For most of the fits, the jump distance l was held fixed at the theoretical value of 3.7 Å. Several different jump distances were tested to determine whether they improved the fit. To simplify calculations, the resolution function was fitted to a sum of five Lorentzians and the convolution was carried out analytically before the orientational average. For the convolution of two Lorentzians the linewidths add linearly.

At finite instrument resolution, the linewidth of the honeycomb net model function $F(Q, \omega, \tau, l, f, A)$ varies with Q in a distinct manner. This is illustrated in Fig. 5.4, where the line widths are plotted for $\tau = 5\,\mathrm{ps}$, $l = 3.7\,\text{Å}$, and $f = 0$ (equivalent to $D = 6.8 \times 10^{-9}\,\mathrm{m^2\,s^{-1}}$) at two different instrument resolutions. The sinusoidal character of the

curve begins to be damped out at coarser resolutions.

The QENS spectra of $KC_{24}(H_2)_{0.5}$ were fit simultaneously over all Q-values to the honeycomb net model function $F(Q, \omega, \tau, l, f, A)$ to optimize a single set of fit parameters $\{\tau,l,f\}$ for a given temperature. The amplitude A was allowed to vary independently for each Q-value however. Fits for the 80 K to 110 K spectra using the theoretical $l = 3.7$ Å jump length are plotted in Figs. 5.5–5.8, respectively. Only the first ten momentum transfer groups are shown due to limited space.[3] The y-axes of the individual plots have a logarithmic scale to facilitate the visualization of the goodness-of-fit in both the peak regions and wing regions of the spectra. Fit parameters are summarized in Table 5.1.

In the 80 K spectra the wings are not well fitted by the model. For the higher temperature spectra, it is clear that the peak regions are not fitted well at larger Q-values. This can be fixed by allowing the elastic-like weighting parameter f to vary with Q. The presence of a Q-dependent elastic-like intensity (sometimes called an EISF) usually indicates the presence of confined dynamics in the system. However there is no intuitive physical basis for such confined motion in KC_{24} since the H_2 molecules are not chemically bonded or trapped within a rigid cage. Further, there is a large amount of correlation between the τ and f parameters, which creates some doubt about the physical significance of the elastic-like intensity.

We must conclude that the honeycomb net jump diffusion model is not sufficient to fully describe the hydrogen dynamics in the $KC_{24}(H_2)_{0.5}$ system. There are a number of possibilities for this shortcoming. First, the model ignores the rotational motion of the H_2 molecules. Since H_2 has a large rotational constant, the characteristic frequencies are expected to be well above the range measured here. Nevertheless, there is expected to be

[3] The eleventh group has a momentum transfer of $Q = 1.74\,\text{Å}^{-1}$.

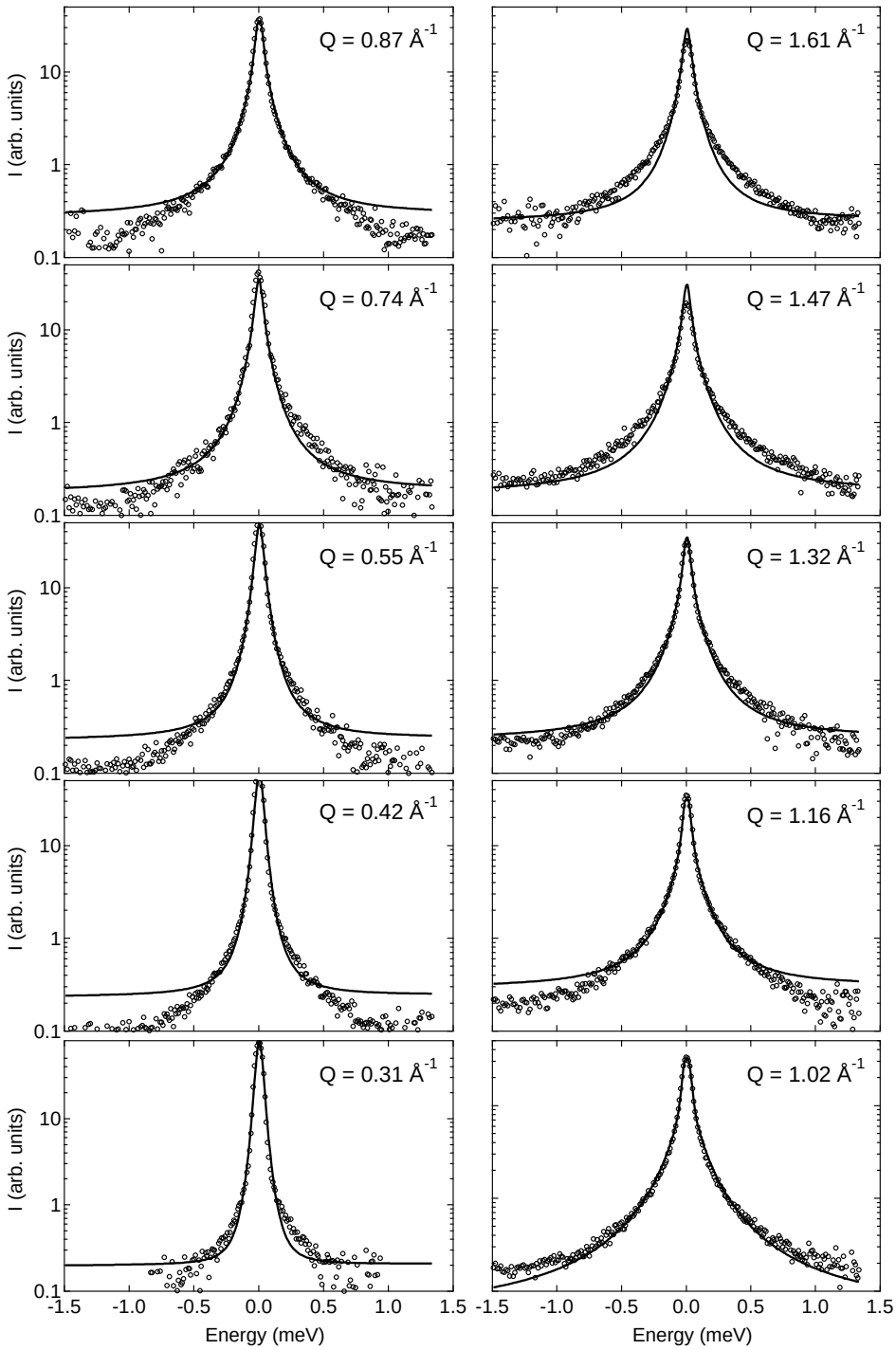

Figure 5.5: QENS spectra of $KC_{24}(H_2)_{0.5}$ at 80 K fitted to the honeycomb net jump diffusion model.

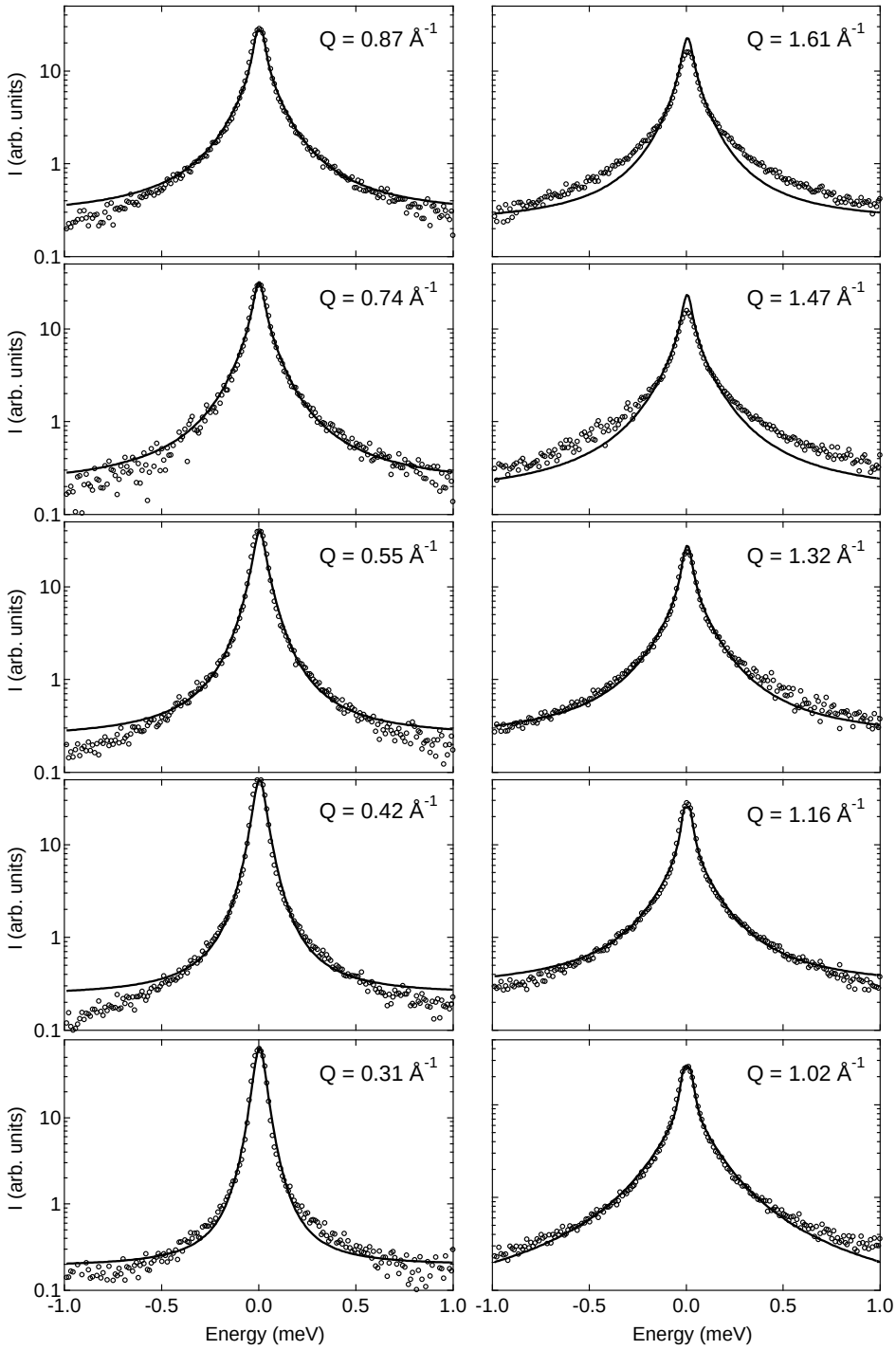

Figure 5.6: QENS spectra of $KC_{24}(H_2)_{0.5}$ at 90 K fitted to the honeycomb jump diffusion model. The reduced energy range of ± 1 meV was used because fits to the full energy range of ± 1.5 meV did not converge successfully.

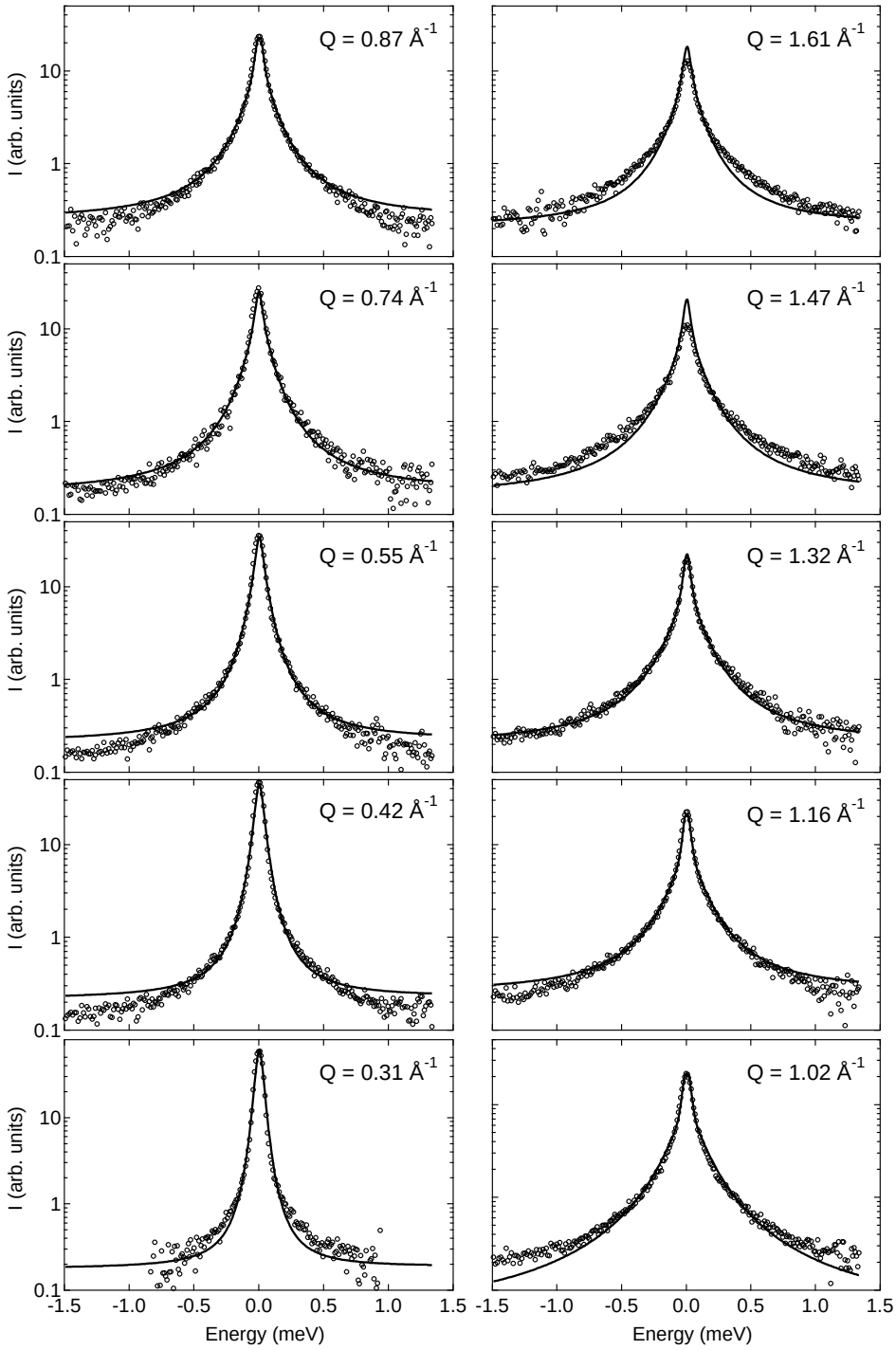

Figure 5.7: QENS spectra of $KC_{24}(H_2)_{0.5}$ at 100 K fitted to the honeycomb jump diffusion model.

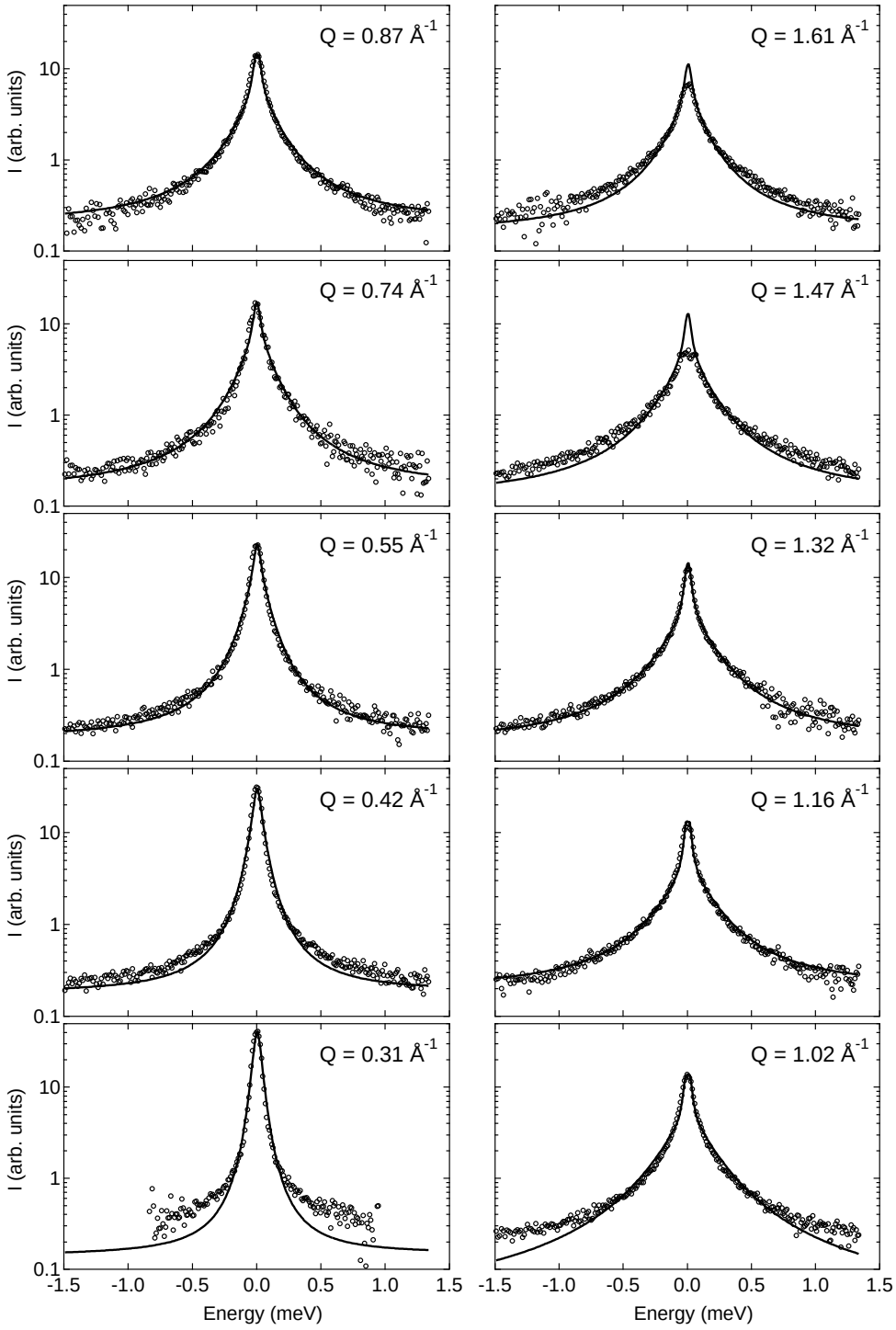

Figure 5.8: QENS spectra of $KC_{24}(H_2)_{0.5}$ at 110 K fitted to the honeycomb jump diffusion model.

Table 5.1: Honeycomb net jump diffusion model parameters from fits to the $KC_{24}(H_2)_{0.5}$ data

Temperature (K)	τ (ps)	l (Å)[a]	f	D (10^{-9} m^2 s^{-1})[b]
80	10.36(4)	3.7	0.214(2)	3.30(1)
90	7.80(2)	3.7	0.167(1)	4.39(1)
100	6.38(2)	3.7	0.146(1)	5.36(2)
110	4.29(1)	3.7	0.126(1)	7.98(3)

[a] Jump length (l) was held fixed at 3.7 Å.
[b] The diffusion coefficient assumes two-dimensional translation.

some coupling between the rotational and translational dynamics which can affect peak shape. Second, it is probably incorrect to impose a single jump frequency on the diffusion process. As described later in the chapter, there are a wide range of jump frequencies present in the $KC_{24}(H_2)_{0.5}$ system. Developing a model with a *distribution* of jump frequencies is far from trivial, however. In the next section we use several "mechanism-independent" methods to estimate the diffusion coefficients and residence times of the $KC_{24}(H_2)_{0.5}$ system.

5.6 Estimates of diffusion coefficients

5.6.1 Low-Q limit

In the limit of low Q, the honeycomb net jump diffusion model (Eq. 5.7) reduces to the expression for continuous two-dimensional diffusion (Eq. 5.2). Before fitting to data from polycrystalline samples, the orientational average must be calculated. The powder-averaged function can actually be determined analytically, as discussed by Lechner [90, 91]. The resulting expression is given by

$$\langle S_{\mathrm{inc}}(Q,\omega)\rangle = \frac{1}{8\pi k^3 DQ^2}\left(\frac{1+k^2}{\cos\alpha/2}\ln\frac{1+2k\cos\alpha/2+k^2}{1-2k\cos\alpha/2+k^2} + \frac{2\left(1-k^2\right)}{\sin\alpha/2}\arctan\frac{2k\sin\alpha/2}{k^2-1}\right), \quad (5.26)$$

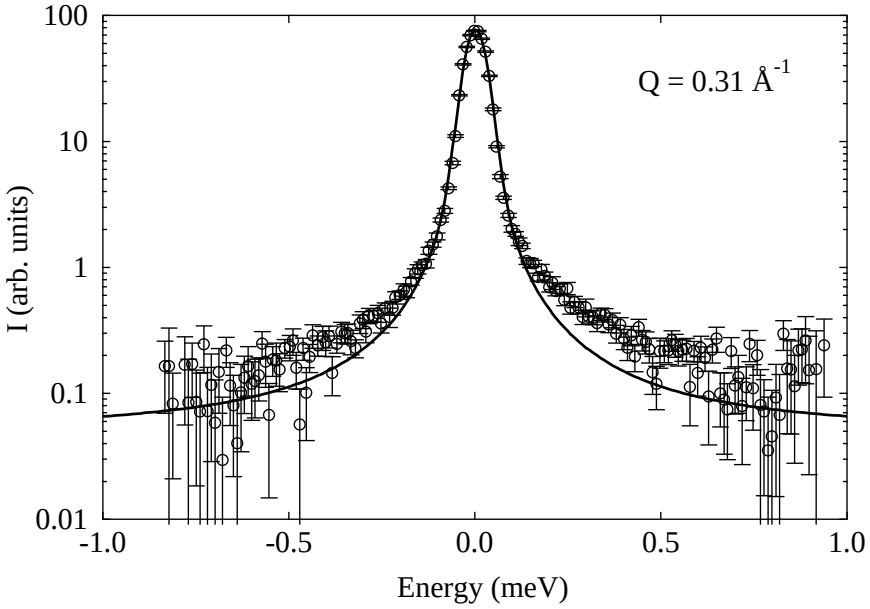

Figure 5.9: Experimental $KC_{24}(H_2)_{0.5}$ spectra measured at 110 K (with $Q = 0.31\,\text{Å}^{-1}$) fitted to the two-dimensional continuous diffusion model.

where the following terms need to be substituted in,

$$k = \left[1 + \left(\frac{\omega}{DQ^2}\right)^2\right]^{1/4} \qquad \sin\alpha/2 = \left(\frac{1-\cos\alpha}{2}\right)^{1/2} \tag{5.27}$$

$$\cos\alpha = \left[1 + \left(\frac{\omega}{DQ^2}\right)^2\right]^{-1/2} \qquad \cos\alpha/2 = \left(\frac{1+\cos\alpha}{2}\right)^{1/2} \tag{5.28}$$

This expression (Eq. 5.26) was fitted to experimental spectra at low Q. The fitted curve for the smallest momentum transfer group ($Q = 0.31\,\text{Å}^{-1}$) of the 110 K spectra is displayed in Fig. 5.9. From the fit parameters we obtain a two-dimensional self-diffusion coefficient of $D = 9.3(1) \times 10^{-9}\,\text{m}^2\,\text{s}^{-1}$. This is slightly larger than the self-diffusion coefficient of $7.8 \times 10^{-9}\,\text{m}^2\,\text{s}^{-1}$ obtained from the honeycomb net jump diffusion model. It can be seen in Fig. 5.9 that the goodness-of-fit in the wing regions is not sufficient. The chi-squared value for the fit was $\chi^2 = 7.8$. The values of the fitted parameter D are summarized in Table 5.2 for all the temperatures.

Table 5.2: Comparison of the hydrogen self-diffusion coefficients for $KC_{24}(H_2)_{0.5}$ extracted from QENS data by fitting to different diffusion models

	D $(10^{-9}\ \mathrm{m^2\,s^{-1}})^a$		
Temperature (K)	Honeycomb[b]	Low-Q limit[c]	High-Q limit[d]
80	3.30(1)	2.16(4)	5.9(3)
90	4.39(1)	5.42(3)	6.2(3)
100	5.36(2)	6.53(4)	6.7(4)
110	7.98(3)	9.29(7)	7.5(4)

[a] Self-diffusion coefficients are two-dimensional.
[b] Honeycomb net jump diffusion model.
[c] Two-dimensional continuous diffusion in the low-Q limit.
[d] Geometry-independent jump diffusion in the high-Q limit.

5.6.2 High-Q limit

When Eq. 5.7 is averaged over large Q values, the incoherent scattering function reduces to a Lorentzian with an average linewidth of $\langle\Gamma(Q)\rangle = 1/\tau$. In other words, the average quasielastic linewidth in the limit of large Q is approximately independent of the geometry of the system and depends only on the the jump frequency. To estimate τ, a resolution-broadened model function consisting of a Lorentzian function, a delta function, and a flat background was fitted to the experimental spectra. An example of fits to the five largest Q-values of the 110 K data is displayed in Fig. 5.10. Values of τ were obtained by averaging $\Gamma(Q)$ over the range $1.16\,\mathrm{Å}^{-1}$ to $1.74\,\mathrm{Å}^{-1}$. Residence times varied from 4.6 ps to 5.9 ps for the experimental temperatures. Two-dimensional self-diffusion coefficients were then calculated from the expression $D = l^2/4\tau$, using the jump length $l = 3.74\,\mathrm{Å}$. Values are summarized in Table 5.2. There is a modest discrepancy between the diffusion coefficients obtained from the rigorous honeycomb net model and from the approximate methods.

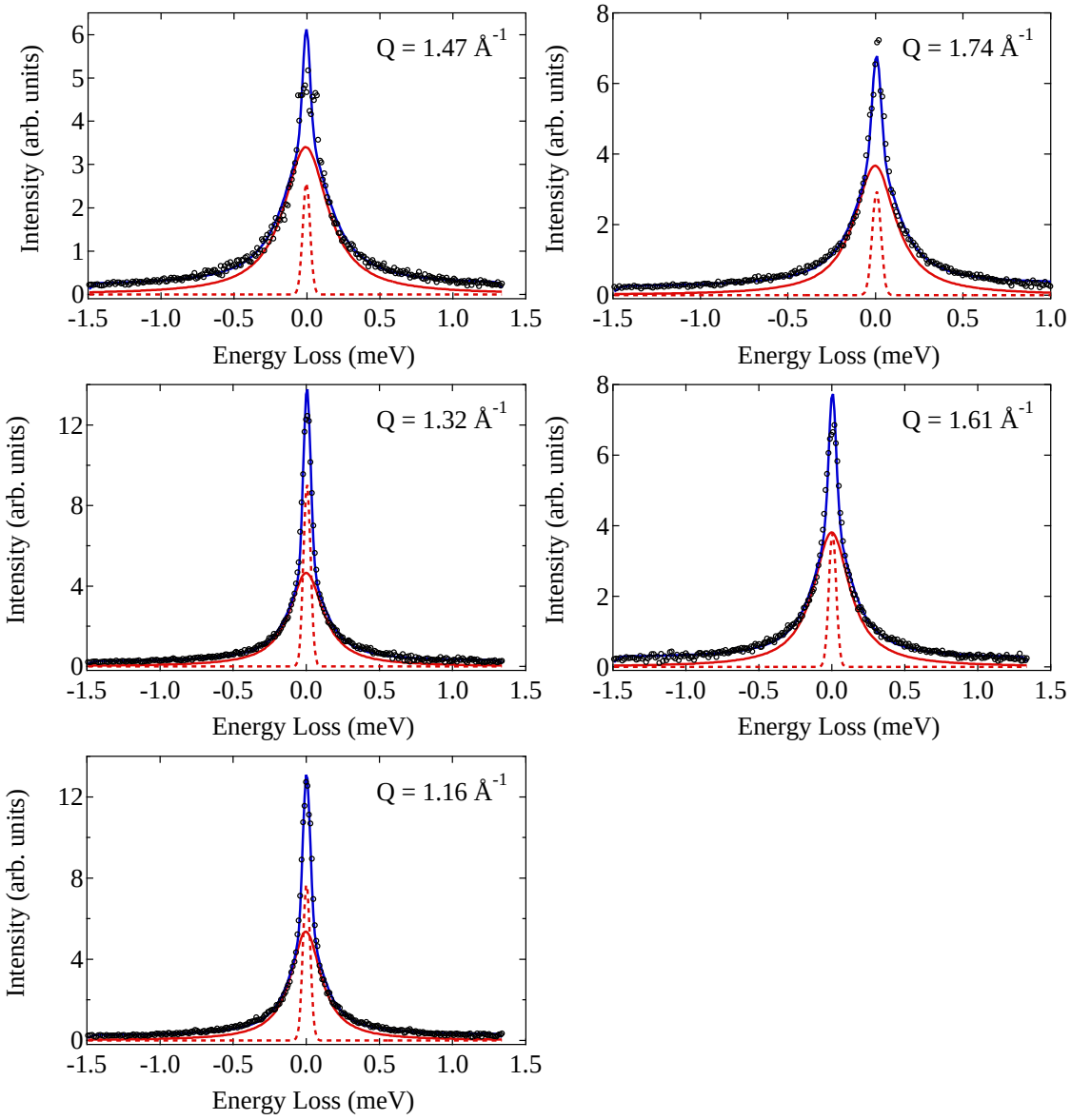

Figure 5.10: The five largest momentum-transfer groups of the QENS spectra at 110 K. Fitted curves: quasielastic (red, solid line), elastic (red, dashed line), and total (blue, solid line). The elastic line is the convolution of a delta function with instrument resolution. As illustrated, the quasielastic curve is a Lorentzian before convolution with resolution. The flat background is not shown.

5.6.3 Distribution of jump frequencies

The presence of more than a single jump frequency in the $KC_{24}(H_2)_{0.5}$ system is a highly intractable problem in the analysis and interpretation the QENS data. From data collected on a backscattering spectrometer (see Sec. 5.7), we know that there is also a slower diffusion process present in the H_2/KC_{24} system with a residence time on the order of 100 to 1000 ps. This leads to the possibility that there are a *distribution* of diffusive jump frequencies. Incorporating such a frequency distribution into a rigorous jump diffusion model is problematic. Even for the simplest case of two hopping frequencies on a Bravais lattice, the resulting expression is too complicated to be fit to the QENS spectra from a two-dimensional, polycrystalline system.

The intermediate scattering function for unrestricted diffusion is a simple exponential decay, $I(\mathbf{Q},t) = \exp(-t/\tau)$, where τ is the characteristic relaxation time. This expression simply reflects how the system relaxes back to its equilibrium state after some external perturbation is switched off. If there are numerous hopping frequencies present in the system, however, we need to take a linear superposition of the exponential decays. This can be approximated by a *stretched* exponential,

$$I(Q,t) = \exp\left[-\left(\frac{t}{\tau}\right)^{\beta}\right], \tag{5.29}$$

where the stretching factor β is taken to be between 0 and 1. This empirical relation is often referred to as the Kohlrausch-Williams-Watts (KWW) function. It describes a fairly broad distribution of relaxation times. The scattering function, $S(Q,\omega)$, is obtained by taking the Fourier transform of the KWW function.

The FT-KWW function was fitted to the QENS spectra of $KC_{24}(H_2)_{0.5}$ as a way of

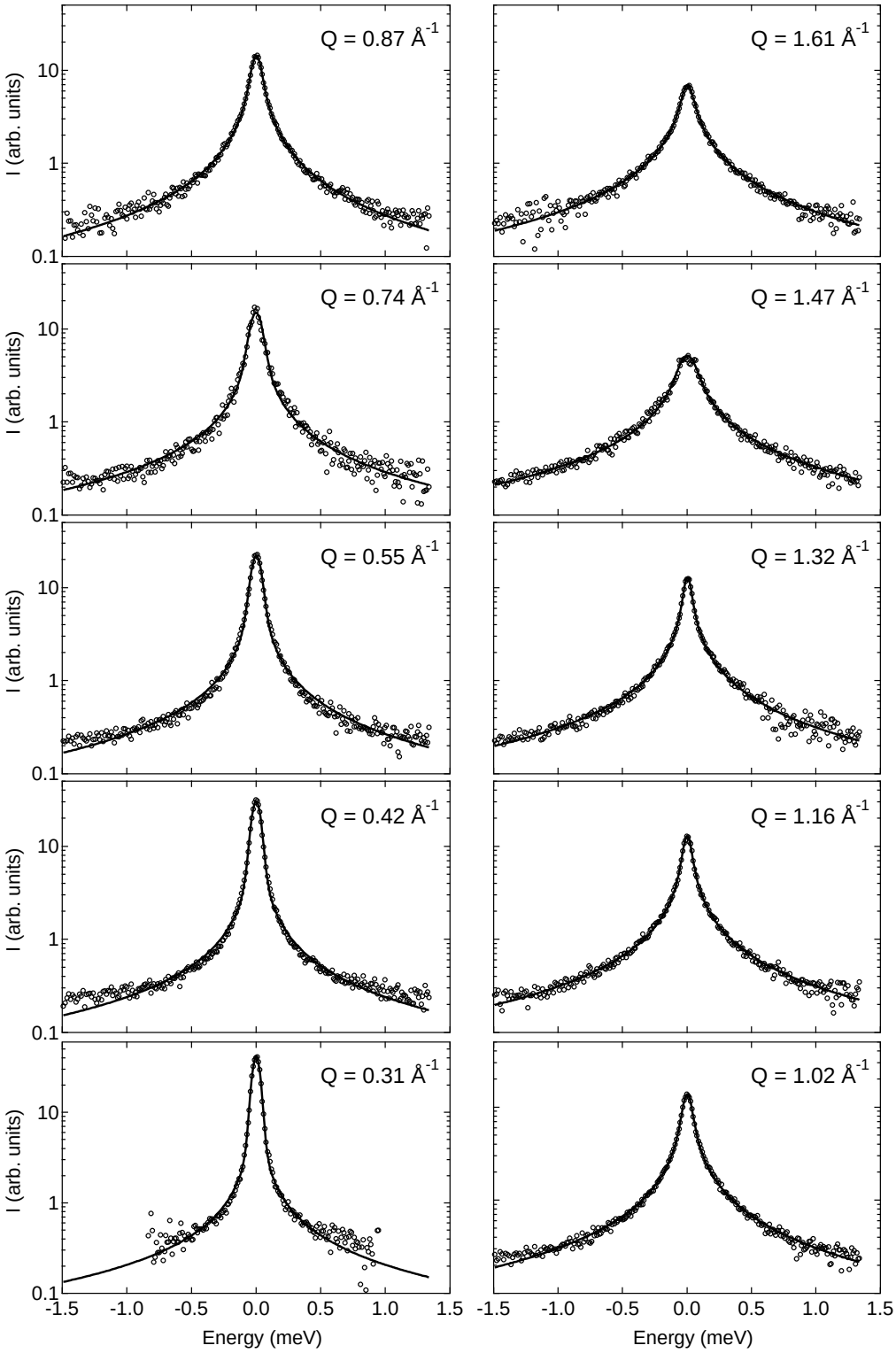

Figure 5.11: The QENS spectra of $KC_{24}(H_2)_{0.5}$ collected at 110 K, fitted to the FT-KWW function.

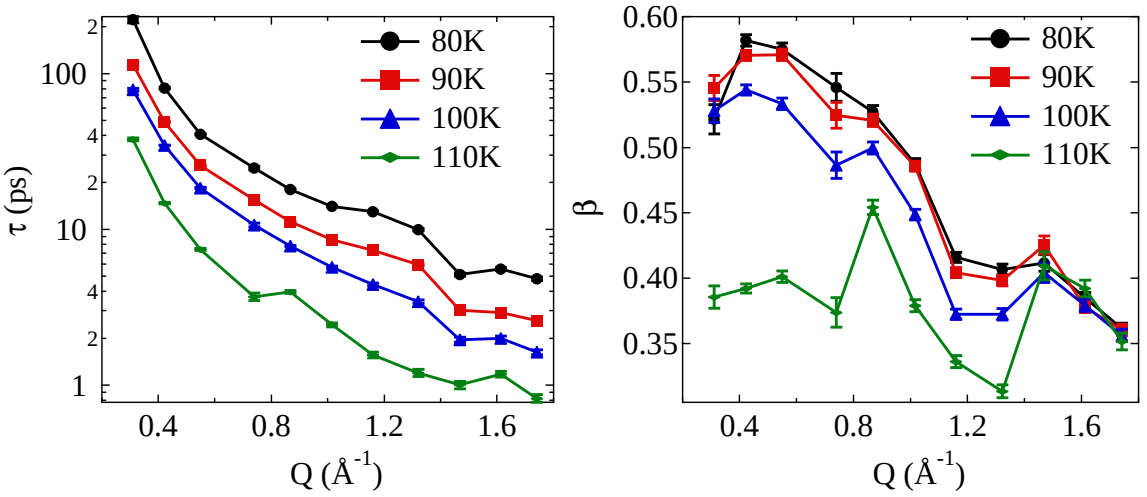

Figure 5.12: Parameters for the FT-KWW function fitted to the QENS spectra of $KC_{24}(H_2)_{0.5}$. Top: Best-fit values for τ as a function of momentum transfer. Bottom: Best-fit values for β as a function of momentum transfer.

gauging the importance of multiple hopping frequencies on the H_2 dynamics. The detailed expression used for the fits is given by the LHS of the following equation,

$$\mathcal{F}\left[e^{-\left(\frac{t}{\tau}\right)^{\beta}} \times \mathcal{F}\left[Ae^{-\frac{\omega^2}{2\sigma^2}}\right]\right] = \mathcal{F}\left[e^{-\left(\frac{t}{\tau}\right)^{\beta}}\right] * Ae^{-\frac{\omega^2}{2\sigma^2}}, \tag{5.30}$$

where the Gaussian function is used to describe the instrument resolution.[4] The σ parameters were determined by fits to the DCS resolution function and were held fixed during the fits. The convolution that appears on the RHS is due to the fact that the Fourier transform of a product equals the convolution of two individual Fourier transforms (i.e., convolution theorem). Also utilized is the fact that two successive Fourier transforms of a Gaussian yields the original Gaussian. During the least-squares fits, the outermost transform on the LHS was computed numerically. Fit parameters $\{\tau, \beta, A\}$ were allowed to vary independently in each momentum-transfer group. The resulting fits are shown in Fig. 5.11, and the fit parameters are summarized in Fig. 5.12. These are the best fits obtained so far, and

[4]The resolution function of the DCS instrument is well-described by a Gaussian function.

are certainly superior to those obtained for the honeycomb net jump diffusion model. Although the FT-KWW function is not a rigorous jump diffusion model, it can be considered a phenomenological indicator of the importance of a multiple hopping frequencies in the $KC_{24}(H_2)_{0.5}$ system.

5.7 Measurements at longer timescales

5.7.1 Overview

The high-flux backscattering spectrometer (HFBS)[5] located at NCNR has an energy resolution of better than 1 μeV [92]. This allows it to detect very slow dynamical processes with characteristic times from 100 ps to 10 ns, processes which are not resolvable on DCS. Measurements were collected on a $KC_{24}(H_2)_1$ system in order to verify whether there were slower H_2 hopping frequencies present.[6] For comparison, measurements on the same $KC_{24}(H_2)_1$ system were also performed on DCS over the same temperature range. The important finding from these measurements is that there are at least two distinct H_2 hopping frequencies in the KC_{24} system.

5.7.2 Methods

The HFBS instrument was operated in both the fixed window and dynamic window modes. In the fixed window mode, the Doppler drive was stopped and only elastic scattering was recorded. A heating rate of $0.5\,\mathrm{K\,s^{-1}}$ was used for the temperature scan experiments and the total intensity was obtained by summing over all 16 detector banks. In the dynamic window

[5]The HFBS spectrometer is an indirect geometry instrument which utilizes the fact that the wavelength spread of a Bragg-diffracted neutron beam decreases as the scattering angle 2θ approaches 180°. Incident energies of the neutrons are varied by the Doppler motion of the monochromator (i.e., controlled by a Doppler drive).

[6]Compared to other measurements, a larger hydrogen filling of $x = 1$ was used here, in order to improve the counting statistics on HFBS.

mode, the Si[111] crystal monochromator was operated at 24 Hz, providing a dynamic range of $\pm$ 17 μeV, a Q-range of 0.25 Å^{-1} to 1.75 Å^{-1}, and an energy resolution of 0.85 μeV at the elastic peak.

5.7.3 Quasielastic scattering

QENS measurements were collected on the $KC_{24}(H_2)_1$ system using both the DCS and HFBS spectrometers. In Fig. 5.13a, the DCS spectra show resolution-limited elastic scattering at 40 K and quasielastic line broadening at higher temperatures. For the HFBS spectra illustrated in Fig. 5.13b, elastic scattering is dominant 45 K, while quasielastic broadening is significant at 55 K and 65 K. The combination of a sharp elastic-like component and broad quasielastic component is present in both the DCS and HFBS spectra. The peak intensity decreases with temperature, but in Fig. 5.13 the spectra have been scaled to equal height to facilitate comparison. Quasielastic broadening is present at the same temperature range in *both* the HFBS and DCS data. However the energy scales for the two spectra are vastly different. This means that there are at least two different hopping frequencies present in $KC_{24}(H_2)_1$. The characteristic residence times for these hopping motions were estimated from the high-Q spectra (following the method discussed in Sec. 5.6.2) and are summarized in Table 5.3.

5.7.4 Elastic intensity

Using the fixed window mode of operation on HFBS, we measured the elastic intensity of the H_2/KC_{24} system as a function of temperature. These scans are displayed in Fig. 5.14. The curve for KC_{24} does not show any major changes between 4 K and 100 K. In contrast, the $KC_{24}(H_2)_1$ and $KC_{24}(H_2)_2$ curves show a rapid decrease in the elastic intensity starting at

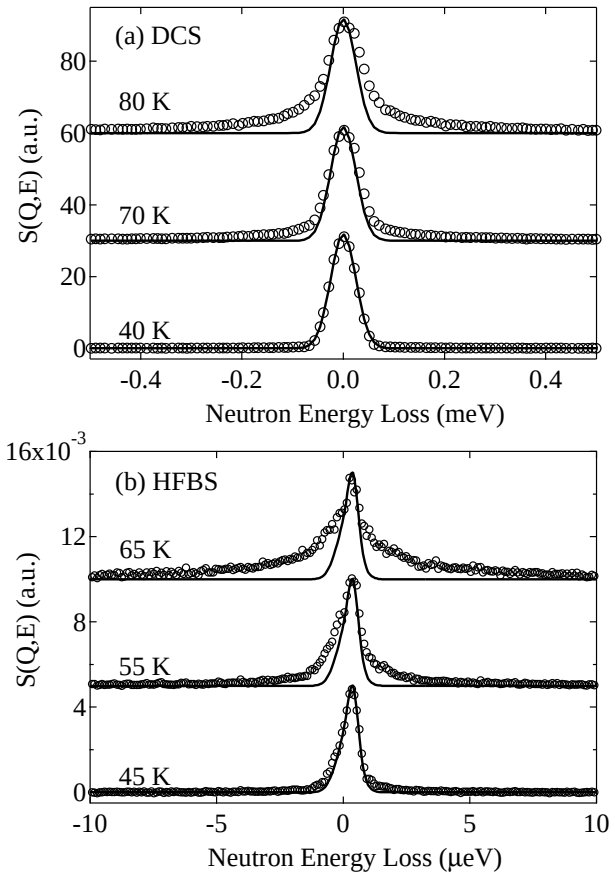

Figure 5.13: Quasielastic neutron scattering spectra of $KC_{24}(H_2)_1$: (a) from the DCS spectrometer, for the $Q = 1.84\,\text{Å}^{-1}$ group; (b) from the HFBS spectrometer, for the $Q = 0.87\,\text{Å}^{-1}$ group. The instrument resolution is included for comparison to the spectra at each temperature. The experimental spectra have been scaled to equal height, and offset for clarity.

Table 5.3: Residence times for thermally activated H_2 jump diffusion in $KC_{24}(H_2)_1$.

DCS data[a]		HFBS data[b]	
T (K)	τ (ps)	T (K)	τ (ps)
60	13.4 ± 0.2	45	1330 ± 36
70	9.4 ± 0.1	55	699 ± 12
80	7.0 ± 0.1	65	372 ± 7

[a] Measurements on DCS probe the faster diffusion process.
[b] Measurements on HFBS probe the slower diffusion process.
[c] Residence times (τ) were determined from the high-Q limit, as described in Sec. 5.6.2.

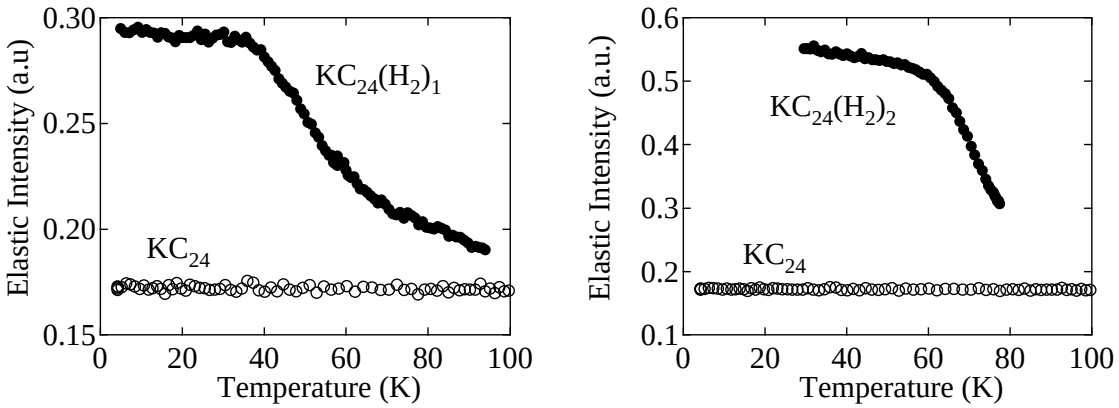

Figure 5.14: Elastic intensity from (left) $KC_{24}(H_2)_1$ and (right) $KC_{24}(H_2)_2$ as a function of temperature. Base intensity from KC_{24} is also presented.

35 K and 60 K, respectively. The sudden drop in elastic signal is accompanied by the growth in quasielastic intensity (see Fig. 5.13), indicating the presence of hydrogen diffusion. Scans obtained from heating and cooling the sample at the same rate did not have any significant differences except that the $KC_{24}(H_2)_1$ heating curve was slightly more rounded near the transition point at 35 K compared to the cooling curve.

One possibility that needed to be ruled out was that desorption of H_2 could also contribute to the decrease in elastic scattering at higher temperatures. For the composition $KC_{24}(H_2)_1$ this is unlikely because the equilibrium pressure at 60 K is close to 0 kPa, and the decrease begins at an even lower temperature of 35 K. Nevertheless, to be certain that the elastic intensity was not affected by H_2 desorption, we monitored the equilibrium pressure with a high resolution manometer over the entire temperature scan. We are confident that the concentration of adsorbed H_2 did not change significantly over the measured temperature range, and would not have contributed to the large decrease in the elastic intensity.

5.8 Molecular dynamics simulations

5.8.1 Computational details

To better understand the hydrogen diffusion mechanism in KC_{24}, molecular dynamics simulations were performed and compared with the experimental results. The theoretical $\left(\sqrt{7} \times \sqrt{7}\right)$ structure with stoichiometry KC_{28} was used for all simulations. To reduce the size of the supercell, the structure consisted of two graphite layers and one potassium metal layer in a A|A stacking sequence with an interlayer spacing of 5.69 Å for the intercalated layer and 3.35 Å for the unintercalated layer. The relaxed supercell was contained within a simulation box with parameters $a = 51.9837$ Å, $b = 45.0192$ Å, and $c = 9.04$ Å. Periodic boundary conditions were enforced. The host graphite structure was held constant in all simulations. For the 1:1 H_2:K ratio, the supercell had the stoichiometry $K_{64}C_{1792}(H_2)_{64}$, which consists of 64 unit cells.[7]

The program GULP V.3.4 was used as the computational engine for the simulation [93]. Forcefields were taken directly from the literature without further optimization. Hydrogen molecules were treated as Lennard-Jones spheres, which ignores the fact that they are quantum rotors. Because the dimensions of the KC_{24} system are on the order of the hydrogen de Broglie wavelength, it is necessary to account for quantum effects in the simulations. This is done using the Feynman-Hibbs (FH) variational approach. A quantum particle of mass m is represented by a Gaussian with a width $\sqrt{\beta\hbar^2/12\mu}$ that accounts for the spread in position due to the uncertainty principle [24]. The quantum partition function of N

[7] The $KC_{24}(H_2)_1$ stoichiometry was used in order to increase the number of hydrogens in the supercell, thereby increasing the quality of the calculated mean-squared-displacement and the intermediate scattering function.

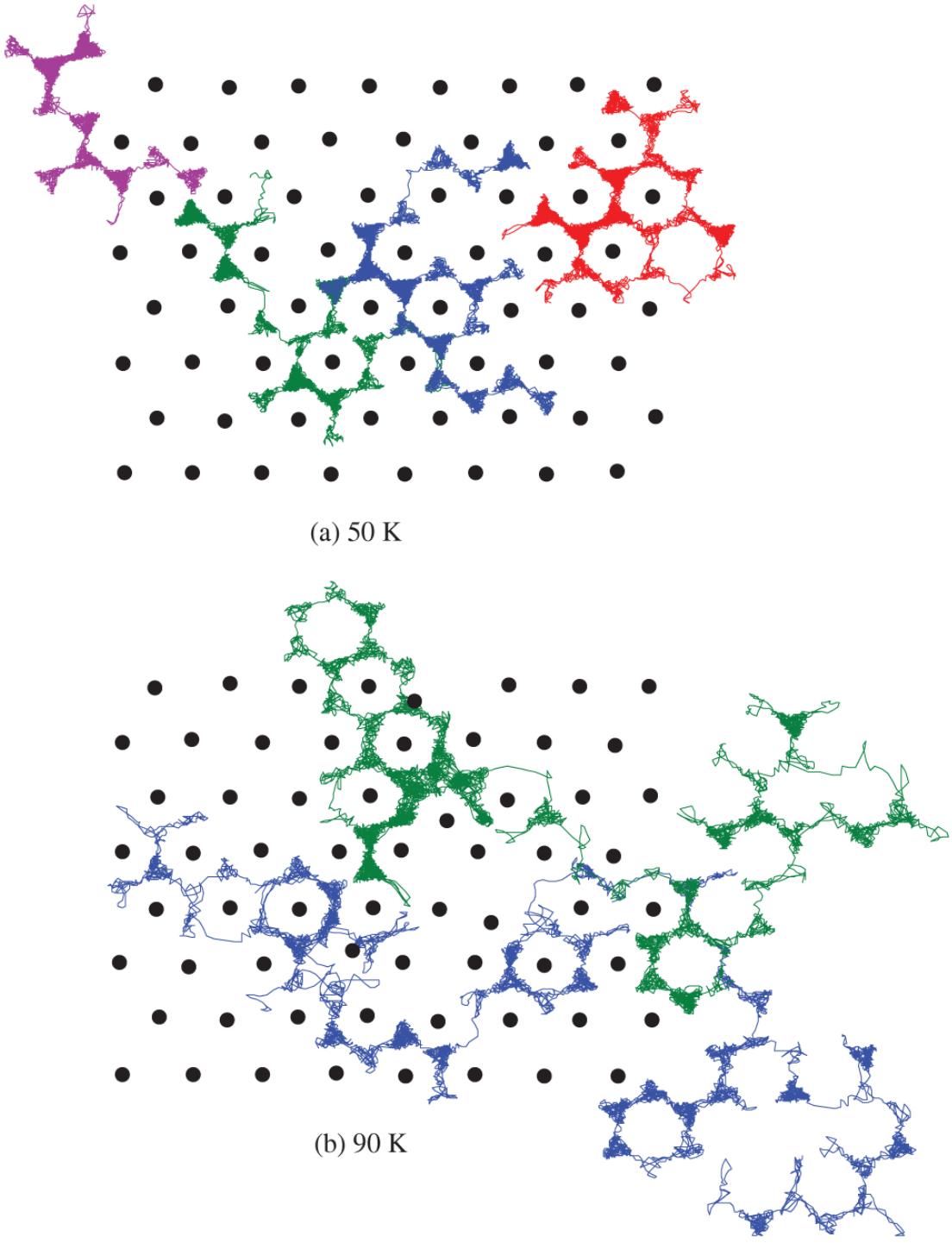

Figure 5.15: Molecular dynamics trajectories of hydrogen particles in KC_{24} at (top) 50 K and (bottom) 90 K. Total simulation time is 500 ps for each trajectory. Trajectories of four different particles are shown for 50 K while trajectories of two particles are shown for 90 K. Individual trajectories are identified by the color of the traces. Black circles indicate the final positions of potassium atoms. Carbon atoms are not shown.

particles is

$$Z = \frac{1}{N!}\left(\frac{m}{2\pi\beta\hbar^2}\right)^{3N/2}\int\cdots\int dr_1\ldots dr_N \exp\left[-\beta\sum_{i<j}U_{\mathrm{FH}}(r_{ij})\right] \tag{5.31}$$

where $\beta = 1/k_{\mathrm{B}}T$ and

$$U_{\mathrm{FH}}(r) = \left(\frac{6\mu}{\pi\beta\hbar^2}\right)^{3/2}\int U(|r+R|)\exp\left(-\frac{6\mu}{\beta\hbar^2}R^2\right)dR. \tag{5.32}$$

Here $U_{\mathrm{FH}}(r)$ is the effective potential between a pair of molecules with reduced mass μ. The integral in Eq. 5.31 is difficult to evaluate. As described in Ref. [24], the term $U(|r+R|)$ is expanded around r to the fourth order in R to obtain a more tractable expression. This approximation to the FH potential was incorporated into all of the molecular dynamics simulations. The carbon and potassium potentials were extracted from Ref. [94], which were based on empirical fits to lattice parameters, elastic moduli, and infrared-Raman data for graphite and potassium-intercalated graphite. The hydrogen potentials were taken from Ref. [24] in which they successfully reproduced bulk hydrogen data. The forcefield has a tapered 12.0 Å cutoff. Since intercalate layers are separated by a distance of 9.04 Å, this means that interlayer interactions in the simulation are very weak. Simulations were run using an NVT ensemble with a leapfrog-verlet integrator and a time-step of 1 fs. Temperature was controlled with a Nose-Hoover thermostat. Simulations were equilibrated for 50 ps (50 000 steps), followed by a production run of 500 ps (500 000 steps).

5.8.2 Results

Molecular dynamics trajectories of $KC_{24}(H_2)_1$ were run at temperatures of 30 K, 40 K, 50 K, 70 K, and 90 K. Sample H_2 trajectories are illustrated in Fig. 5.15 for the 50 K and 90 K

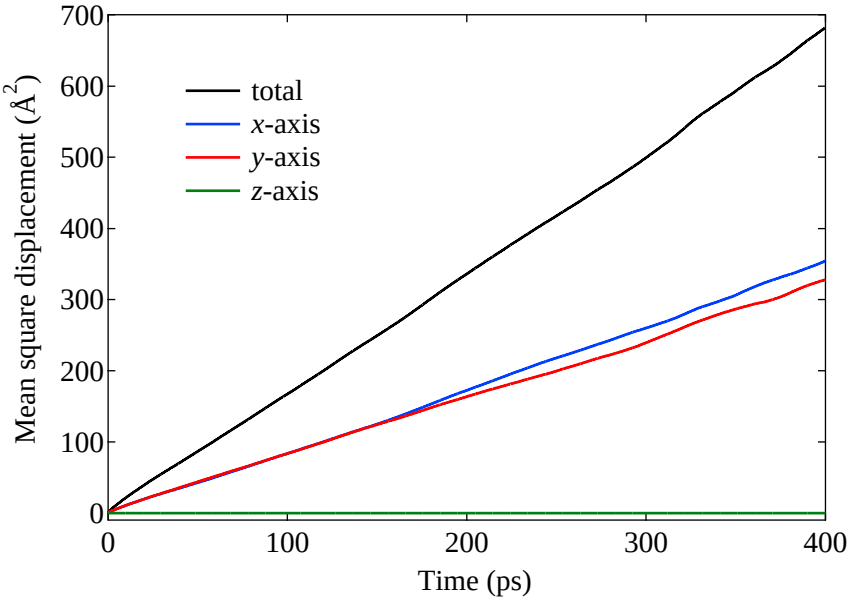

Figure 5.16: Total mean square displacement of H_2 particles in $KC_{24}(H_2)_1$ at 70 K. The projections of the MSD along the x-axis, y-axis, and z-axis of the simulation box are also shown.

simulations. Each single-colored trace depicts the trajectory of a single H_2 particle for a 500 ps production run. As can be seen in the trajectories, hydrogens rattle around inside of the triangular cages formed from three potassium atoms for extended periods of time before jumping into a neighboring triangular site. As expected for thermally activated diffusion, the jump frequency appears to be much larger at 90 K than at 50 K. In a jump diffusion model, it is assumed that the particle vibrates around its equilibrium position between jumps. This vibrational motion can be decoupled from the diffusive motion and distilled into a separate Debye-Waller factor. For the $KC_{24}(H_2)$ system, however, the particles seem to jump rapidly between three local energy minima within the triangular sites (evident in the triangular shaped motifs present in Fig. 5.15). The potassium atoms do not diffuse at the temperatures investigated here, but mainly vibrate around their equilibrium positions (though several potassiums did actually jump to neighboring graphite hexagons during the 90 K run).

Dynamical properties were calculated from H_2 trajectories using the nMOLDYN package [95]. The mean square displacement (MSD), with respect to a particular axis $\mathbf{n}$, is calculated for a system of N particles with the expression,

$$\Delta^2(t) = \frac{1}{N}\sum_{i=1}^{N}\left[\mathbf{n}\cdot(\mathbf{R}_i(t) - \mathbf{R}_i(0))\right]^2. \tag{5.33}$$

For illustration, the MSD of H_2 at 70 K is plotted in Fig. 5.16. As expected, the diffusion is two-dimensional and the MSD along the z-axis is zero. The sum of the x-projection and y-projection give the total MSD. We calculate the 2D self-diffusion coefficient from the slope of the MSD in the long-time limit, using the Einstein relation

$$\lim_{t\to\infty}\Delta^2(t) = 4Dt. \tag{5.34}$$

In Fig. 5.17 the simulated self-diffusion coefficients are plotted with the experimental diffusion coefficients (calculated from the DCS residence times listed in Table 5.3). Agreement between the experimental and simulated self-diffusivities is remarkably good, especially considering that the MD forcefields were used without optimization. The fact that simulated values are larger than than experimental values might be due to the FH corrections, which have the overall effect of increasing the hydrogen mobility. The fact that such excellent agreement is obtained with experimental data with an unoptimized forcefield perhaps indicates that the layered geometry, not the fine form of the intermolecular potentials, is the main determining factor in the dynamics.

Between 40 K and 90 K, the simulated diffusivities follow the expected Arrhenius relation

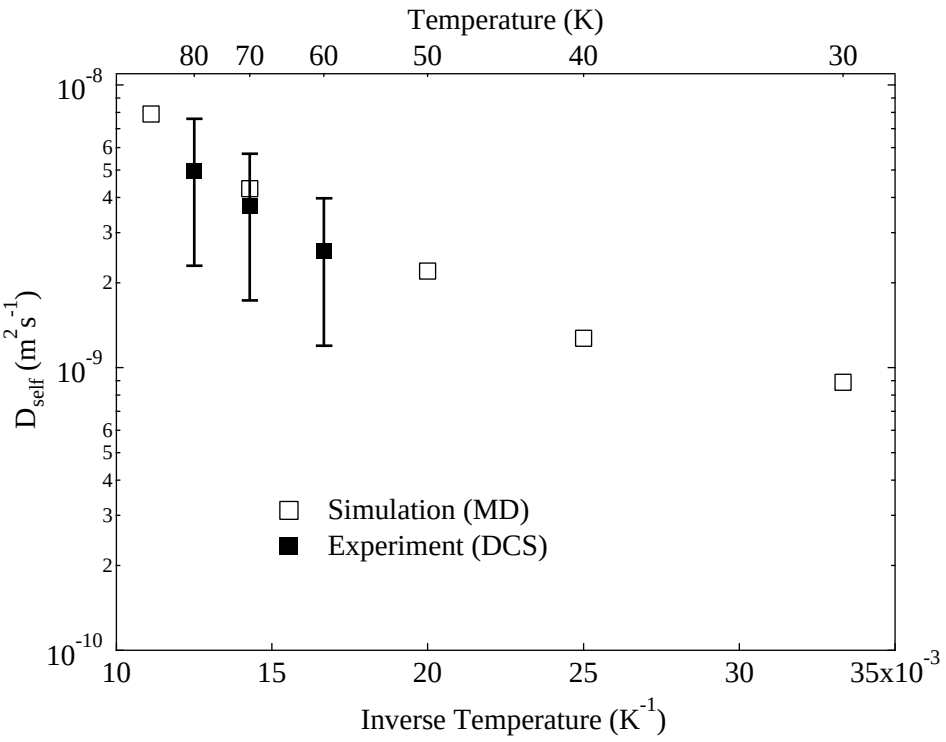

Figure 5.17: Comparison of self-diffusion coefficients of H_2 in $KC_{24}(H_2)_1$ obtained from experiment and from MD simulation. Experimental self-diffusivities were obtained from QENS data collected on the DCS instrument.

for a thermally activated process,

$$D = D_0 \exp\left(-\frac{E_\mathrm{a}}{T}\right), \tag{5.35}$$

where D is the self-diffusion coefficient, D_0 is the pre-factor, and E_a is the activation coefficient. For experimental diffusivities we obtain values of $D_0 = 3.43 \times 10^{-8}\,\mathrm{m^2\,s^{-1}}$ and $E_\mathrm{a} = 155\,\mathrm{K}$. For the simulated self-diffusivities the values are $D_0 = 2.99 \times 10^{-8}\,\mathrm{m^2\,s^{-1}}$ and $E_\mathrm{a} = 128\,\mathrm{K}$.

5.8.3 Concentration effects

The jump diffusion model is only valid in the dilute limit where site-blocking and correlation are absent (see Section 5.2.4). In other words, at large H_2 concentrations we cannot apply

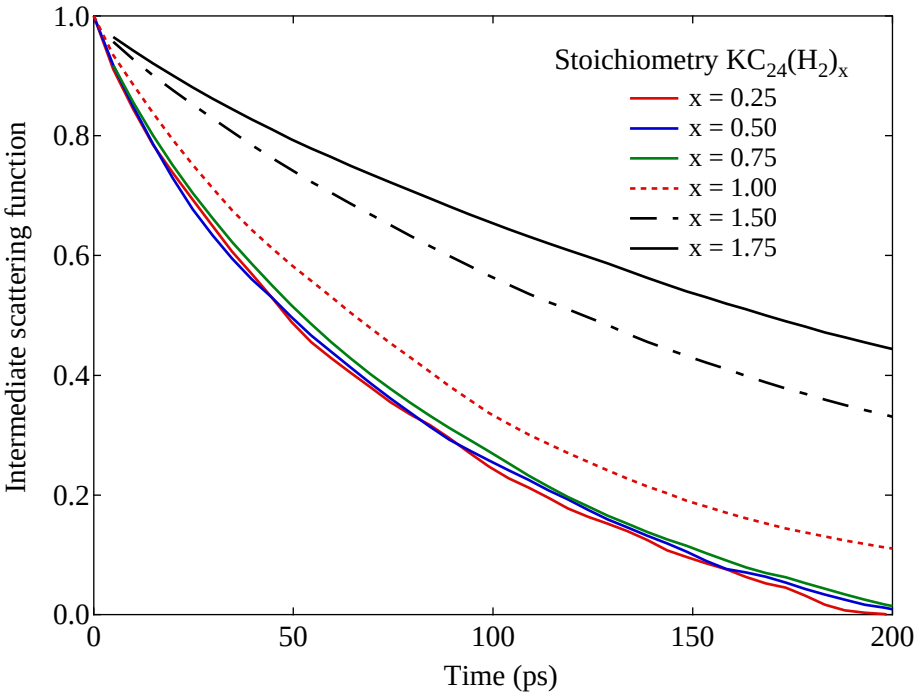

Figure 5.18: Intermediate scattering function at $Q = 1.0\,\text{Å}^{-1}$ calculated from MD trajectories of hydrogen in the theoretical $KC_{28}(H_2)_1$ structure. Changes in the ISF with concentration indicate site-blocking and correlation effects on the line shape.

a jump diffusion model to obtain a meaningful diffusion coefficient. In fact, the lineshape itself might not be well-described by the jump diffusion model at large concentrations. Therefore it is best to remain in the dilute-limit where the correlation between successive jumps is negligible and the diffusivity only needs to be corrected for site-blocking. To test whether the dilute-limit approximation can be applied to the experimental QENS data, MD simulations were performed at 90 K for various H_2 fillings. Computational details were otherwise the same as the previous simulations.

For direct comparison of line shapes it was convenient to calculate the incoherent intermediate scattering function,

$$I_{\text{inc}}(\mathbf{Q},t) = \frac{1}{N}\sum_{i}^{N}\sigma_{\text{inc},i}^{2}\langle \exp\left[-i\mathbf{Q}\cdot\mathbf{R}_i(0)\right]\exp\left[i\mathbf{Q}\cdot\mathbf{R}_i(t)\right]\rangle, \tag{5.36}$$

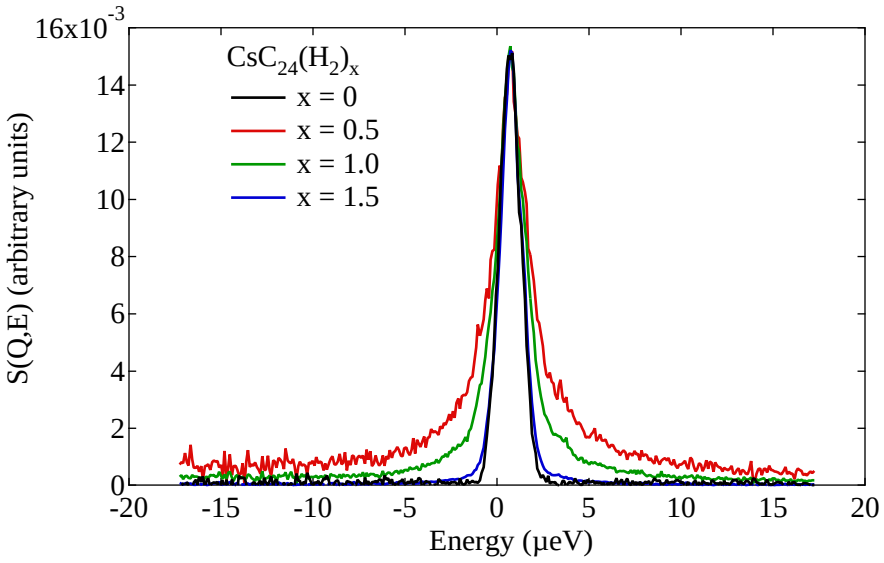

Figure 5.19: QENS spectra at 65 K collected on HFBS for three different hydrogen fillings in CsC_{24}. The background signal from CsC_{24} at 4 K is also displayed. Spectra are scaled to equal height.

which describes correlation between the initial position and the final position. In unrestricted translational diffusion, $I_{\text{inc}}(\mathbf{Q}, t)$ should decay to zero at infinite time. Powder-averaged ISFs were calculated from the MD trajectories at $Q = 1.0\,\text{Å}^{-1}$. They are plotted in Fig. 5.18. The effect of correlations on the line shape becomes noticeable above at a stoichiometry of $x = 1.0$. Therefore, it seems that the dilute-limit approximation is not valid for $x > 1$. However, the dilute-limit approximation at $x = 0.5$ (for which most QENS measurements were collected) is clearly sufficient. Concentration effects on hydrogen diffusion in a $CsC_{24}(H_2)_x$ sample were investigated experimentally on the HFBS instrument.[8] Spectra were collected at three different hydrogen loadings and are shown in Fig. 5.19. It is clear that the breadth of the quasielastic peak decreases at large concentrations.

[8]It would have been better to have collected data on a KC_{24} sample rather than a CsC_{24} sample. On a qualitative level, though, concentration effects should be similar in both systems.

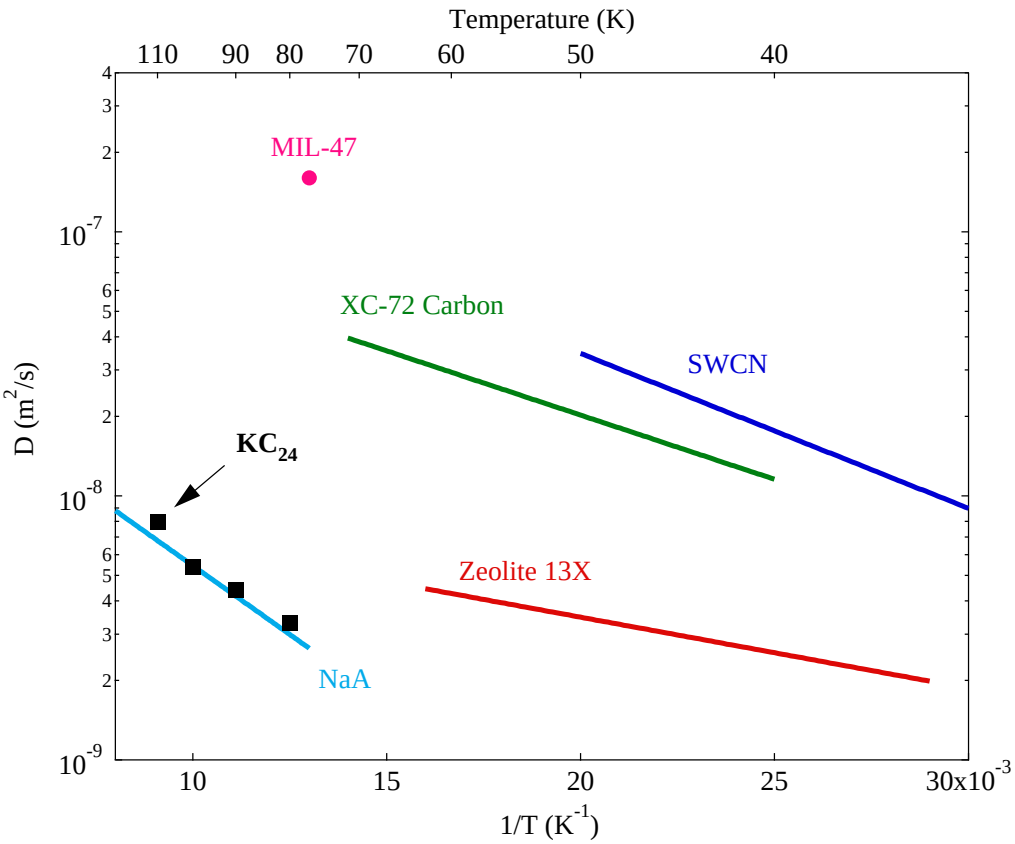

Figure 5.20: Comparison of hydrogen diffusivity in a variety of adsorbents. Hydrogen self-diffusion coefficients in KC_{24} are plotted as black squares. Values for single-walled carbon nanotubes (SWCN) and a carbon black material (XC-72) are illustrated. Data is also included for a type A zeolite (NaA), a type X zeolite (13X), and a metal-organic framework (MIL-47).

5.9 Discussion

5.9.1 Comparison with carbons, zeolites, and MOFs

In Fig. 5.20 the hydrogen diffusivity[9] in KC_{24} is plotted as a series of solid black squares, and is compared to values for single-walled carbon nanotubes [96] and the carbon black XC-72 [97]. Also plotted are self-diffusion coefficients for the type-A zeolite NaA [98], the type-X zeolite 13X [99], and the metal-organic framework MIL-47 [100]. It should be noted that the self-diffusion coefficients for KC_{24} are two-dimensional, and should actually be multiplied by a factor of 2/3 for direct comparison to three-dimensional systems.

[9]Extracted from fits of the honeycomb net jump diffusion model to the QENS spectra of $KC_{24}(H_2)_{0.5}$.

Hydrogen diffusivity in KC_{24} is more than an order-of-magnitude slower than in other carbon sorbents. It is similar in magnitude to diffusivities in the microporous zeolites (13X and NaA). Both KC_{24} and the 13X/NaA zeolites share a nanoporous geometry. Hydrogen diffuses in KC_{24} through narrow channels formed between closely spaced graphene layers. Similarly, diffusion in NaA and 13X occurs though intra-crystalline channels with molecular-sized windows. The widths of these cavities are on the order of the H_2 molecule diameter. For example, the windows of NaA have a van der Waals diameter of about $\sigma \approx 2.9\,\text{Å}$, while the interlayer separation of $KC_{24}(H_2)_{0.5}$ has a van der Waals diameter of $\sigma \approx 2.3\,\text{Å}$. The narrow intra-crystalline channels of KC_{24}, and of zeolites NaA and 13X, act as steric barriers that slow down the diffusion considerably. Interestingly, the steric barriers are also reflected in the molecular-sieve properties of these materials. In comparison, hydrogen diffuses mostly on the outer surfaces of carbon blacks and SWCNs, subject to fewer steric diffusion barriers. Geometry appears to be a dominant factor in determining the diffusion properties of hydrogen adsorbed in porous materials, while the actual chemical identity of the sorbent material appears to be of secondary importance.

5.9.2 Diffusion on two time-scales

A puzzling feature of the QENS data for $KC_{24}(H_2)_1$ is that it shows diffusion processes occurring on two distinct time scales (see Table. 5.3). The extremely slow diffusivity measured on HFBS is fairly unique and cannot be easily explained with a simple jump diffusion model. This type of slow diffusion (detectable on a backscattering spectrometer) is sometimes observed in metal hydrides and is typically attributed to H trapping at strong attractive sites. The origin of trapping sites in KC_{24} is not clear however. Dual timescales in certain metal hydrides have also been linked to the simultaneous presence of fast, localized motions

between closely spaced interstitial sites and slower, long-range diffusion [101]. Similarly, elastic-like features in the QENS spectra of H_2/sorbent systems are usually explained in terms of a slow-diffusing population of hydrogen molecules [96, 99, 102].

One possible explanation is that the fast process originates from rapid individual jumps of the H_2 molecules while the slow process originates from in-plane jumps of the potassiums. Hydrogen molecules tend to cluster around the potassiums due to both electrostatic and dispersion interactions. When a potassium atom jumps, the fast-moving H_2 molecules quickly reconfigure around the new site of the potassium atom. This fluctuation in H_2 particle density can be detected by the backscattering spectrometer as slow diffusion. An alternative theory can be developed by hypothesizing that the adsorbed hydrogen forms a new phase. Lateral interactions between the adsorbed hydrogens may cause them to coalesce into tightly packed islands. Molecules in the interior of an island will have less mobility than the molecules at the island periphery. Measurements on a completely filled $KC_{24}(H_2)_2$ composition would provide some indirect information on the H_2 diffusivity in a tightly packed arrangement. The possibilities of phase transformations in the H_2 adsorbate will be discussed further in the next subsection.

5.9.3 Phase transformations

For a system consisting of H_2 monolayers on a clean graphite surface, transitions between commensurate and incommensurate solid 2D phases are determined by a competition between the hydrogen-hydrogen interactions and the hydrogen-surface interactions. At low H_2 concentrations, interactions with the periodic graphite corrugation potential are dominant, resulting in a commensurate, solid-like adsorbate phase [103]. As the surface coverage is increased and the lateral interactions between hydrogen molecules grow more important,

the commensurate solid monolayer becomes unstable relative to the formation of long-range dislocations, leading to a domain-wall intermediate phase [104]. In the Kosterlitz-Thouless theory of two-dimensional phase transformations, this type of intermediate phase is sometimes called a hexatic phase [105–107]. It is unique to two-dimensional systems and does not occur for three-dimensional systems. Diffusion along the fluid-like domain wall boundaries is considerably faster than within the domain interior [108]. This can result in the two time-scales for the system diffusivity. If the temperature is increased, an isotropic two-dimensional liquid is eventually formed. For the H_2/graphite system this transition occurs at around 20 K.

We studied the phase behavior of the H_2/KC_{24} system by measuring the elastic intensity as a function of temperature (see Fig. 5.14). There is a distinct drop in elastic intensity starting at around 35 K which exceeds the expected decrease from the Debye-Waller factor. This is due to the onset of H_2 diffusion within the measurable time window of the instrument. However, the decrease in intensity with further heating is gradual, not abrupt. This means that there is no discrete H_2 melting transition in KC_{24} such as is observed for H_2 on a graphite surface. Instead, there is a gradual increase in hydrogen mobility with temperature. The corrugated potential of the host KC_{24} is dominant compared to the lateral interactions between hydrogen molecules. What occurs, therefore, is a gradual thermally-induced increase in diffusion through a solid-like sublattice, rather than a distinct solid-to-fluid bulk phase transition.

Bulk H_2 melts at a temperature of around 14 K. Confinement of H_2 in a porous material is known in some cases to lower the freezing temperature. For H_2 in Vycor, a porous glass with cavities of ∼60 Å, the freezing temperature has been measured at 8 K. In the smaller pores (∼20 Å) of the silica glass MCM-48, though, the melting temperature is little

changed from the bulk value of 14 K [109]. The strong binding interactions between H_2 and KC_{24} appear to have the opposite effect on the "melting" behavior.[10] Hydrogen diffusivity (within the instrument time window) in $KC_{24}(H_2)_1$ is not detected until a temperature of 35 K, considerably higher than the bulk melting point. However there is not enough information to determine whether this actually is a phase transition. To make more conclusive observations of the phase behavior in the H_2/KC_{24} system, other experimental techniques such as calorimetry or diffraction should be utilized.

5.10 Conclusions

Hydrogen self-diffusion in KC_{24} was studied with QENS measurements and with MD simulations. The diffusivity in KC_{24} is over an order of magnitude smaller than in other carbon adsorbents. It appears that steric diffusion barriers from the molecular-sized pore dimensions of KC_{24} are the main factors in slowing down the diffusion. The hydrogen self-diffusion coefficients follow the Arrhenius relation for a thermally activated process. Good agreement is observed between the experimental and simulated diffusivities in KC_{24} without optimization of the forcefields, hinting once again that geometry is the significant factor. Experimental quasielastic scattering was observed from an extremely slow process ($\tau \sim 1000$ ps) and a faster process ($\tau \sim 10$ ps). The origin of the slow process is still unclear. There was no sharp melting transition in $KC_{24}(H_2)_1$, but rather a gradual increase in H_2 mobility with temperature.

[10] Since most measurements were collected above the critical temperature of hydrogen, it may not be accurate to denote this as melting.

Chapter 6

Hydrogen binding sites in potassium intercalated graphite

6.1 Introduction

Hydrogen adsorption in KC_{24} has a relatively flat isosteric heat of adsorption (see Fig. 4.2). A relevant question is whether this behavior can be traced to the presence of a narrow distribution of nearly-homogeneous adsorption sites in the KC_{24} host structure. Due to the exceptionally large incoherent cross-section of hydrogen, inelastic-incoherent-neutron scattering (IINS) can be used effectively as a local structural probe for the adsorbed H_2 molecules. Phonon and rotational energy levels of the adsorbed H_2 molecules can both be determined from IINS spectra and compared with calculated values. In this chapter, IINS spectra of the $KC_{24}(H_2)_x$ are measured over a low energy range (0–2.5 meV), an intermediate energy range (5–45 meV), and a high energy range (35–100 meV). We investigate whether the one-dimensional hindered rotor model can successfully describe peak positions in the low and high energy ranges. In the intermediate energy range, we attempt to describe the rich spectral features in terms of multi-excitations of phonon and rotational energy levels. We also assess the significance of rotational-translation coupling on the dynamics of the $KC_{24}(H_2)_x$ system. Finally, the ground state potential energy surface of the theoretical

$KC_{28}(H_2)_1$ system is mapped from first-principles calculations, and energy levels of phonon and rotational modes are estimated.

6.2 Background

6.2.1 Rotational energy levels of the free hydrogen molecule

The free hydrogen molecule can be modeled as a rigid quantum rotor, which is well-known textbook example [110]. The eigenfunctions for the rigid rotor are the spherical harmonics $Y_l^m(\theta, \phi)$, where l is the principal angular momentum quantum number and m has the allowed values $\{0, \pm 1, \pm 2, \ldots \pm l\}$. The quantized energy levels for the rigid rotor are

$$E_{l,m} = l\,(l+1)\,B_{\mathrm{rot}}. \tag{6.1}$$

The energy levels are $(2l+1)$-fold degenerate in quantum number m. For the H_2 molecule, the rotational constant is equal to

$$B_{\mathrm{rot}} = \frac{\hbar}{4\pi\mu d^2} = 7.35\,\mathrm{meV}, \tag{6.2}$$

where $\mu = 0.5$ is the reduced mass, and $d = 74.6\,\mathrm{pm}$ is the H_2 bond length. This model is appropriate for a free H_2 molecule in a spherically symmetric potential or in a vacuum.

6.2.2 Ortho- and para-hydrogen

The nuclear spin and rotational degrees of freedom of the H_2 molecule are coupled due to the quantum mechanical symmetry restrictions. Since individual hydrogen nuclei are indistinguishable fermions, the total H_2 wavefunction must be antisymmetric under exchange.

The total wavefunction is constructed from both the rotational and nuclear spin wavefunctions, $\psi_{\text{total}} = Y_l^m(\theta, \phi)\psi_{\text{spin}}$. The symmetry of the rotational wavefunction under exchange can be written as $Y_l^m(\pi - \theta, \phi + \pi) = (-1)^l Y_l^m(\theta, \phi)$, which means that even values of l correspond to symmetric wavefunctions while odd values of l correspond to antisymmetric wavefunctions. The symmetric nuclear spin wavefunction (called *ortho*-hydrogen, or *o*-H_2) corresponds to the triplet state with total spin 1. The antisymmetric nuclear spin state (called *para*-hydrogen, or *p*-H_2) corresponds to the singlet state with total spin 0. In order for ψ_{total} to be anti-symmetric, even rotational states $l = 0, 2, 4, \ldots$ must be paired with the antisymmetric nuclear spin state (*para*-H_2). Similarly, the odd rotational states $l = 1, 3, 5, \ldots$ must be paired with the symmetric nuclear spin state (*ortho*-H_2). Normal hydrogen contains a 3:1 mixture of *ortho*- and *para*-hydrogen at room temperature.

6.2.3 One-dimensional hindered diatomic rotor

For an H_2 molecule in an anisotropic potential, Eq. 6.1 no longer describes the rotational energy levels. The simplest case is the one-dimensional hindered rotor model [52, 53]. The Hamiltonian for an H_2 molecule in this potential is given by

$$\hat{H} = \frac{\hat{L}^2}{2I} + \frac{V_2}{2}\left(1 - \cos 2\theta\right), \tag{6.3}$$

where V_2 is the potential energy barrier height, $\hat{L}$ is the angular momentum operator, I is the moment of inertia, and θ is the angle that the molecular axis makes with the z-axis. This one-dimensional Schrödinger equation is solved by diagonalizing the Hamiltonian matrix. After expanding the rotational potential with a spherical harmonics basis set, the

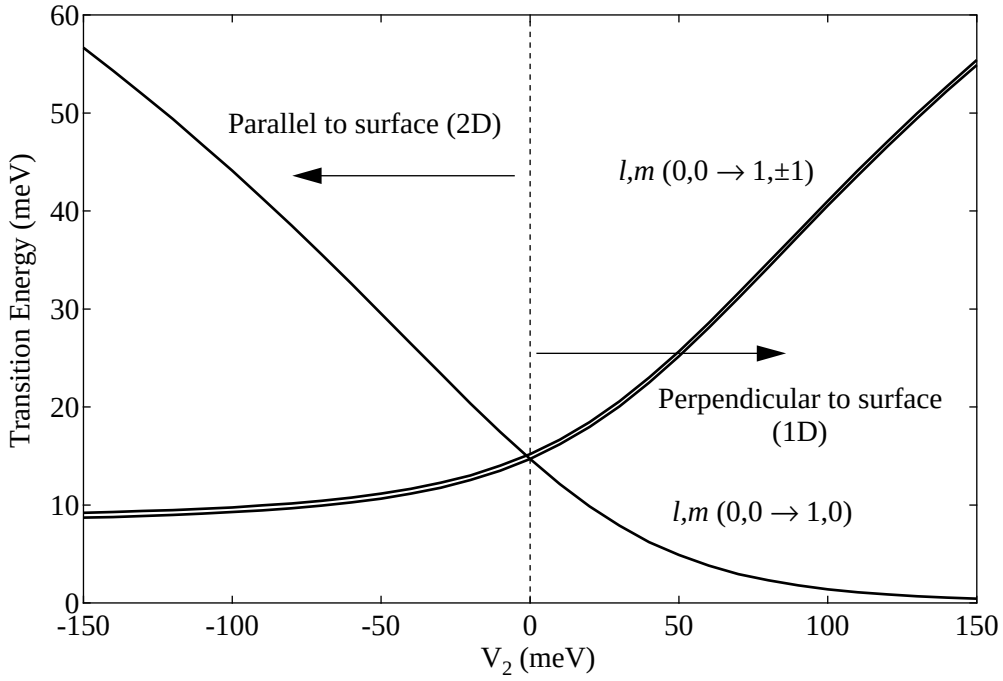

Figure 6.1: One-dimensional hindered rotor model. Rotational energy level transitions for an H_2 molecule from an $l, m(0, 0)$ initial state to the first two excited states. Plotted as a function of the barrier height parameter V_2. The degenerate $l, m(1, +1)$ and $l, m(1, -1)$ states are offset slightly for clarity.

Hamiltonian matrix elements are written

$$H_{l',m',l,m} = l(l+1)B_{\rm rot}\delta_{l',l}\delta_{m',m} + \langle Y_{l'}^{m'}|\tfrac{V_2}{2}\,(1-\cos 2\theta)|Y_l^m\rangle. \tag{6.4}$$

When V_2 is positive, the H_2 molecule aligns perpendicular to the surface (1D case), and when V_2 is negative, the molecule prefers to align parallel to surface (2D case). One effect of an anisotropic potential is a lifting of the degeneracy of rotational energy levels. This is illustrated in Fig. 6.1, which plots the rotational energy level transitions from a $l, m(0, 0)$ initial state as a function of V_2. The energy levels of $l, m(1, \pm 1)$ are still degenerate, but the $l, m(1, 0)$ level is not. This model predicts that the single $l(0 \rightarrow 1)$ transition of free H_2 will be split into two peaks when the molecule is placed in a one-dimensional rotational potential energy well.

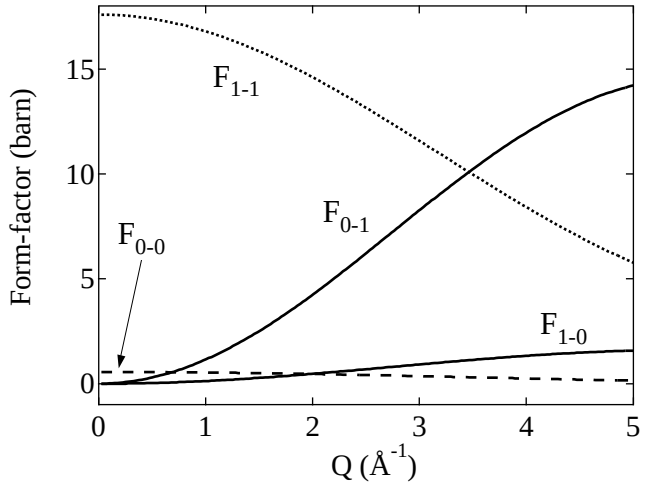

Figure 6.2: Molecular form factors for pure rotational transitions of the H_2 molecule, plotted as a function of momentum transfer. Only the transitions for the ground and first excited state are plotted.

6.2.4 Scattering law for rotational transitions of molecular hydrogen

Neutrons interact strongly with the H_2 molecule by a spin-flip transition. By flipping the nuclear spin state from paired to unpaired (or visa versa), the neutron thereby induces a transition in the H_2 rotational level. The spin of the neutron ($= \pm 1/2$) must flip sign in this scattering event. For example, the $l(0 \rightarrow 1)$ transition has the following mechanism,

$$(\uparrow\downarrow)^{l=0}_{\mathrm{H_2}} + (\uparrow)^{E_i}_{n} \xrightarrow{\sigma_{\mathrm{inc}}} (\uparrow\uparrow)^{l=1}_{\mathrm{H_2}} + (\downarrow)^{E_f}_{n} \,, \tag{6.5}$$

where the neutron energy loss is given by $\Delta E_{0-1} = E_i - E_f$. The double differential neutron scattering cross-section for a pure rotational transition of free H_2 has been calculated by Young and Koppel [111]. The basic idea is to use Fermi's "golden rule" to calculate the matrix element for a transition in which one or more more quantum numbers of the scatterer are changed and an equivalent amount of energy is transferred to the neutron. It is assumed that vibrations and rotations of the H_2 molecule are not coupled and that the molecule is in

the ground vibrational state. For a transition between the initial and final rotational levels l and l', the double differential scattering cross-section is expressed as

$$\frac{\mathrm{d}^2\sigma}{\mathrm{d}\Omega \mathrm{d}E} = \frac{k}{k_0} F_{l-l'}(Q) \exp(-2W) \delta(E - E_{l'} + E_l), \tag{6.6}$$

where k and k_0 are the magnitudes of the final and initial neutron wavevectors, W is the Debye-Waller factor, $F_{l-l'}(Q)$ is the molecular form factor, and the delta function enforces conservation of energy. Based on the Young-Koppel model, the molecular form factors are given by

$$F_{0-0} = 4 b_{\mathrm{c}}^2 j_0^2 \left(Qd/2\right) \tag{6.7}$$

$$F_{0-1} = 12 b_{\mathrm{inc}}^2 j_1^2 \left(Qd/2\right) \tag{6.8}$$

$$F_{1-0} = \tfrac{4}{3} b_{\mathrm{inc}}^2 j_1^2 \left(Qd/2\right) \tag{6.9}$$

$$F_{1-1} = 4 \left(b_{\mathrm{c}}^2 + \tfrac{2}{3} b_{\mathrm{inc}}^2\right) \left[2 j_2^2 \left(Qd/2\right) + j_0^2 \left(Qd/2\right)\right], \tag{6.10}$$

where b_{c} and b_{inc} are the coherent and incoherent scattering lengths, d is the H_2 bond length, and j_i is the i^{th} order spherical Bessel functions of the first kind. These molecular form-factors are plotted in Fig. 6.2. An important feature of this analysis is that the $l(0 \rightarrow 1)$ transition (and also the $l(1 \rightarrow 1)$ non-transition) is weighted by the large incoherent scattering length. However, the $l(0 \rightarrow 2)$ transition (and $l(0 \rightarrow 0)$ non-transition) is weighted by the negligibly small coherent scattering length. This means that the IINS spectrum of pure H_2 will contain a large peak at 14.7 meV for the $l(0 \rightarrow 1)$ transition. Further, for scattering events in which the rotational level is unchanged (e.g., pure phonon excitation), scattering from p-H_2 is negligibly small compared to o-H_2 since they are weighted by b_{c}

and b_{inc} respectively. However, if the transition of p-H_2 consists of a one-phonon + one-rotational multi-excitation, then the scattering cross-section will still contain the large b_{inc} factor. Therefore, the strict selection rules for rotational transitions of molecular hydrogen can be useful in interpreting the features of the IINS spectrum.

Coupling between rotational level and nuclear spin states is absent in the HD molecule since the two nuclei are distinguishable. The rotational constant for HD is equal to $B_{\mathrm{rot}} = 5.54\,\mathrm{meV}$, which means that the $l(0 \rightarrow 1)$ transition is shifted down in energy by a factor of three-fourths compared to H_2. The D_2 molecule obeys Bose statistics in which the $l = 0, 2, 4, \ldots$ states correspond to *ortho*-deuterium and the $l = 1, 3, 5, \ldots$ states correspond to *para*-deuterium. The rotational constant for D_2 is $B_{\mathrm{rot}} = 3.70\,\mathrm{meV}$, meaning that the $l(0 \rightarrow 1)$ transition is shifted by a factor of one-half compared to H_2.

6.3 Experimental methods

Inelastic neutron scattering experiments on the $KC_{24}(H_2)_x$ system were performed using the FANS instrument at NCNR [80], an indirect geometry spectrometer described in Sec. 3.2.4. Sample synthesis, handling and setup were the same as described in Sec. 5.3. The mass of KC_{24} used for this experiment was 2.935 g. A cylindrical aluminum sample can was used without an annular insert, resulting in a larger sample thickness and consequently a significant amount of multiple scattering. Due to the lack of Q-resolution on the FANS instrument, and the qualitative nature of the measurements, this was considered acceptable. The FANS instrument contains two types of focusing monochromators bracketed between two Söller collimators of 20 inch divergence. The PG(002) monochromator can measure energy transfers of 5 meV to 45 meV, while the Cu(220) monochromator can measure energy transfers of 35 meV to 100 meV. It is necessary to correct the spectra for a fast-background,

caused by neutrons reaching the detector with incident energies higher than the filter cut-off limit. This fast-background contribution is easily determined by placing a cadmium shield between the sample can and the detector bank and measuring the neutron counts. Furthermore, the PG(002) monochromator suffers from some $\lambda/2$ contamination (due to higher order Bragg reflections), which can create spurious peaks at energies of $E/4$ if there is strong scattering from the sample at high energies. These features are sharper than the resolution, and can easily be identified.

To simplify interpretation of the FANS spectra, p-H_2 was used instead of normal H_2. The p-H_2 was prepared from normal H_2 by holding liquid hydrogen in a sample cell with a paramagnetic catalyst at about 10 K for at least 72 h prior to the experiment. To dispense the prepared p-H_2, the temperature of the holding cell was slowly increased until a specific vapor pressure was reached. In this manner, small aliquots of p-H_2 were introduced to the KC_{24} sample until the desired loading was reached. Background measurements on bare KC_{24} were first performed, followed by measurements on several $KC_{24}(pH_2)_x$ compositions. Data were also collected on $KC_{24}(HD)_{0.5}$ and $KC_{24}(D_2)_{0.5}$ compositions. Hydrogen was loaded at 60 K, and the sample was allowed to equilibrate for at least 20 min before lowering to base temperature. All spectra were collected at 4 K. To isolate scattering from the adsorbed H_2, background scattering from bare KC_{24} was subtracted and the fast background was also subtracted.

Low energy-transfer measurements were performed on the DCS spectrometer. The setup was identical to that described in Sec. 5.3 in reference to the quasielastic measurements, with the exception of the incident neutron wavelength. For the current inelastic measurements, the DCS spectrometer was operated in low resolution mode with an incident neutron wavelength of 4.8 Å, a chopper speed ratio setting of 2/3, and a minimum sample-detector time

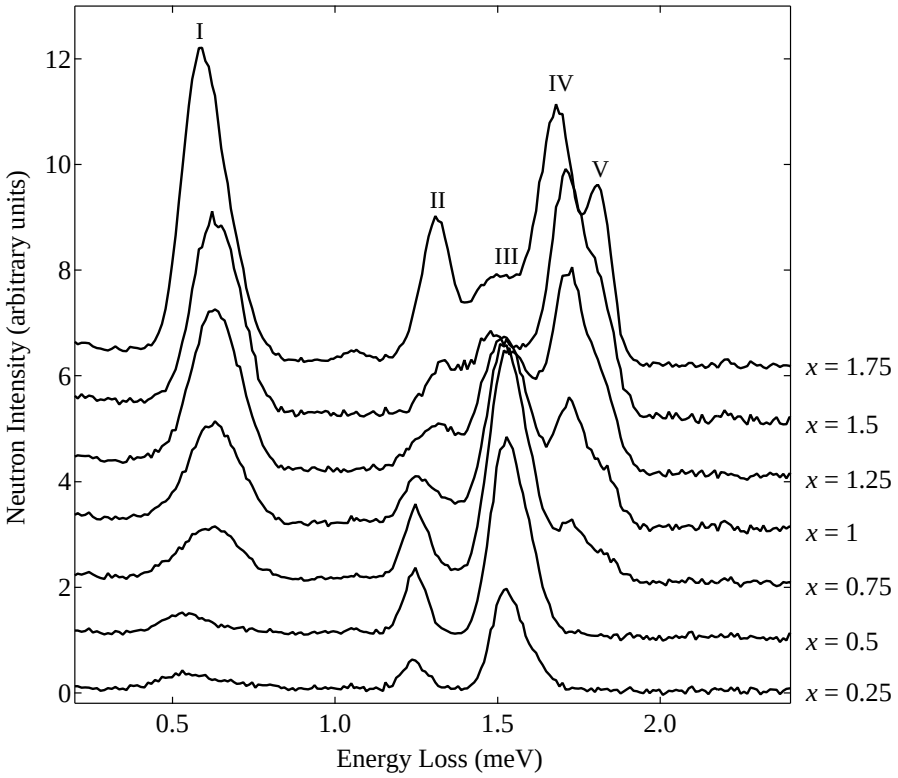

Figure 6.3: Low-energy IINS spectra of $KC_{24}(H_2)_x$ as a function of increasing H_2 concentration. Scattering from bare KC_{24} has been subtracted. Spectra are vertically offset for clarity.

of 1500. These settings give a resolution of about 120 μeV at the elastic line and a resolution of about 90 μeV at an energy transfer of 1 meV. The maximum energy loss that can be measured is roughly 2.79 meV. The momentum-transfer range is about $0.1\,\text{Å}^{-1}$ to $2.5\,\text{Å}^{-1}$ at the elastic line, and roughly $0.7\,\text{Å}^{-1}$ to $1.8\,\text{Å}^{-1}$ at the maximum energy transfer. The IINS spectra were reduced from the $S(Q,\omega)$ by summing over the complete momentum-transfer range and grouping the counts into energy bins of 0.01 meV width. For diffraction patterns, the $S(Q,\omega)$ was summed over the nearly-elastic interval -0.1 meV to 0.1 meV and binned into $0.008\,\text{Å}^{-1}$ increments. Once again, scattering from H_2 was isolated by subtracting the scattering from bare KC_{24}. Normal H_2 was used for all measurements on DCS.

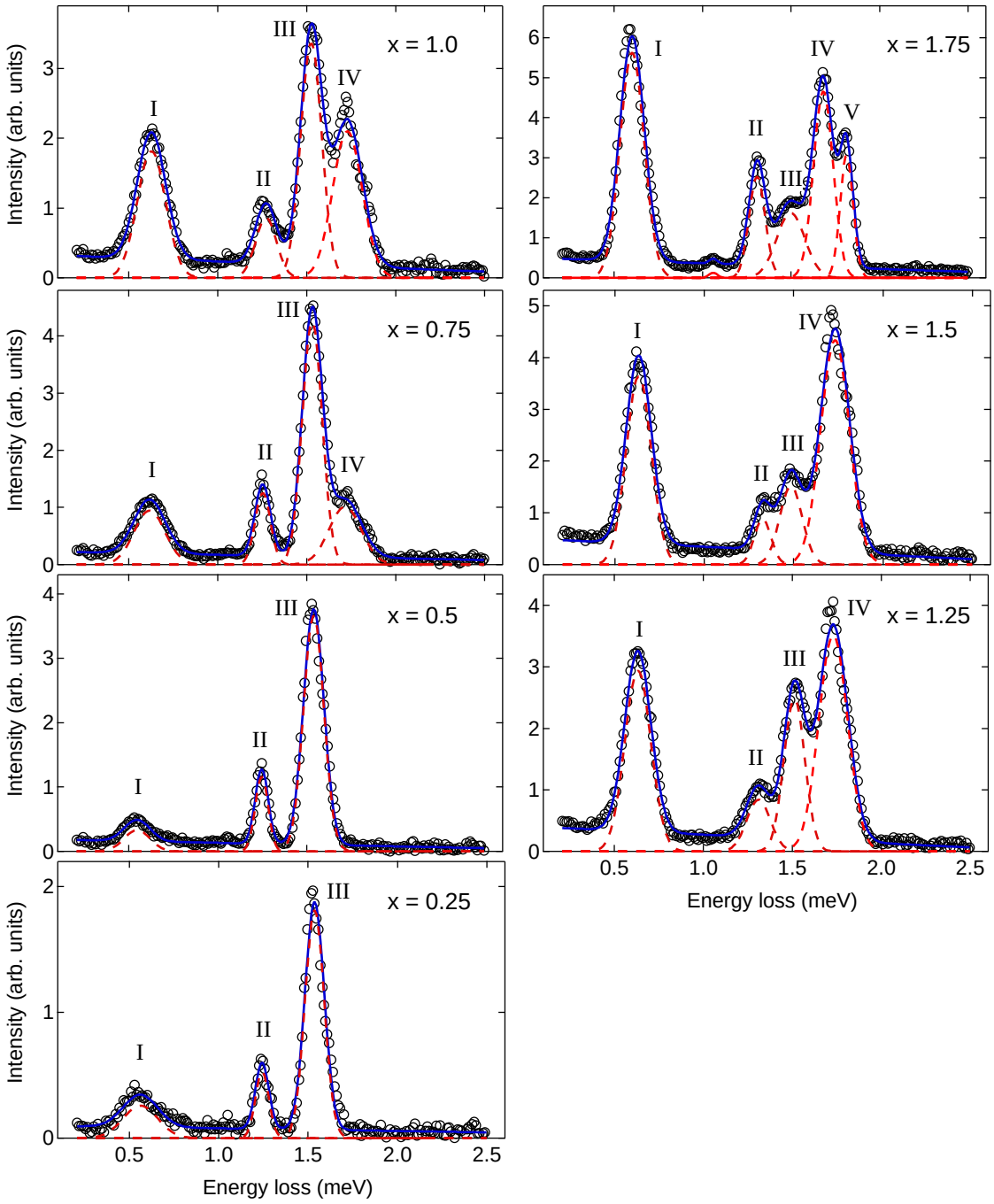

Figure 6.4: Decomposition of the low-energy-transfer IINS spectra of $KC_{24}(H_2)_x$ into a sum of Gaussian curves (plus a flat background which is not pictured).

Table 6.1: Summary of peak positions and peak areas of the low-energy IINS spectra

	Peak I		Peak II		Peak III		Peak IV		Peak V	
x^a	Center (meV)	Area (a.u.)	Center (meV)	Area (a.u.)	Center (meV)	Area (a.u.)	Center (meV)	Area (a.u.)	Center (meV)	Area (a.u.)
0.25	0.56	0.06	1.24	0.05	1.54	0.24				
0.50	0.55	0.06	1.25	0.11	1.54	0.53				
0.75	0.62	0.21	1.25	0.14	1.53	0.59	1.72	0.23		
1.00	0.63	0.36	1.27	0.13	1.53	0.50	1.73	0.43		
1.25	0.63	0.54	1.31	0.14	1.51	0.37	1.73	0.72		
1.50	0.63	0.64	1.33	0.10	1.49	0.24	1.73	0.87		
1.75	0.60	0.96	1.31	0.29	1.50	0.32	1.68	0.64	1.81	0.28

[a] Denotes the H_2 composition of a $KC_{24}(H_2)_x$ sample
[b] Errors not listed for the fit parameters

6.4 Results

6.4.1 Low-energy IINS spectra

Low-energy-transfer IINS spectra of $KC_{24}(H_2)_x$ collected on DCS are shown in Fig. 6.3. Background scattering from bare KC_{24} has been subtracted. The spectra contain at least five distinct peaks whose intensities vary with H_2 concentration. To determine peak locations and areas, the spectra were decomposed into a sum of Gaussian curves plus a flat background. The results of these fits are shown in Fig. 6.4. Even at the lowest hydrogen concentration, there are three distinct peaks. Peaks I and II appear to shift gradually to higher energy as the hydrogen concentration is increased. Due to the finite instrument resolution, though, it is not really possible to distinguish the fine structures of peaks containing features narrower than 90 μeV. Interestingly, there is a fairly strong transfer of intensity from peak III to peak IV as the H_2 loading is increased. At the highest hydrogen loadings, peak IV appears to split into peak IV and peak V. The presence of distinct low-energy peaks in the IINS spectrum are likely an indicator of distinct adsorption sites for H_2 in KC_{24} as described in greater detail in the discussion section. Changes in the fine structure of peaks may be caused by increasing interactions between the H_2 molecules as the concen-

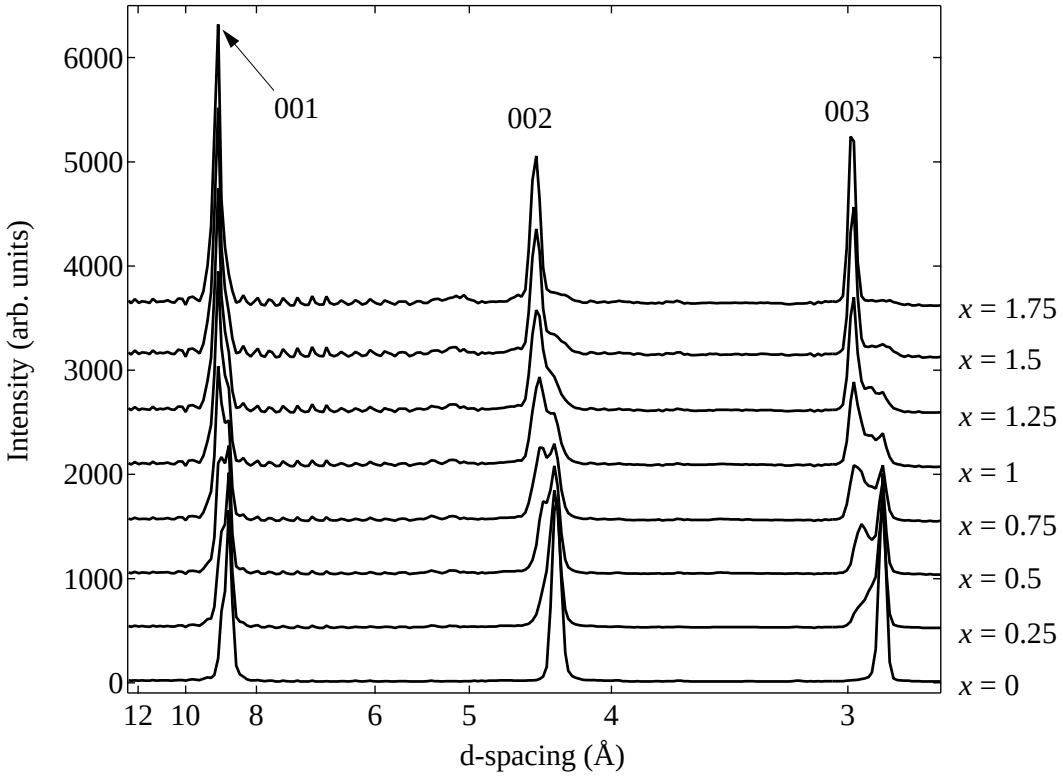

Figure 6.5: Diffraction pattern of $KC_{24}(H_2)_x$ measured on DCS at 4 K.

tration increases. However, the collapse of peak III, and associated growth of peak IV, may indicate a reconstruction of the in-plane KC_{24} lattice. Similar behavior has been noted for the $CsC_{24}(H_2)_x$ system [112]. Peak positions and areas for the low-energy IINS spectra are summarized in Table 6.1.

6.4.2 Diffraction pattern from low-energy IINS spectra

The DCS instrument contains an angular array of detectors from which diffraction information can be obtained by the time-of-flight method. It should be emphasized that DCS is *not* optimized as a diffractometer, and that the resolution in Q is quite coarse. Nevertheless, a qualitative diffraction pattern can be extracted from the measured $S(Q,\omega)$ by plotting the integrated intensity under the elastic peak as a function of momentum-transfer. The

diffraction pattern obtained from the low-energy IINS measured on DCS is illustrated in Fig. 6.5. For the $x = 0$ filling, the (001), (002), and (003) reflections have a d-spacing of 8.73 Å, 4.33 Å, and 2.90 Å, respectively. This translates to an average KC_{24} interlayer spacing of 5.34 Å. As H_2 is introduced to the sample, there is a gradual transfer of intensity to the second set of peaks with a slightly larger d-spacing. The fully hydrogenated sample has an interlayer spacing of 5.63 Å. In other words, the adsorption of H_2 causes the KC_{24} layers to expand by about 5%. These results are fully consistent with data reported in Ref. [64]. Given the low Q-resolution of the instrument, a quantitative analysis of diffraction data is not appropriate. Nevertheless, the diffraction data verifies three things. First, the KC_{24} sample is not contaminated by stage-1 or stage-3 compounds. Second, hydrogen is being adsorbed between the layers of KC_{24} resulting in an expansion of the interlayer spacing. Finally, the fact that there is a transfer of intensity between two distinct, co-existent peaks, rather than the shift of a single peak, implies that $KC_{24}(H_2)_x$ contains co-existent regions of the hydrogenated and pure KC_{24} phase.

6.4.3 Intermediate and high-energy IINS spectra

Intermediate-energy IINS spectra of $KC_{24}(pH_2)_x$ were measured as a function of hydrogen filling on the FANS instrument using the PG(002) monochromator. They are displayed in Fig. 6.6. As explained in the methods section, *para*-hydrogen was used instead of normal hydrogen to simplify the interpretation of spectral peaks. To determine peak positions and areas, the intermediate-energy spectra were fitted to a sum of Gaussian curves plus a flat background, and the fits are indicated in the figure. At the two lowest hydrogen fillings of $x = 0.2$ and $x = 0.5$, the spectra appear similar, except for the overall increase in intensity with hydrogen concentration. Peak I (11.9 meV) and Peak II (29.2 eV) are the dominant

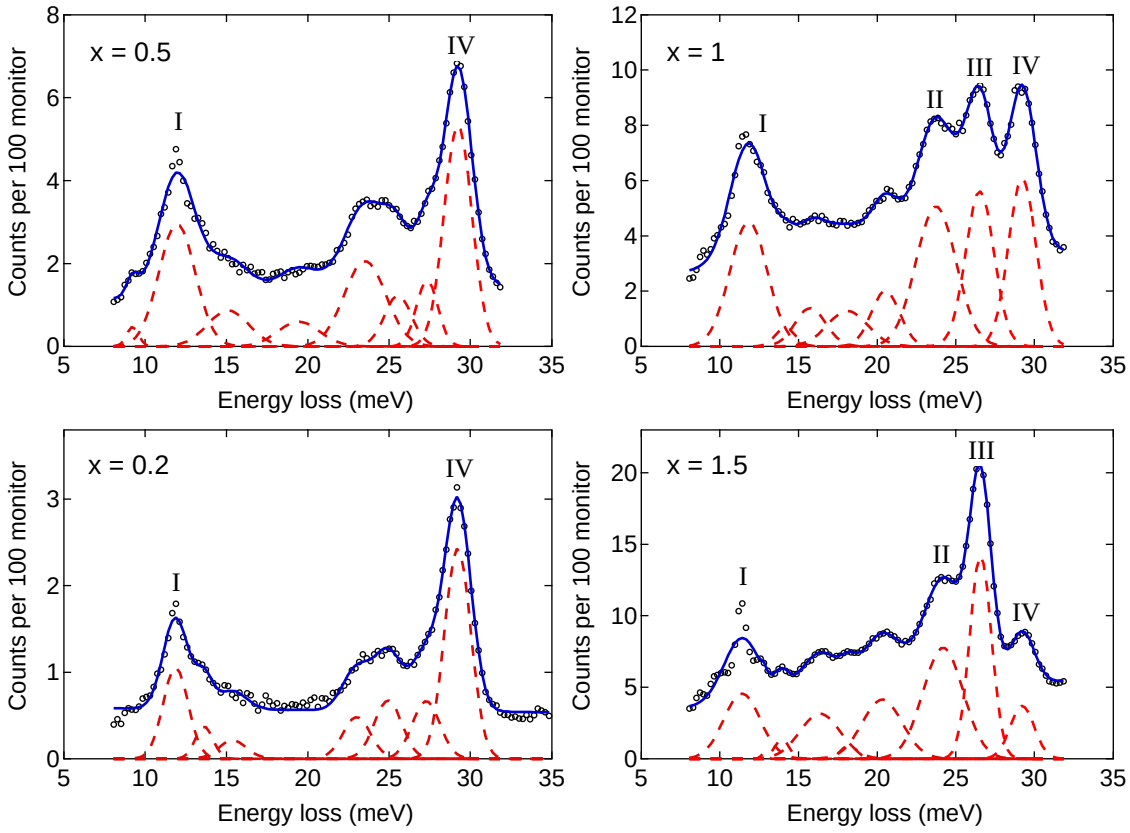

Figure 6.6: Intermediate-energy IINS spectra of $KC_{24}(pH_2)_x$ as a function of hydrogen filling. Solid blue lines represent fits to a sum of Gaussian curves plus a flat background. Individual Gaussian curves are plotted as dashed red lines. Flat background is not shown. Data points below 8 meV and above 32 meV were removed prior to the nonlinear regression fit.

features. Nascent peaks at 23 meV and 25 meV are somewhat difficult to distinguish from the large background intensity. As hydrogen filling is increased to $x = 1$, two new peaks emerge at 23.7 meV (Peak II) and 26.5 meV (Peak III). As hydrogen composition is further increased to $x = 1.5$, there is a strong increase in Peak III, but little increase in the other peaks. The sharp feature that appears at Peak I at the $x = 1.5$ filling may be an instrument artifact from $\lambda/2$ contamination of the incident beam, due to the large transition ca. 50 meV. In all of the intermediate-energy spectra, there is a large background intensity which may be due to the overlap of closely-spaced peaks. With the modest energy resolution of FANS (i.e., 1.2 meV), however, individual peaks are often difficult to distinguish. Peak positions and areas for the intermediate-energy IINS are summarized in Table 6.2.

High-energy IINS spectra of $KC_{24}(pH_2)_x$ are plotted in Fig 6.7 as a function of hydrogen filling. Spectra were only measured for $x = 0.5$ and $x = 1.0$. The dominant feature in both spectra is Peak VII, which has a greater intensity than any other peak. It should be noted that the curves in Fig 6.7 are not artificially offset. The vertical offset is due to the large background intensity, which may indicate a large amount of H_2 recoil associated with the scattering. At the higher $x = 1.0$ filling, upon closer examination, Peak VII appears to have a fine structure comprising two sub-peaks. The increase in intensity of the lower-energy sub-peak is what causes the apparent shift of the total peak from 50.9 meV at $x = 0.5$ to 49.4 meV at $x = 1$. Peak positions and areas for the high-energy IINS spectra are listed in Table 6.2.

6.4.4 IINS spectra of HD and D_2 adsorbed in KC_{24}

The richly-structured IINS spectra of $KC_{24}(pH_2)_x$ contain numerous overlapping peaks, making it difficult to accurately identify and interpret the origins of the spectral features. One method of obtaining more information from the inelastic spectra is to substitute the

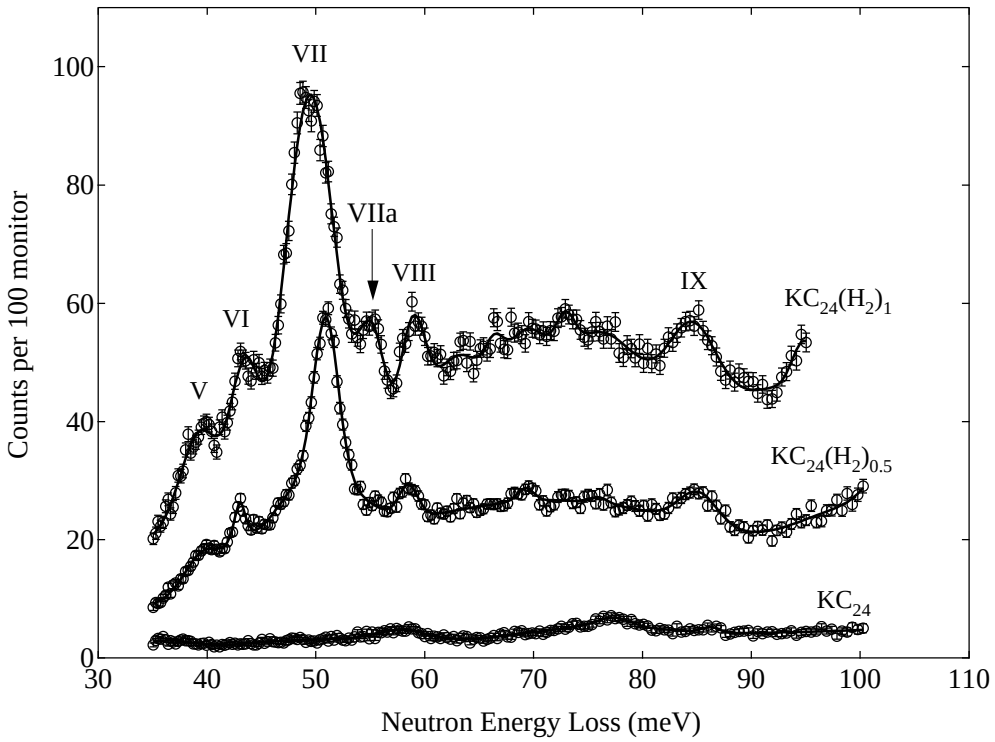

Figure 6.7: High-energy IINS spectra of $KC_{24}(pH_2)_x$ measured with the Cu(022) monochromator. Solid lines represent fits to a sum of Gaussian curves plus flat background. Individual curves are *not* manually offset.

Table 6.2: Summary of peak positions and peak areas of the intermediate and high-energy IINS spectra

	$x = 0.2$		$x = 0.5$		$x = 1.0$		$x = 1.5$	
Peak	Center (meV)	Area (a.u.)	Center (meV)	Area (a.u.)	Center (meV)	Area (a.u.)	Center (meV)	Area (a.u.)
I	11.9	2.02	11.8	5.84	11.8	13.4	11.4	13.2
II					23.7	16.2	24.2	24.8
III					26.5	12.7	26.6	24.6
IV	29.2	4.94	29.3	8.71	29.2	13.3	29.2	7.10
V			39.4	2.83	39.4	71.6		
VI			43.0	21.1	43.5	71.3		
VII			50.9	93.8	49.4	360.		
VIII			58.5	7.76	59.1	33.2		
IX			85.2	27.2	84.7	37.9		

[a] Peak parameters were obtained from fitting the spectra to a sum of Gaussian curves plus a flat background.

[b] Peaks I–IV are from the PG(002) spectra (see Fig. 6.6), while peaks V–IX are from the Cu(220) spectra (see Fig. 6.7). The integrated areas from the two different spectra are not directly comparable.

H_2 adsorbate with a hydrogen isotope containing a different mass, specifically HD and D_2. Shifts in peak positions as a function of mass can sometimes reveal the rotational or vibrational origin of a spectral peak. For a pure rotational transition of a free diatomic molecule, energy is proportional to the inverse of the reduced mass (see Eq. 6.2). Relative to H_2, the rotational transitions of HD will be reduced by a factor of 0.75, and for D_2 they will be reduced by a factor of 0.5. For a whole-molecule vibrational mode (i.e., governed by a power-law potential $V(x) = Ax^2$), the energy levels scale with mass as $m^{-1/2}$. Relative to H_2, the vibrational transitions of HD will be reduced by a factor of $\sqrt{2/3} \approx 0.82$, and for D_2 the transitions will be reduced by a factor of $\sqrt{1/2} \approx 0.71$.

IINS spectra were collected for HD and D_2 samples.[1] These spectra are compared with the p-H_2 spectra in the three panels of Fig. 6.8. Ratios between the peak positions for the three isotopes are summarized in Table 6.3. Unfortunately, it is difficult to identify the peaks for each isotope which correspond to the same transition. This is especially true for HD, which contains a complex spectrum due to the absence of symmetry restrictions on the rotational and nuclear spin states. Figure 6.8 contains my best guess for the peaks which correspond to equivalent transitions. Peaks are labeled with either an "a", "b" or "c" depending on whether the isotope is H_2, HD, or D_2, respectively.

The only peak ratio which can be easily categorized is Peak I, which seems to follow the $m^{-1/2}$ scaling expected for a pure vibrational transition. However, the cross-section of p-H_2 for a pure vibrational transition (with no change in the rotational level) is proportional to σ_c and is very small (see Sec. 6.2.4). Peaks originating from pure phonon excitations should not be visible in the spectrum of $KC_{24}(pH_2)_{0.5}$. Since the cross-section for a one-phonon

[1] Due to the smaller scattering cross-section of deuterium, it was necessary to collect data for a considerably longer time period. Even with longer collection times, the error bars on the D_2 spectra are much larger than those of the other samples.

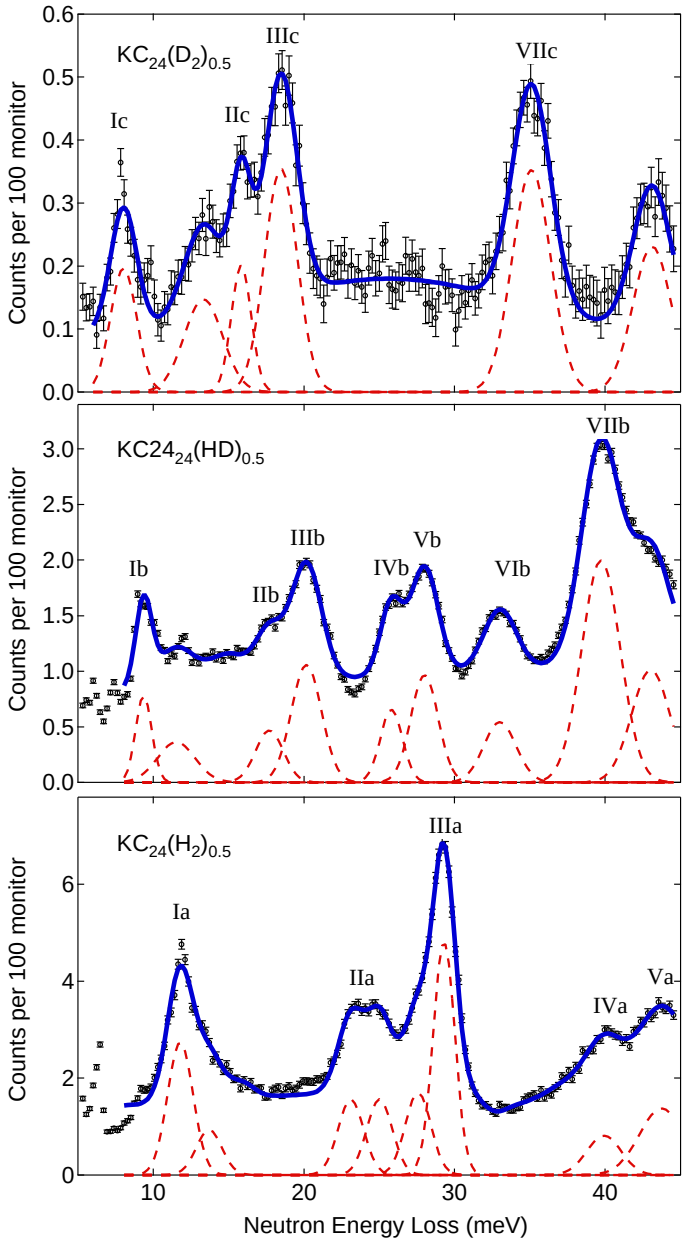

Figure 6.8: Intermediate-energy IINS spectra of D_2, HD, and p-H_2 adsorbed in KC_{24}. Solid lines represent fits to a sum of Gaussian curves plus a flat background. The Gaussian curves are shown as dashed, red lines. Fit components not corresponding to a clear, discrete peak are not illustrated. Peaks thought to correspond to the same transition are labeled with the same Roman numeral, with an "a", "b" or "c" to identify the isotope.

Table 6.3: Peaks positions in the intermediate IINS spectra for different hydrogen isotopes

Peak	H_2 Position[a]	HD Position	HD/H_2 Ratio	D_2 Position	D_2/H_2 Ratio
I	11.9	9.36	0.79	8.02	0.68
II	24.1	18.1	0.75	15.9	0.66
III	29.3	20.2	0.69	18.5	0.63
IV	39.9	25.8	0.65		
V	43.8	28.0	0.64		
VI		33.0			
VII		43.0		35.1	

[a] H_2 peak positions were obtained from the p-H_2 spectra.
[b] Peak positions are reported in units of meV.
[c] Composition was $x = 0.5$ for all isotopes.

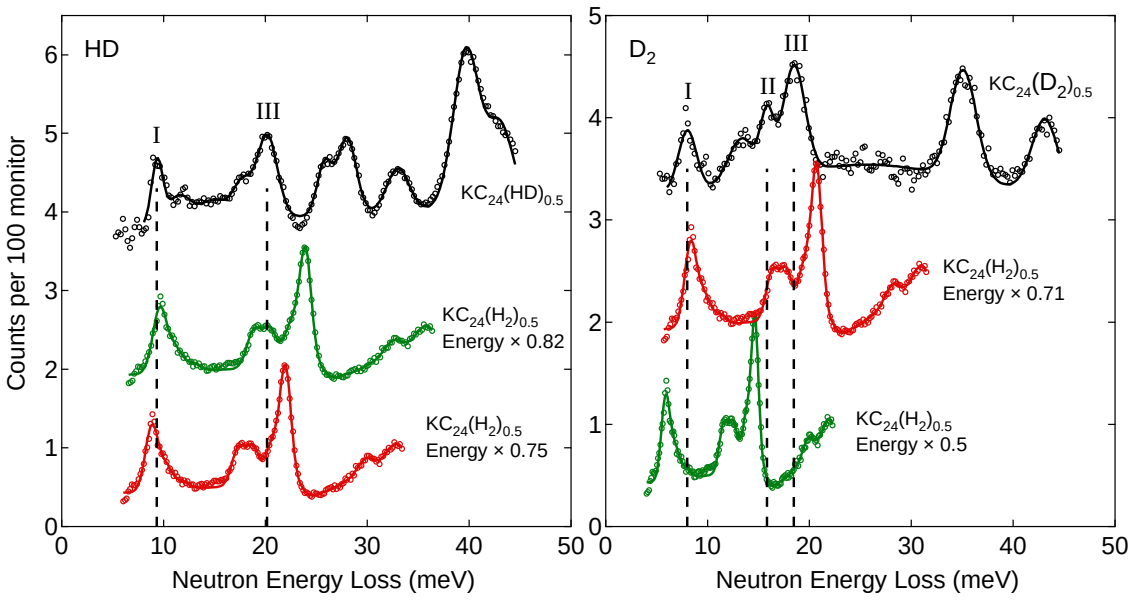

Figure 6.9: Comparison of the IINS spectra of the p-H_2, HD, and D_2 loaded samples. The p-H_2 spectra have been rescaled along the energy axis with the μ^{-1} factor ($\times 0.75$ for HD and $\times 0.5$ for D_2) of a pure rotational transition and the $m^{-1/2}$ factor ($\times 0.82$ for HD and $\times 0.71$ for D_2) of a pure phonon transition.

+ one-rotational multi-excitation in p-H_2 contains the large incoherent scattering length, many of the spectra features may therefore be due to multi-excitation transitions.

Isotopic shifts in the IINS spectra are directly compared in Fig. 6.9. The p-H_2 spectra are rescaled on the energy axis with the μ^{-1} factor of a pure rotational transition and the $m^{-1/2}$ factor of a pure phonon transition. In this manner, peak positions for the isotopes can be directly compared to determine whether there are any good matches. Once again it is evident that none of the peaks (except for Peak I) follow the simple scaling relations expected for a pure phonon or rotational transition.

6.5 Hydrogen bound states studied by DFT

6.5.1 Computational details

To estimate the energy levels of H_2 bound states in KC_{24}, first-principles calculations were performed using density function theory (DFT), as implemented in the Vienna *Ab intio* Simulation Package [113]. A plane-wave basis set was used with a projector-augmented-wave potential and a Perdew-Burke-Ernzerhof exchange-correlation functional in the generalized gradient approximation (GGA) [114]. Although GGA does not treat the correlations between electron fluctuations which give rise to van der Waals interactions, it can still be used to calculate the electrostatic and orbital interactions. In general, GGA is known to underbind H_2 in physisorption systems with significant van der Waals contributions.

The theoretical $\left(\sqrt{7} \times \sqrt{7}\right) R\,19.11^\circ$ structure with chemical formula KC_{28} was used for the in-plane potassium structure. A stacking sequence for the potassium layers was generated by translating each layer 1.41 Å (i.e., equal to the C−C bond length) in the direction of the x-axis.[2] This sequence of potassium layers repeats after 21 layers. The graphite stacking

[2] See the top panel of Fig. 6.13 for the orientation of the x and y axes.

sequence follows the standard A|AB|BC|CA pattern (see Fig. 2.2a). Three-dimensional periodic boundaries are applied to the unit cell. The c-axis interlayer spacing of the $KC_{28}(H_2)_1$ compound was optimized at 5.4 Å, but all other geometrical parameters were fixed at their theoretical values. To sample the Brillouin zone, a Gamma-centered k-point grid was generated. Based on convergence tests, it was found that a plane-wave basis set energy cutoff of 500 eV and a $8 \times 8 \times 6$ k-point grid was necessary to obtain an accuracy of 1 meV atom^{-1}. Due to limited computational resources, however, a plane-wave cutoff of 300 meV was used in conjunction with a $4 \times 4 \times 3$ k-point grid. Lattice parameters and atom positions were held fixed at their theoretical values for the $\left(\sqrt{7} \times \sqrt{7}\right)$ $R\,19.11°$ structure. These calculations must therefore be considered as qualitative rather than quantitative. The potential energy surface can still provide useful insights into bound states of the H_2 molecule.

6.5.2 Results

Total ground state energies were calculated as a function of H_2 center-of-mass position and molecular orientation. First, the potential energy surface of the $KC_{28}(H_2)_1$ system was sampled over a grid of 58 positions within the unit cell, with the H_2 molecule oriented perpendicular to the basal plane, and vertically centered in the gallery. The results are illustrated in Fig. 6.10. The contribution of both the graphite corrugation potential and the K–H_2 interaction are evident from the results. Because the H_2 molecule was oriented vertically, the repulsive interactions between the hydrogens and the carbons are substantial. The local minima are located near the hexagon centers.

The general goal of these first-principles calculations is to determine the energy levels of bound center-of-mass H_2 vibrational modes (i.e., phonons). Thus, a complete calculation would involve the construction and diagonalization of the classical, three-dimensional

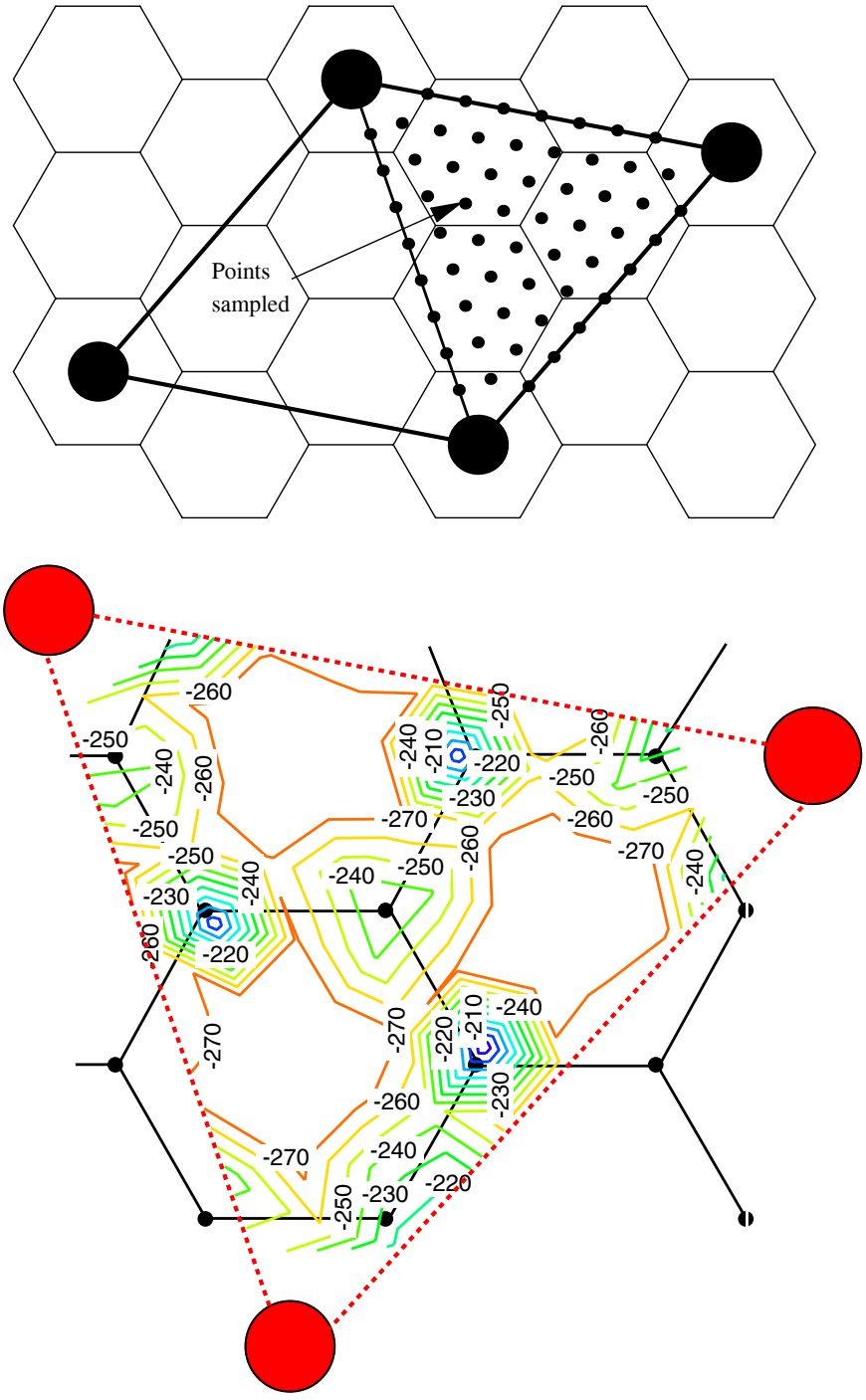

Figure 6.10: Top: Grid of 58 H_2 center-of-mass positions within the KC_{28} unit cell for which the total ground state energy was calculated. Bottom: Potential energy surface constructed from the grid of calculated ground state total energies. The H_2 molecule was oriented perpendicular to the graphite basal plane.

force-constant matrix for the H_2 center-of-mass at the minimum in the PE surface. This calculation is quite computationally expensive for the large $KC_{28}(H_1)_1$ unit cell. An approximation of the phonon energy levels can be calculated from 1D slices through the center-of-mass PE surface.

As shown in Fig. 6.11, one-dimensional slices through the PE surface were calculated along the in-plane paths labeled "scan-1" and "scan-2." Energies were also calculated along the z-axis (out-of-plane) through the point labeled $E_{\min}$ in Fig. 6.11, but are not illustrated. The H_2 molecule was oriented perpendicular to the basal plane for all calculations. The energy minimum for all three scans occurs at point $E_{\min}$, which has a K–H_2 distance of about 2.7 Å. Neglecting all other degrees of freedom, the 1D Schrödinger equations were solved for the three calculated potential energy wells using the Fourier grid Hamiltonian method [115]. The quantum energy levels are displayed in Fig. 6.11 as dashed lines. For scan 1, the fundamental $n(0 \rightarrow 1)$ transition occurs at 8 meV, with an overtone at 26 meV. For scan-2, the fundamental transition is at 12 meV, with an overtone at 25 meV. For out-of-plane translations, the fundamental transition occurs at 77 meV, well above the spectral peaks under consideration.

The total energy of the H_2 molecule was calculated along scan-1 for three different orientations. Results are shown in Fig. 6.12. The 'tee" and "aligned" orientations are both in-plane, while the "vertical" orientation is out-of-plane. Based on these results, it can be seen that the energy minimum is strongly coupled to the molecular orientation. Having the H_2 molecule aligned towards the potassium increases a repulsive interaction at short separations. This implies that there is a significant amount of rotational-translational coupling in the KC_{24}-H_2 system.

The rotational potential was calculated over an 18×24 grid of H_2 orientations (θ, ϕ).

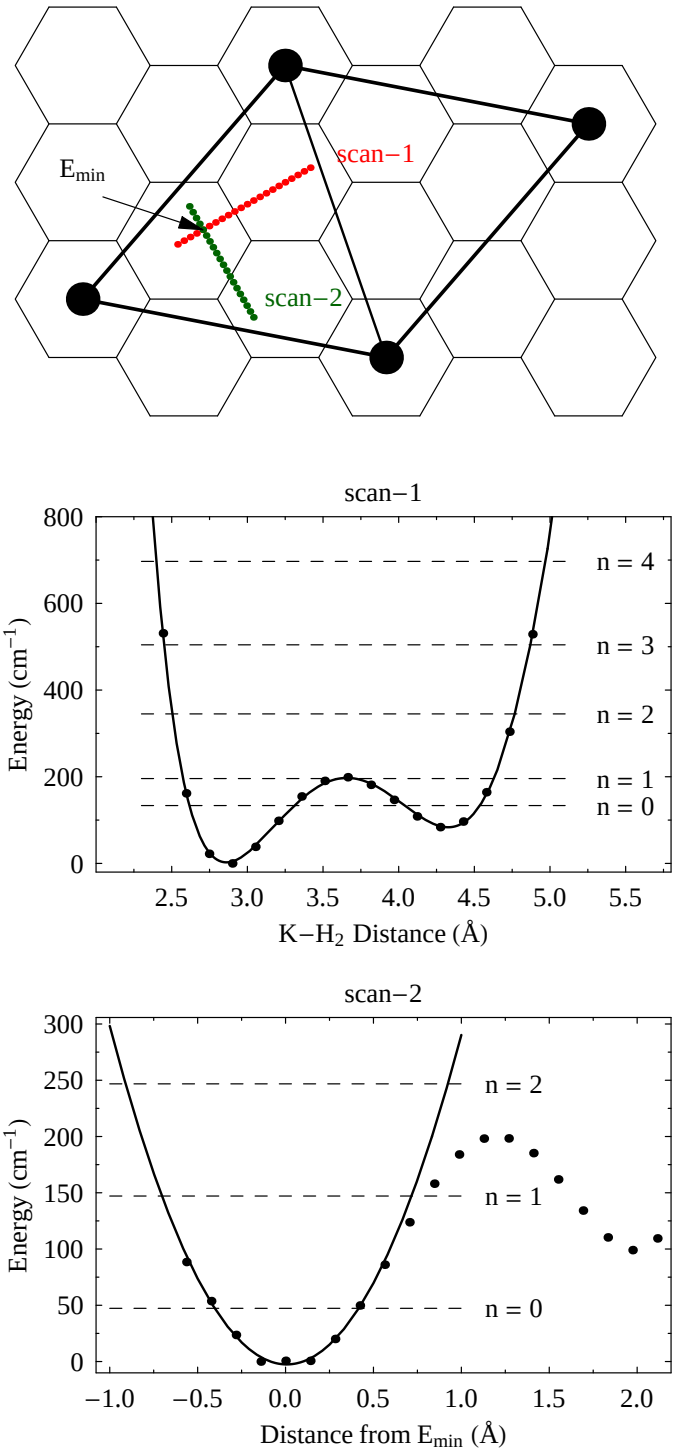

Figure 6.11: Top: One-dimensional slices through the potential energy surface. The H_2 molecule was oriented perpendicular to the basal plane for both scans. Middle: Potential energy well for scan-1. Bottom: Potential energy well for scan-2. Quantum energy levels are plotted as dashed lines. Note that energies are reported in units of cm^{-1}.

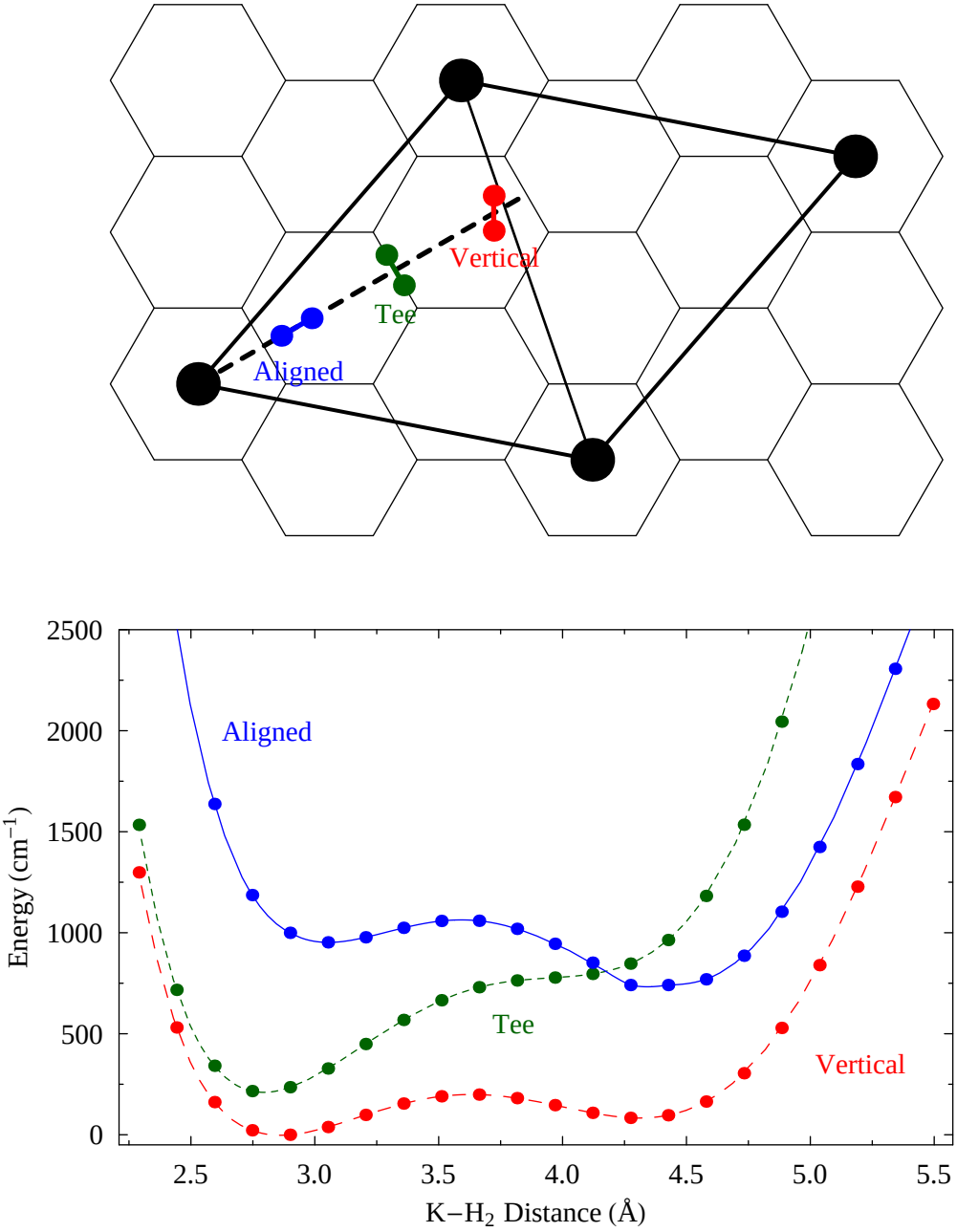

Figure 6.12: Top: Three different orientations of the H_2 molecule as it is moved along the K−H_2 axis indicated by the dashed line. The *tee* and *aligned* orientations are both parallel to the basal plane (in-plane), while the *vertical* orientation is perpendicular to the basal plane (out-of-plane). Bottom: Total energy of the H_2 molecule as a function of K−H_2 distance for the three orientations of the molecule. Note that energy is reported in units of cm^{-1}.

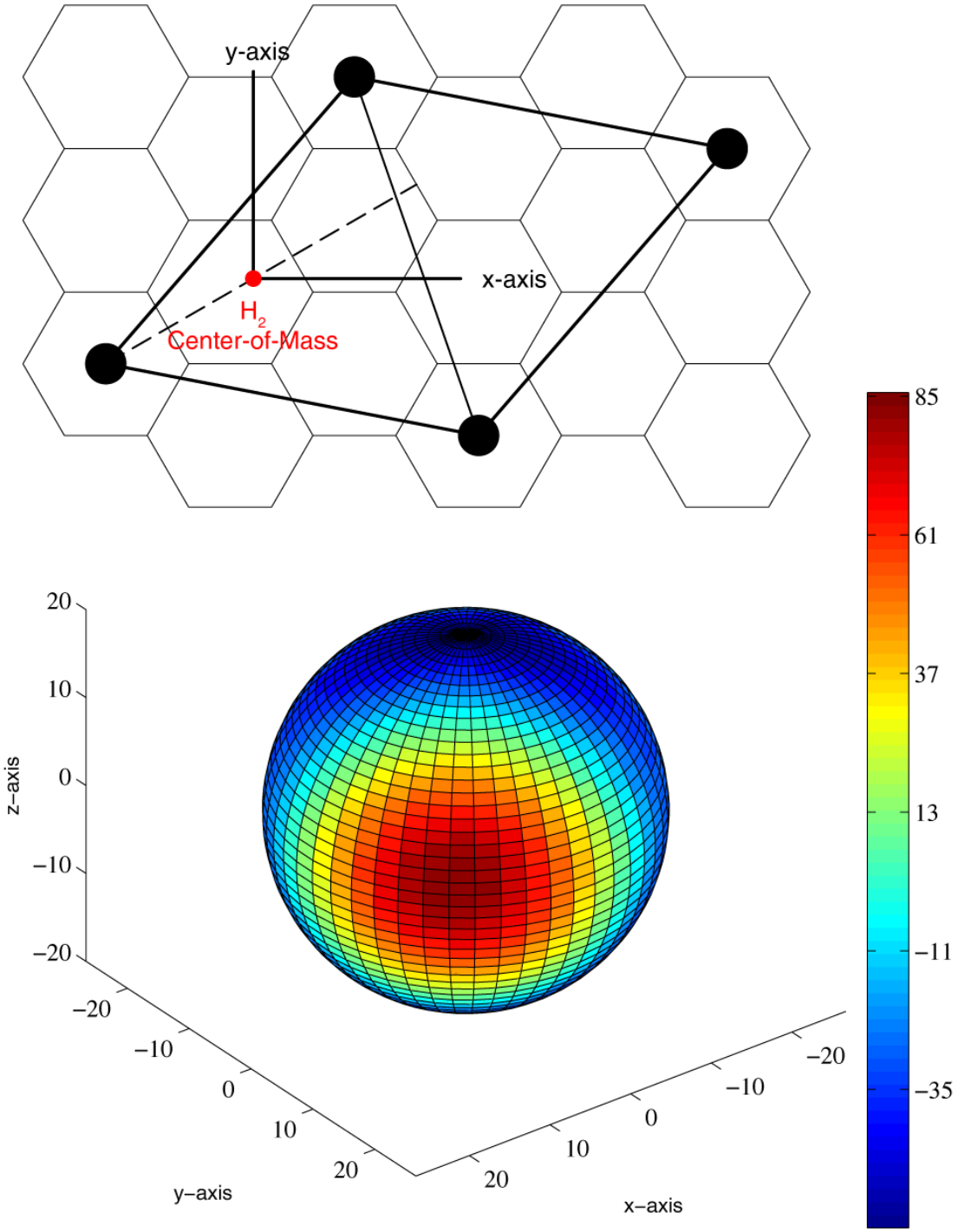

Figure 6.13: Top: Coordinate system which describes the H_2-orientation. The x and y axes are both in-plane, while the z axis is out-of-plane. The H_2 center-of-mass is fixed at the energy minimum. Bottom: Contour plot of the rotational potential mapped onto a sphere representing the H_2 orientation (ϕ, θ). This coordinate system is consistent with the one depicted in the top panel.

We define θ as the angle between the H_2 molecular axis and the z-axis, and ϕ as the angle between the x-axis and the projection of the H_2 molecular axis along the x-y-plane. For all calculations the H_2 center-of-mass was fixed at the minimum energy site roughly 2.7 Å from the potassium center and centered between the graphite planes. The calculated orientational potential is illustrated in the bottom panel of Fig. 6.13. The red color corresponds to the energy maximum while the blue color indicates the energy minimum. It is clear that the maximum energy occurs when the H_2 molecule is pointed directly at the potassium in an "aligned" formation. The minimum energy orientation occurs for either a "tee" or "vertical" formation, with the H_2 molecule facing the potassium side-on. The rotational potential is very well-described by a two-dimensional, anisotropic hindered rotor potential,

$$V(\theta,\phi) = \frac{a + b\sin(2\phi + c)}{2}(1 - \cos 2\theta), \tag{6.11}$$

where $a = 72.92\,\text{meV}$, $b = -47.65\,\text{meV}$ and $c = -158.6°$. The extra phase factor, c, does not affect the rotational energy levels of the system and is ignored in the remaining calculations. Hamiltonian matrix elements were calculated for a spherical harmonics basis set, $\{Y_0^0, Y_1^{-1}, Y_1^0, Y_1^1, \ldots, Y_6^6\}$. The resulting 49×49 matrix has the form,[3]

$$\hat{H} = \begin{pmatrix} E_0 + \langle Y_0^0|V|Y_0^0\rangle & \langle Y_0^0|V|Y_1^{-1}\rangle & \cdots & \langle Y_0^0|V|Y_6^6\rangle \\ \langle Y_1^{-1}|V|Y_0^0\rangle & E_1 + \langle Y_1^{-1}|V|Y_1^{-1}\rangle & \cdots & \langle Y_1^{-1}|V|Y_6^6\rangle \\ \vdots & \vdots & \ddots & \vdots \\ \langle Y_6^6|V|Y_0^0\rangle & \langle Y_6^6|V|Y_1^{-1}\rangle & \cdots & E_6 + \langle Y_6^6|V|Y_6^6\rangle \end{pmatrix} \tag{6.12}$$

[3]For slightly better numerical accuracy, a 64×64 matrix is recommended [116]. Due to the somewhat qualitative nature of the rotational potential, the current matrix size is probably sufficient for estimating the rotational energy levels.

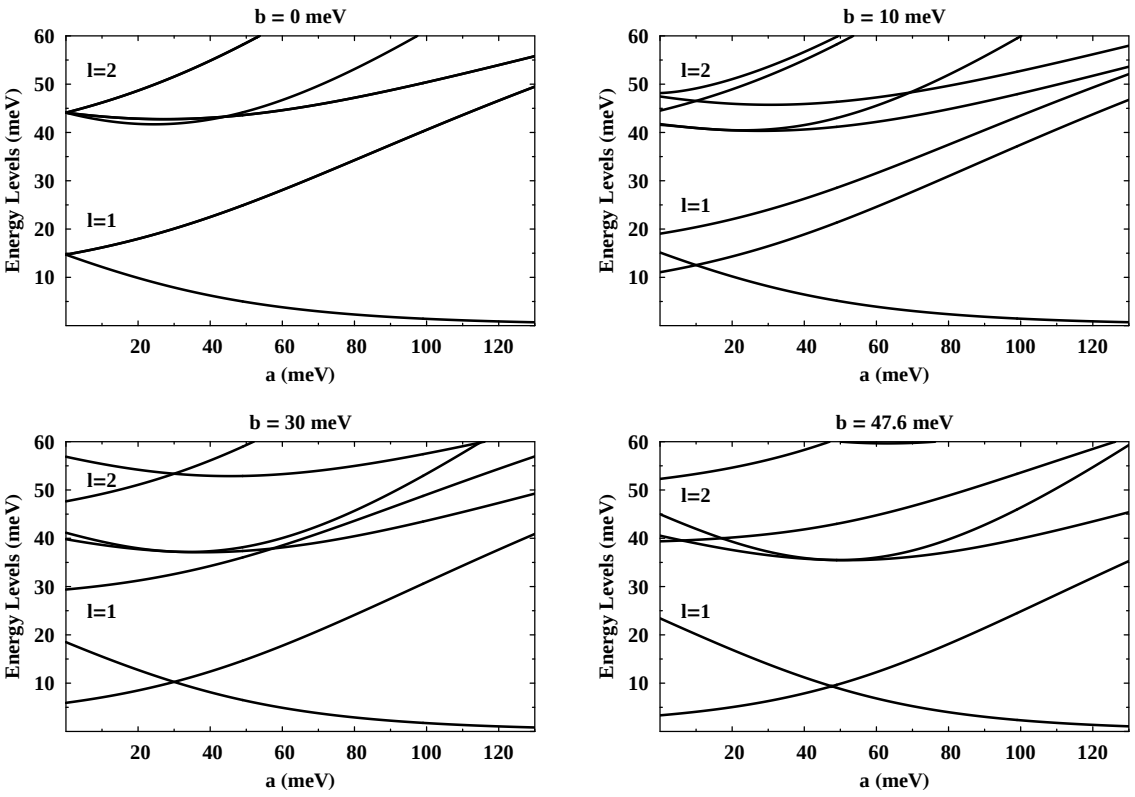

Figure 6.14: Energy levels for a two-dimensional, anisotropic hindered rotor model relative to the ground $l = 0$ state. Energies are plotted as a function of the θ-based rotational barrier, a, and evalulated for four different values of the ϕ-based azimuthal rotational barrier, b.

where $E_l = l\,(l+1)\,B_{\rm rot}$, and the inner products are equal to

$$\langle Y_{l'}^{m'}|V|Y_l^m\rangle = \int_0^{2\pi}\int_0^{\pi} Y_{l'}^{m'}(\theta,\phi)^* V(\theta,\phi) Y_l^m(\theta,\phi)\sin\theta d\theta d\phi. \tag{6.13}$$

Eigenenergies were determined from an exact diagonalization of the matrix. In Fig. 6.14 the calculated rotational energy levels for the $l = 1$ and $l = 2$ states, relative to the $l = 0$ state, are plotted as a function of a for two different values of b. For $b = 0$ we recover the familiar one-dimensional hindered rotor model, in which the $l, m(1, \pm 1)$ energy levels are degenerate. For non-zero values of b this degeneracy is lifted. Transition energies for the calculated orientational potential ($a = 72.92\,$meV, $b = -47.65\,$meV) occur at $4.9\,$meV,

15.9 meV, 36.4 meV, 38.0 meV and 47.3 meV, consistent with the values reported in Ref. [64]. Unfortunately, these values are clearly inconsistent with the experimental peak positions. Therefore, introducing a large ϕ-dependence into the orientation potential does not appear to be realistic. As described in the next section, a simple one-dimensional hindered rotor model, evaluated at three different barrier heights, does a much better job of describing the spectral peaks at both low energies and high energies. One possible explanation is that quantum delocalization of the H_2 center-of-mass over the three minimum-energy sites (see Fig. 6.10) results in an effective potential that does not have a ϕ-dependence [64].

6.6 Discussion

The IINS data of $KC_{24}(H_2)_x$ contains a complex progression of spectral peaks. Based on previous studies of RbC_{24} and CsC_{24} [51, 64, 65, 117, 118], it is known that the low energy peaks (ca. 1 meV) and the high energy peaks (ca. 50 meV) originate from the splitting of the $l(0 \rightarrow 1)$ rotational transition in the presence of a strong anisotropic field. The one-dimensional hindered rotor model provides a reasonable description of the peak positions, but requires the presence of multiple barrier heights. Referring to Fig. 6.1, it can be verified that a rotational barrier height of 139 meV corresponds to peak positions at 0.56 meV and 52 meV, which does match experimental peak positions in the $KC_{24}(H_2)_{0.5}$ spectrum. Barrier heights of 105 meV and 96 meV provide good matches to other peaks in the $KC_{24}(H_2)_{0.5}$ and $KC_{24}(H_2)_1$ spectra, as summarized in Table 6.4. These values also compare well with rotational barrier heights determined from first-principles calculations, which varied up to 121 meV for an H_2 molecule fixed at the energy minimum in the center-of-mass PE surface.

The need for multiple rotational barrier heights is consistent with the existence of dif-

Table 6.4: Transition energies predicted by the one-dimensional hindered rotor model compared to experimental peak positions for the $KC_{24}(H_2)_{0.5}$ and $KC_{24}(H_2)_1$ samples

(a) 1D-type Potential ($V_2 > 0$)

$KC_{24}(H_2)_{0.5}$			$KC_{24}(H_2)_1$		
Barrier Height (meV)	ΔE_1[a] (meV)	ΔE_2[b] (meV)	Barrier Height (meV)	ΔE_1 (meV)	ΔE_2 (meV)
139	0.56 (0.55)[c]	52.0 (50.9)	133	0.63 (0.63)	50.3 (49.4)
105	1.25 (1.25)	42.1 (43.0)	105	1.24 (1.27)	42.1 (43.5)
96	1.55 (1.54)	39.3 (39.4)	96	1.55 (1.53)	39.3 (39.4)
			91	1.75 (1.73)	37.7 (39.4)

(b) 2D-type Potential ($V_2 < 0$)

$KC_{24}(H_2)_{0.5}$			$KC_{24}(H_2)_1$		
Barrier Height (meV)	ΔE_1 (meV)	ΔE_2 (meV)	Barrier Height (meV)	ΔE_1 (meV)	ΔE_2 (meV)
-49	29.2 (29.3)	10.7 (11.8)	-29	23.1 (23.7)	11.8 (11.8)
			-49	29.2 (29.3)	10.7 (11.8)

[a] ΔE_1 refers to the $l, m(0, 0 \rightarrow 1, 0)$ transition.
[b] ΔE_2 refers to the $l, m(0, 0 \rightarrow 1, \pm 1)$ transition.
[c] Experimental peak positions are listed in parentheses.

ferent adsorption sites in KC_{24}. At the dilute $x = 0.25$ composition, the three distinct low-energy peaks originate from the dominant H_2-sorbent interaction, with little contribution from H_2-H_2 interactions. Each peak can be assigned to an adsorption site with a specific barrier to rotation. Simultaneous filling of these distinct sorption sites is indicated by the IINS data, as opposed to the preferential filling of the less-hindered sites.[4] In the $\left(\sqrt{7} \times \sqrt{7}\right) R\,19.11°$ structure used for the first-principles calculations, there is only one type of sorption site. As described in Sec. 2.3, though, the relaxed close-packed structure illustrated in Fig. 2.3b is the most compelling structure model for KC_{24}. For this structure there are a large number of sorption sites, each having a distinct crystal field symmetry. The filling of these sites would presumably produce multiple low-energy IINS peaks. However, many of these peaks may be experimentally indistinguishable due to the limited resolution

[4] Rotation barrier is not necessarily correlated to the adsorption enthalpy. It is not clear, therefore, whether the sites with a smaller rotational barrier would be energetically preferable.

of the spectrometer. The appearance of new peaks at large H_2 filling may indicate either the filling of energetically unfavorable sites, or the increasing contribution of H_2-H_2 interactions to the rotational potential.

Applying a simple hindered rotor model to a complex system has its limitations. For example, the model assumes a single, fixed adsorption site in an unchanging external crystal field, neglecting the effects of hydrogen-hydrogen interactions. The two-dimensional, anisotropic rotor model (with calculated rotational barriers) gives values that are clearly inconsistent with experiment. Furthermore, even the one-dimensional rotor model does not describe the intensities of observed peaks in a consistent manner. It pairs the weak 0.56 meV peak with the strong 52 meV peak, and pairs the strong 1.5 meV peak with the weak 39 meV peak. Moreover, it fails to explain the intermediate-energy spectral peaks between 10 meV and 30 meV. We can invoke a negative potential barrier of -29 meV which predicts transitions at 12 meV and 23 meV, in reasonable agreement with the observed data. From the first-principles calculations, however, there is no strong evidence for the existence of a negative rotational barrier in which the H_2 molecule tends to align parallel to the basal plane surface.

On the other hand, there is empirical evidence that the intermediate-energy peaks are somehow linked to the low-energy peaks. There is a strikingly similar pattern in the evolution of both the low-energy and intermediate-energy spectra as a function of H_2 filling. In the low-energy spectrum (see Fig. 6.4), Peak III begins to collapse at the $x = 1.5$ filling, while Peak IV increases sharply in intensity. In the intermediate-energy spectrum (see Fig. 6.6), Peak IV collapses at a concentration of $x = 1.5$ in conjunction with the rapid growth in Peak III. Based on this observation, a case can be made that the intermediate-energy peaks originate from multiple-excitations of both rotational and phonon modes. In

Sec. 6.5 the in-plane phonon transitions were estimated at around 8 meV (with an overtone at 26 meV), and at 12 meV (with an overtone at 25 meV). Therefore, a one-phonon + one-rotational excitation would be expected at $8 + 1 = 9$ meV or $12 + 1 = 13$ meV, close to the observed peak at 12 meV. Similarly, a two-phonon + one-rotational excitation would occur at $26 + 1 = 27$ meV, close to the experimental peak at 29 meV. Multiple phonon-rotation excitations therefore help to explain the complex spectral features observed in the intermediate-energy-loss range. They also explain why the mass-scaling rules for pure phonon or rotational transitions are not observed. It should be recalled, however, that the phonons were calculated for a fixed H_2 orientation. In fact, the center-of-mass PE surface depends strongly on the molecular orientation, implying a strong translational-rotational coupling. Solving the phonon-rotation spectrum in such a situation is a complex problem. The presence of strong translational-rotational coupling may explain why we still observe large discrepancies between model and experiment for the IINS spectrum of $KC_{24}(H_2)_x$.

6.7 Conclusion

A combination of IINS data and first-principles calculations have provided insights into the thermodynamics of H_2 adsorption in KC_{24}. Evidence for multiple adsorption sites is present in the low-energy IINS spectra, particularly at the dilute $x = 0.25$ composition which probes the H_2-sorbent interactions. At more concentrated hydrogen compositions, the increasing H_2-H_2 interactions are reflected in the development of a fine-structure in the original three low-energy peaks. The one-dimensional hindered rotor model provides a reasonable description of the low-energy and high-energy IINS peaks, though further refinement of the rotational potential is needed. Dramatic changes in the low-energy spectra perhaps reflect a reconstruction of the potassium monolayer in response to large H_2 concen-

trations. Intermediate-energy spectral features are explained by multi-excitations of both phonon and vibrational modes. First principles calculations indicate strong coupling of the rotational and vibrational degrees of freedom for the adsorbed H_2 molecules.

Chapter 7

Conclusions

7.1 Summary

The general subject of this work was the physisorption of hydrogen in modified carbon adsorbents. Physisorption involves the binding of an H_2 molecule to a surface without the formation of a chemical bond, making it a simple and easily reversible storage method (i.e., no complicated reaction pathways). This topic has particular relevance for the ongoing effort to develop systems which store hydrogen at high densities while operating at modest temperatures. It is estimated that an adsorption enthalpy of about $-18\,\mathrm{kJ\,mol^{-1}}$ is needed to optimize the usable capacity of a physisorption storage system at room temperature [7].

Graphite intercalation compounds of the heavy alkali metals are one of the few systems that come close to meeting this optimum adsorption enthalpy. Cesium intercalated graphite was measured in Sec. 4.3 to have an average adsorption enthalpy of $-14.9\,\mathrm{kJ\,mol^{-1}}$. The origin of this surprisingly large enthalpy is still not well understood, though it may originate from the highly polarizing environment created by electron transfer from the alkali metals to the empty graphite conduction bands. This unresolved question reflects a significant issue in the study of adsorption systems: the electrostatic and dispersion forces which dominate physisorption are notoriously difficult to treat in a first principles approach.

Strategies for increasing the hydrogen binding interaction in a modified carbon adsorbent include incorporating the following structural elements into the host structure: (1) optimally spaced graphene basal planes, held open in a pillared fashion by guest intercalate species; (2) curved graphene surfaces, such as those found in single-walled carbon nanotubes; (3) chemically modified carbon adsorbents, which interact with H_2 molecules by strong electrostatic forces. Graphite intercalation compounds, it turns out, contain both a pillared structure *and* chemical dopants. Separating the effects of these two distinct structural elements poses a separate challenge.

Pressure-composition-temperature diagrams of the $MC_{24}(H_2)_x$ system were measured for M = K, Rb, Cs. Temperatures were between 77 K and 150 K. Detailed adsorption enthalpies were measured as a function of H_2 concentration. The enthalpy for all three systems is remarkably flat as a function of hydrogen composition. This is attributed to a fairly homogeneous distribution of sorption sites in the graphite intercalates. The adsorption enthalpy is positively correlated with the interlayer spacing of the GIC. At large H_2 concentrations the adsorption kinetics becomes exceedingly sluggish, due in part to the effects of site-blocking and correlation on the microscopic H_2 self-diffusivity.

Hydrogen diffusivity in KC_{24} was studied in detail by quasielastic neutron scattering and empirical molecular dynamics calculations. The QENS spectra were fitted to a model for jump diffusion on a two-dimensional honeycomb net. It was found that the diffusion coefficients for H_2 are over an order of magnitude slower than those for H_2 diffusion in other carbon sorbents such as single-walled nanotubes, nanohorns, and carbon blacks. Instead, the diffusivity in KC_{24} is about the same magnitude as in zeolites with molecular-sized cavities. This means that H_2 diffusion in adsorbents is influenced very strongly by the pore geometry, and less by the chemical nature of the pore surface. Furthermore, the diffusion

process is very complex, with the presence of at least two distinct jump frequencies.

High-resolution inelastic neutron scattering spectra for $KC_{24}(H_2)_x$ were collected for the first time over the *entire* energy-loss range spanning 0 meV to 100 meV. Spectral peaks were interpreted in terms of single- and multi-excitation transitions of the H_2 phonon and rotational modes. Rotational energy levels were calculated from the one-dimensional hindered rotor model, while phonon energy levels were estimated from first-principles calculations. Evidence was found for the existence of multiple H_2 sorption sites in KC_{24}. Further refinements of the calculations of H_2 phonon and rotational energy levels are needed. Contributions from the large zero-point motions of the bound H_2 molecules also need to be integrated into the model.

7.2 Future work

7.2.1 Thermodynamic trends

For the MC_{24} compounds, the hydrogen adsorption enthalpy is positively correlated with the size of the intercalant (Cs > Rb > K). The fundamental principles behind this trend are still unclear. Dispersion forces are expected to become larger with atomic mass due to the greater number of electrons. Trends in electrostatic interactions are less clear, since we would expect the larger alkali metal atoms to have greater screening of the nuclear charge. The relative contribution of dispersion and electrostatic forces on the total binding energy therefore needs to be clarified. Variations in the charge transfer between different alkali metals and the graphite, determined quantitatively from the ground state electron density (from DFT calculations), can provide useful information on this topic. Trends in the dispersion interactions can be studied by introducing a semi-empirical van der Waals

correction to the GGA functional, as implemented in the CPMD code [119].

7.2.2 Two-dimensional diffusion

Past neutron scattering studies of H_2-GIC systems almost exclusively use polycrystalline GIC samples. This substantially complicates the quasielastic analysis since it introduces a powder average into the jump diffusion model. Further, it reduces the amount of information that can be directly extracted from the QENS data. Single crystal GIC samples can be synthesized from monolithic HOPG pieces and then stacked together to form a bulk sample. This strategy should allow us to obtain direct information on the characteristic geometries and frequencies of the adsorbed H_2 dynamics without the need for orientational averages. Diffusion is expected to be two-dimensional, and this should be directly measurable with single-crystal samples. In order to successfully explain the quasielastic peak shape, we must develop a jump diffusion model incorporating a distribution of jump frequencies.

7.2.3 Translational-rotational coupling

A valid model must explain *all* the peaks in the IINS spectrum of $KC_{24}(H_2)_x$, including peaks at intermediate energies. An attempt was made in this thesis to interpret the peaks in terms of single- and multi-excitations of phonon and rotational modes. However, large inadequacies remain with this model. A relevant model must take into account the strong coupling between rotations and translations of the H_2 molecule. A promising approach is to use first-principles based path integral molecular dynamics (PIMD) to obtain both the center-of-mass and rotational trajectories as a function of real time while also incorporating the effect of quantum delocalization. This work is computationally costly, but highly-scalable *ab intio* MD codes have recently become available which make them feasible [120].

Appendix A

Effect of porous texture on hydrogen adsorption in activated carbons

A.1 Introduction

Physisorption-based hydrogen (H_2) storage in microporous carbons has a trade-off between adsorption capacity and adsorption enthalpy [5]. Conceptually, this problem is best illustrated in terms of the ideal slit pore formed from two parallel, semi-infinite graphite slabs. Packing density is maximized when the pore width is several times larger than the diameter of the H_2 molecule, since it permits the formation of several hydrogen monolayers within the pore [16]. At supercritical temperatures, however, condensation within pores does not occur. Characteristic H_2 adsorption enthalpies associated with large slit pores therefore approach the enthalpy of H_2 adsorption on carbon, typically measured between $4\,\mathrm{kJ\,mol^{-1}}$ to $6\,\mathrm{kJ\,mol^{-1}}$ [15, 121]. With smaller pores, the adsorption enthalpy increases due to the overlap of potentials fields from each face of the pore. The packing density begins to decrease, though, when the pore is no longer wide enough to accommodate two H_2 monolayers. *Ab initio* calculations of hydrogen adsorption in ideal slit pore carbons

Portions of this chapter were published in the article: J. J. Purewal, H. Kabbour, J. J. Vajo, C. C. Ahn and B. Fultz, *Nanotechnology* **2009**, *20*, 204012.

are largely consistent with this picture [16, 122]. The fundamental limitations of hydrogen storage in activated carbons are difficult to study experimentally because uniform slit pore structures do not occur in nature. To extend the slit pore concept to realistic carbon adsorbents, the distribution of pore sizes must be understood.

Due to their microporosity, activated carbon fibers (ACF) are an excellent material for a fundamental study of H_2 adsorption capacity and enthalpy. ACFs are synthesized from polymeric carbon precursors and contain narrow pore size distributions [6, 123]. Images of ACFs from scanning tunneling microscopy have revealed networks of elongated slit-shaped and ellipsoid-shaped pores [124, 125]. Edge terminations in graphitic layers are thought to be the most reactive sites during the physical activation process, resulting in a gradual lengthening of slit shaped pores as a function of burn-off [126]. ACFs subjected to less burn-off will have smaller pore volumes and a greater abundance of narrow pores widths. With longer activation times, the pores grow larger resulting in a larger amount of mesopores. This offers a convenient control for an experimental study of pore structure and hydrogen adsorption.

In the current study, the pore size distributions (PSD) of ACFs are compared to the hydrogen adsorption enthalpy and adsorption capacity. Two ACF samples subjected to different degrees of activation are characterized. The microstructure of the activated carbon samples is investigated first with high resolution transmission electron microscopy (HRTEM). Then the PSD is obtained from argon adsorption measurements using the density functional theory method. Supercritical hydrogen adsorption isotherms are measured, and the enthalpies and capacities are determined. Measurements are also performed on a microporous, coconut-derived activated carbon as a control sample.

A.2 Experimental Methods

Kynol™ activated carbon fiber samples ACF-1603-10 (ACF-10) and ACF-1603-20 (ACF-20) were obtained from Kynol Inc. These ACFs are produced by carbonization and gasification of a phenolic resin precursor. The last two digits in the labels are an approximate indication of surface area in hundreds of $m^2\,g^{-1}$. The commercial, coconut-shell-derived activated carbon CNS-201 (CNS-201) was purchased from A.C. Carbon Canada Inc. Since CNS-201 is known to be highly microporous (90 % of pores are smaller than 1.3 nm), it is a useful reference material for the microporous ACFs. Textural parameters were obtained from Ar isotherms (87 K) for ACF-10 (0.2811 g) and ACF-20 (0.3222 g), and from a N_2 isotherm (77 K) for CNS-201 (0.1019 g). For illustration, the Ar isotherm for ACF-10 is displayed in Fig. A.1a. Surface areas and saturation pore volumes are calculated from the BET equation, given by

$$\frac{p/p^\circ}{n\,(1-p/p^\circ)} = \frac{1}{n_\mathrm{m}C} + \frac{C-1}{n_\mathrm{m}C}\,(p/p^\circ)\,. \tag{A.1}$$

The monolayer capacity, n_m, is determined from the slope and y-intercept of the fitted line in Fig. A.1c. We can then calculate the BET surface area, a(BET), from the molecular cross-sectional area (σ) using the formula,

$$a(\mathrm{BET}) = n_\mathrm{m} N_\mathrm{a} \sigma, \tag{A.2}$$

where N_a is the Avogadro constant.

Total pore volumes are calculated from the Dubinin-Astakhov equation, given by

$$\log(n) = \log(n_\mathrm{p}) - D\,[\log(p^\circ/p)]^x\,, \tag{A.3}$$

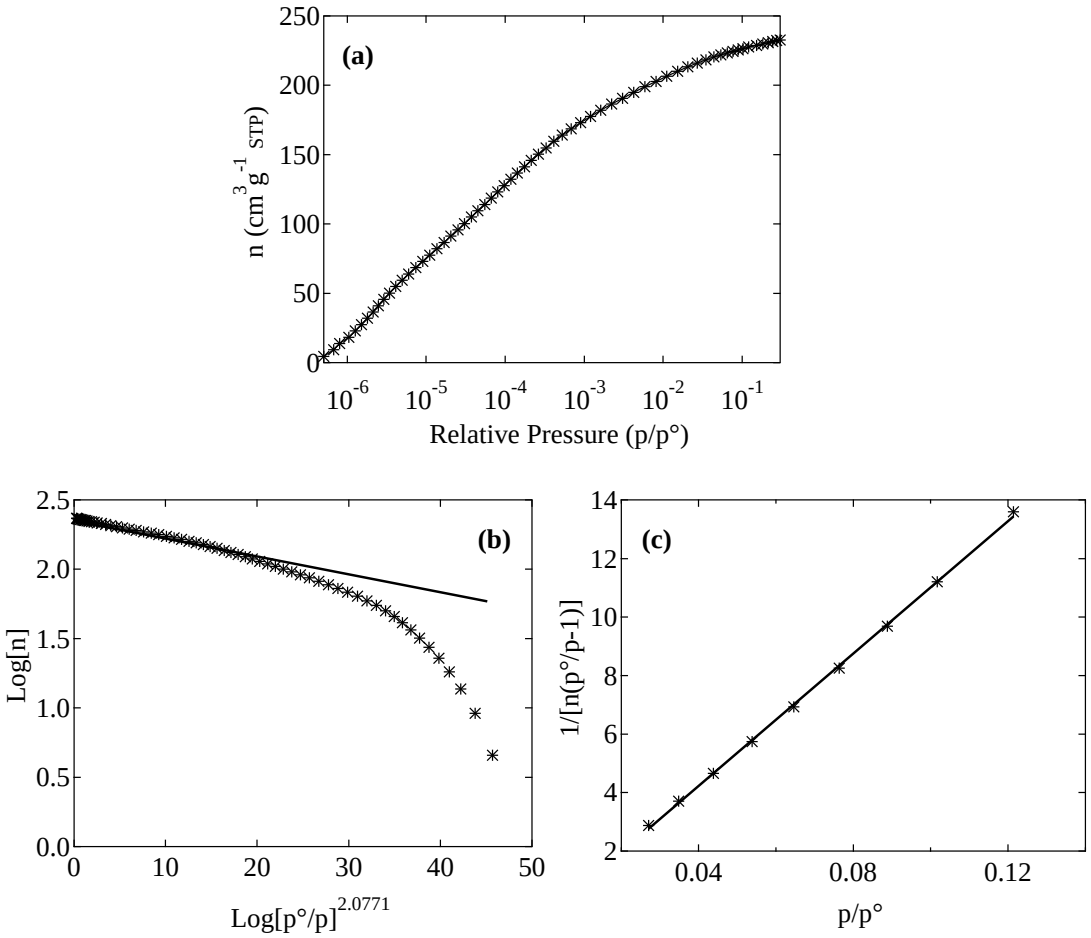

Figure A.1: Surface texture analysis for sample ACF-10. (a) Ar isotherm measured at 87 K. (b) Dubinin-Astakhov transformed isotherm plot. (c) BET surface area plot.

where D are x are empirical constants.[1] The pore capacity, n_{p}, is determined from the y-intercept of the fitted line in Fig. A.1b. It is then used to calculate the pore volume

$$V_{\mathrm{p}} = n_{\mathrm{p}} \times M/\rho, \tag{A.4}$$

where M and ρ are the molar mass and liquid density (at 87 K) of Ar. Pore size distributions were calculated using the original DFT method as implemented in Micromeritics ASAP 2020 Version 3.01 software.[2]

[1] Note that x was optimized as 2.0771 for ACF-10, as indicated on the x-axis of Fig. A.1b.

[2] Ar and N_2 isotherms, and DFT modeling performed by Micromeritics Analytical Services.

High resolution TEM micrographs were acquired on a Tecnai F30-UT operated at 300 keV. Sample preparation consisted of grinding about 10 mg of the sample in isopropanol and dispersing it on a carbon grid. High-pressure H_2 isotherms were measured with the custom-built Sieverts apparatus at temperatures of 77 K, 87 K, and 195 K. This instrument was described in detail in Sec. 3.1.3. The sample weights used for the hydrogen adsorption measurements were 0.1782 g (ACF-10), 0.2114 g (ACF-20) and 0.903 g (CNS-201). Prior to adsorption measurements, samples were degassed by heating at 200 ℃ under vacuum for 12 h. Sample masses were measured again after the adsorption experiment to check for changes in mass due to removal of residual water. The void volume of the sample was estimated by assuming a skeletal density of 2.1 g ml^{-1}, which is typically sufficient for most carbon samples.

A.3 Results

An HRTEM micrograph of ACF-10 is presented in A.2. ACFs are known to be more graphitic than typical activated carbons [126], but this is not obvious from the image. The microstructure appears similar to the highly disordered microstructures typically observed for activated carbons. Micropore structures were not visible in the HRTEM analysis. However, the combination of finite sample thickness and non-periodicity tends to conceal micropore structures.

The BET surface areas and total pore volumes for ACF-10, ACF-20, and CNS-201 are listed in A.1. As expected, ACF-10 (subject to less burn-off than ACF-20) has a smaller pore volume and smaller BET surface area than ACF-20. The activated coconut carbon CNS-201 appears to have a BET surface area and pore volume which is intermediate between the two

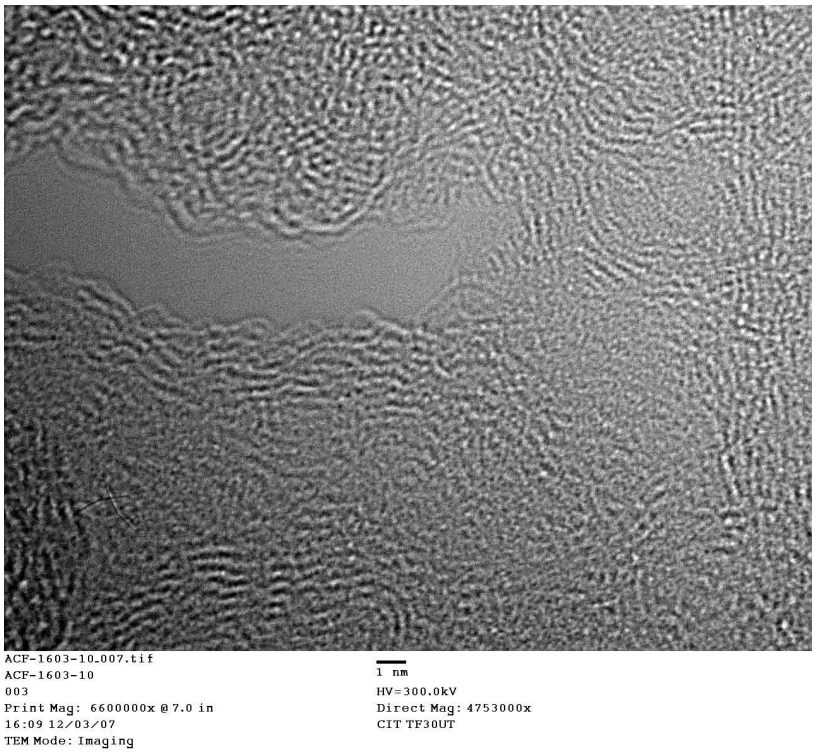

Figure A.2: High-resolution TEM image of ACF-10. Length scale in indicated in the figure.

ACFs.[3] Calculated surface areas of activated carbons are often unrealistically high, since the micropore adsorption mechanism is not equivalent to the multilayer process assumed in the BET model. Nevertheless, the BET method is useful for comparisons between different materials.

Pore size distributions obtained from the DFT method are displayed in Fig. A.3. The pore width is defined as $L - d$, where L is the internuclear spacing between the walls of the slit pore and d is the van der Waals diameter of carbon (3.4 Å). Since graphite has an interlayer spacing of $L = 3.35$ Å, a slit pore formed from a single missing graphene plane has a width of 3.3 Å. A slit pore formed from two missing graphite planes has a width of 6.7 Å, and a pore formed from three missing graphite planes has a width of 10 Å. Taking into account the finite diameter of Ar (2.8 Å) and N_2 (3.0 Å), the cutoff in the pore spectrum

[3]Note that textural parameters were obtained from Ar isotherms for the ACFs and from N_2 isotherms for CNS-201. For direct comparison between samples it would have been better to have used the same adsorptive. Textural parameters obtained by Ar and N_2 data are still sufficient for the qualitative comparison done here.

Table A.1: Surface texture parameters

Sample	SSA $(m^2\,g^{-1})^a$	V_{pore} $(cm^3\,g^{-1})^b$
ACF-10	801	0.296
ACF-20	1817	0.706
CNS-201	1158	0.452

[a] Specific surface areas obtained by the BET method.
[b] Total specific pore volumes obtained from the Dubinin-Astakhov equation.
[c] The textural parameters of ACF-10 and ACF-20 were obtained from Argon measurements at 87 K while those of CNS-201 were obtained from N_2 measurements at 77 K.

must be above 3 Å.[4]

The pore size distributions displayed in Fig. A.3 all show a sharp increase in intensity just below 5.0 Å, which corresponds to a width that is between the predicted pore widths for one or two removed graphite planes. This may simply reflect the smallest pore width which is measurable by the specific probe molecule. Another possibility is that after the removal of two layer planes, the slit pore structure relaxes to the observed 5 Å spacing. The pore distribution of ACF-10 is narrow, consisting of the single large peak at 5 Å. Since burn-off in ACF-10 was minimized, larger pore structures did not develop fully, and are present only as a small tail in the PSD. For ACF-20 there is a broad distribution of pore widths from 5 Å to 20 Å with a small positive skew. Since ACF-20 was subject to a greater degree of burn-off, larger pores were formed during the activation process.[5] The activated carbon CNS-201 also appears to have a distribution of pore widths between 5 Å and 20 Å with a positive skew. This broad distribution of pore widths in ACF-20 and CNS-201 may reflect the presence of slit pores formed from the removal of up to six graphite planes.

[4]Smaller probe molecules, such as helium, could measure pore widths below this cutoff.

[5]The minima near 6 Å and 10 Å are likely to be model-induced artifacts which are independent of the actual sorbent material [127]. The minima in the distributions have been proposed to originate from packing effects where the pore width transitions from being able to support one adsorbed layer to two, and from two layers to three. This width is governed by the functional form used for the adsorbing molecule, for example, a Lennard-Jones potential. However, the fact that the maxima in the distributions are separated by integrals of the graphite layer spacing distance suggests that the maxima may be real and correspond to pores formed from removal of one, two, three, etc, graphitic planes.

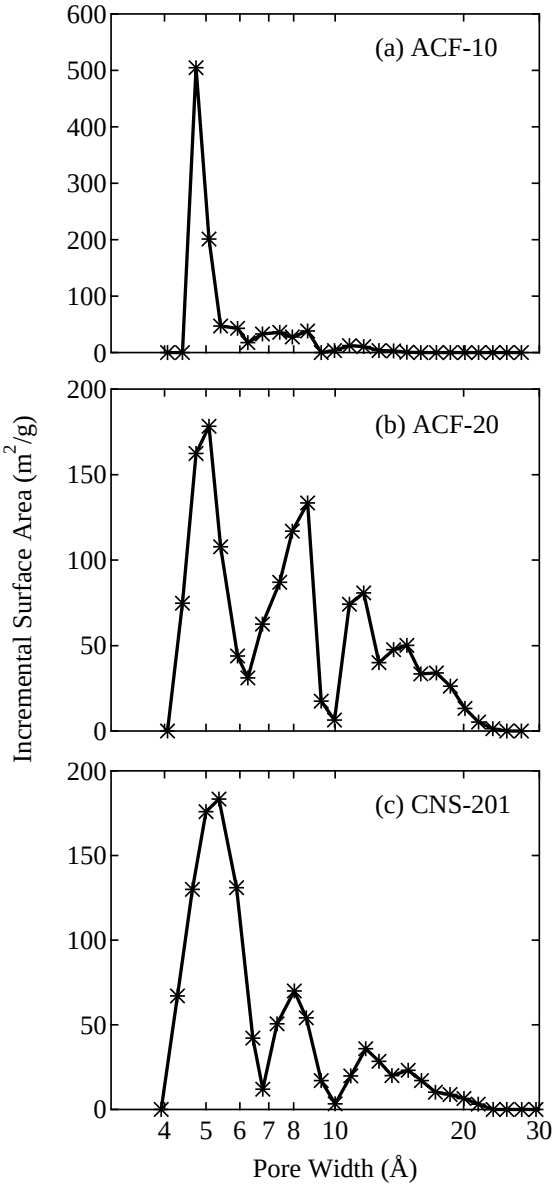

Figure A.3: Pore size distributions determined by the DFT method for (a) ACF-10, (b) ACF-20, and (c) CNS-201. The bottom axis is shown in logarithmic scale.

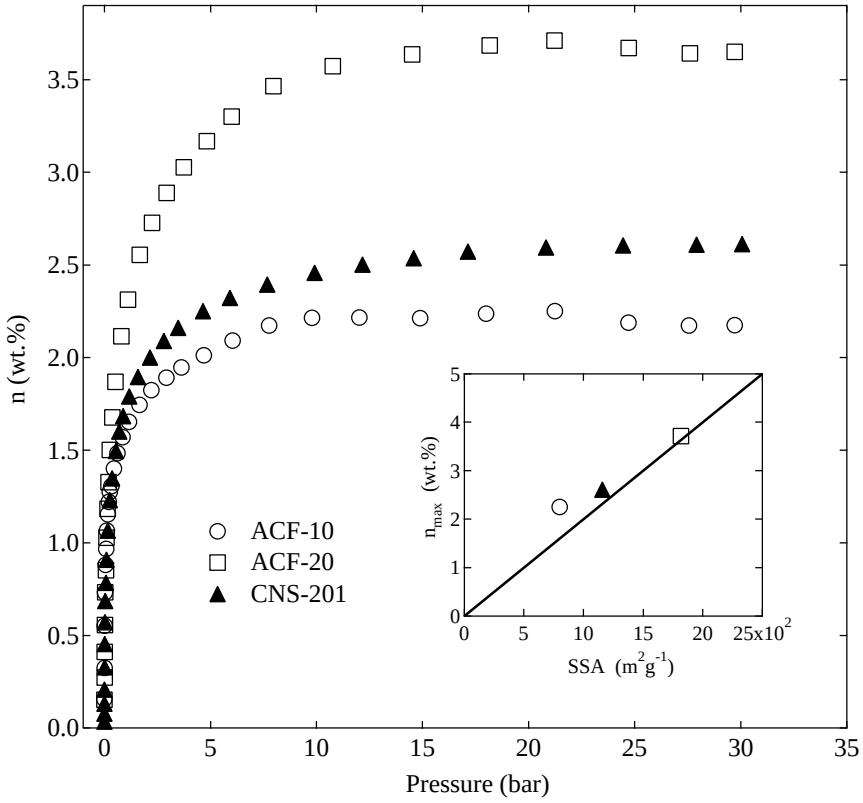

Figure A.4: Hydrogen adsorption isotherms at 77 K for ACF-10, ACF-20, and CNS-201. Inset: Maximum H_2 adsorption capacity (wt%) at 77 K versus BET specific surface area ($m^2\,g^{-1}$), with the solid line signifying a 1 wt% per $500\,m^2\,g^{-1}$ linear relationship.

Supercritical H_2 isotherms are displayed in Fig. A.4. As discussed in Sec. 1.6.7, comprehensive studies of H_2 adsorption in activated carbons typically report a linear dependence of n_{max} at 77 K with specific surface area [19, 20, 128]. An increase of approximately 1 wt% hydrogen for every $500\,m^2\,g^{-1}$ of surface area is the rule-of-thumb. As shown in the inset of Fig. A.4, the hydrogen adsorption capacities of ACF-10, ACF-20, and CNS-201 at 77 K roughly follow the rule-of-thumb, although ACF-10 does show a substantial positive deviation. Since ACF-10 is almost exclusively microporous, with little contribution from mesopores,[6] this may explain why it shows a large positive deviation from the $500\,m^2\,g^{-1}$ per 1 wt% rule. On the other hand, ACF-20 has a wider distribution of both micropores

[6]Small mesopores can produce large BET surface areas, but contribute little to hydrogen adsorption capacity.

Table A.2: Hydrogen adsorption parameters

Sample	$\Delta\dot{h}_0$ (kJ mol^{-1})[a]	ΔH_{avg} (kJ mol^{-1})[b]	n_{max} (wt%)[c]
ACF-10	8.92	6.64	2.1
ACF-20	7.63	5.85	3.5
CNS-201	8.59	6.07	2.5

[a] Enthalpy of hydrogen adsorption in the zero-coverage limit.
[b] Average isosteric heats between 0 wt% and 1.8 wt%.
[c] Maximum hydrogen adsorption capacity at 77 K.

and mesopores, which may explain why it does not show the same positive deviation from the rule-of-thumb.

Accurate adsorption amounts were measured in the low-pressure region using a high-resolution pressure gauge. Henry's law constants were then calculated at 77 K, 87 K, and 195 K from the zero-order virial coefficient $C_0 = \ln(k_H)$ in Eq. 3.11. The differential enthalpy of adsorption was calculated from the temperature variation of k_H using the van't Hoff expression (Eq. 3.12). For all the samples we find that $\ln(k_H)$ varies linearly with $1/T$, and an accurate estimate of $\Delta\dot{h}_0$ is obtained from the slope. Values of enthalpy in the zero coverage limit are summarized in Table A.2. The largest adsorption enthalpy (8.92 kJ mol^{-1}) is observed for ACF-10, which has the greatest fraction of narrow pores. In ACF-20, which has larger pore widths, the adsorption enthalpy (7.32 kJ mol^{-1}) is smaller. An intermediate enthalpy is observed for the activated carbon CNS-201.

The isosteric heat was calculated by fitting the 77 K and 87 K isotherms to the virial-type thermal equation (Eq. 3.8). As displayed in Fig. A.5, all of the samples are energetically heterogeneous, and the enthalpy decreases substantially with increasing n. Heterogeneity is especially pronounced for ACF-10. In the inset to Fig. A.5, the isosteric heat is also plotted against the fractional adsorption amount. When viewed as a function of fractional adsorption, the isosteric heat of ACF-10 remains higher than ACF-20 until a fractional

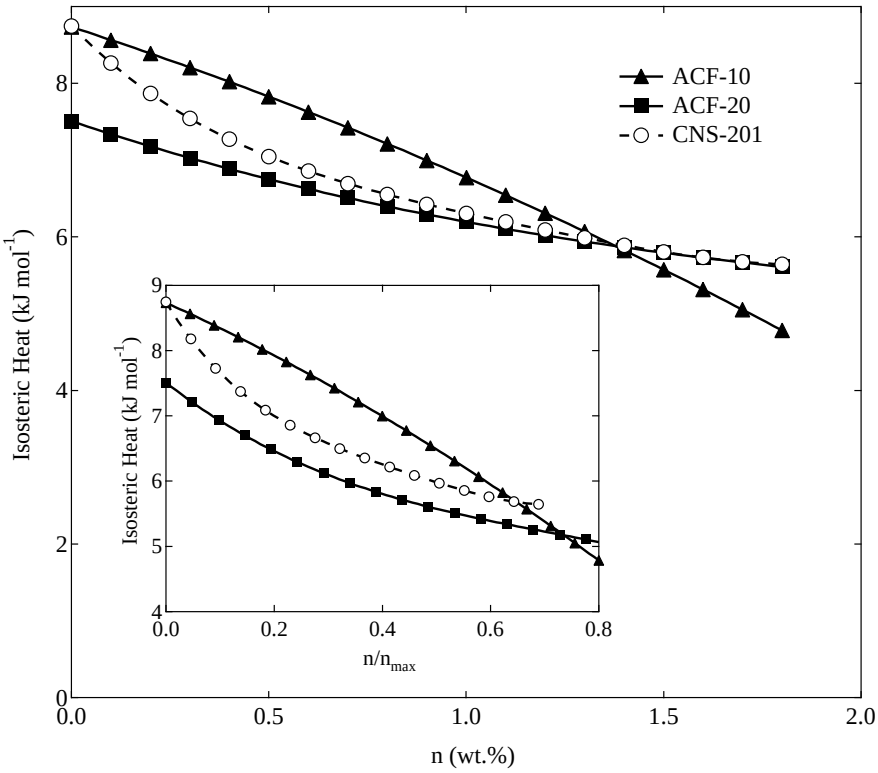

Figure A.5: The H_2 isosteric enthalpy of adsorption for ACF-10, ACF-20, and CNS-201 as a function of surface excess adsorption. Inset: The isosteric heat is plotted as a function of the fractional amount of adsorption (excess adsorption divided by the saturation adsorption amount at 77 K).

filling of about 0.7. For comparison between the different samples, the isosteric heats were averaged from $0\,\mathrm{mmol\,g^{-1}}$ to $9.5\,\mathrm{mmol\,g^{-1}}$, and these values are summarized in Table A.2.

A.4 Discussion

Heterogeneity in the adsorption potentials of microporous carbons is modeled using a distribution of widths of the slit pores. Recent studies have also stressed the importance of fluctuations in pore wall thickness on the adsorption potential [5, 129]. Narrow pores have deeper potential wells and should be filled at the lowest pressures. This is followed by the gradual filling of larger pores at higher pressures. At a given equilibrium pressure, p, there should be a critical pore width, below which all pores are filled and above which all pores

are vacant [73]. The zero coverage heat of H_2 adsorption, $\Delta\dot{h}_0$, reflects the initial filling of pores and therefore should depend on the PSD of the three samples.

Since ACF-10 contains a narrow peak at 5 Å in the PSD, the filling of these small pores presumably leads to the large zero coverage H_2 adsorption enthalpy. ACF-10 also contains a small fraction of wider pores, and it is the filling of these larger pores that apparently causes the steep decrease in the isosteric heat of adsorption at higher coverage. In ACF-20, there is a broad distribution of pore widths. In theory, the smallest 5 Å pores should fill first, leading to a similar zero coverage H_2 adsorption enthalpy as ACF-10. Measurements indicate, however, that ACF-20 has a significantly smaller zero coverage enthalpy than ACF-10. The exclusive filling of the smallest pores at low pressures, in isolation from the larger pores, may not be a realistic view. Simultaneous filling of pores with widths from 5 Å to 20 Å, on the other hand, might explain this smaller-than-expected zero coverage adsorption enthalpy. Therefore it is the relative abundance of the smallest pores relative to the larger pores which seems to have the greatest influence on the zero-coverage enthalpy.

In all three samples, the isosteric heat of adsorption decreases with the excess adsorption amount. Since the samples have different adsorption capacities, a better comparison can be made by plotting the isosteric heats as a function of fractional adsorption. This is displayed in the inset to Fig. A.5. The isosteric heats of both ACF-10 and ACF-20 decrease almost uniformly at low filling, but ACF-10 eventually falls below ACF-20 at a fractional filling of 0.7. At least some of the decrease in isosteric heat can be attributed to repulsive interactions between the adsorbed H_2 molecules. These unfavorable interactions are likely to be greater in small slit pores than in larger slit pores, leading to the observed behavior.

Heats of adsorption in the Henry's Law region (listed in Table A.2) are considerably greater than the 4–6 kJ mol^{-1} heats typically observed for H_2 adsorption on the surface of

carbon. This is due to strong interactions between adsorbed hydrogen molecules and the slit pore potential fields. Average isosteric heats of adsorption fall between 5.8–6.7 kJ mol^{-1} for the three samples, closer to the characteristic values for carbon. The H_2 adsorption enthalpy (ACF-10 > CNS-201 > ACF-20) is negatively correlated with the total H_2 adsorption capacity (ACF-20 > CNS-201 > ACF-10) for the three samples that were studied.

A.5 Conclusion

Pore size distributions and supercritical H_2 isotherms for two microporous activated carbon fibers and one coconut-derived activated carbon were measured and compared. The low surface area sample, ACF-10, has a narrow peak in the PSD at 5 Å with a very small tail at larger widths. The high surface area sample, ACF-20, has a broad PSD which contains widths from 5 Å to 20 Å and has a small positive skew. The coconut-derived activated carbon CNS-201 also has a broad PSD with widths from 5 Å to 20 Å. The zero coverage enthalpy of hydrogen adsorption depends strongly on the relative intensity of the smallest pore widths in the PSD. Zero-coverage enthalpies vary from 8.92 kJ mol^{-1} for low surface area ACF-10 to 7.63 kJ mol^{-1} for high surface area ACF-20.

Appendix B

Hydrogen absorption behavior of the ScH_2-$LiBH_4$ system

B.1 Introduction

Complex metal hydrides are basically salts consisting of an anionic complex $[MH_n]^-$ and a cation A^+ to balance the charge. Complexes containing light elements have been the focus of most research, due to their favorable gravimetric hydrogen densities. One such complex metal hydride is $LiBH_4$, which can release up to 13.8 wt% hydrogen by thermal decomposition:

$$LiBH_4 \longrightarrow LiH + B + \tfrac{3}{2}H_2. \tag{B.1}$$

Like most complex metal hydrides, $LiBH_4$ is a very stable compound. It requires temperatures well above 200 °C to release hydrogen. The standard reaction enthalpy is 61 kJ mol^{-1}, which translates to 1 bar equilibrium pressure at 400 °C [130, 131].

Chemical destabilization of $LiBH_4$ offers a versatile way to lower the desorption enthalpy [132–136]. Recent work has focused on adding an additional metal or metal hydride species which reacts to form a stable metal boride phase, lowering the overall reaction enthalpy.

Portions of this chapter were published in the article: J. Purewal, S. Hwang, R.C. Bowman, E. Rönnebro, B. Fultz and C.C. Ahn, *J. Phys. Chem. C* **2008**, *112*, 8481-8485.

Vajo et al. demonstrated that adding MgH_2 to $LiBH_4$ lowered the dehydrogenation enthalpy by $25\,kJ\,mol^{-1}$ [131]. Motivated by such successes, a comprehensive evaluation of potential chemically destabilized metal hydride systems was initiated, using density functional theory to evaluate formation and reaction enthalpies [137–139]. A significant result from this study was the identification of ScH_2 as a destabilizing agent with ideal thermodynamics [140]. The following decomposition pathway

$$ScH_2 + 2\,LiBH_4 \longrightarrow ScB_2 + 2\,LiH + 4\,H_2 \tag{B.2}$$

has a calculated reaction enthalpy of $34.1\,kJ\,mol^{-1}$ at room temperature. This system can release up to 8.9 wt% upon completion. An equilibrium pressure of 1 bar is calculated to occur at 57 ℃.

It is important to note, however, that first principles DFT calculations provide no direct information about either the reaction mechanism or the activation barriers. It is likely that the rate limiting steps would involve the breakdown of ScH_2 ($\Delta H_f = 200\,kJ\,mol^{-1}$) and the formation of ScB_2 ($\Delta H_f = 248\,kJ\,mol^{-1}$), both of which are stable compounds. While first-principles calculations have proved accurate in reproducing experimental PCT diagrams for the destabilized MgH_2-$LiBH_4$ system, it is uncertain whether similar success will be achieved for a system in which the reactant and product phases have considerably larger formation enthalpies. High energy ball-milling can improve reaction kinetics to some degree by reducing diffusion distances and increasing the concentration of reaction interfaces. It does not necessarily mitigate the large activation barriers to ScH_2 and ScB_2 decomposition however.

The aim of the present work is to experimentally investigate the importance of kinetic

barriers in determining hydrogen absorption and desorption behavior. Isothermal kinetic H_2 adsorption and desorption of the $ScH_2/LiBH_4$ system was measured at various temperatures. Reaction products were characterized using powder XRD, magic angle spinning NMR, and Raman spectroscopy. We were unable to verify the formation of ScB_2 in the product phase, and there was no evidence for the proposed reaction pathway (Eq. B.2). Rather, the $LiBH_4$ was found to decompose independently into LiH and amorphous boron without the reaction of ScH_2.

B.2 Experimental Details

Samples of ScH_2 were synthesized by heating small scandium pieces (99.9% purity, Standford Materials Corporation) in ultrahigh purity H_2 at approximately 350 °C. The resulting formation of scandium hydride was rapid and highly exothermic. This is illustrated in Fig. B.1, where the hydrogenation reaction is shown to complete within a minute or so. The large amount of released heat is evident from the spike in reactor temperature. Hydrogenation was allowed to proceed for 3 h to ensure equilibration. Volumetric analysis and X-ray diffraction both indicate that the reaction product is ScH_2. Roughly 10 g of a 2:1 molar mixture of $LiBH_4$ (95% purity, Sigma Aldrich) and freshly-prepared ScH_2 was loaded under argon atmosphere into a sealed 80 mL stainless steel vessel containing five 0.5 in. diameter stainless steel balls. The vessel was sealed with a rubber gasket and clamp and loaded into a planetary mill (Fritsch-pulverizette 6). Different mixtures were milled at 400 rpm for either 1 h or 10 h. For possible catalytic enhancement of the reaction rates, 2 mol% $TiCl_3$ (Sigma Aldrich) was added to several samples prior to milling. All samples were handled in argon atmosphere gloveboxes to prevent air and moisture contamination.

Isothermal kinetic desorption measurements were conducted on a custom built stainless

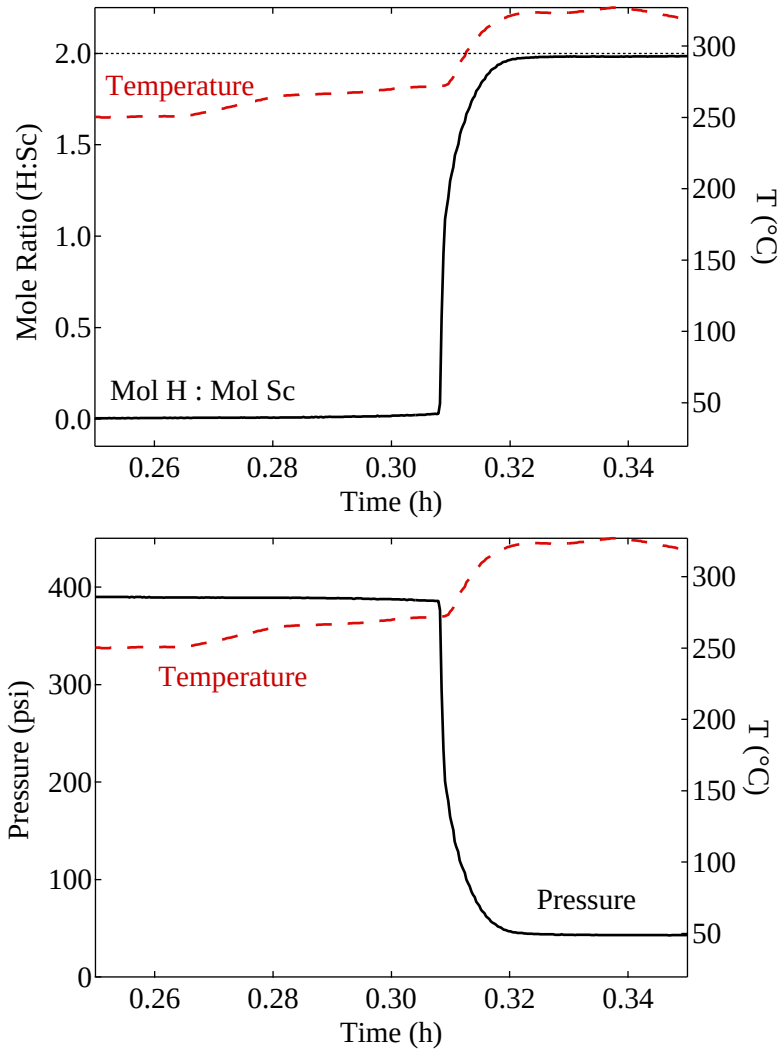

Figure B.1: Synthesis of scandium hydride. Top: Molar ratio of H to Sc in the solid scandium-hydrogen phase versus time. Bottom: Pressure of free H_2 in the reactor system versus time.

steel Sieverts apparatus. In a typical experiment, a 1 g sample was loaded into a 14 mL stainless steel reactor assembly sealed with a 0.5 in. Swagelok VCR filter gasket connection. The reactor was then mounted on the Sieverts system and enclosed in a thick, tight-fitting aluminum collar to maintain temperature uniformity. The furnace setup included a Watlow band heater fastened around the aluminum collar, with two thermocouples inserted into dedicated ports in the aluminum heat sink. The quantity of desorbed hydrogen was determined by volumetric measurements. Weight percents are reported with respect to the fully

hydrogenated samples, excluding the weight of the added catalyst. Powder XRD and Raman spectroscopy measurements were collected on samples sealed in 1.0 mm glass capillary tubes, following the procedure described in Sec. 2.6.

Solid-state magic angle spinning nuclear magnetic resonance (MAS NMR) measurements were performed using a Bruker Avance 500 MHz spectrometer equipped with a Bruker 4 mm boron-free cross-polarization (CP) MAS probe. The spectral frequencies were 500.23, 160.5, 121.6, and 73.6 MHz for the ^{1}H, ^{11}B, ^{45}Sc, and ^{6}Li nuclei, respectively. Samples were loaded into 4 mm ZrO_2 rotors, and each was sealed with a tight-fitting kel-F cap under argon atmosphere and spun at 13 kHz. The one-dimensional ^{11}B, ^{45}Sc, and ^{6}Li NMR spectra were acquired after a short (0.5 μs) single pulse (i.e., $< \frac{\pi}{12}$ for ^{11}B) with application of a strong ^{1}H decoupling pulse of the two-pulse phase modulation (TPPM) scheme [141]. The NMR shifts were reported in parts per million (ppm) with respect to "zeroes" set to standard external references: tetramethylsilane (TMS) for ^{1}H, $BF_3{-}Et_2O$ for ^{11}B, 1.0 M LiCl aqueous solution for ^{6}Li, and 1.0 M $Sc(NO_3)_3{-}HNO_3$ aqueous solution for ^{45}Sc nuclei.

B.3 Results

The hydrogen desorption behavior for the as-prepared $ScH_2 + 2\,LiBH_4$ mixtures were studied with kinetic desorption measurements using a series of temperature steps (Fig. B.2). Samples were heated inside a 72 mL volume to a final temperature of 450 °C. For samples maintained at this temperature, there was a release of 4.5 wt% hydrogen over 20 h. This is roughly half of the theoretical capacity of 8.91 wt% predicted for Eq. B.2. Longer milling times resulted in a small enhancement of the desorption capacity (an increase of less than 0.5 wt%) with no observable change in desorption kinetics. The composition of the desorbed gas was sampled using a residual gas analyzer (SRS, model RGA200) and found to

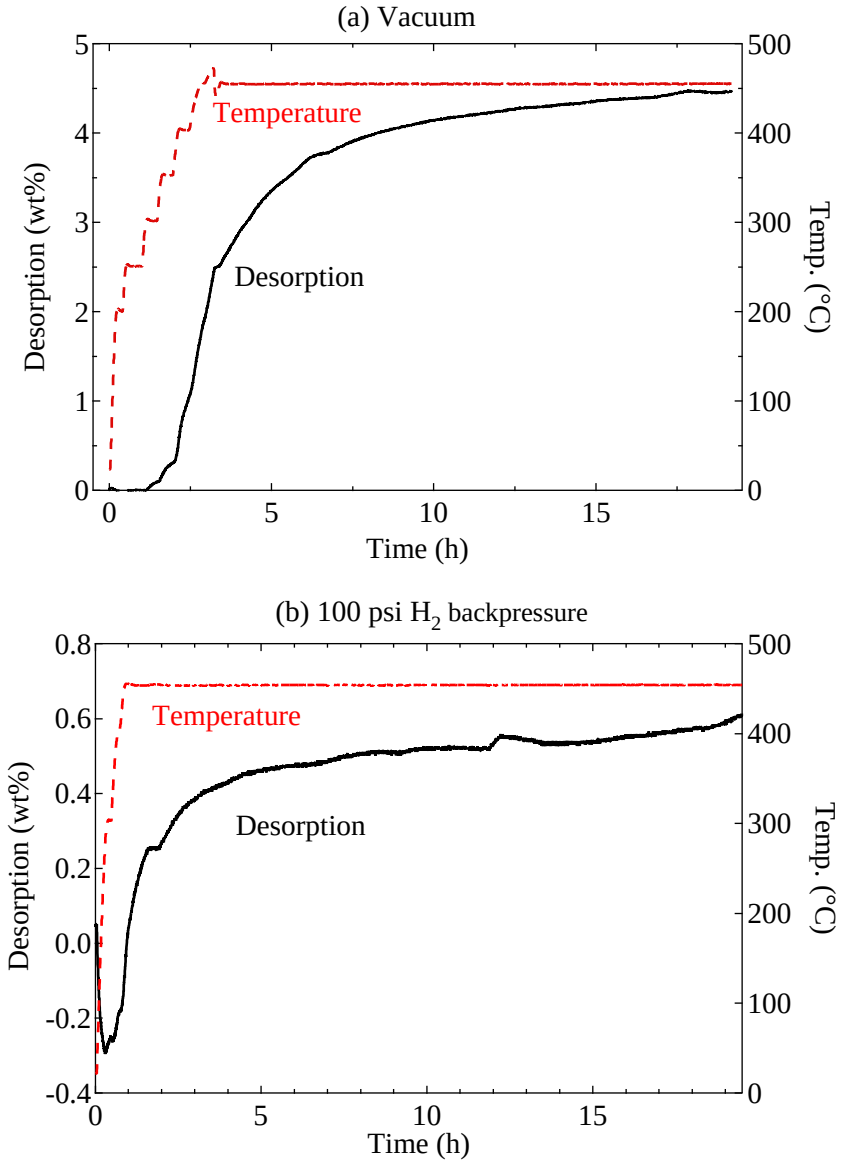

Figure B.2: Kinetic desorption data for the $ScH_2 + 2\,LiBH_4$ system. Top: Desorption into initially evacuated volume. Bottom: Desorption into 100 psi hydrogen backpressure.

contain over 99% hydrogen. Significant hydrogen desorption began at 350 °C, close to the temperature range at which the thermal decomposition of $LiBH_4$ is known to occur [142]. The 4.5 wt% of H_2 released at 450 °C is consistent with decomposition due solely to $LiBH_4$.[1]

Desorption measurements were also performed with an initial hydrogen backpressure of 100 psi, which was not found to enhance kinetics or to increase the hydrogen gas yield. Desorption from a $ScH_2 + 2\,LiBH_4 + 0.02TiCl_3$ sample was studied to assess the effect of a Ti catalyst on the reaction kinetics. At 280 °C, the desorption capacity was increased five-fold in the Ti-containing sample compared to the uncatalyzed sample. It should be noted that overall desorption capacity was still low, at 0.5 wt%. However, at 350 °C and 450 °C, the presence of $TiCl_3$ did not enhance either the kinetics or capacity.

The reverse direction of Eq. B.2 was also studied. A ball-milled $ScB_2 + 2\,LiH + 0.02TiCl_3$ sample was prepared and its hydrogen adsorption properties were studied. Starting with a 135 bar hydrogen pressure, a 0.8 g sample was heated to 300 °C for 48 h. No statistically significant hydrogen uptake was determined from a volumetric analysis. Powder XRD and MAS NMR analysis also failed to detect the formation of the expected product phases: $LiBH_4$ and ScH_2. A subsequent absorption experiment was performed with an 896 bar hydrogen pressure, with the sample kept at 460 °C for 48 h. A ^{11}B MAS NMR spectrum (see Fig. B.4a) of this sample revealed the presence of a small peak at -41 ppm, indicating a very limited $LiBH_4$ formation (about 3 mol%) in the reaction product. We note, however, that this pressure falls well out of the range of interest for technologically relevant metal hydride storage systems.

Figure B.3 shows the powder XRD measurements of the $ScH_2 + 2\,LiBH_4$ system before milling, after milling for 10 h, and after desorption at 450 °C for 20 h. The XRD pattern of

[1] Excluding the mass of the unreacted ScH_2, this would give 9 wt%, which is consistent with desorption measurements taken on unmixed $LiBH_4$.

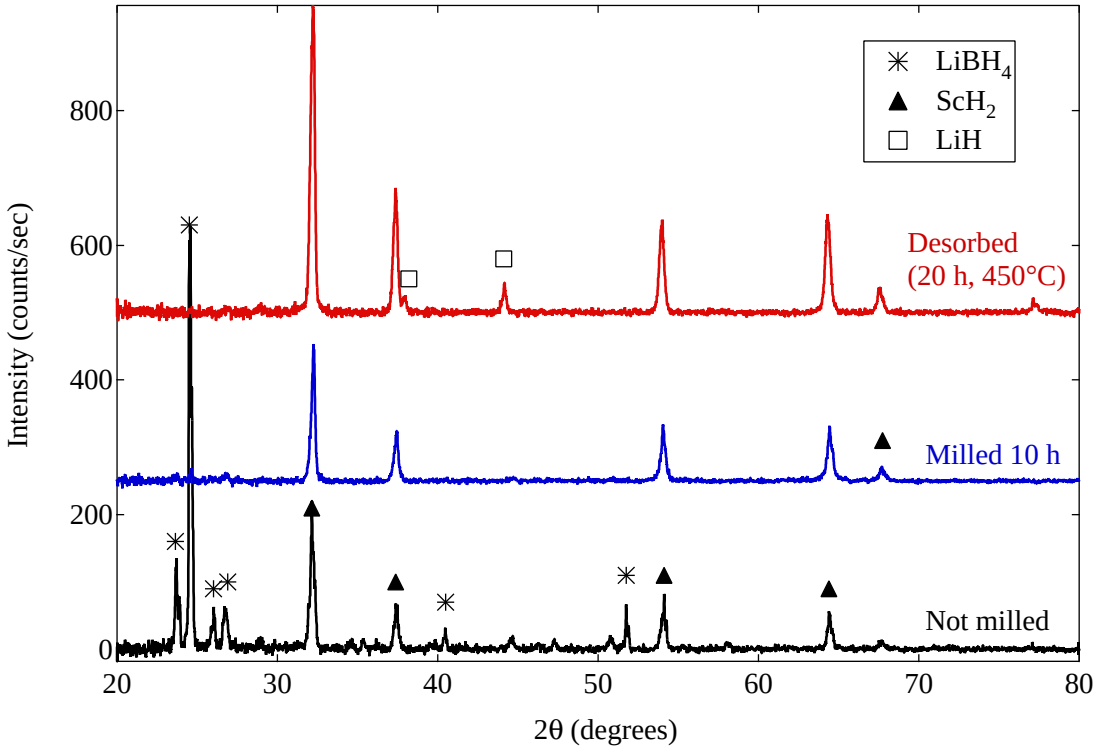

Figure B.3: Powder X-ray diffraction patterns for the $ScH_2 + 2\,LiBH_4$ system: before milling; after milling for 10 h; and after desorption at 450 ℃ for 20 h. Peak assignments were made with ICDD PDF2 card data for known or expected phases, including $LiBH_4$, ScH_2, LiH, ScB_2, Sc, and B.

the 450 ℃ desorption product reveals the presence of LiH and unreacted ScH_2. Since LiH is also an expected decomposition product of unmixed $LiBH_4$ [142], this does not provide evidence that the ScH_2 has participated in the reaction. A large background was also present due to the abundance of amorphous phases, presumably originating from the melting and re-solidification of $LiBH_4$ as well as from the formation of amorphous intermediate phases [143]. No peaks from the expected ScB_2 phase could be detected in the desorbed material.

Because a large fraction of the desorption product was amorphous, MAS NMR was utilized to complement the powder XRD results. Figure B.4 shows the ^{11}B, ^{45}Sc, and ^{6}Li MAS NMR data for the $ScH_2 + 2\,LiBH_4$ system after milling and after dehydrogenation (450 ℃ for 20 h). From ^{11}B NMR spectra, no noticeable change of the $LiBH_4$ peak was observed after ball-milling. The ^{11}B MAS and CPMAS spectra (Fig. B.4a and b) show the

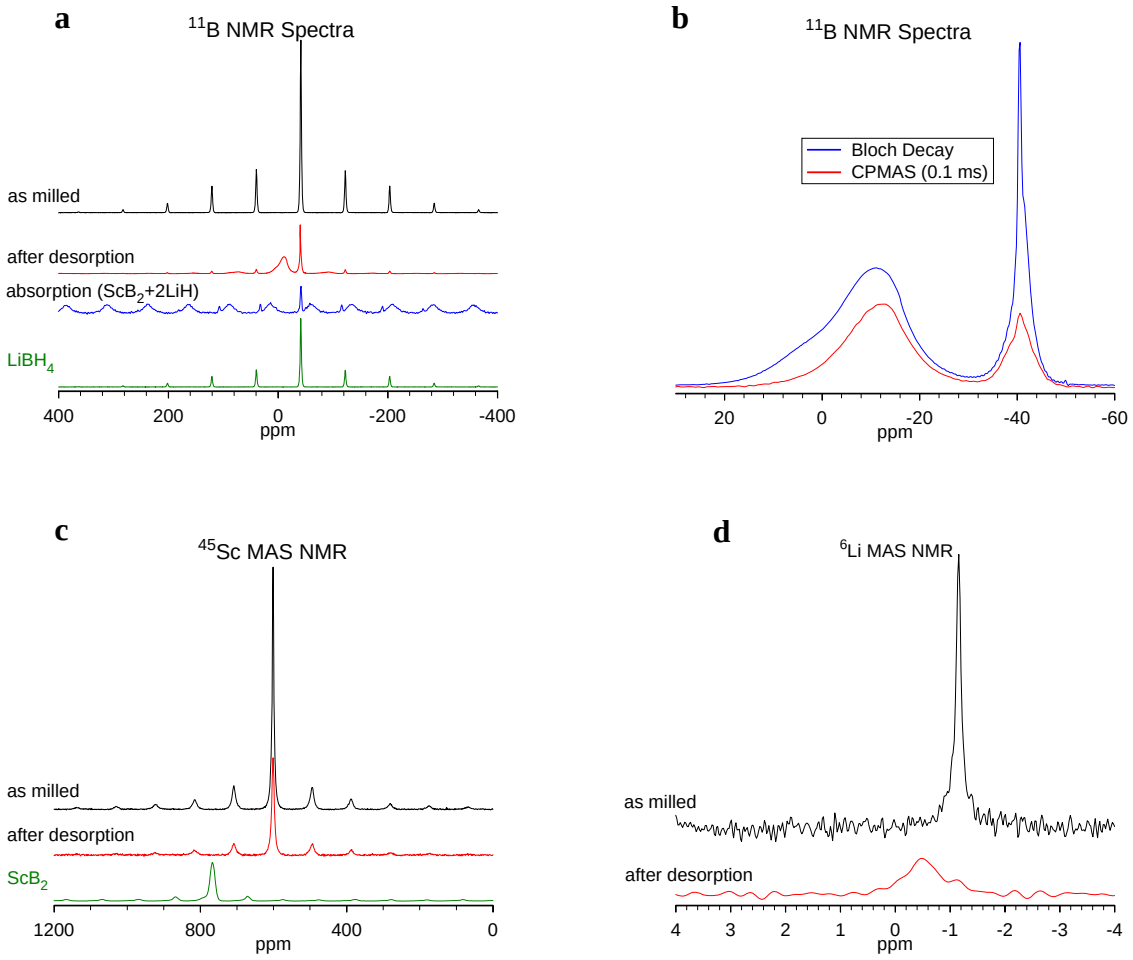

Figure B.4: NMR spectra of milled and dehydrogenated $ScH_2 + 2\,LiBH_4$. (a) Bloch decay ^{11}B MAS NMR spectra with neat $LiBH_4$ added as reference. Note that a spectrum of the $ScB_2 + 2\,LiH$ system after absorption treatment at high H_2 pressure (896 bar; see text) is also included, where the broader spinning sidebands in this spectrum are due to unreacted ScB_2. (b) ^{11}B MAS and CPMAS NMR spectra (contact time = 0.1 ms) of desorbed sample. (c) ^{45}Sc MAS NMR spectra with pure ScB_2. (d) ^{6}Li MAS NMR spectra

formation of elemental boron in the amorphous phase (broad shoulder at ~ 5 ppm) and the formation of an intermediate phase (with peak at -12 ppm) that was recently identified as an $[B_{12}H_{12}]^{2-}$ species [144]. We note also that some unreacted $LiBH_4$ is still present (seen from the peak at around -40 ppm) in the dehydrogenated product.

While unreacted ScH_2 is still present in the desorption products, ScB_2 is not detectable in the ^{45}Sc MAS NMR spectra presented in Fig. B.4c. Note that the ^{45}Sc signal was

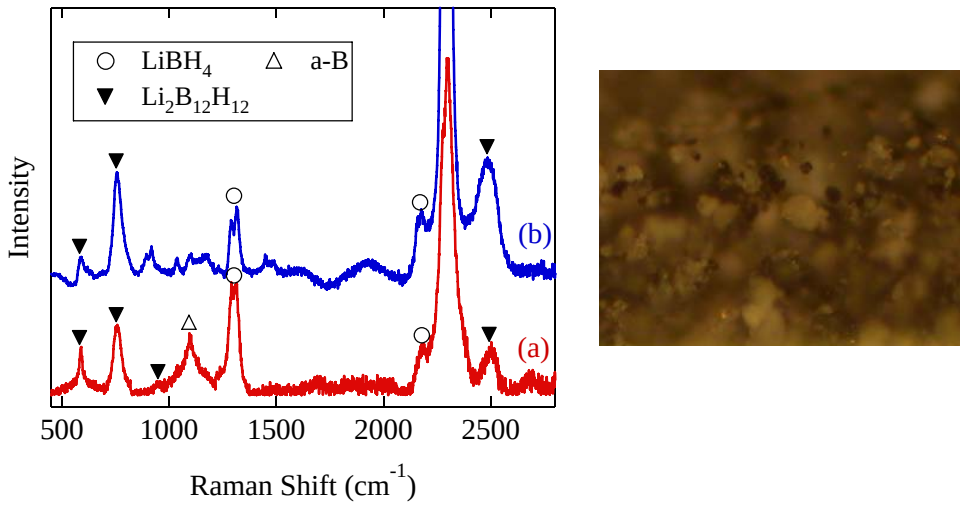

Figure B.5: Left: Raman spectra of the dehydrogenation products of (a) ScH_2+2 $LiBH_4$ system and (b) neat $LiBH_4$. Spectrum (a) corresponds to the white particles shown in the optical micrograph. The solid down-triangle, open circle, and open up-triangle identify Raman modes from $Li_2B_{12}H_{12}$, $LiBH_4$, and amorphous boron, respectively. Right: Optical micrograph of a $ScH_2 + 2\,LiBH_4$ system after desorption.

significantly reduced after the desorption reaction, which we tentatively attribute to the inhomogeneous separation of the solid ScH_2 phase and $LiBH_4$ melt, and the correspondingly nonuniform distribution of ScH_2 particles in the resulting NMR sample. The ^{6}Li MAS NMR spectra (shown in Fig. B.4d) also provide a distinctive signature of phase changes from $LiBH_4$ (-1.1 ppm) to $Li_2B_{12}H_{12}$ (-0.5 ppm). The presence of LiH was confirmed by independent ^{6}Li CPMAS NMR measurements (not shown) because extremely long spin-lattice relaxation behavior inhibited its observation during recording of the MAS spectra in Fig. B.4d. As with the XRD data, the NMR results identify the decomposition products of $LiBH_4$, but provide no evidence that ScH_2 has reacted to form the ScB_2 product.

Raman spectroscopy was used to probe the chemical composition of a $ScH_2 + 2\,LiBH_4$ mixture desorbed at 400 °C for 20 h. The results are shown in Fig. B.5. It was found that the desorption product segregated into two phases, which are visible in Fig. B.5 as white particles and dark particles. The dark particles and the as-milled $ScH_2 + 2\,LiBH_4$ mixture

did not have any Raman-active modes. However, the spectrum of the white particles bears a strong similarity to that of dehydrogenated $LiBH_4$. The B−H bending and stretching modes of $LiBH_4$ around $1300\,cm^{-1}$ and $2300\,cm^{-1}$ are present in both samples and, as observed previously, are not affected by decomposition at temperatures below 400 ℃ [143]. The broad peak at $1100\,cm^{-1}$ corresponds to vibrations in amorphous boron. The additional B−H bending and stretching modes around 500–1000 and $2500\,cm^{-1}$ are consistent with the calculated and measured B−H vibrational modes in $Li_2B_{12}H_{12}$ [145]. These results lead us to believe that the ball-milled $ScH_2 + 2\,LiBH_4$ mixture segregates back into its initial components upon the melting and solidifying of $LiBH_4$. The dark particles consist mainly of ScH_2, while the white particles consist mostly of $LiBH_4$ and its thermal decomposition products.

B.4 Discussion

The rate limiting steps of the absorption and desorption reaction of simple metal hydrides such as MgH_2 have been identified [146], but the reaction pathways of most destabilization-based reactions are still not well understood. Based on calorimetric and *in situ* XRD measurements, desorption in the $MgH_2 + 2\,LiBH_4$ system has been found to proceed in two distinct steps [147]:

$$MgH_2 \longrightarrow Mg + H_2 \tag{B.3}$$

$$Mg + 2\,LiBH_4 \longrightarrow MgB_2 + 2\,LiH + 3\,H_2. \tag{B.4}$$

An equivalent reaction pathway for the $ScH_2 + 2\,LiBH_4$ system would not work for the temperature range investigated here. Decomposition of ScH_2 does not occur until 900 ℃

[148, 149]. Well below this temperature, thermal decomposition of $LiBH_4$ should have already occurred independently. In principle, nanocrystalline ScH_2 may have a lower decomposition temperature due to excess surface energies and excess grain boundary enthalpies in the hydride phase. Reductions in the heat of formation of MgH_2 up to 30% have been estimated for crystallites smaller than 5 nm [150]. In practice, crystal grains with a minimum size of 10–15 nm are typically obtained with high energy ball-milling. Our own measurements of XRD peak broadening after ball-milling indicate an average ScH_2 crystallite size larger than 20 nm in the experiments. Moreover, the effect of nanocrystalline ScH_2 is complicated by the fact that $LiBH_4$ melts at 280 °C. Our results indicate that, above this melting temperature, the milled $ScH_2 + 2\,LiBH_4$ mixture segregates back into distinct phases. Another important insight is obtained by studying the desorption of a $Sc + LiBH_4$ system, which does not require the initial dehydriding of ScH_2. Significantly, it has been found that this reaction results in the formation of ScH_2 rather than ScB_2 [136]. From these results, it can be summarized that ScH_2 is not effective in destabilizing $LiBH_4$. Until the reaction mechanism is better understood, there is no simple way to surmount the significant reaction barriers present in this system.

B.5 Conclusion

Hydrogen sorption studies were performed on the $ScH_2 + 2\,LiBH_4$ system, identified by first-principle calculations as having favorable thermodynamics. Our experimental results demonstrate that H_2 desorption is consistent only with independent decomposition of $LiBH_4$. Extensive spectroscopic characterization (XRD, MAS NMR, Raman) failed to detect the ScB_2 product of the destabilization reaction. Due to the stability of ScH_2 and ScB_2, activation barriers in both directions appear to inhibit the predicted reaction at tem-

peratures below 450 °C. Sluggish kinetics mean that the destabilization reaction is unfavorable compared to competing reactions such as the independent decomposition of $LiBH_4$. Application of a H_2 pressure of ~ 900 bar to a heated $ScB_2 + 2\,LiH$ mixture was found to yield a minimal amount (i.e., $\sim$ 3 mol%) of the desired $LiBH_4$ phase. Furthermore, our findings suggest that the ball-milled $LiBH_4$-ScH_2 mixture segregates back into $LiBH_4$-rich and ScB_2-rich phases, due to the melting of $LiBH_4$. There was no indication that $TiCl_3$ assisted the destabilization reaction, although there was an improvement in the desorption kinetics.

Bibliography

[1] S. Studer, S. Stucki, and J. D. Speight. Hydrogen as a fuel. In A. Züttel, A. Borgschulte, and L. Schlapbach, editors, *Hydrogen as a Future Energy Carrier*. Wiley-VCH Verlag GmbH & Co. KGaA, Weinheim, 2008.

[2] A. Züttel. Hydrogen storage materials. *Naturwissenchaften*, 91:157–172, 2004.

[3] C. Read, G. Thomas, G. Ordaz, and S. Satyapal. U.S. Department of Energy's system targets for on-board vehicular hydrogen storage. *Material Matters*, 2(2):3–4, 2007. Material Matters is a publication of Aldrich Chemical Co., Inc.

[4] S. Satyapal, J. Petrovic, C. Read, G. Thomas, and G. Ordaz. The US Department of Energy's National Hydrogen Storage Project: Progress towards meeting hydrogen-powered vehicle requirements. *Catalysis Today*, 120(3-4):246–256, 2007.

[5] S. K. Bhatia and A. L. Myers. Optimum conditions for adsorptive storage. *Langmuir*, 22:1688, 2006.

[6] F. Rouquerol, J. Rouquerol, and K. Sing. *Adsorption by Powders and Porous Solids*. Academic Press, London, 1999.

[7] N. Stetson. (Private communication).

[8] J. K. Johnson and M. W. Cole. Hydrogen adsorption in single-walled carbon nanotubes. In E. J. Bottani and J. M. D. Tascón, editors, *Adsorption by Carbons*, chapter 15, pages 369–401. Elsevier, 2008.

[9] V. A. Parsegian. *Van der Waals Forces.* Cambridge University Press, New York, 2006.

[10] R. Lochan and M. Head-Gordon. Computational studies of molecular hydrogen binding affinities: The role of dispersion forces, electrostatics, and orbital interactions. *Phys. Chem. Chem. Phys.*, 8:1357–1370, 2006.

[11] G. J. Kubas. Fundamental of H_2 binding and reactivity on transition metals underlying hydrogenase function and H_2 production and storage. *Chem. Rev.*, 107:4152–4205, 2007.

[12] W. Zhou and T. Yildirim. Nature and tunability of enhanced hydrogen binding in metal-organic frameworks with exposed transition metal sites. *J. Phys. Chem. C Lett.*, 112:8132–8135, 2008.

[13] A. C. Dillon and M. J. Heben. Hydrogen storage using carbon adsorbents: past, present and future. *Appl. Phys. A*, 72:133, 2001.

[14] R. Ströbel, J. Garche, P. T. Moseley, L. Jörissen, and G. Wolf. Hydrogen storage by carbon materials. *J. Power Sources*, 159:781–801, 2006.

[15] E. L. Pace and A. R. Siebert. Heat of adsorption of parahydrogen and orthodeuterium on Graphon. *J. Phys. Chem.*, 63:1398–1400, 1959.

[16] Q. Wang and J. K. Johnson. Molecular simulation of hydrogen adsorption in single-walled carbon nanotubes and idealized carbon slit pores. *J. Chem. Phys.*, 110(1):577, 1999.

[17] M. Rzepka, P. Lamp, and M. A. de la Casa-Lillo. Physisorption of hydrogen on microporous carbon and carbon nanotubes. *J. Phys. Chem. B*, 102:10894–10898, 1998.

[18] S. Patchkovskii and T. Heine. Evaluation of the adsorption free energy of light guest molecules in nanoporous host strutures. *Phys. Chem. Chem. Phys.*, 9:2697–2705, 2007.

[19] M. G. Nijkamp, J. E. M. J. Raaymakers, A. J. van Dillen, and K. P. de Jong. Hydrogen storage using physisorption—materials demands. *Appl. Phys. A*, 72:619–623, 2001.

[20] B. Panella, M. Hirscher, and S. Roth. Hydrogen adsorption in different carbon nanostructures. *Carbon*, 43:2209–2214, 2005.

[21] F. S. Baker, C. E. Miller, A. J. Repik, and E. D. Tolles. Activated Carbon. In *Kirk-Othmer Encyclopedia of Chemical Technology*, volume 4, page 741. John Wiley and Sons, 2003.

[22] M. Felderhoff, C. Weidenthaler, R. von Helmolt, and U. Eberle. Hydrogen storage: The remaining scientific and technological challenges. *Phys. Chem. Chem. Phys.*, 9:2643–2653, 2007.

[23] S. H. Jhung, J. W. Yoon, J. S. Lee, and J.-S. Chang. Low-temperature adsorption/storage of hydrogen on FAU, MFI, and MOR zeolites with various Si/Al ratios: Effect of electrostatic field and pore structures. *Chem. Eur. J.*, 13(S):6502–6507, 2007.

[24] A. V. A. Kumar, H. Jobic, and S. Bhatia. Quantum effects of adsorption and diffusion of hydrogen and deuterium in microporous materials. *J. Phys. Chem. B*, 110:16666–16671, 2006.

[25] N. L. Rosi, J. Eckert, M. Eddaoudi, D. T. Vodak, J. Kim, M. O'Keeffe, and O. M. Yaghi. Hydrogen storage in microporous metal-organic frameworks. *Science*, 300:1127, 2003.

[26] H. K. Chae, D. Y. S.-P., J. Kim, Y. Go, M. Eddaoudi, A. J. Matzger, M. O'Keeffe, and O. M. Yaghi. A route to high surface area porosity and inclusion of large molecules in crystals. *Nature*, 427:523–527, 2004.

[27] H. Furukawa, M. A. Miller, and O. M. Yaghi. Independent verification of the saturation hydrogen uptake in MOF-177 and establishment of a benchmark for hydrogen adsorption in metal-organic frameworks. *J. Mater. Chem.*, 17:3197–3204, 2007.

[28] M. Dincă, A. Dailly, Y. Liu, C. M. Brown, D. A. Neumann, and J. R. Long. Hydrogen storage in a microporous metal-organic framework with exposed Mn^{2+} coordination site. *J. Am. Chem. Soc.*, 126:16876–16883, 2006.

[29] Craig M. Brown, Yun Liu, Taner Yildirim, Vanessa K Peterson, and Cameron J Kepert. Hydrogen adsorption in HKUST-1: a combined inelastic neutron scattering and first-principles study. *Nanotechnology*, 20:204025, 2009.

[30] Y. Liu, H. Kabbour, C. M. Brown, D. A. Neumann, and C. C. Ahn. Increasing the density of adsorbed hydrogen with coordinatively unsaturated metal center in metal-organic frameworks. *Langmuir*, 24:4772–4777, 2008.

[31] A. Züttel, P. Sudan, P. Mauron, and P. Wenger. Model for the hydrogen adsorption on carbon nanostructures. *Appl. Phys. A*, 78:941–946, 2004.

[32] N. Texier-Mandoki, J. Dentzer, T. Piquero, S. Saadallah, P. David, and C. Vix-Guterl. Hydrogen storage in activated carbon materials: Role of the nanoporous texture. *Carbon*, 42:2744–2747, 2004.

[33] P. Bénard and R. Chahine. Storage of hydrogen by physisorption on carbon and nanostructured materials. *Scr. Mater.*, 56:803–808, 2007.

[34] A. Züttel, P. Sudan, Ph. Mauron, T. Kiyobayashi, Ch. Emmenegger, and L. Schlapbach. Hydrogen storage in carbon nanostructures. *Int. J. Hydrogen Energy*, 27(2):203–212, 2002.

[35] E. Poirier, R. Chahine, and T. K. Bose. Hydrogen adsorption in carbon nanostructures. *Int. J. Hydrogen Energy*, 26:831–835, 2001.

[36] Y. Zhao, Y.-H. Kim, A. C. Dillon, M. J. Heben, and S. B. Zhang. Hydrogen storage in novel organometallic buckyballs. *Phys. Rev. Lett.*, 94(15):155504, Apr 2005.

[37] T. Yildirim, J. Íñiguez, and S. Ciraci. Molecular and dissociative adsorption of multiple hydrogen molecules on transition metal decorated C_{60}. *Phys. Rev. B*, 72(15):153403, Oct 2005.

[38] I. Cabria, M. J. López, and J. A. Alonso. Hydrogen storage in pure and Li-doped carbon nanopores: Combined effects of concavity and doping. *J. Chem. Phys.*, 128(14):144704, 2008.

[39] W.-Q. Deng, X. Xu, and W. A. Goddard. New alkali doped pillared carbon materials designed to achieve practical reversible hydrogen storage for transportation. *Phys. Rev. Lett.*, 92(16):166103, 2004.

[40] Y. Zhao, Y.-H. Kim, L. J. Simpson, A. C. Dillon, S.-H. Wei, and M. J. Heben. Opening space for H_2 storage: Cointercalation of graphite with lithium and small organic molecules. *Phys. Rev. B*, 78(14):144102, 2008.

[41] S. Challet, P. Azaïs, R. J. M. Pellenq, O. Isnard, J. L. Soubeyroux, and L. Duclaux. Hydrogen adsorption in microporous alkali-doped carbons (activated carbon and single wall nanotubes). *J. Phys. Chem. Solids*, 65(2-3):541–544, 2004.

[42] F. E. Pinkerton, B. G. Wicke, C. H. Olk, G. G. Tibbetts, G. P. Meisner, M. S. Meyer, and J. F. Herbst. Thermogravimetric measurment of hydrogen adsorption in alkali-modified carbon materials. *J. Phys. Chem. B*, 104:9460–9467, 2000.

[43] K. Fredenhagen and G. Cadenbach. Die Bindung von Kalium durch Kohlenstoff. *Z. anorg. Chem.*, 158(1):249–263, 1926.

[44] A. Herold. Recherches sur les composes dinsertion du graphite. *Bull. Soc. Chim. Fr*, 187:999–1004, 1955.

[45] W. Rüdorff and E. Schulze. Über Alkaligraphitverbindungen. *Z. anorg. Chem.*, 277(3–4):156–171, 1954.

[46] D. E. Nixon and G. S. Parry. Formation and structure of the potassium graphites. *Brit. J. Appl. Phys. (J. Phys. D.)*, 1:291–299, 1968.

[47] A. Herold and D. Saehr. Effects of hydrogen on insertion compounds of graphite with alkali metals. *Compt. rend.*, 250:545, 1960.

[48] K. Watanabe, T. Kondow, M. Soma, T. Onishi, and K. Tamaru. Molecular-sieve type sorption on alkali graphite intercalation compounds. *Proc. R. Soc. London, Ser. A*, 333:51–67, 1973.

[49] P. Lagrange, D. Guerard, J. F. Mareche, and A. Herold. Hydrogen storage and isostopic protium-deuterium exchange in graphite-potassium intercalation compounds. *Journal of the Less-Common Metals*, 131:371–378, 1987.

[50] T. Terai and Y. Takahashi. Formulation of isotherms for low-temperature absorption of H_2 and D_2 on KC_{24} prepared from natural graphite. *Synth. Met.*, 34:329–334, 1989.

[51] J. P. Beaufils, T. Crowley, T. Rayment, R. K. Thomas, and J. W. White. Tunnelling of hydrogen in alkali metal intercalation compounds. *Molecular Physics*, 44(6):1257–1269, 1981.

[52] L. Pauling. The rotational motion of molecules in crystals. *Physical Review*, 36(3):430–443, 1930.

[53] T. E. Stern. The symmetric spherical oscillator, and the rotational motion of homopolar molecules in crystals. *Proc. R. Soc. London, Ser. A*, 130(815):551–557, 1931.

[54] S. A. Solin and H. Zabel. The physics of ternary graphite intercalation compounds. *Advances in Physics*, 37(2):87–254, 1988.

[55] T. Enoki, S. Miyajima, M. Sano, and H. Inokuchi. Hydrogen-alkali-metal-graphite ternary intercalation compounds. *J. Mater. Res.*, 5(2):435–466, 1990.

[56] R. Nishitani, Y. Uno, and H. Suematsu. In situ observation of staging in potassium-graphite intercalation compounds. *Phys. Rev. B*, 27:6572, 1983.

[57] S. B. DiCenzo. Relaxed incommensurate structure of the intercalant layer in higher-stage graphite intercalation compounds. *Phys. Rev. B*, 26(10):5878–5881, 1982.

[58] Y. Arai, Y. Shirikawa, and S. Tamaki. Structural properties of low dimensional potassium metal in intercalated graphite. *Journal of Non-Crystalline Solids*, 205-207:803–806, 1996.

[59] J. B Hastings, W. D. Ellenson, and J. E. Fischer. Phase transitions in potassium-intercalated graphite: KC_{24}. *Physical Review Letters*, 42(23):1552, 1979.

[60] D. E. Nixon and G. S. Parry. Order-disorder transformation in potassium graphite. *Nature*, 216:909–910, 1967.

[61] F. Rousseaux, R. Moret, D. Guerard, and P. Lagrange. X-ray study of the liquid and solid phases of the alkali metals in KC_{24} and CsC_{24}-intercalated graphite single crystals. *Phys. Rev. B*, 42(1):725, 1990.

[62] R. Clarke, J. N. Gray, H. Homma, and M. J. Winokur. Evidence for discommensurations in graphite intercalation compounds. *Phys. Rev. Lett.*, 47(19):1407, 1981.

[63] G. R. S. Naylor and J. W. White. Structure of second-stage graphite-rubidium, $C_{24}Rb$. *J. Chem. Soc., Faraday Trans.*, 83:3447–3458, 1987.

[64] A. Lovell, F. Fernandez-Alonso, N. T. Skipper, K. Refson, S. M. Bennington, and S. F. Parker. Quantum delocalization of molecular hydrogen in alkali-graphite intercalates. *Phys. Rev. Lett.*, 101:126101, 2008.

[65] A. P. Smith, R. Benedek, F. R. Trouw, and L. H. Yang M. Minkoff. Quasi-two-dimensional quantum states of H_2 in stage-2 Rb-intercalated graphite. *Phys. Rev. B*, 53(15):10187, 1996.

[66] J. J. Murray and A. R. Ubbelohde. Electronic properties of some synthetic metals derived from graphite. *Proc. Roy. Soc. A.*, 312:371–380, 1969.

[67] M. S. Dresselhaus and G. Dresselhaus. Intercalation compounds of graphite. *Advances In Physics*, 51(1):1–186, 2002.

[68] T. Terai and Y. Takahashi. Sorption of hydrogen isotopes on potassium-carbon intercalation compounds at low temperatures. *Synthetic metals*, 7:46–55, 1983.

[69] I. Cabria, M. J. López, and J. A. Alonso. Enhancement of hydrogen physisorption on graphene and carbon nanotubes by Li doping. *J. Chem. Phys.*, 123:204721, 2005.

[70] K. Ichimura, E. Takamura, and M. Sano. Hydrogen in alkali-metal-graphite intercalation compounds. *Synth. Met.*, 40:355–368, 1991.

[71] C. C. Ahn, J. J. Vajo, B. Fultz, R. Yazami, and D. W. Brown. Neutron diffraction of stage 2 and stage 4 deuterided K-intercalated graphite at Los Alamos National Laboratory. Technical report, LANSCE Proposal # 20011042, 2002.

[72] A. J. Kidnay and M. J. Hiza. High pressure adsorption isotherms of neon, hydrogen, and helium at 76 K. *Adv. Cryog. Eng.*, 12:730–740, 1967.

[73] L. Zhou. Adsorption isotherms for the supercritical region. In József Tóth, editor, *Adsorption: Theory, Modeling, and Analysis*, volume 107 of *Surfactant Science Series*, page 211. Marcel Dekker, Inc., 2002.

[74] L. Czepirski and J. Jagiello. Virial-type thermal equation of gas-solid adsorption. *Chem. Eng. Sci.*, 44:797–801, 1989.

[75] H. W. Brinks, A. Fossdal, R. C. Bowman, and B. C. Hauback. Pressure–composition isotherms of $TbNiAlH_x$. *J. Alloys Compd.*, 417(1-2):92–95, 2006.

[76] E. W. Lemmon, M. L Huber, and M. O. McLinden. *NIST Standard Reference Database 23: Reference Fluid Thermodynamic and Transport Properties-REFPROP*. Number Version 8.0 in Standard Reference Data Program. National Institute of Standards and Technology, Gaithersburg, 2007.

[77] T. P. Blach and E. M. Gray. Sieverts apparatus and methodology for accurate determination of hydrogen uptake by light-atom hosts. *J. Alloys Compd.*, 446-447:692–697, 2007.

[78] B. Fultz and J. M. Howe. *Transmission Electron Microscopy and Diffractometry of Materials*. Springer, 2002.

[79] G. L. Squires. *Introduction to the Theory of Thermal Neutron Scattering*. Cambridge University Press, 1978.

[80] J. R. D. Copley, D. A. Neumann, and W. A. Kamitakahara. Energy distributions of neutrons scattered from C_{60} using the beryllium detector method. *Can. J. Phys.*, 73:763, 1995.

[81] J. R. D. Copley and J. C. Cook. The disk chopper spectrometer at NIST: a new instrument for quasielastic neutron scattering studies. *Chem. Phys.*, 292:477, 2003.

[82] W. Zhou, H. Wu, M. R. Hartman, and T. Yildirim. Hydrogen and methane adsorption in metal-organic frameworks: A high-pressure volumetric study. *J. Phys. Chem. C*, 111(44):16131–16137, 2007.

[83] G. H. Vineyard. Scattering of slow neutrons by a liquid. *Phys. Rev.*, 110:999–1010, 1958.

[84] R. Stockmeyer, H. J. Stortnik, and H. M. Conrad. Diffusive motions of molecules on catalytic surfaces. In *Proceedings of conference on neutron scattering*, page 303, Gatlinburg, Tennessee, 1976.

[85] P. L. Hall and D. K. Ross. Incoherent neutron scattering function for molecular diffusion in lamellar systems. *Mol. Phys.*, 36(5):1549–1554, 1978.

[86] C. T. Chudley and R. J. Elliott. Neutron scattering from a liquid on a jump diffusion model. *Proc. Phys. Soc. London*, 77:353, 1961.

[87] J. M. Rowe, K. Sköld, and H. E. Flotow. Quasielastic neutron scattering by hydrogen in the α and β phase of vanadium hydride. *J. Phys. Chem. Solids*, 32:41–54, 1971.

[88] D. K. Ross. Neutron scattering studies of metal-hydrogen systems. In H. Wipf, editor, *Topics in Applied Physics, Vol. 73*, page 153. Springer-Verlag, Berlin, Heidelberg, 1997.

[89] U. Stuhr, H. Wipf, R. K. Kremer, H. Mattausch, A. Simon, and J. C. Cook. A neutron-spectroscopy study of two-dimensional hydrogen diffusion in the hydride halide $YBrH_{0.78}$. *J. Phys.: Condens. Matter*, 6:147–158, 1994.

[90] R. E. Lechner. Effects of low-dimensionality in solid-state protonics conductors. *Solid State Ionics*, 77:280–286, 1995.

[91] A. J. Dianoux and F. Volino. Incoherent scattering law for neutron quasi-elastic scattering in liquid crystals. *Mol. Phys.*, 30(4):1181–1194, 1975.

[92] A. Meyer, R. M. Dimeo, P. M. Gehring, and D. A. Neumann. The High Flux Backscattering Spectrometer at the NIST Center for Neutron Research. *Rev. Sci. Instrum.*, 74:2759, 2003.

[93] J. D. Gale and A. L. Rohl. The general utility lattice program. *Mol. Simul.*, 29:291, 2003.

[94] G. Chen, Y. Guo, N. Karasawa, and W. A. Goddard III. Electron-phonon interactions and superconductivity in K_3C_{60}. *Phys. Rev. B*, 48:13959–13970, 1993.

[95] T. Róg, K. Murzyn, K. Hinsen, and G. R. Kneller. nMoldyn: A program package for a neutron scattering oriented analysis of molecular dynamics simulations. *Journal of computational chemistry*, 24(5):657–667, 2003.

[96] D. G. Narehood, J. V. Pearce, P. C. Eklund, P. E. Sokol, R. E. Lechner, J. Pieper, J. R. D. Copley, and J. C. Cook. Diffusion of H_2 adsorbed on single-walled carbon nanotubes. *Phys. Rev. B*, 67:205409, 2003.

[97] O.-E. Haas, J. M. Simon, S. Kjelstrup, A. L. Ramstad, and P. Fouquet. Quasielastic neutron scattering investigation of the hydrogen surface self-diffusion on polymer electrolyte membrane fuel cell catalyst support. *J. Phys. Chem. C*, 112:3121–3125, 2008.

[98] R. Kahn and E. Viennet E. C. De Lara. Diffusivity of the hydrogen molecule sorbed in NaA Zeolite by a neutron scattering experiment. *J. Chem. Phys.*, 91(8):5097–5102, 1989.

[99] H. Fu, F. Trouw, and P. E. Sokol. A quasi-elastic and inelastic neutron scattering study of H_2 in zeolite. *J. Low Temp. Phys.*, 116(3/4):149–165, 1999.

[100] F. Salles, H. Jobic, G. Maurin, MM Koza, PL Llewellyn, T. Devic, C. Serre, and G. Ferey. Experimental evidence supported by simulations of a very high H_2 diffusion in metal organic framework materials. *Physical Review Letters*, 100(24):245901, 2008.

[101] A. V. Skripov, M. A. Gonzalez, and R. Hempelmann. Evidence for a two-site localized hydrogen motion in C15-type YMn_2H_2. *J. Phys.: Condens. Matter*, 18:7249–7256, 2006.

[102] F. Fernandez-Alonso, F. J. Bermejo, C. Cabrillo, R. O. Loutfy, V. Leon, and M. L. Saboungi. Nature of the bound states of molecular hydrogen in carbon nanohorns. *Phys. Rev. Lett.*, 98:215503, 2007.

[103] H. Freimuth, H. Wichert, and H. J. Lauter. The commensurate-incommensurate transition of hydrogen monolayers physisorbed on graphite. *Surface Science*, 189/190:548–556, 1987.

[104] S. N. Coppersmith, D. S. Fisher, B. I. Halperin, P. A. Lee, and W. F. Brinkman. Dislocations and the commensurate-incommensurate transition in two dimensions. *Phys. Rev. B*, 25(1):349–363, 1982.

[105] J. M. Kosterlitz and D. J. Thouless. Ordering, metastability and phase transitions in two-dimensional systems. *J. Phys. C: Solid State Phys.*, 6:1181–1203, 1973.

[106] B. I. Halperin and D. R. Nelson. Theory of two-dimensional melting. *Phys. Rev. Lett.*, 41(2):121–124, 1978.

[107] K.J. Strandburg. Two-dimensional melting. *Rev. Mod. Phys.*, 60(1):161–207, 1988.

[108] H. Zabel, A. Magerl, J. J. Rush, and M. E. Misenheimer. Diffusion and melting in two dimensions: A quasielastic neutron scattering study of alkali metals in graphite. *Phys. Rev. B*, 40(11):7616–7632, 1989.

[109] Y. J. Glanville, J. V. Pearce, P. E. Sokol, B. Newalker, and S. Komarneni. Study of H_2 confined in the highly ordered pores of MCM-48. *Chem. Phys.*, 292:289–293, 2003.

[110] C. Cohen-Tannoudji, B. Diu, and F. Laloë. *Quantum Mechanics*, volume 1, chapter 6, pages 712–726. Wiley-Interscience, 1977.

[111] J. A. Young and J. U. Koppel. Show neutron scattering by molecular hydrogen and deuterium. *Phys. Rev.*, 135(3A):603–611, 1964.

[112] I. P. Jackson and J. W. White. Domain mobility and rotational tunneling of hydrogen in graphite intercalates. *Chem. Phys. Lett.*, 1987:397–399, 134.

[113] G. Kresse and J. Furthmüller. Efficient iterative schemes for ab initio total-energy calculations using a plane-wave basis set. *Phys. Rev. B*, 54(16):11169–11186, Oct 1996.

[114] J. P. Perdew, K. Burke, and M. Ernzerhof. Generalized gradient approximation made simple. *Phys. Rev. Lett.*, 77(18):3865–3868, Oct 1996.

[115] C. C. Marston and G. G. Balint-Kurti. The Fourier grid Hamiltonian method for bound state eigenvalues and eigenfunctions. *J. Chem. Phys.*, 91:3571, 1989.

[116] P. C. H. Mitchell, S. F. Parker, A. J. Ramirez-Cuesta, and J. Tomkinson. *Vibrational Spectroscopy with Neutrons*, chapter 6. World Scientific, Singapore, 2005.

[117] W. J. Stead, I. P. Jackson, J. McCaffrey, and J. W. White. Tunnelling of hydrogen in alkali-metal-graphite intercalation compounds. *J. Chem. Soc., Faraday Trans. 2*, 84(10):16669–1682, 1988.

[118] C.J. Carlile, G.J. Kearley, G. Lindsell, and J.W. White. Structural and dynamics aspects of the tunnelling of hydrogen in caesium-intercalated graphite. *Physica B*, 241-243:491–494, 1998.

[119] S. Grimme. Semiempirical GGA-type density functional constructed with a long-range dispersion correction. *Journal of computational chemistry*, 27(15):1787, 2006.

[120] `http://charm.cs.uiuc.edu/OpenAtom/`.

[121] H. S. Cheng, A. C. Cooper, G. P. Pez, M. K. Kostov, P. Piotrowski, and S. J. Stuart. Molecular dynamics simulations on the effects of diameter and chirality on hydrogen adsorption in single-walled carbon nanotubes. *J. Phys. Chem. B*, 109:3780, 2005.

[122] A. Gigras, S. K. Bhatia, A. V. Anil Kumar, and A. L. Myers. Feasibility of tailoring for high isosteric heat to improve effectiveness of hydrogen storage in carbons. *Carbon*, 45:1043, 2007.

[123] F. Stoeckli, T. A. Centeno, A. B. Fuertes, and J. Muniz. Porous structure of polyarylamide-based activated carbon fibers. *Carbon*, 34:1201, 1996.

[124] M. A. Daley, D. Tandon, J. Economy, and E. J. Hippo. Elucidating the porous structure of activated carbon fibers using direct and indirect methods. *Carbon*, 34(10):1191–1200, 1996.

[125] J. I. Paredes, A. Martínez-Alonso, and J. M. D. Tascón. Characterization of microporosity and mesoporosity in carbonaceous materials by scanning tunneling microscopy. *Langmuir*, 17:474, 2001.

[126] R. T. Yang. *Adsorbents: Fundamental and Applications*. Wiley Interscience, Hoboken, New Jersey, 2003.

[127] J. P. Olivier. Improving the models used for calculating the size distribution of micropore volume of activated carbons from adsorption data. *Carbon*, 36:1469, 1998.

[128] H. Kabbour, T. F. Baumann, J. H. Satcher Jr., A. Saulnier, and C. C. Ahn. Toward new candidates for hydrogen storage: High-surface-area carbon aerogels. *Chem. Mater.*, 18(26):6085, 2006.

[129] T. X. Nguyen and S. K. Bhatia. Characterization of activated carbon fibers using argon adsorption. *Carbon*, 43:775, 2005.

[130] A. Züttel, A. Borgschulte, and S.I. Orimo. Tetrahydroborates as new hydrogen storage materials. *Scr. Mater.*, 56(10):823–828, 2007.

[131] J. J. Vajo, S. L. Skeith, and F. Mertens. Reversible storage of hydrogen in destabilized $LiBH_4$. *J. Phys. Chem. B*, 109(9):3719–3722, 2005.

[132] J. J. Vajo, F. Mertens, C. C. Ahn, R. C. Bowman, and B. Fultz. Altering hydrogen storage properties by hydride destabilization through alloy formation: LiH and MgH_2 destabilized with Si. *J. Phys. Chem. B*, 108(37):13977–13983, 2004.

[133] J. J. Vajo and G. L. Olson. Hydrogen storage in destabilized chemical systems. *Scr. Mater.*, 56(10):829–834, 2007.

[134] J. J. Vajo, T. T. Salguero, A. F. Gross, S. L. Skeith, and G. L. Olson. Thermodynamic destabilization and reaction kinetics in light metal hydride systems. *J. Alloys Compd.*, 446:409–414, 2007.

[135] F. Pinkerton, M. Meyer, G. Meisner, M. Balogh, and J. Vajo. Phase boundaries and reversibility of $LiBH_4/MgH_2$ hydrogen storage material. *J. Phys. Chem. C*, 111(35):12881–12885, 2007.

[136] J. Yang, A. Sudik, and C. Wolverton. Destabilizing $LiBH_4$ with a Metal (M= Mg, Al, Ti, V, Cr, or Sc) or Metal Hydride (MH_2= MgH_2, TiH_2, or CaH_2). *J. Phys. Chem. C*, 111(51):19134–19140, 2007.

[137] S. V. Alapati, J. K. Johnson, and D. S. Sholl. Stability analysis of doped materials for reversible hydrogen storage in destabilized metal hydrides. *Phys. Rev. B*, 76(10):104108, 2007.

[138] S. V. Alapati, J. K. Johnson, and D. S. Sholl. Using first principles calculations to identify new destabilized metal hydride reactions for reversible hydrogen storage. *Phys. Chem. Chem. Phys.*, 9(12):1438–1452, 2007.

[139] D. J. Siegel, C. Wolverton, and V. Ozoliņš. Thermodynamic guidelines for the prediction of hydrogen storage reactions and their application to destabilized hydride mixtures. *Phys. Rev. B*, 76(13):134102, 2007.

[140] S. V. Alapati, J. K. Johnson, and D. S. Sholl. First principles screening of destabilized metal hydrides for high capacity H_2 storage using scandium. *J. Alloys Compd.*, 446:23–27, 2007.

[141] A. E. Bennett, C. M. Rienstra, M. Auger, K. V. Lakshmi, and R. G. Griffin. Heteronuclear decoupling in rotating solids. *J. Chem. Phys.*, 103(16):6951–6958, 1995.

[142] A. Züttel, P. Wenger, S. Rentsch, P. Sudan, P. Mauron, and C. Emmenegger. $LiBH_4$: a new hydrogen storage material. *J. Power Sources*, 118(1-2):1–7, 2003.

[143] S. Orimo, Y. Nakamori, N. Ohba, K. Miwa, M. Aoki, S. Towata, and A. Züttel. Experimental studies on intermediate compound of $LiBH_4$. *Appl. Phys. Lett.*, 89(2):021920, 2006.

[144] S. J. Hwang, R. C. Bowman Jr, J. W. Reiter, J. Rijssenbeek, G. L. Soloveichik, J. C. Zhao, H. Kabbour, and C. C. Ahn. NMR Confirmation for formation of $[B_{12}H_{12}]^{2-}$ complexes during hydrogen desorption from metal borohydrides. *J. Phys. Chem. C*, 112:3164–3169, 2008.

[145] N. Ohba, K. Miwa, M. Aoki, T. Noritake, S. Towata, Y. Nakamori, S. Orimo, and A. Züttel. First-principles study on the stability of intermediate compounds of $LiBH_4$. *Phys. Rev. B*, 74(7):075110, 2006.

[146] M. Dornheim, S. Doppiu, G. Barkhordarian, U. Boesenberg, T. Klassen, O. Gutfleisch, and R. Bormann. Hydrogen storage in magnesium-based hydrides and hydride composites. *Scr. Mater.*, 56(10):841–846, 2007.

[147] U. Bösenberg, S. Doppiu, L. Mosegaard, G. Barkhordarian, N. Eigen, A. Borgschulte, T.R. Jensen, Y. Cerenius, O.Gutfleisch, T. Klassen, M. Dornheim, and R. Bormann. Hydrogen sorption properties of MgH_2-$LiBH_4$ composites. *Acta Mater.*, 55(11):3951–3958, 2007.

[148] C. Kempter and J. McGuire. U.S. Patent 3,152,868. Preparation of Scandium Hydrides, 1964.

[149] Estimate of equilibrium compositions made using *Outokumpu HSC Chemistry* for Windows, version 4.0 (ChemSC, Inc., 1999).

[150] V. Bérubé, G. Radtke, M. Dresselhaus, and G. Chen. Size effects on the hydrogen storage properties of nanostructured metal hydrides: A review. *Int. J. Energy Res.*, 31(6):637–663, 2007.